

Studying the Metal Sites of Metallo-proteins by Electrochemistry and Spectroelectrochemistry



Yu Sun

St Cross College

Trinity 2024

A Thesis submitted to the Board of the Faculty of Physical Sciences, for
the Degree of Doctor of Philosophy, University of Oxford

Abstract

This thesis details the development and refinement of spectroelectrochemical methodologies aimed at advancing the study of redox-active protein complexes, particularly those containing iron-sulfur (FeS) clusters. Initially, a UV-Vis spectroelectrochemical cell (UV-Vis SEC) was engineered to facilitate in situ analysis of redox processes in FeS proteins, which proves crucial for understanding the redox behaviour of nitrogenase reductases and their homologues. Despite its utility, the complexity of certain catalytic components rendered UV-Vis SEC inadequate for all systems, hence the approach of electrochemical infrared microspectroscopy (ECIRM) was explored. This technique was applied to study the [FeFe] hydrogenase from *Desulfovibrio desulfuricans* (DdHydAB), serving as a model to explore application of this technique to oxygen-sensitive samples with intricate active sites that have the additional complication of catalysing proton reduction (H₂ evolution). The findings demonstrated that ECIRM is particularly effective in elucidating the complex redox dynamics and active site changes under experimentally challenging conditions.

Through these advanced methods, significant insights were gained into the stability of all-ferrous states and the environmental factors influencing them in proteins like NifH and AnfH. Challenges encountered with redox mediators in the presence of nucleotides underscored the need for novel mediators to avoid unwanted interactions during redox titrations. Furthermore, this research has not only enriched our understanding of FeS cluster chemistry in enzymatic systems

but also highlighted the critical need for innovative tools to accurately dissect the sophisticated mechanisms of redox proteins.

Overall, the establishment of UV-Vis SEC and ECIRM for these sensitive metalloproteins has opened new avenues for probing complex redox systems, marking a significant advancement in the field of bioinorganic chemistry.

Acknowledgements

I would first like to express my sincere gratitude to Professor Kylie Vincent for giving me the opportunity to work on such an exciting project in her lab. Throughout my time here, Kylie has provided consistent guidance and support. Her invaluable advice and steadfast encouragement over the last few years have been crucial to my progress and development.

I am immensely grateful to Dr. Patricia Rodriguez for her extensive support and guidance on my research, including her assistance with [FeFe] hydrogenase preparation, FTIR, and electrochemistry. Beyond her professional help, she has also been a true friend outside of the lab. Her dedication and kindness have been invaluable to my project,

I extend my heartfelt appreciation to all the past and present members of the Vincent group. To Ting, Shiny, Wangzhe, Xu, Jiaao, Jiaowen, Lucy, Maya, and Sam—I am profoundly grateful for the joy and companionship you have provided since the beginning. The memories we have created together are invaluable, and I look forward to witnessing the future achievements of each one of you.

I would also like to extend my deepest gratitude to our collaborators, whose contributions were vital to the success of our research. Prof. Lance Seefeldt from Utah State University, USA, generously provided the samples of NifH and AnfH from nitrogenases. Prof. Jürgen Moser from the Institut für Mikrobiologie, Technische Universität Braunschweig, Germany, supplied the critical samples of N₂B₂ and L₂ protein from dark-operative protochlorophyllide

oxidoreductase (DPOR). Additionally, our collaboration on electron paramagnetic resonance (EPR) spectroscopy with Dr. William Myers from CAESR was invaluable. Moreover, I am profoundly thankful for the expertise and support provided by Dr. Stephen Carr at the Research Complex at Harwell, who assisted in crystallising the *DdHydAB* sample. Their expertise, time, and resources have greatly enriched our work and I am immensely appreciative of their generosity and collaboration.

I would like to express my deepest gratitude to my family members, especially my parents and sister. Even though I am far from home, their encouragement and trust during my moments of doubt have been unwavering. With their support, I have been able to focus on my studies and research with peace of mind.

Statement on DPhil Progress Disruption Due to the COVID-19 Pandemic

The progress of my DPhil research has been substantially impacted by the COVID-19 pandemic, resulting in significant delays and disruptions. Initially, the closure of the host department from the end of March 2020 until mid-June 2020 forced our team to adopt remote working arrangements, entirely preventing access to laboratory facilities during this critical period. When the department reopened, stringent social distancing measures required a reduced building occupancy, limiting my laboratory work to an average of only 2 days per week over two terms.

Additionally, my personal health was directly affected as I contracted COVID-19 twice, leading to approximately one month of quarantine. This not only hindered my physical well-being but also further curtailed my ability to conduct essential experimental work. The impact of the pandemic extended to my supervisory support; my supervisor, Kylie, faced her challenges, including the need to work from home while caring for two children, which significantly reduced the frequency and efficacy of our meetings.

The broader academic opportunities were also compromised during this period. The pandemic prevented my attendance at several key conferences, crucial for networking and staying updated with the latest research developments. Furthermore, a planned collaboration involving work at a partner

institution's laboratory was cancelled due to travel restrictions and ongoing safety concerns.

These combined factors: departmental closures, restricted lab access, health issues, reduced supervisory support, and missed academic opportunities, have necessitated a revision of the timelines and objectives of my research project.

Each of these disruptions, driven by circumstances beyond my control, has contributed to the slowed progress of my DPhil program.

Abbreviations

ADP	Adenosine diphosphate
ATP	Adenosine triphosphate
ATR	Attenuated total reflectance
BAPTA	1,2-bis(o-aminophenoxy)ethane-N,N,N',N'-tetraacetic acid
CE	Counter electrode
Chlide	Chlorophyllide
CV	Cyclic voltammetry
<i>DdHydAB</i>	[FeFe] hydrogenase from <i>Desulfovibrio desulfuricans</i>
DPOR	Dark-operative protochlorophyllide oxidoreductase
DTPA	Diethylenetriamine-N,N,N',N'',N''-pentaacetate
<i>E</i>	Electrode potential
<i>E_m</i>	Midpoint potential
<i>E</i> [°]	Standard reduction potential
<i>E. coli</i>	<i>Escherichia coli</i>
ECIRM	Electrochemical IR microspectroscopy
EGTA	Ethylene glycol-bis(2-aminoethylether)-N,N,N',N'-tetraacetic acid
ET	Electron transfer
Eu-L	Europium-ligand complexes
FdI	Spinach ferredoxin
HAR	Hexaammineruthenium (III) chloride
IR	Infrared
MB	Methylene blue
MV	Methyl viologen

NaDT	Sodium dithionite
PFE	Protein film electrochemistry
Pchl _a	Protochlorophyllide
RE	Reference electrode
WE	Working electrode
SCE	Saturated calomel electrode
SEC	Spectroelectrochemistry
SHE	Standard hydrogen electrode
UV-Vis	Ultraviolet-visible
UV-Vis SEC	Ultraviolet-visible spectroelectrochemistry

Table of Contents

Studying the Metal Sites of Metallo-proteins by Electrochemistry and Spectroelectrochemistry	i
Abstract	i
Acknowledgements	iii
Statement on DPhil Progress Disruption Due to the COVID-19 Pandemic.....	v
Abbreviations	vii
Chapter 1 Introduction	1
1.1 Protein-bound FeS clusters	1
1.1.1 Overview of FeS clusters	1
1.1.2 Classification of Fe-S Redox Centres and general structural motif	2
1.2 MoFe Nitrogenase	4
1.2.1 Catalytic component of MoFe nitrogenase: the MoFe protein (NifDK)	5
1.2.2 Electron transfer component: the Fe protein (NifH)	6
1.2.3 Catalytic mechanism of nitrogenases	8
1.3 Alternative Nitrogenases.....	9
1.3.1 VFe Nitrogenase	10
1.3.2 FeFe nitrogenase	11
1.4 Nitrogenase homologues.....	14
1.4.1 Catalytic component: the N ₂ B ₂ protein (BchNB).....	16
1.4.2 Electron transfer component: the L ₂ protein (BchL).....	18
1.4.3 Comparison with nitrogenases.....	20
1.5 [FeFe] hydrogenases	21
1.5.1 Categories of [FeFe] hydrogenases.....	22
1.5.2 Overall structure of <i>DdHydAB</i>	24
1.5.3 H-cluster of [FeFe] hydrogenases.....	25
1.5.4 Catalytic cycle of [FeFe] hydrogenases.....	26
1.6 Typical methods employed to study FeS cluster containing proteins	28
1.6.1 UV-Vis spectroscopy	28
1.6.2 Electrochemistry	29
1.6.3 Electron paramagnetic resonance spectroscopy	30
1.6.4 Mössbauer spectroscopy.....	32
1.6.5 X-ray crystallography	33
1.7 Aim and scope of this thesis	34
Chapter 2 Experimental Methods and Theory.....	37
2.1 IR spectroscopy	37

2.1.1	π -acid ligands: CO and CN ⁻ in IR spectroscopy	37
2.1.2	IR spectroscopy modes	40
2.1.3	IR spectroscopy methods	41
2.2	UV-Vis spectroscopy	43
2.2.1	Introduction to UV-Vis spectroscopy	43
2.2.2	Beer-Lambert law	45
2.2.3	UV-visible spectroscopy of proteins	46
2.3	Electron paramagnetic resonance	47
2.3.1	Introduction to EPR.....	47
2.3.2	EPR study of metalloproteins and FeS proteins in particular	47
2.4	Electrochemistry	49
2.4.1	The three-electrode system	50
2.4.2	Cyclic voltammetry.....	51
2.4.3	Chronoamperometry	52
2.4.4	Electron transfer.....	53
2.5	Spectroelectrochemistry	54
2.5.1	Ultraviolet-visible spectroelectrochemistry	54
2.5.2	Electrochemical IR microspectroscopy	55
2.6	Over-expression of <i>DdHydAB</i> in <i>E. coli</i>	57
2.7	General methods, reagents and equipment.....	61
2.7.1	Protein source and handling.....	61
2.7.2	Anaerobic handling.....	62
2.7.3	Buffer preparation	62
2.7.4	Reference electrode potential conversion	62
2.7.5	MgATP/MgADP solution preparation	62
2.7.6	Other instrumentations	62
Chapter 3 Spectroelectrochemical studies of the [4Fe-4S] cluster in the Fe protein of nitrogenase: defining redox midpoint potentials		63
3.1	Cell development for the UV-vis spectroelectrochemistry.....	66
3.1.1	A review of the existing UV-Vis spectroelectrochemistry cells	66
3.1.2	The design of the UV-Vis spectroelectrochemistry cell.....	68
3.1.3	Redox mediators	73
3.1.4	Preliminary UV-Vis SEC experiment with Azurin	78
3.1.5	Data analysis with Nernst equation	80
3.2	Formation and characterisation of the all-ferrous state of the NifH.....	84
3.2.1	Formation of the all-ferrous state of the NifH	84

3.2.2	Stability of the all-ferrous state of NifH	87
3.2.3	Reversibility of formation of the all-ferrous state	89
3.3	Redox states of Fe protein controlled by electrochemistry	91
3.3.1	Attempt to form all-ferrous state electrochemically	91
3.3.2	Determining the potential range for redox titration	93
3.4	Determination of the redox potentials of the NifH	94
3.4.1	Redox titration of NifH in the absence of nucleotides	95
3.4.2	Redox titration of NifH in the presence of MgATP	98
3.4.3	Redox titration of NifH in the presence of MgADP	104
3.5	EPR studies of the NifH	107
3.6	Redox behaviour of the AnfH	111
3.6.1	Formation of the three oxidation states of the AnfH	112
3.6.2	Redox titration attempt on AnfH	113
3.7	Conclusion	115
Chapter 4	Redox behaviour of the Fe protein homologues	119
4.1	Development of the potentiometric titration method	121
4.1.1	Preliminary test with ferredoxin	121
4.2	Exploration of the all-ferrous state in DPOR	126
4.2.1	Exploration of the all-ferrous state in L ₂ protein	126
4.2.2	Exploration of the all-ferrous state in N ₂ B ₂ protein	128
4.3	Redox titration of the L ₂ protein	130
4.3.1	UV-Vis SEC titration on L ₂ protein	131
4.3.2	Potentiometric titration on L ₂ protein	133
4.4	Attempted redox titration of the N ₂ B ₂ protein	135
4.4.1	UV-Vis SEC titration on N ₂ B ₂ protein	136
4.4.2	Potentiometric titration on N ₂ B ₂ protein	138
4.5	Electrochemical reduction catalysis of Pchlide with N ₂ B ₂ protein	141
4.6	Conclusion	146
Chapter 5	Studies on DdHydAB via IR microspectroscopy on single crystals	148
5.1	Characterization of DdHydAB after Production and Artificial Maturation	150
5.2	Protection of DdHydAB with oxygen-stable H _{inact} state and reactivation	154
5.2.1	Preparation of the H _{inact} -state DdHydAB	155
5.2.2	Reactivation of DdHydAB from the H _{inact} state with electrochemistry	157
5.3	Probing the redox states of DdHydAB <i>in crystallo</i> via IR microspectroscopy	159
5.3.1	The reduction of the H _{ox} state	160
5.3.2	Myoglobin protection of the H cluster	168

5.3.3	Conclusion.....	172
5.4	Probing the redox states of <i>DdHydAB in crystallo</i> via IR microspectroscopy	
	Electrochemical IR microspectroscopy of <i>DdHydAB</i> crystals under various conditions	173
5.4.1	Spectroscopic Analysis of Redox-Dependent Changes in <i>DdHydAB</i> Crystals	174
5.4.2	The nature of 1933 cm ⁻¹ band	175
5.4.3	The reversibility of H-cluster states	177
5.4.4	Detecting the H _{hyd:ox} and H _{hyd:red} states of <i>DdHydAB in crystallo</i>	179
5.5	Conclusion	187
Chapter 6	Conclusion.....	190
References	193

Chapter 1 Introduction

1.1 Protein-bound FeS clusters

Iron-sulfur (FeS) clusters are structurally and functionally diverse cofactors that are found in a wide range of organism. [1] Typically, these clusters are composed of Fe ions, which, with few exceptions, are positioned in a distorted tetrahedral geometry and coordinated by inorganic sulfur atoms (S^{2-}) as well as sulfur-containing amino acid residues, predominantly from cysteine. [2] The adaptability of FeS clusters in structure and redox behaviour confers a diverse array of functions, making FeS clusters effective donors or acceptors of electrons in a wide range of biological activities, as well as catalysing enzyme reactions. [3, 4] Because of their importance, this thesis starts with a general review of proteins containing FeS clusters.

1.1.1 Overview of FeS clusters

FeS proteins are among the planet's oldest metalloproteins, as suggested by phylogenetic, protein-folding, and comparative biochemical analyses. [5-7] FeS proteins were first identified in the 1960s owing to an unusual $g = 1.9$ EPR signal that arises when they are reduced, which had never been seen previously in any metalloprotein. [8-10] The prevalence of these proteins, along with their distinct spectral characteristics and typically highly charged nature, made their purification and analysis easier.

FeS clusters are made up of inorganic S and Fe ions that are directly attached to the cysteinyl sulfurs of the related protein. These proteins accommodate various Fe to S stoichiometries, allowing for a wide diversity of FeS cluster configurations and a large array of reduction potentials, functioning as electron carriers in a variety of organisms

(Figure 1.1). [11] While the FeS centres are famous for their contribution to ET relays, they are also found at the active sites of many enzymes, where they perform a variety of functions [12] such as disulfide bond reduction, initiation or stabilisation of radical chain reactions, [13, 14] or functioning as Lewis acids. [15, 16] Furthermore, the FeS centres' oxidant sensitivity and a wide variety of redox states make them ideal candidates for sensing oxidative and metal stress and restoring cellular oxidative equilibrium. [13, 14, 17, 18]

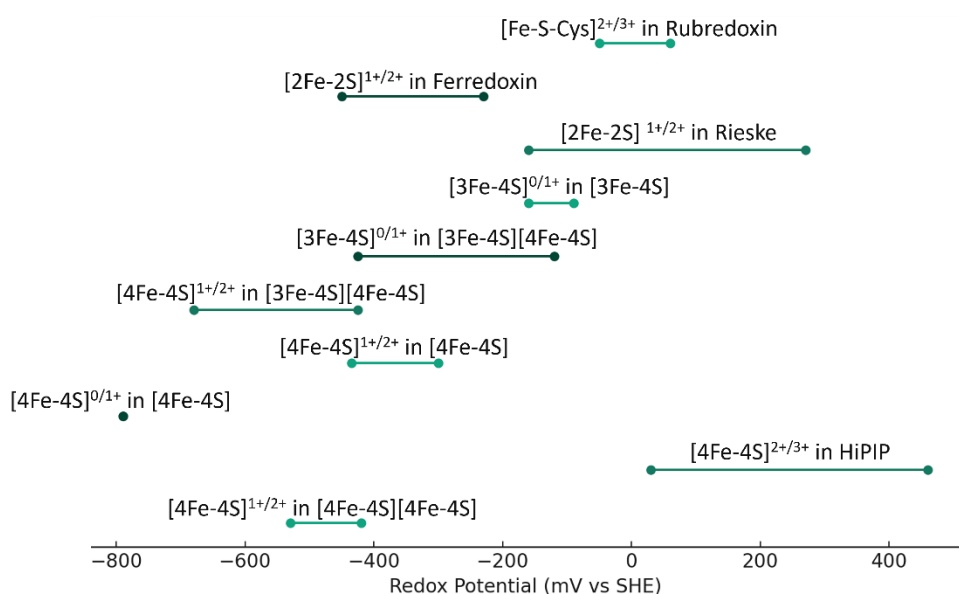


Figure 1. 1 Redox potential range of FeS clusters in the electron transfer process

1.1.2 Classification of Fe–S Redox Centres and general structural motif

As proposed by the Nomenclature Committee of the International Union of Biochemistry (IUB) in 1989, FeS clusters are usually classified according to the number of iron and sulfur atoms in the cluster. [19] Another more prevailing way to classify FeS is based on the certain protein type, structural motifs and spectroscopic and electrochemical characteristics, rather than merely the number of iron and sulfur atoms. The FeS proteins are broken down into four primary categories in this classification: rubredoxins, ferredoxins, Rieske proteins and high-potential iron–sulfur proteins

(HiPIPs), in addition to more complicated FeS proteins with several FeS cofactors or FeS cofactors associated with other cofactors (e.g. heme). [18, 20-24]

Within each class, FeS proteins share a similar structural motif despite specific differences in structural elements. Though structural motifs differ across classes, the geometries of the FeS clusters, particularly within each cluster class, are relatively similar. In nearly every FeS protein, a total number of four sulfur atoms from cysteine or inorganic sulfur coordinate to each iron atom, forming a distorted tetrahedral geometry. [4]

The [2Fe-2S] cluster of Ferredoxin I (FdI) from *Spinacia oleracea* resembles those of other ferredoxins, hence here it is taken as an example to illustrate the common structural motif accommodated by FeS proteins. The FdI is constituted by an α -helix ($\alpha 1$) and β -sheet (five strands $\beta 1$ - $\beta 5$) underneath the helix. A loop region thus is created by linking $\alpha 1$ and $\beta 3$, where the [2Fe-2S] cluster is located (Figure 1.2). Three of the four cysteine residues (Cys39, Cys44, and Cys47) that coordinate the two Fe atoms are located in this loop region. In this [2Fe-2S] cluster, the S-S distance is 3.6 Å, which is 1.3 times longer than the Fe-Fe distance (2.8 Å). The cluster is oriented in such a way that the Fe1 atom is more exposed to solvent, whilst Fe2 is located within the protein interior. The functional significance of the variations in the chemical environments of the two Fe atoms is that the more hydrophilic environment of Fe1 is expected to favour the localisation of the extra electron on Fe1 that is picked up by the cluster after protein reduction. [25] Due to the ability to take up electrons and the simple structure of the FdI, it is used as a model system to optimise the spectroelectrochemical cell for the study of FeS proteins (nitrogenase homologues) in this thesis (section 4.1).

As rubredoxins, Rieske proteins and high-potential iron–sulfur proteins (HiPIPs) are not studied in this thesis, they are not the focus of the introduction. In the following sections of this chapter, FeS enzymes that have been studied in this thesis will be introduced more elaborately, e.g. nitrogenase, nitrogenase homologues and hydrogenase.

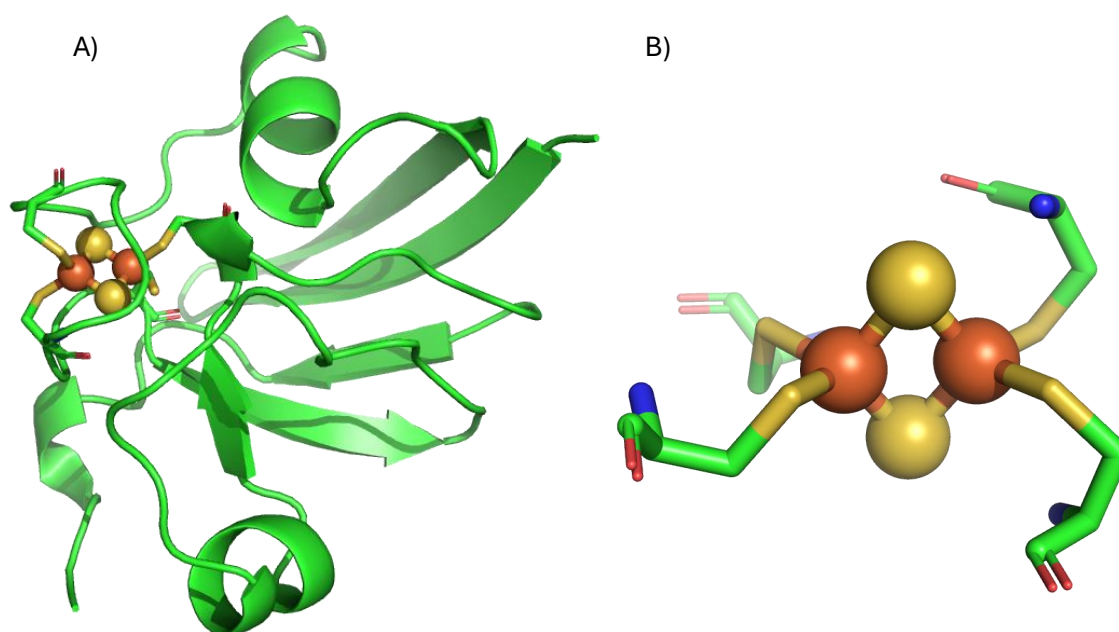


Figure 1. 2 A) Structure of the mutant E92K of [2Fe-2S] ferredoxin I from *Spinacia oleracea*; B) the [2Fe-2S] cluster residence in the loop region; PDB: 1A70

1.2 MoFe Nitrogenase

Nitrogenases are complex enzymes that catalyse the reduction of atmospheric nitrogen (N_2) to ammonia (NH_3), playing a crucial role in the nitrogen fixation process essential for biological nitrogen cycling. There are three types of nitrogenases according to the metal present in their active site: MoFe, VFe and FeFe nitrogenases, among which the MoFe nitrogenase is the most well-studied. [26] All types of nitrogenases consist of two proteins, a [4Fe-4S] cluster containing protein, called the Fe protein, that serves as electron transfer protein to shuttle electrons to the active site via the P-cluster;

and a catalytic protein MFe (where $\text{fmofeM} = \text{Mo, V, or Fe}$). The catalytic protein includes two metal cofactors, the P-cluster, a $[\text{8Fe-7S}]$ cofactor which also serves as an electron transfer centre, and the FeMco cluster (where $\text{M} = \text{Mo, V, or Fe}$ depending on the type of nitrogenases). FeMco is the catalytic cofactor where N_2 binds and gets reduced.

1.2.1 Catalytic component of MoFe nitrogenase: the MoFe protein (NifDK)

The MoFe protein from *Azotobacter vinelandii* ($M_r \sim 220$ kDa) is a $\alpha_2\beta_2$ -heterotetramer, encoded by *nifDK* genes. [27] Two metalloclusters that are crucial for catalysis reside in each $\alpha\beta$ -dimer, named the P-cluster and the MoFe cofactor, FeMoco (Figure 1.5). [28] The $[\text{8Fe-7S}]$ P-cluster can be viewed as two $[\text{4Fe-3S}]$ clusters partially bridged by sulfide. It sits at the $\alpha\beta$ -subunit interface and shuttles electrons between the $[\text{4Fe-4S}]$ cluster of the Fe protein (NifH) and FeMoco. The important electron-gating role played by the P-cluster is facilitated by its ability to reversibly reorganize its structure, thereby maintaining its capability to cycle through three oxidation states (P^{2+} , P^{1+} , P^{N}) and deliver electrons to FeMoco. [29]

The MoFe cofactor is the active site of the MoFe nitrogenase where substrates bind and get reduced. It is a $[\text{MoFe}_7\text{S}_9\text{C}]$ cluster, housed within the α -subunit of the MoFe protein (NifDK), [27] and is covalently bound to the MoFe protein via only two amino acid residues, the α -275Cys to the terminal Fe atom and the α -442His to the Mo atom. The Mo atom is coordinated by homocitrate. Spectroscopic, mutagenesis and crystallographic studies performed on the MoFe protein have led to the hypothesis that the most likely substrate binding site is either one or more of the central iron atoms on the $[\text{MoFe}_7\text{S}_9\text{C}]$ cluster. [30, 31]

1.2.2 Electron transfer component: the Fe protein (NifH)

The Fe protein of MoFe nitrogenase is a ~60 kDa homodimer encoded by the gene *nifH*. NifH plays an essential role in nitrogenase biosynthesis and catalysis. Aside from acting as the electron transfer partner to the MoFe protein during catalysis, it inserts the Mo and homocitrate for the maturation of the MoFe cluster and facilitates the biosynthesis of the P-cluster. [26, 32]

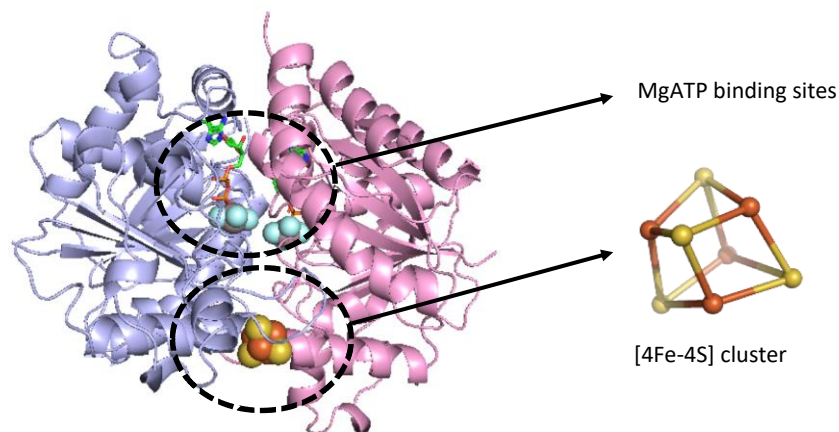


Figure 1.3 Left: Crystal structure of NifH from *Azotobacter vinelandii* (PDB: 1N2C). Right: close-up of the [4Fe-4S] cluster.

The electron transfer capabilities of the NifH are enabled by a solvent-exposed [4Fe-4S] cluster that sits at the homodimer interface and is attached to each subunit via Cys residues (Figure 1.3). This [4Fe-4S] cluster has been found to cycle between three different redox states: the most oxidised state [4Fe-4S]²⁺, the one-electron reduced [4Fe-4S]¹⁺ and the two-electron reduced [4Fe-4S]⁰ (also called all-ferrous or super-reduced state). It has been suggested that the [4Fe-4S] cluster in NifH only cycles between the oxidised [4Fe-4S]²⁺ and the one-electron reduced [4Fe-4S]¹⁺ states during catalytic turnover, however, it remains unclear whether the all-ferrous state takes part in native catalysis. [26, 33] The potential at which this all-ferrous state is formed remains highly controversial, and is suggested to be very negative. An all-ferrous state has also been

observed in small synthetic clusters but was reported to be very unstable. [34, 35] Interestingly, such a state seems to be stabilised in Fe protein of nitrogenase [36, 37]

The first formation of the all-ferrous state ($[4\text{Fe-4S}]^0$) at mild potential using methyl viologen (around -460 mV vs Standard Hydrogen Electrode, SHE) sparked new interest, as it suggested that this state could be physiologically relevant, enabling a more efficient two-electron transfer process between the $[4\text{Fe-4S}]^{2+}$ and $[4\text{Fe-4S}]^0$ states coupled with the hydrolysis of two ATP molecules. [38] Watt *et al.* found that flavodoxin hydroquinone (FldHQ), a physiologically relevant flavodoxin reductant, can reduce NifH to the all-ferrous state with 2 electrons from the $2+$ state, with a spin state $S = 0$ and a midpoint potential (E_m) of -460 mV, vs SHE. [39] On the other hand, studies by Mössbauer and electron paramagnetic resonance (EPR) gave evidence of a different all-ferrous state in NifH, formed at much more negative potentials, using Ti(III) citrate ($E_m < -800$ mV vs SHE) and Cr(II)-EDTA ($E_m = -1000$ mV vs SHE) as reductants. [40] This all-ferrous state was reported to have a spin state $S = 4$ and $E_m = -790$ mV, vs SHE. [36, 40] This species exhibits an unusual pink colour (the colour of $[4\text{Fe-4S}]$ containing proteins is usually brown), and a peak in the UV-Vis around 520 nm. This all-ferrous state was also reported in another publication where the very negative reducing agent Eu(II)-DTPA ($E_m = -1040$ mV vs SHE) was added to NifH to form $[4\text{Fe-4S}]^0$. However, here the E_m of the all-ferrous state was not determined. [37] A recent study showed that Eu(II)-DTPA-reduced NifH (i.e. the all-ferrous state, $[4\text{Fe-4S}]^0$) can reduce CO_2 to CO, which was confirmed by gas chromatography-mass spectrometry (GC-MS). [41] This non-native reactivity of the $[4\text{Fe-4S}]^0$ state of NifH is particularly interesting, but is perhaps not surprising as the potential

of the $S = 4$ all-ferrous state is very low c.a. -790 mV vs SHE, [40] and it contains the two electrons necessary to reduce CO_2 to CO.

1.2.3 Catalytic mechanism of nitrogenases

Most of the mechanistic information known about nitrogenases comes from the MoFe nitrogenase. [42] Reduction of N_2 involves a complex interaction between the two protein components, electrons, magnesium ATP (MgATP) and protons. [31, 43] The stoichiometry of the N_2 reduction occurring at the FeMoco cluster of the three types of nitrogenases is presented below:



During catalysis, NifH functions as an ATP-dependent electron donor to NifDK, and its $[4\text{Fe}-4\text{S}]$ cluster is thought to cycle between $1+$ and $2+$ redox states in a dynamic process that involves the association and dissociation of NifH and NifDK. It is believed that the reduced NifH has its $[4\text{Fe}-4\text{S}]$ cluster in the $1+$ oxidation state with two bound MgATP molecules. It was suggested that this reduced state is the one that temporarily binds to NifDK. [44-46] In this binding process, two MgATP molecules are hydrolysed into two MgADP molecules, and one electron is supposedly transferred from the $[4\text{Fe}-4\text{S}]^{1+}$ cluster of NifH to the $[8\text{Fe}-7\text{S}]$ cluster (the P-cluster) of NifDK (Figure 1.4 A). [47] Then, this electron is transferred from the P-cluster to FeMoco, where it is believed that substrates bind, and catalysis happens.

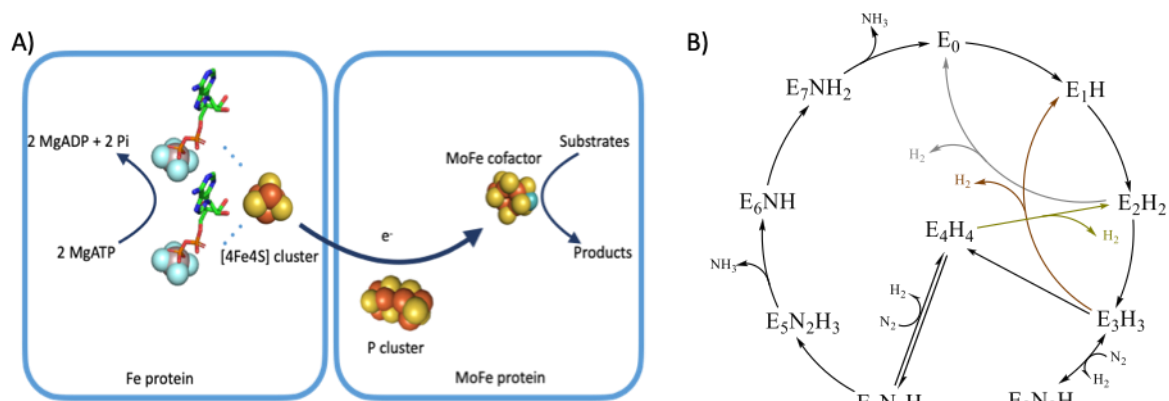


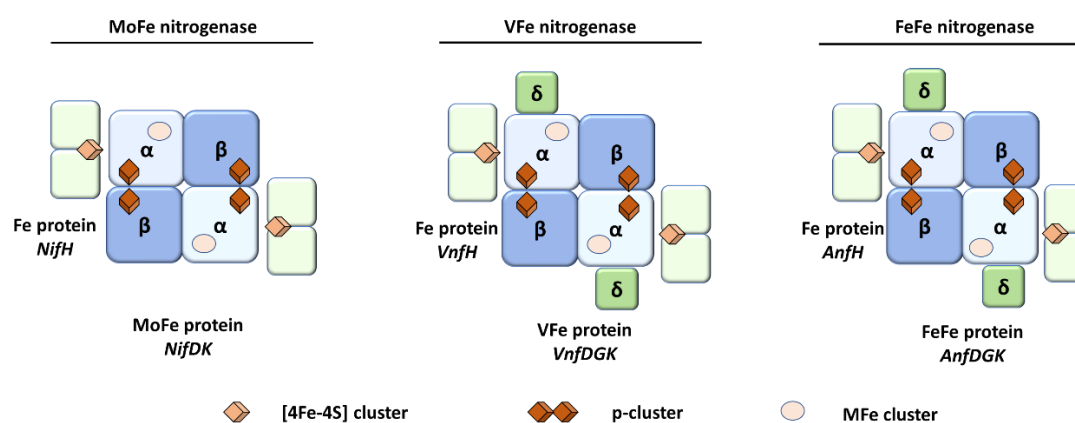
Figure 1.4 A) The ATP-coupled electron transfer among the clusters within the nitrogenase, illustrated with MoFe nitrogenase as example. Picture drawn with Pymol (PDB: 1N2C). B) Eight-electron reduction scheme for nitrogenase catalysis according to the Thorneley and Lowe model. [33, 48]

To date, at least eight catalytic intermediates (E₀, E₁, E₂, ..., E₈) have been proposed to take part in the catalytic cycle of nitrogenases, [33] as shown in Figure 1.4 B. E₀ is the resting state which is oxidised and cannot bind substrates. Different substrates bind to different reduced states, for instance, acetylene binds to a less-reduced state (E₂) than N₂, and N₂ is believed to bind to the E₄ states, with the release of one equivalent of H₂. It is thought that the redox levels have hydrides bound to the metals of FeMoco; each step involving the release of H₂ effectively leaves the metallocluster reduced by two electrons, and hence H₂ is an essential side product of nitrogenase catalysis. [48]

1.3 Alternative Nitrogenases

When Mo is deficient, diazotrophs induce the production of alternate nitrogenases (VFe and FeFe nitrogenases) as a vital backup. These nitrogenases lack the catalytic N₂ reduction efficiency of MoFe nitrogenase, but they have distinct catalytic activity of their own. For example, when MoFe nitrogenase reduces C₂H₂, it nearly always produces ethylene (C₂H₄), whereas VFe and FeFe nitrogenases produce a combination of C₂H₄ and completely reduced ethane (C₂H₆). [49, 50] The electrons are significantly more directed toward proton reduction during C₂H₂ reduction with alternative

nitrogenases than with MoFe nitrogenase, resulting in less efficient reduction of C_2H_2 . In addition, wild-type VFe nitrogenase from *A. vinelandii* has demonstrated unique reactivity in converting CO and H^+ into liquid hydrocarbon compounds, e.g. ethylene (C_2H_4), ethane (C_2H_6) and propane (C_3H_8). [51] CO, on the other hand, is a strong non-competitive inhibitor of MoFe nitrogenase. [52] The structural comparison of these three nitrogenase is illustrated in Scheme 1.1, more structural details will be included in the subsections.



Scheme 1. 1 Schematic representation of the catalytic components of the three nitrogenases found in *Azotobacter vinelandii*. Compared to MoFe nitrogenase, VFe and the FeFe nitrogenase is constructed with an extra subunit δ , encoded by *vnfG* and *anfG* genes, respectively

1.3.1 VFe Nitrogenase

The presence of molybdate (MoO_4^{2-}) and NH_3 suppresses the production of the *vnf* genes; in their absence, together with the availability of a sufficient vanadium supply (e.g. Na_3VO_4), the VFe nitrogenase can be expressed. [53, 54] Similar to MoFe nitrogenase, VFe nitrogenase is composed of a reductase component VnfH and a catalytic component VnfDGK. VnfH and NifH have 91% sequence identity. Rodhe *et al.* solved the structure of ADP-bound VnfH from *Azotobacter vinelandii* to 2.2 Å resolution. It reveals that VnfH shares the same conformation as NifH. VnfH and NifH differ by 27 amino acid exchanges, among which only H174 in NifH and N173 in VnfH is within the surface area

where the protein interacts with the respective catalytic component. [55] The [4Fe-4S] cluster of VnfH is observed in three oxidation states like NifH, including the all-ferrous state. [41]

VnfDKG or the VFe protein is the catalytic component of the VFe nitrogenase. It is an $\alpha_2\beta_2\delta_2$ hexamer composed of an $\alpha_2\beta_2$ core similar to NifDK, with the addition of two small δ subunits, encoded by vnfG, to NifDK. The atomic-resolution crystal structures provided a detailed insight into the architecture of the VFe cofactor. [56] The characterised P-cluster structure within VnfDGK is found nearly identical to that of NifDK. The P-cluster in 1+ state contributes to a $S = \frac{1}{2}$ EPR signal of VnfDGK. [57, 58] The crystal structure also reveals a significant difference between the VFe and MoFe cofactor. Mostly unexpectedly, the μ -2-sulfide in MoFe cofactor is replaced with a bridging CO_3^{2-} in VFe cofactor, making it a [V:7Fe:8S:C]: CO_3 :homocitrate cluster (Figure 1.5). [56]

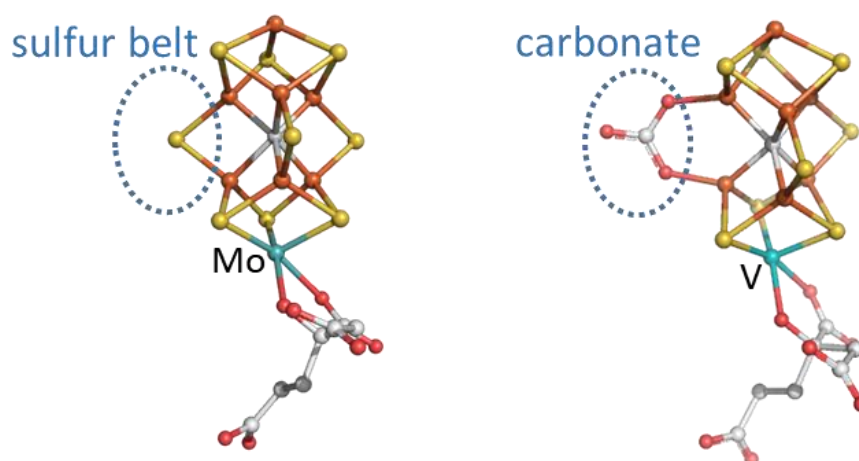


Figure 1.5 Structures of MoFe and VFe cofactors, where the sulfur belt in the MoFe cofactor is replaced with a bridging carbonate ligand in the VFe cofactor.

1.3.2 FeFe nitrogenase

The expression of FeFe nitrogenase is suppressed in the presence of Mo and V. First purified in 1988 from *Azotobacter vinelandii*, the FeFe nitrogenase is the least understood of the nitrogenase family. [59] The Fe-nitrogenase is an intriguing system for

exploring substrate reduction since it is capable of catalysing nitrogen fixation without the need of a heterometal such as Mo or V. From the perspective of being an all-Fe system for nitrogen fixation, FeFe nitrogenase is similar to the catalyst for the commercial Haber–Bosch process which fixes nitrogen under high-temperature, high-pressure. [60, 61] Furthermore, as evidenced by its capacity to support a methylophilic bacterium in co-culture when given CO₂ as a substrate, FeFe nitrogenase appears to be able to convert carbon dioxide (CO₂) to methane (CH₄). [62]

Davis *et al.* characterised AnFDGK from *Rhodospirillum rubrum* with perpendicular-mode EPR. The EPR spectrum is dominated by a signal in the $g = 1.94$ region, representing a rhombic $S = 1/2$ signal. This $S = 1/2$ signal is also observed in VnFDGK, which is thought to arise from a small percentage P-cluster in the P¹⁺ state. Compared to its heterometal-containing counterparts, the FeFe cofactor exhibits virtually nothing in the $g = 3.65$ region that represents $S = 3/2$ features. [63] Recently, Trncik *et al.* have reported the three-dimensional structure of FeFe nitrogenase from *Azotobacter vinelandii*, highlighting its FeFe cofactor, which features an [8Fe:9S:C]:homocitrate cluster. [64] This cluster includes an interstitial carbide and an organic homocitrate ligand attached to the apical iron. The conformation of the homocitrate ligand in the FeFe cofactor is strikingly similar to those in the FeMo and FeV cofactors. The consistent presence of homocitrate across all three types of nitrogenase suggests it plays a crucial functional role. Schmidt *et al.* using cryogenic electron microscopy (cryo-EM) determined the structure of the FeFe nitrogenase complex, stabilised by adenosine diphosphate-aluminum fluoride (ADP·AlF₃), at a resolution of 2.35 Å. The complex structure suggests that the G subunit of the FeFe nitrogenase plays a role in stabilising the FeFe cofactor, binding the reductase AnfH and channelling substrates. [65]

The reductase component of the FeFe nitrogenase AnfH is exceptional among the three Fe proteins of *Azotobacter vinelandii*. While NifH and VnfH were essentially identical, AnfH only share 60.8% and 61.5% sequence identity respectively with NifH and VnfH. In addition, cross-reactivity assays with the three nitrogenases showed that NifH and VnfH are compatible with each other's catalytic component, while AnfH is compatible to AnfDGK, and to a lesser extent with VnfDGK, but not with NifDK. Recently, Trncik *et al.* solved the crystal structure of the ADP-bound reductase component AnfH to 2.0 Å resolution. [62] The comparison of overall structures shows that AnfH from the diazotroph *Azotobacter vinelandii* adopts the same conformation as its counterparts NifH and VnfH in the ADP-bound state. It is found that at the surface area that interacts with their corresponding catalytic component, four residues from AnfH (residues K69, D141, K173 and Q174) are different from those of NifH (D69, E141, N173 and S174), while there is only one different interface residue between NifH (N173) and VnfH (H174), Figure 1.6.

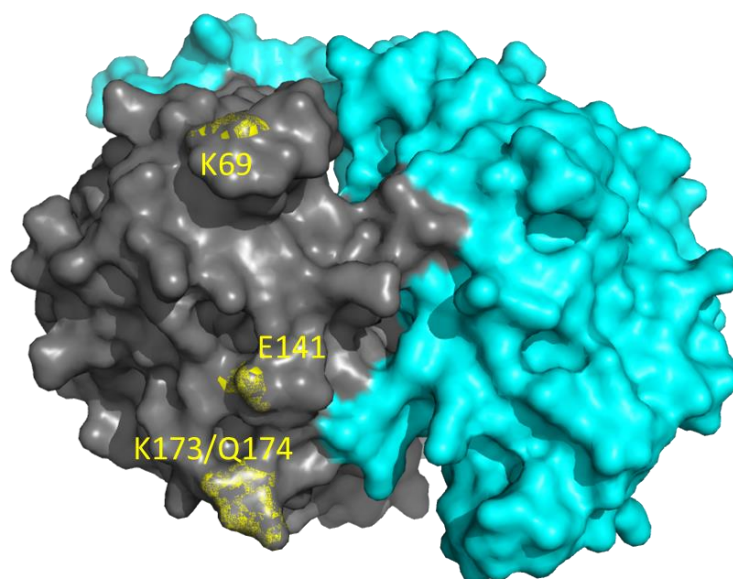


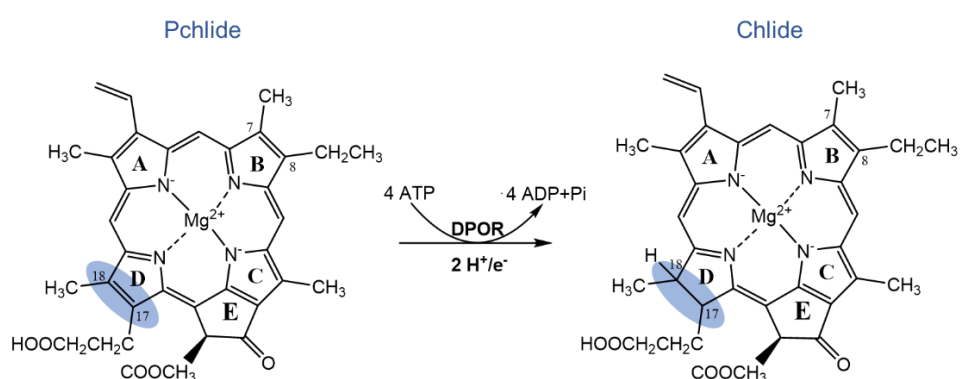
Figure 1. 6 Surface representation of the interaction surface of AnfH, modified from PDB 1N1P. The four residues in this region that differ from NifH K69, D141, K173 and Q174, are shown in yellow.

In the research by Trncik *et al.*, they found that less than 20% of N₂ reduction activity is retained when AnfH is used as the reductase to the catalytic component NifDK. The disturbance to the catalytic activity that arose from the changes of as few as four amino residues in the surface region is rather significant. As hypothesised in the paper, the transition from a negatively charged D69 in NifH, which interacts with residue K400 in NifDK, to a positively charged K70 in AnfH is expected to cause coulombic repulsion, which might disrupt the AnfH-NifDK interaction. Structural models of the Anfdgk and its complex with AnfH will be necessary to fully interpret the molecular basis for the compromised AnfH-NifDK interaction. [62]

1.4 Nitrogenase homologues

Aside from three types of nitrogenases (MoFe, VFe and FeFe nitrogenases), in recent years, a homologue enzyme to the nitrogenases called dark-operative protochlorophyllide oxidoreductase (DPOR) has been identified. [66]

Chlorophylls (Chl) and bacteriochlorophylls (Bchl) are crucial pigments employed in photosynthesis. [67] One step of their synthesis processes requires the reduction of the C17=C18 double bond at the ring D of protochlorophyllide (Pchlde) to form chlorophyllide (Chlide), which is catalysed by DPOR (Scheme 1.2). Similar to nitrogenases, DPOR is a two-component metalloprotein consisting of an electron transfer (reductase) component and a catalytic component (Figure 1.7).



Scheme 1. 2 Reduction of the C17=C18 double bond at the ring D of protochlorophyllide (Pchlde) to form chlorophyllide (Chlide) by DPOR with the consumption of 4 ATP, two protons and two electrons

The two components of DPOR form a functional complex during catalysis, which allows electron transfer from the reductase component to the catalytic component for the subsequent reduction of Pchlde in the N₂B₂ protein.[68] Although DPOR is not capable of reducing N₂, it catalyses double-bond reduction in a light-independent fashion. It is able to catalyse other two-electron reductions, e.g. reduction of N³⁻ or N₂H₄ to NH₃. [69] DPOR shares striking similarities in structure with nitrogenases but has a different function, therefore it is worth exploring this nitrogenase homologue, especially, the electron transfer component (L₂ protein) to see whether the [4Fe-4S] cluster in this protein is as unusual as the one in the Fe protein of the nitrogenase.

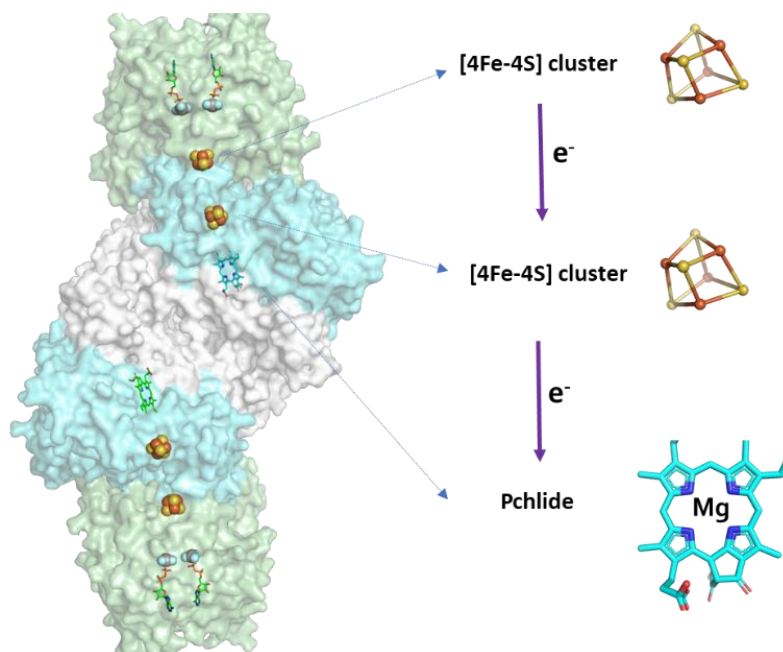


Figure 1. 7 Surface presentation (transparent) of the structure of the DPOR. The reductase L₂ protein is coloured light green; the two subunits of the catalytic component, N₂B₂ protein are coloured cyan and grey respectively. The clusters involved in electron transfer during catalysis are shown on the right side. (PDB: 2YNM). [70]

1.4.1 Catalytic component: the N₂B₂ protein (BchNB)

The N₂B₂ protein is the catalytic component, coded by *bchNB/chlNB* sharing 15% sequence identity with the MoFe protein (NifDK). Muraki *et al.* first elucidated the crystal structure of BchNB from *Rhodobacter capsulatus* at a resolution of 2.3 Å in 2010. [71] Later in the same year, a crystal structure of ChlNB from cyanobacterium *Thermosynechococcus elongatus* at a resolution of 2.4 Å were determined by Bröcker *et al.* [72] The tertiary and quaternary structures of BchNB and ChlNB complexes exhibit a great degree of resemblance with subtle differences.

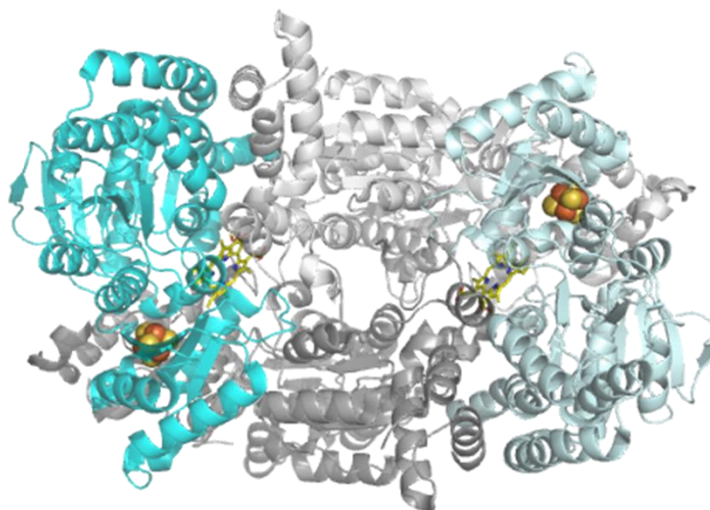


Figure 1. 8 Crystal structure of ChNB of DPOR; PDB code 2XDQ. The heterotetrameric catalytic complex of DPOR consists of two symmetrically positioned heterodimers of the related proteins ChlN and ChlB. The [4Fe-4S] cluster as shown in sphere mode; and the bound Pchlide as shown in stick mode coloured yellow.

Within expectation, the overall structure of ChlNB is comparable to that of the MoFe protein in nitrogenase. It is a symmetric $\alpha_2\beta_2$ - heterotetramer, with each $\alpha\beta$ subunit containing one [4Fe-4S] cluster (NB-cluster) and a Pchlide binding site. The NB-cluster in *T. elongatus* is bound at the ChlN/ChlB subunit interface, and coordinated by three conventional cysteine residues Cys22, Cys47, and Cys107 from ChlN and a unique aspartate residue, Asp36, from ChlB. Similarly, the NB-cluster in *R. capsulatus* is also coordinated by three cysteine residues and an aspartate residue (Asp36). The [4Fe-4S] cluster coordinated by aspartate found in BchNB/ChlNB is unprecedented in FeS enzymes, though aspartate has been found to ligate [4Fe-4S] clusters in ferredoxin. [73] The role of Asp36 has been evaluated by mutational analysis study, which has demonstrated that the cluster still assembles when Asp36 is replaced with Cys, Ser or Ala, but the catalytic activity is almost abolished in the variants.

The crystal structure of Pchlide-bound BchNB from *R. capsulatus* has shown that the Pchlide-binding cavity resides at the interface of four subunits of the BchNB complex,

surrounded by many hydrophobic residues. The shortest distance between Pchlide rings and the NB-cluster is 10.0 Å, which is short enough for the occurrence of electron transfer. [74] Halfway between the NB-cluster and Pchlide, a Phe residue (Phe25) that is completely conserved across all known BchN/ChlN proteins is found. [71] The Phe25 is suggested to play a significant role in through-space electron transfer, as the catalytic activity is halved once Phe25 is replaced with Ala. [75]

Two protons are required to attack the Pchlide D ring from opposite directions to trans-specifically reduce the C17=C18 bond simultaneously with electron transfer. The Asp 274 of BchB is the most likely candidate to donate a proton to C17 since the distance to the D ring is only 4.9 Å, though it is still too far for the H⁺ tunnelling. Besides the mutational studies demonstrate the loss of catalytic activity upon replacement of Asp 274 with Ala. The proton donated to C18 is proposed to be from the propionate itself of Pchlide. It is supported by the catalytic study of the substrate analogue of which acrylate is in the place of propionate. [71, 75]

1.4.2 Electron transfer component: the L₂ protein (BchL)

The L₂ protein is the electron transfer component (*bchL/chlL* genes), and shares up to 30% sequence identity with the Fe protein (NifH). Sarma *et al.* expressed L₂ protein (BchL) of (DPOR) from *Rhodobacter sphaeroides* in an *Azotobacter vinelandii* expression system, and determined the X-ray structure of it in the MgADP-bound state at 1.6 Å resolution. [66] BchL and the nitrogenase Fe protein are shown to have structural similarities overall, including the subunit bridging [4Fe-4S] cluster and nucleotide binding sites. Like the Fe protein, it is a homodimer in which each subunit has a MgATP binding site, and the two subunits are bridged by a [4Fe-4S] cluster (Figure 1.9). [46] [44] [44] [44] [44] [44] [44] [44] [44] [44] [44] [44] [44] [44] The four iron atoms of the

cluster are coordinated by the thiol ligands of Cys126 and Cys160 from each subunit. In addition to the cysteines, the cluster interacts with protein residues mainly through NH-S bonds. The [4Fe-4S] cluster of BchL has a similar structural environment to its counterpart in the Fe protein, with NH-S bonds formed with Gly residues of BchL and the sulfur atoms of the cluster. [66]

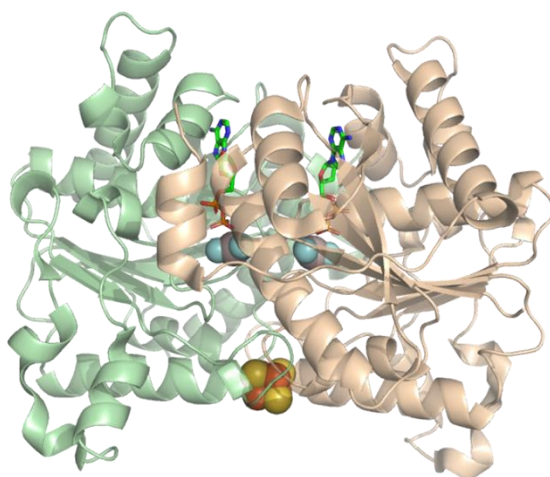
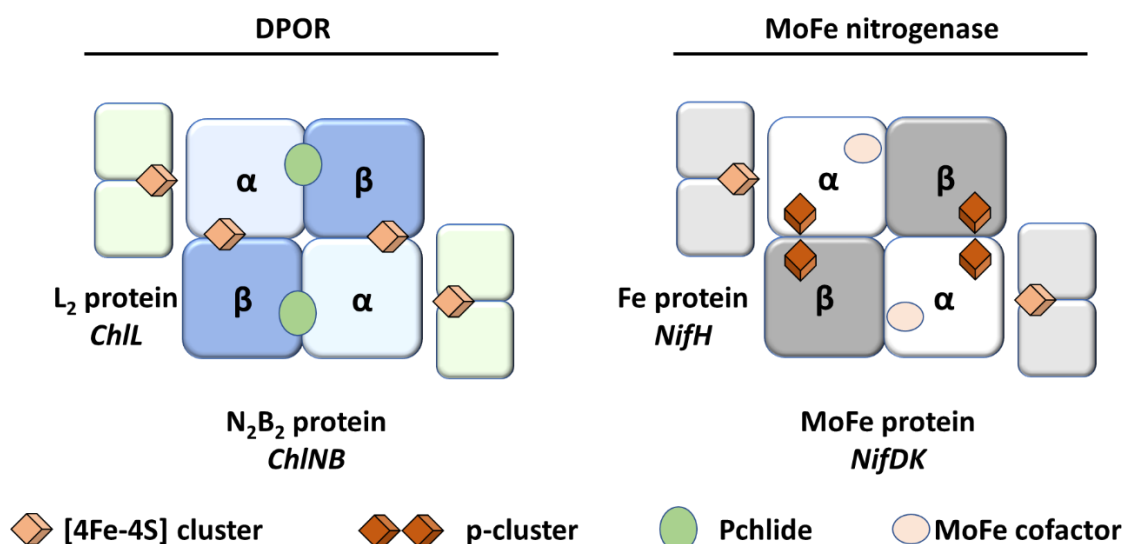


Figure 1. 9 Crystal structure of BchL of DPOR; PDB code: 3FWY. The homodimeric BchL has a MgATP binding site on each subunit, and the two subunits are bridged by a [4Fe-4S] cluster. The [4Fe-4S] cluster is shown as sphere mode, and the two identical subunits are shown as ribbon in green and beige.

There are considerable differences in surface charge of BchL and the Fe protein, notably at the putative docking faces for protein-protein interactions with their respective partners (BchNB and NifDK). Compared to the Fe protein, the docking face of BchL is more evenly positively charged. Cys126, Tyr129, Glu133, Gly161, Glu168, and His169 residues of BchL are involved in formation of the DPOR complex, while Cys97, Arg100, Thr104, Gly133, Arg140, and Glu141 of the Fe protein reside in analogous positions. [76] These residues differ significant in chemical properties as well as charges. In contrast to BchL, the residues of the Fe protein at the docking face are mainly negatively charged, apart from a few positively charged residues in the region of the [4Fe-4S] cluster.

In spite of their considerable structural resemblance, BchL and the Fe protein are not functionally compatible, which might be due to the significant differences at the docking surface. BchL is unable to replace the Fe protein as an electron donor to MoFe protein in a nitrogenase proton reduction assay. [77]



Scheme 1. 3 Schematic comparison of DPOR, and MoFe nitrogenase. The [4Fe-4S] clusters are shown as orange cube; the P-cluster of MoFe nitrogenase is shown as two connected brown cubes; the binding site for Pchlide in DPOR is shown as a green circle; and the binding site for MoFe cofactor in MoFe nitrogenase is shown as a pink circle.

1.4.3 Comparison with nitrogenases

As a homologue of the well-investigated nitrogenase, DPOR is similar to nitrogenase in many aspects. As illustrated in Scheme 1.3, they both form a complex with the electron-transfer homodimer and the catalytically-active heterotetramer during the catalytic cycle. The accommodation of several metallo-cofactors and their diverse substrates are the two main distinctions between DPOR and nitrogenase. NifDK bears the bigger P-cluster in a similar location to the intersubunit [4Fe-4S] cluster in ChINB. Contrarily, the second cofactor of NifDK, FeMoco, lacks a direct cofactor equivalent in DPOR. Nevertheless, the substrate Pchlide itself resides in the intersection of the

heterotetramer, ChlN, ChlB, and ChlN subunits, where it occupies the respective location of FeMoco in nitrogenase (structurally 6–7 Å away). [46]

Moser *et al.* studied the catalytic activity of DPOR towards artificial "small-molecule substrates" in comparison to those of nitrogenase and FeMoco-deficient apo nitrogenases. It is found that, akin to the catalytic activity of FeMoco-deficient apo nitrogenases, DPOR is able to catalyse the two-electron reductions of N^{3-} or N_2H_4 to NH_3 . [69]. Unlike nitrogenase, it cannot perform more complicated catalytic reduction of CO and N_2 that demands more than two electrons transferred. At the respective P-cluster site of the nitrogenase, it contains a pair of [4Fe-4S]-like clusters instead of the [8Fe-7S] cluster in the apo nitrogenase. Moser *et al.* hypothesise that lack of P-cluster is one of the causes for the limited substrate spectrum of DPOR. [78]

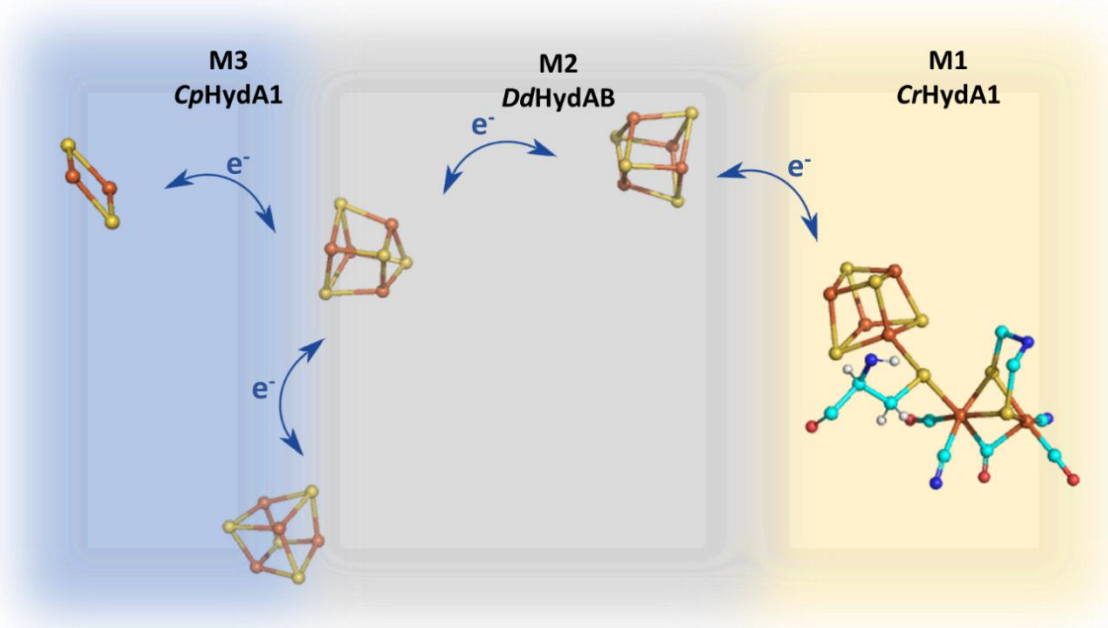
1.5 [FeFe] hydrogenases

Hydrogenases were first discovered and named by Stephenson and Stickland in 1931, and the structure and catalytic machinery of which have been broadly studied ever since. [79] The metal composition of their active site defines the category of the hydrogenases, and specifies them as [NiFe], the [FeFe], the [Fe]- hydrogenases. [80] Among all hydrogenases, the [FeFe] hydrogenases have gained special interest as they show the most efficient catalytic activity for hydrogen turnover, producing H_2 up to 8,000 $\mu\text{mol s}^{-1} \text{mg}^{-1}$ protein. [81] To design novel catalysts for effective H_2 generation, it is valuable to have a comprehensive understanding of the structural and reactivity characteristics of the active sites of [FeFe] hydrogenases. Recent advancements in synthetic, electrochemical, and spectroscopic techniques have expanded our knowledge of how electrons and protons interact at the active centre, as well as the

improved maturation protocols for recombinant [FeFe] hydrogenases producing sufficient amounts of protein for research. [82]

1.5.1 Categories of [FeFe] hydrogenases

Based on phylogenetic analysis, [FeFe] hydrogenases are divided into four categories: prototypical and bifurcating (group A), ancestral (group B), sensory (group C) and M2e (group D) enzymes. [83, 84] The prototypical [FeFe] hydrogenases of group A are the most characterised due to their high rates of hydrogen conversion. They feature a common H-domain that accommodates a catalytically active H cluster. [85] The structural differences of the proteins, especially the existence of additional FeS clusters (F-clusters), distinguish various subclasses of group A, as shown in Scheme 1.4



Scheme 1. 4 Schematic representation of electron relay in three types of [FeFe] hydrogenases. Subtype M1 only contains a 6-Fe H-cluster; subtype M2 contains two more [4Fe-4S] F-clusters; and subtype M3 contains a further [4Fe-4S] cluster and a plant-type ferredoxin [2Fe-2S] cluster.

Hydrogenase from the green algae *C. reinhardtii* (CrHydA1) represents the simplest subtype (M1) that only contains an H-cluster without auxiliary F-clusters. [86]

Crystallographic and spectroscopic research on relatively uncomplicated CrHydA1 have shed light on the catalytic mechanism including the significance of the proton-coupled electronic rearrangement between the two sites in the H-cluster. [87-91]

However, most [FeFe] hydrogenases possess auxiliary F-clusters, one function of which is to mediate electron transfer between the protein surface and the H-cluster. M2 subtype features an additional bacterial ferredoxin domain bound with two [4Fe-4S] F-clusters at the N-terminus of the H-domain. [92] The well-studied *DdHydAB* of *Desulfovibrio desulfuricans* is classified as this subtype, and the crystal structure has been determined, which will be described in the latter section 1.5.2. Apart from the two F-clusters in the M2 subtype, the M3 subtype contains two further N-terminal F-clusters, a [4Fe-4S] cluster ligated by three cysteine and one histidine, and a plant-type ferredoxin [2Fe-2S] cluster. Clostridial enzyme *CpHydA1* of *Clostridium acetobutylicum* falls into this subtype. [93] The M4 and M5 subtypes comprise up to two more C-terminal cluster binding motifs compared to the M3 subtype. They are less well characterised and not shown in Scheme 1.4. [94]

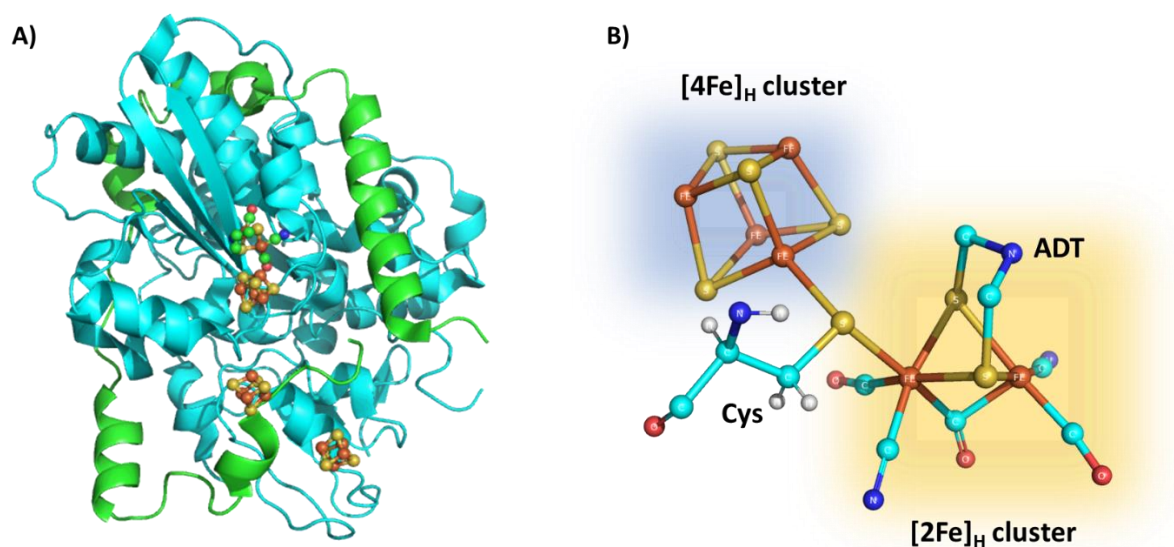


Figure 1. 10 A) Crystal structure of *DdHydAB* of *Desulfovibrio desulfuricans*; PDB code 1HFE. It is a heterodimer composed of a large subunit (ribbon in cyan) and a small subunit (ribbon in green). B) The structure of H-cluster in [FeFe] hydrogenases; sulfur (yellow), iron (brown), nitrogen (blue), carbon (cyan) and oxygen (red) atoms are represented as spheres.

1.5.2 Overall structure of *DdHydAB*

The crystal structure at 1.6 Å resolution of [FeFe] hydrogenase from *Desulfovibrio desulfuricans* (*DdHydAB*) was determined by Nicolet *et al.* in 1999. [95] It revealed that *DdHydAB* is a heterodimer composed of a large 42 kDa subunit and a small 11 kDa subunit, and is encoded by nearly identical genes to that of *DvHydAB* (from *Desulfovibrio vulgaris*). The small subunit (green in Figure 1.10 A) constitutes a stretched polypeptide chain with random coils and four α-helical structures, and this chain peculiarly wraps around the large subunit as a belt (cyan in Figure 1.10 A). Two cubical [4Fe-4S] F-clusters and one H-cluster are evenly spaced in the large subunit, providing an electron-transfer relay between the active site and the protein surface. The significance of the H-cluster as the catalytic active centre cannot be stressed enough, and it will be introduced in section 1.5.3.

1.5.3 H-cluster of [FeFe] hydrogenases

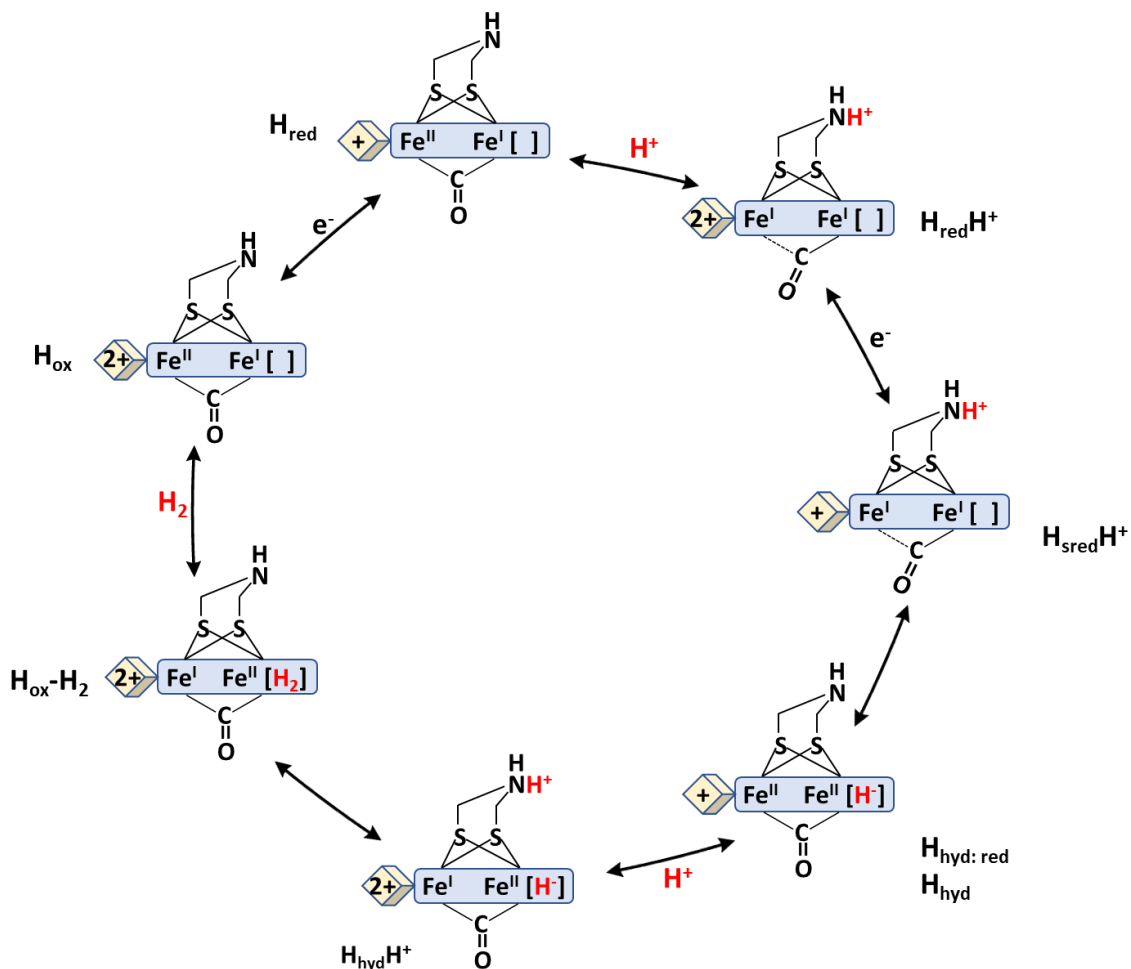
Before the publication of the first crystal structure of the [FeFe]-hydrogenase from *C. pasteurianum* by Peters *et al.*, the knowledge of the H-cluster was limited to the understanding that it was an FeS cluster with Fe atoms coordinated by light atoms from magnetic circular dichroism (MCD) studies. [96, 97] The light atoms are later confirmed to be CN⁻ and CO by infrared spectra of [FeFe] hydrogenase. [98] Around 2000, a breakthrough occurred in the research into this cluster when the X-ray studies of [FeFe] hydrogenase from *C. pasteurianum* (CpHydA1 or Cpl) and from *D. desulfuricans* (DdHydAB or DdH) presented a consensus structure for the H-cluster. [99] This consensus structure reveals the H cluster is composed of a [4Fe-4S] cubane and a binuclear [2Fe] centre bridged via a cysteine. The two Fe atoms in the [2Fe] centre were found linked by a unique dithiolate bridging group. The centre atom in the dithiolate group was not identified due to the resolution of the crystal structure, putatively O, C or N. It was identified as an N atom using ¹⁴N hyperfine sublevel correlation spectroscopy (¹⁴N-HYSCORE) in 2009, [100] and later was further confirmed when an artificially-matured [FeFe] hydrogenase containing 2-azapropane-1,3-dithiolate (ADT) showed identical catalytic activity to the biosynthesised enzyme. [82] The structure of the unique H cluster will be described below (Figure 1.10 B).

The H-cluster is composed of two FeS sites, a [4Fe-4S] cubane ([4Fe]_H) and a diiron centre ([2Fe]_H), linked via a cysteine thiolate bridge. The [4Fe]_H cluster is coordinated by four cysteine residues, with three of them attached to the protein scaffold, and the fourth bridging to the [2Fe]_H cluster. The distance of Fe-S-Fe between these two FeS clusters is as short as 4 Å which enables an efficient electronic coupling.

The $[2\text{Fe}]_{\text{H}}$ cluster is the binding site of substrates, and has distinct differences from other common FeS clusters. The proximal Fe (Fe_p) is the connection point to the $[4\text{Fe}]_{\text{H}}$ cluster via the cysteine residue. Furthermore, it is coordinated by one CO molecule and a CN^- group that stabilises the cluster by forming a hydrogen bond to the protein scaffold (labelled $_p\text{CO}$ and $_p\text{CN}^-$ respectively). [101] Equally, the distal Fe (Fe_d) possesses one CO and one CN^- as intrinsic ligands ($_d\text{CO}$ and one $_d\text{CN}^-$), with one coordination site open for substrate binding. These two iron centres are bridged by a third CO ligand and a distinct ADT group. This ADT group represents the key feature of the $[2\text{Fe}]_{\text{H}}$ cluster which remained mysterious for decades as stated in preceding text. The amine moiety of ADT is assumed to function as a proton relay from the open coordination site at the Fe_d to the $[4\text{Fe}]_{\text{H}}$ subcluster. [102]

1.5.4 Catalytic cycle of $[\text{FeFe}]$ hydrogenases

As a M1 type $[\text{FeFe}]$ hydrogenase, CrHydA1 is the most popular candidate for the studies of catalytic mechanism of $[\text{FeFe}]$ hydrogenase, since the spectroscopic signals of its only H-cluster remain unperturbed from any additional F cluster contained in other types. Based on the crystallographic and spectroscopic studies, two predominant models under heated discussions are proposed. Herein, the dominant model favoured by more researchers will be described and discussed (Scheme 1.5).



Scheme 1. 5 A model of catalytic cycle of [FeFe] hydrogenase. The electron transfer process is coupled with proton transfer. The $[4\text{Fe}-4\text{S}]_{\text{H}}$ clusters are shown as yellow cubes labelled with oxidation state; and the terminal CO and CN⁻ ligands of $[2\text{Fe}]_{\text{H}}$ cluster are not shown for simplicity.

It is worth remarking that the H-cluster is composed a $[2\text{Fe}]_{\text{H}}$ cluster and a $[4\text{Fe}-4\text{S}]_{\text{H}}$ cluster. During the turnover the former alternates between an oxidised Fe(II)Fe(I) state, a one-electron reduced Fe(II)Fe(I) state and a two-electron reduced Fe(I)Fe(I) state, while the latter cluster alternates between the 2+ state and the 1+ state. H_{ox} is the most oxidised active state in the cycle, composed of an Fe(II)Fe(I) $[2\text{Fe}]_{\text{H}}$ cluster and an oxidised $[4\text{Fe}-4\text{S}]_{\text{H}}$ cluster. The one-electron reduction of H_{ox} could happen either on the $[2\text{Fe}]_{\text{H}}$ cluster or the $[4\text{Fe}-4\text{S}]_{\text{H}}$ cluster. At high pH, the $[4\text{Fe}-4\text{S}]_{\text{H}}$ cluster is reduced to the 1+ state forming deprotonated H_{red} , while at lower pH, a protonated form ($\text{H}_{\text{red}}\text{H}^+$) is more stable with the $[2\text{Fe}]_{\text{H}}$ cluster at Fe(I)Fe(I) state. It was proposed that protonation most

likely takes place on the nitrogen of the ADT ligand, forming an NH_2^+ . The forming of $\text{H}_{\text{red}}\text{H}^+$ involves an essential proton-coupled electron transfer (PCET) process, which leaves the $[\text{4Fe-4S}]_{\text{H}}$ site in its oxidised 2+ state. Further reduction of the $[\text{4Fe-4S}]_{\text{H}}$ site results in a super-reduced state ($\text{H}_{\text{sred}}\text{H}^+$) with a protonated ADT amine. The electrons and protons of $\text{H}_{\text{sred}}\text{H}^+$ rearrange to yield a $\text{H}_{\text{hyd:red}}$ (H_{hyd}) state possessing a terminal hydride at Fe_{d} . One proton and a pair of electrons have been acquired to form H_{hyd} from H_{ox} , and only one more proton is demanded to generate hydrogen. The protonation of H_{hyd} on the ADT amine leads to the formation of hydrogen. The catalytic cycle is completed when the H_{ox} state is regenerated upon the release of the product. [90, 103, 104]

1.6 Typical methods employed to study FeS cluster containing proteins

A unique feature of FeS proteins is the presence of mixed-valence species, which have long been the focus of research. Due to the rich electronic structure and magnetic properties of Fe atoms, a wealth of techniques can be used to study Fe-containing centres. Most of the conventional bioinorganic methods have been applied to study FeS proteins, including EPR, X-ray crystallography, Mössbauer and UV-vis. Electrochemistry is also frequently used to study FeS proteins because of their intriguing redox properties.

1.6.1 UV-Vis spectroscopy

Ultraviolet-visible (UV-Vis) spectroscopy is absorption spectroscopy or reflectance spectroscopy of electromagnetic radiation in the range of near-UV (180–390 nm) or visible (390–780 nm) light. The energy carried by the UV-Vis radiation can be absorbed by chromophores and cause electronic transitions. The UV-Vis spectra are usually broad and inadequately show fine structure due to the superposition of

subspectra arising from vibrational and rotational transitions. For this reason, it is primarily used for the quantitative analysis of the chemical species in the solution. According to Beer-Lambert law, the concentration of a certain chromophore varies linearly relative to the absorbance of the solution under controlled conditions.

UV-Vis spectroscopy is highly exploited in biochemistry being a relatively inexpensive, non-destructive and rapid methodology. It is especially useful for the concentration determination and kinetics measurements and can be combined with the electrochemical methods to determine the redox potentials of enzymes. This methodology including typical spectroscopic features of FeS proteins will be further introduced in chapter 2.2.

1.6.2 Electrochemistry

Electrochemistry is used to study the interrelation of electrical and chemical effects. By applying an external voltage in an electrochemical cell, redox reactions can be driven and followed by measuring the electrical current. [70] Electrochemical techniques are useful for studying a dynamic system like a redox enzyme. Hence they are commonly used to investigate FeS proteins which are known for their roles in electron transfer.

The application of electrochemical method is not limited to redox potential determination. It plays a pivotal role in the studies of thermodynamics and kinetics of the catalytic reactions of enzymes. For instance, the protonation and substrate binding following electron transfer could be studied kinetically with electrochemical control. Since it allows precise potential control and very high temporal resolution, this method could be used to measure the turnover rate of enzymes.

Voltammetry and amperometry are two of the commonly used electrochemical techniques. Voltammetry is a technique that monitors the current while the potential is varied in a regular manner. For example, the redox chemistry of *Sulfolobus acidocaldarius* 7Fe ferredoxin was studied using cyclic voltammetry. [105] The protein sample was adsorbed at a pyrolytic graphite electrode. The two redox transitions of the [3Fe-4S] cluster (1+/0 and 0/2-), and of the [4Fe-4S] cluster (2+/1+) were revealed by cyclic voltammetry, as well as the redox potentials.

Amperometry monitors current changes analogous to voltammetry, but at fixed potentials where molecules can undergo electrochemical oxidation or reduction. The generated current is related to the concentration or the activity of the redox species at the interface. For example, a chronoamperometry study of nitrate reductase showed that its activation is irreversible after the first time upon reduction, and a high concentration of nitrate inhibits its activity at a moderate potential. [106]

In this project, electrochemical techniques will be mainly used for controlling the redox state of enzymes. More details including the electron transfer process will be introduced in Chapter 2.4.

1.6.3 Electron paramagnetic resonance spectroscopy

Electron paramagnetic resonance (EPR), also known as electron spin resonance (ESR), is a powerful analytical method, mostly used to detect and analyse the properties of unpaired electrons in substances. Most of the electrons in a molecule are paired, and according to the Pauli exclusion principle, the electrons in each pair must be one spin up and one spin down, so the magnetic moments cancel each other out. [107] Therefore,

particles with unpaired electrons are paramagnetic and show the phenomenon of magnetic resonance.

The principle of electron spin resonance is analogous to that of nuclear magnetic resonance with electron spins excited instead of nuclear spins. In contrast to optical spectroscopy, the EPR samples are exposed to a microwave of fixed frequency, while the applied magnetic field is varied. Absorption occurs when the difference of electron energy levels caused by the magnetic field matches the microwave energy, and the unpaired electrons can move between the two energy levels.

Since the state of electrons in a substance has a great influence on its properties and function, the evaluation of EPR has become increasingly important. In biology, EPR is applicable to whole macromolecular protein complexes to identify the metal content and the coordination environment etc. FeS clusters in redox proteins (e.g. ferredoxins) usually exhibits more than one oxidation state. [108-110] They are EPR-active in at least one state, so FeS proteins are good subjects for EPR techniques and widely investigated by EPR. The most common spin state of paramagnetic FeS clusters is $S = 1/2$. For example, the [4Fe-4S] clusters of Fe protein from nitrogenase in the reduced ($[4\text{Fe-4S}]^{1+}$) state have a $S = 1/2$ state, and are oxidised by one electron to a $[4\text{Fe-4S}]^{2+}$ state with $S = 0$. [111, 112]

EPR is a powerful technique for the study of biological molecules, due to the fact that it only examines paramagnets, and it is often used to give an image of a metal coordination complex in a metalloprotein. In other words, the EPR findings are constrained to specific parts of the protein. Besides, most transition metal systems can only be studied at cryogenic temperatures ($T < 100 \text{ K}$), which limits the usage of EPR *in situ*. Further discussions of EPR will be included later in Chapter 2.3.

1.6.4 Mössbauer spectroscopy

Mössbauer spectroscopy is an established technology for the study of bioinorganic species. The foundation of this spectroscopy is the Mössbauer effect discovered in 1958, which is the recoilless resonance absorption and emission of γ -radiation by atomic nuclei. [113] The isotope ^{57}Fe is mostly investigated among the family of Mössbauer isotopes with a natural abundance of 2.1%. [114] The γ -photon used for ^{57}Fe Mössbauer spectroscopy originates from nuclear decay of radioactive ^{57}Co isotope which yields ^{57}Fe in a metastable excited state. A cascade of γ -transitions is yielded from this metastable ^{57}Fe state, and the photon with the lowest energy ($E_0 = 14.4 \text{ keV}$) emitted from the first excited nuclear state ($I = 3/2$) is selected for the ^{57}Fe Mössbauer experiment. With the fixed nuclear levels in the Mössbauer source, the energy of the γ -photon is modulated by adjusting the relative velocity between the γ -photon light source and the sample absorber according to the Doppler effect. The samples of Mössbauer spectroscopy are usually solids, powders, or frozen solutions, as the recoil energy loss caused by emission and absorption of a γ -photon does not necessarily shift the energy of the γ -photon in these conditions.

^{57}Fe Mössbauer plays a crucial role in providing information regarding the chemical properties of every distinct Fe species present in a Fe-containing sample. Contrary to EPR spectroscopy which only detects paramagnetic atoms, ^{57}Fe Mössbauer responds to signals from all Fe species regardless of their oxidation and spin states. [114, 115] It is also used in the quantitation of all Fe species as the Mössbauer spectrum is the superposition of the individual subspectra of the various Fe sites, weighted according to their relative concentrations. [114, 116] In addition, the electronic and geometric

structures of various FeS clusters can be identified and characterised in detail according to their unique Mössbauer-spectroscopic features.

One factor that impedes the usage of Mössbauer spectroscopy is that the protein samples analysed must be cooled to cryogenic temperature (< 77 K or lower) to significantly reduce the recoil energy loss. Besides, a sample enriched with the ^{57}Fe isotope is often required although some small molecules have been studied with natural abundance ^{57}Fe .

1.6.5 X-ray crystallography

X-ray crystallography is a technique that uses X-rays to study the arrangement of atoms in crystals. More precisely, based on the diffraction of incident X-rays caused by the crystalline structure, X-ray crystallography provides the information on the distribution of electron density in a crystal, from which the position of atoms in the crystal, i.e. the crystal structure, can be analysed.

Since the first protein crystal structure of myoglobin obtained by Kendrew J.C. in the 1950s, X-ray crystallography has become a major research tool in the investigation of proteins. [117] As the basic tools and techniques of structural biology, X-ray crystallography has been extended from solving the simple three-dimensional structure of proteins to solving the structure of various biomolecules, e.g. nucleic acids, proteins or viral particles. The three-dimensional structures of protein give insights into the global folds, atom positions and specific atomic interactions, etc. Hence X-ray crystallography provides answers to structure-related questions, from the substrate binding to the active sites, to the effects of point mutation on its function. For example, the α -70^{Val} on the alpha subunit of MoFe protein is found to play an important role in gating the substrate

access to the binding site, as once it is substituted by α -70^{le}, the catalytic activity of acetylene and dinitrogen is largely suppressed. [118] X-ray crystallography is even more powerful in conjunction with other techniques. For instance, Einsle *et al.* discovered that there is an interstitial light atom X (where X could be carbon, nitrogen, or oxygen) in the active site of MoFe nitrogenase, and with extended x-ray absorption fine structure (EXAFS) study, atomic-resolution x-ray diffraction and electron spin-echo envelope modulation later determined the X is a carbon atom. [119-121]

The production of well-ordered, diffraction-grade crystals of macromolecules is the prerequisite in the process of structural identification by X-ray crystallography, while some macromolecules cannot be crystallised intrinsically. However, whether a specific macromolecule will crystallise cannot be predicted.

1.7 Aim and scope of this thesis

Research in this thesis focuses on the study of metalloenzymes by electrochemical and spectroelectrochemical techniques, including nitrogenases, nitrogenase homologues and [FeFe] hydrogenase. Nitrogen fixation and renewable hydrogen synthesis are both crucial processes that rely on metalloenzymes and catalysts. In nitrogen fixation, the N₂ molecule binds to the Fe ions in nitrogenases, a process akin to the iron-catalysed Haber-Bosch process used industrially for ammonia production. [60, 61] Meanwhile, H₂, as a promising energy carrier, has driven the development of biological systems for sustainable H₂ production. [FeFe] hydrogenases, such as those found in *Desulfovibrio desulfuricans* HydAB (*DdHydAB*) are among the most efficient enzymes for both proton reduction and hydrogen oxidation, operating near the thermodynamic potential of the H₂/H⁺ couple. [122] Understanding the mechanism

of these enzymes' active sites is essential for the development of catalysts that utilise abundant metals like Fe, potentially revolutionizing the production of clean energy.

Electrochemistry plays a vital role across various scientific domains, including physics, chemistry, and biological studies, underpinning key processes such as material transformation, information transfer, and energy conversion and storage. [123] However, traditional analytical electrochemistry methods may not always be directly effective in identifying new species produced during redox reactions. [124] The integration of electrochemistry with spectroscopy, termed spectroelectrochemistry (SEC), has emerged as a solution to this challenge. This interdisciplinary approach has garnered significant interest and adoption among research communities in chemistry and related fields, who have been actively employing and refining this technique in recent years. [125-128] Spectroelectrochemical techniques are used to obtain simultaneous, *in situ* electrochemical and spectroscopic information on redox reactions of these enzymes taking place on the electrode surface. The redox chemistry of the [4Fe-4S] cluster in nitrogenase Fe protein with the similar cluster in the analogue proteins involved in chlorophyll biosynthesis, have been compared. Also, methods which could be potentially used to study crystals of nitrogenase have been established.

Techniques used to perform these studies including ultraviolet-visible spectroelectrochemistry (UV-Vis SEC), infrared spectroelectrochemistry (IR SEC), electron paramagnetic resonance (EPR) spectroscopy *etc*, will be introduced in Chapter 2.

Chapter 3 includes the development of the UV-Vis SEC cell for the redox titration and studies of the redox properties of the nitrogenase Fe protein (NifH and AnfH). The

midpoint potentials for the $[4\text{Fe-4S}]^{2+}/[4\text{Fe-4S}]^{1+}$ and $[4\text{Fe-4S}]^{1+}/[4\text{Fe-4S}]^0$ couples have been measured with the developed UV-Vis SEC cell, as well as the midpoint potential for them in the nucleotides-bound states. In this chapter, EPR insights of their redox states will also be described.

In Chapter 4, attempts have been made to study the redox properties of the nitrogenase homologue DPOR with the UV-Vis SEC cell. Due to the similarity of DPOR to nitrogenases, the all-ferrous state that has been observed in Fe protein was sought in ChL (analogue to the nitrogenase Fe protein) and ChINB (analogue to the nitrogenase MoFe protein). Additionally, the midpoint potentials for the $[4\text{Fe-4S}]^{2+}/[4\text{Fe-4S}]^{1+}$ couple of ChL have been measured, and attempts have been made to measure the midpoint potential for the $[4\text{Fe-4S}]^{2+}/[4\text{Fe-4S}]^{1+}$ couple of ChINB.

Chapter 5 presents the study of crystals of $[\text{FeFe}]$ hydrogenase (*DdHydAB*) under electrochemical control. An infrared spectroelectrochemical (IR SEC) method has been established, which will eventually be able to be extended to nitrogenase single crystals for further understanding of the redox chemistry of nitrogenase. The redox titration of *DdHydAB* at several pH values has been performed with the IR SEC cell.

Chapter 2 Experimental Methods and Theory

2.1 IR spectroscopy

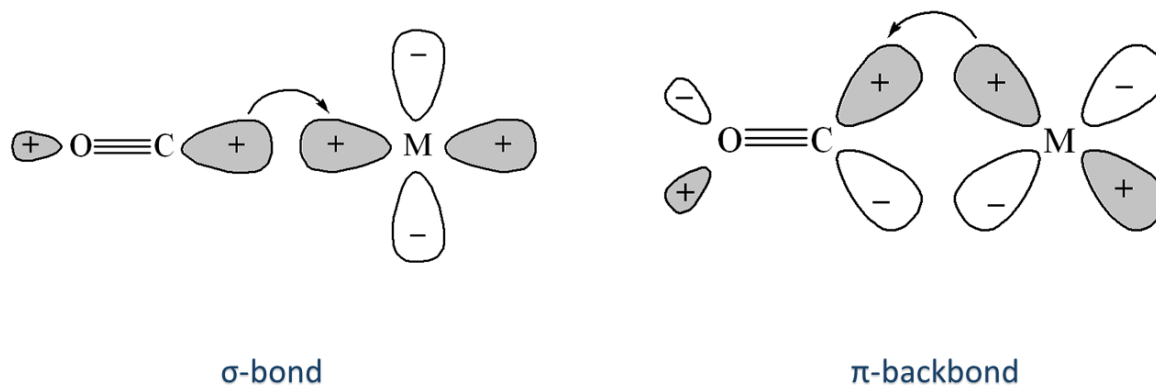
Infrared (IR) spectroscopy is an analytical technique that exploits the vibrational properties of molecules to identify and characterise them. Fundamentally, it involves the absorption of IR light by molecules, causing them to vibrate at specific frequencies that correspond to different chemical bonds. This absorption leads to a unique spectral fingerprint for each molecule, allowing for precise identification. In biological studies, particularly in the examination of FeS cluster proteins, the sensitivity of IR absorption to changes in the local environment of these clusters makes it invaluable for probing their electronic and structural properties.

2.1.1 π -acid ligands: CO and CN^- in IR spectroscopy

Introduction to π -Acid Ligands

π -acid ligands are a class of ligands in coordination chemistry that are characterised by their ability to accept electron density into their π^* antibonding orbitals. This type of ligand bonding is typically observed in complexes involving transition metals. π -acid ligands, particularly carbon monoxide (CO) and cyanide (CN^-), exhibit a special ability to bond synergistically to transition metal centres. This bonding is characterised by a combination of σ -donation and π -backbonding interactions (Scheme 2.1), significantly influencing the ligand's electronic and spectral properties. The σ -donation from the ligand's highest occupied molecular orbital (HOMO) to the metal's vacant σ -acceptor orbital increases electron density on the metal. Concurrently, there is an electron donation from a filled metal d-orbital (of π^* symmetry) to the ligand's lowest

unoccupied molecular orbital (LUMO), which is a π^* -acceptor orbital. The electron density on the ligand is enhanced through π backbonding.



Scheme 2.1 Example of synergistic bonding in metal carbonyls: Illustrating the interaction between π -acid ligands and transition metals. The $2\pi\pi^*$ is antibonding orbital that weakens the CO bond.

The extent of π -backbonding is influenced by various factors, including the electron density on the metal, which is often dictated by the metal's oxidation state. Metals in a lower oxidation state tend to have higher electron density, leading to stronger π -backbonding. This characteristic is crucial in stabilising metals with low formal oxidation states by draining off electron density.

IR Spectroscopy of CO and CN^- Ligands

The study of IR spectroscopy provides valuable insights into the nature of metal-ligand bonding. The $\nu(\text{CO})$ and $\nu(\text{CN})$ stretching modes in IR spectra are particularly sensitive to changes in the metal-ligand bonding environment. For instance, the weakening of the C–O bond in CO due to π -backbonding leads to a red shift (towards lower wavenumber) in the IR spectrum. This shift is a direct consequence of the increased electron density in the C–O bond, resulting from backbonding. In Chapter 5 of

this thesis, CO and CN⁻ are employed as molecular probes to investigate the active site of [FeFe] hydrogenase.

The CO molecule, being a poor σ -donor but a strong π -acceptor, forms a complex with the metal centre through a combination of weak σ bonding and stronger π backbonding. This synergistic interaction, governed by π backbonding, results in a weakened C–O triple bond. The weakening of this bond is directly observable in IR spectra, where the stretching mode $\nu(\text{CO})$ of the CO ligand in a complex is found at a lower wavenumber compared to free CO. For instance, while free CO exhibits an IR absorbance around 2155 cm⁻¹, this shifts to between 1900 and 2100 cm⁻¹ when bound to Fe, sometimes even below 1900 cm⁻¹. [129]

Compared to CO, CN⁻ is a stronger σ -donor and weaker π -acceptor. When CN⁻ forms a complex with metals in a higher oxidation state, it primarily engages in strong σ bonding. This bonding is facilitated by electron transfer from the slightly antibonding highest occupied molecular orbital (HOMO) of CN⁻ to the metal's orbital. Such σ bonding effectively stabilises the C–N bond, leading to an increase in the wavenumber of its CN stretching mode, denoted as $\nu(\text{CN})$. Conversely, when the central metal atom is in a reduced state, the CN⁻ ligand can act as a π acceptor. In this scenario, charge donation occurs from the reduced metal atom to the π^* (anti-bonding) LUMO of CN⁻. This interaction results in a shift of the $\nu(\text{CN})$ peak to a lower wavenumber, indicative of weakened C–N bonding due to increased π back-donation. For instance, in the ferricyanide ion ([Fe(CN)₆]³⁻), the $\nu(\text{CN})$ shows a vibrational peak at 2116 cm⁻¹, whereas in the ferrocyanide ion ([Fe(CN)₆]⁴⁻), the $\nu(\text{CN})$ appears at a lower wavenumber of 2036 cm⁻¹. [130, 131] This difference in the $\nu(\text{CN})$ wavenumber between the two complexes is

a direct reflection of the varying degrees of π back-donation. In ferricyanide, the higher oxidation state of Fe results in less π back-donation, maintaining a stronger C–N bond and hence a higher $\nu(\text{CN})$ value. Conversely, in ferrocyanide, the lower oxidation state of Fe facilitates more π back-donation, weakening the C–N bond and thus lowering the $\nu(\text{CN})$ wavenumber.

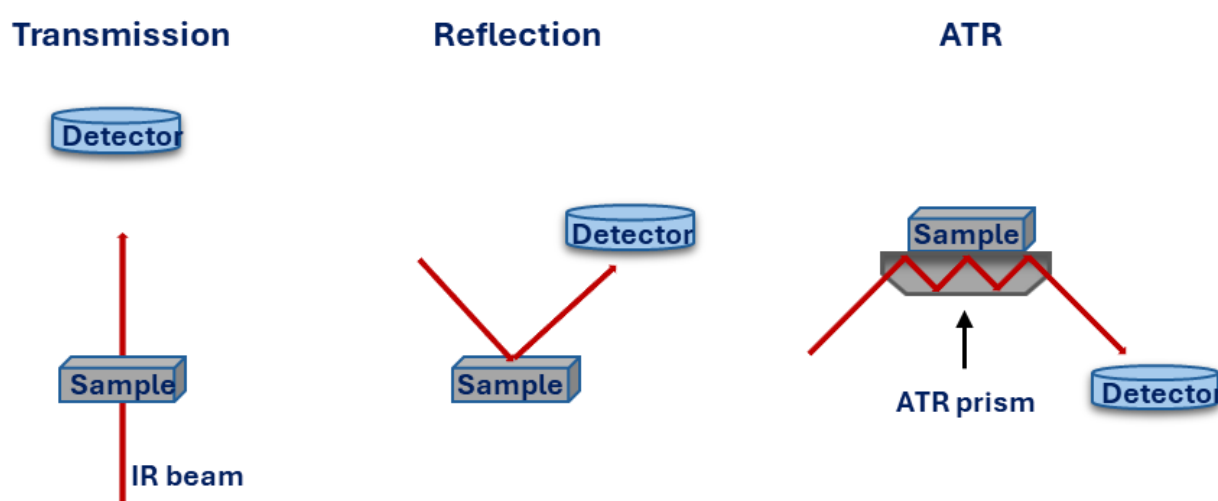
Exploring Metalloenzymes with IR Spectroscopy

As IR probes, CO and CN^- , provide insight into the electronic structure and bonding dynamics at the active sites of enzymes such as nitrogenase and hydrogenase. The investigation of CO interaction with nitrogenase is particularly significant due to CO being one of the important inhibitors of this enzyme. By studying how CO binds to the MoFe or VFe cofactor of nitrogenase, researchers have gained deeper understanding of the mechanisms underlying both the binding process and the subsequent reduction of CO by the enzyme. [132-138] Furthermore, the H-cluster, a sophisticated cofactor within [FeFe] hydrogenase enzymes, illustrates the profound utility of IR spectroscopy in biological chemistry. [139-141] Due to the diamagnetic nature of the more reduced, catalytically relevant states of the H-cluster, techniques like electron paramagnetic resonance (EPR) spectroscopy are limited in their applicability. However, IR spectroscopy emerges as the superior method for studying all states of the H-cluster (both oxidised and reduced). Even the reduction on the [4Fe-4S] of H cluster can be inferred from a subtle shift of CO IR band to lower energy of around $2\text{--}10\text{ cm}^{-1}$. [142]

2.1.2 IR spectroscopy modes

In IR spectroscopy, several analytical methods are employed based on the nature of the sample preparation, namely transmission, reflectance, and attenuated total

reflectance (ATR), as illustrated in Scheme 2.2. Transmission analysis involves the IR light passing through a thin layer of the sample, in order to minimise background solvent absorption. Reflection analysis is suitable for analysing solid samples or thin specimens placed on reflective substrates, as it detects IR light reflected from the sample's surface. Attenuated total reflectance (ATR), another widely used technique in FT-IR microscopy, directs IR light through a crystal e.g. Si or Ge, which is in contact with the sample. The IR light interacts with the sample's surface layer and then returns through the crystal for detection. Each of these methods offers distinct advantages and is chosen based on the sample's characteristics and the specific requirements of the study. [143] In Chapter 5, both transmission and reflection IR modes in conjunction with microscopy have been employed to investigate [FeFe] hydrogenase.



Scheme 2.2 A schematic diagram of the transmission, reflection, and attenuated total reflectance (ATR) modes of infrared detection

2.1.3 IR spectroscopy methods

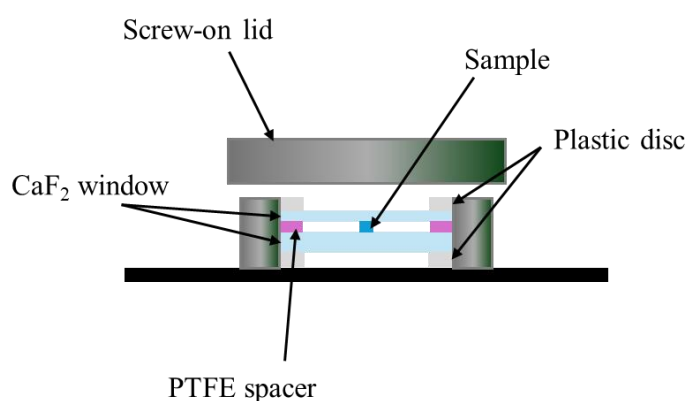
Combining an IR spectrometer with a microscope, a technique known as IR microspectroscopy, allows for the detailed study of very small samples. This approach is exceptionally useful for analysing small-scale objects that pose challenges for

conventional FT-IR spectroscopy. It is adept at precisely examining small particles, thin surface coatings, or single crystals, where detailed analysis is critical. In an IR microspectroscopy setup, the microscope is positioned above the IR sampling compartment. Once the IR beam traverses the sample, it is captured by a Cassegrain objective, creating an image within the microscope's barrel. A variable aperture in the image plane then focuses the beam onto a small-area mercury cadmium telluride (MCT) detector through another Cassegrain condenser. Additionally, the microscope is equipped with glass objectives for direct visual examination of the sample. By altering mirrors in the optical path, the setup can easily switch between transmission and reflectance modes, providing versatility in the analysis of various sample types. [143] This thesis employs a commercially available PIKE transmission cell alongside a specially designed ECIRM (electrochemical IR microspectroscopy) reflection cell for the analysis of [FeFe] dehydrogenase. A cross-sectional diagram of the PIKE transmission cell is presented in Scheme 2.3 A. The specifications and details of the ECIRM reflection cells are discussed in Section 2.5.

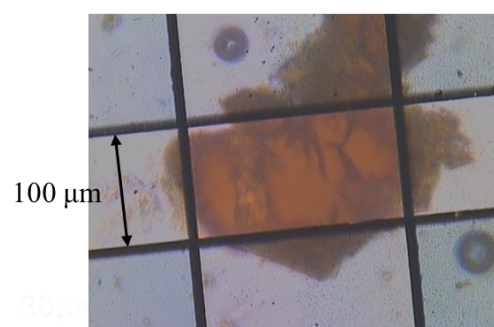
A PIKE cell (Scheme 2.3 A), commonly used in spectroscopy, particularly for transmission measurements, is designed to hold samples through which light can be transmitted for analysis. At the centre, there is a compartment or space where the sample is placed, with the thickness of the sample layer being adjustable by a polytetrafluoroethylene (PTFE) spacer. On either side of the sample area, transparent CaF_2 windows are positioned. These windows are transparent to IR light, allowing the light to pass through the sample without impediment. Surrounding the windows and the sample compartment, plastic discs serve as gaskets to prevent the escape of any gases or liquids from the sample area. The aforementioned components are secured together

by a frame that can be positioned on the IR sampling compartment. The view through the microscope is depicted in Scheme 2.3 B, highlighting the area through which the IR beam passes, marked as the selected area.

A) Cross-section view



B) Protein crystal



Transmission cell

Scheme 2.3 A schematic cross-section view diagram of a commercial PIKE transmission cell; B) The microscopic view of a [FeFe] hydrogenase crystal, indicating the selected area for the passage of the IR beam.

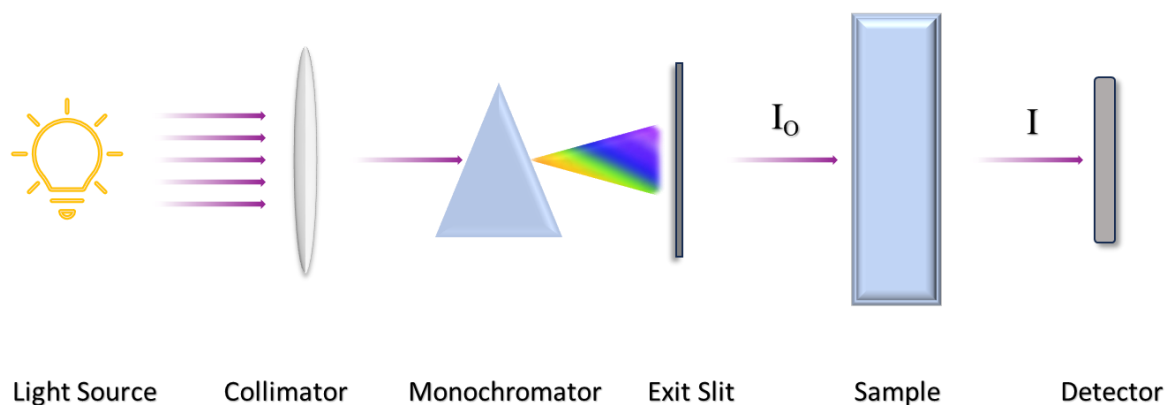
2.2 UV-Vis spectroscopy

2.2.1 Introduction to UV-Vis spectroscopy

Ultraviolet-visible (UV-Vis) spectroscopy stands as a pivotal analytical technique in the realm of molecular biology and chemistry, offering a window into the interactions between biological macromolecules and electromagnetic radiation. This technique is particularly adept at probing the characteristics of proteins and nucleic acids, which absorb light in the UV-Vis region of the electromagnetic spectrum. The fundamental principle of UV-Vis spectroscopy hinges on the absorption of light by these molecules, a process that provides invaluable insight into their concentrations, structural conformations, ligand-binding activities, and enzymatic reactions.

At the heart of UV-Vis spectroscopy lies the concept of electronic excitation. Molecules, especially those with delocalised aromatic systems, absorb light in the near-ultraviolet (150–400 nm) and visible (400–800 nm) regions. This absorption involves the elevation of electrons from a ground state to an excited state, a transition that occurs within the energy range of approximately 150-400 kJ/mol. [144] By measuring the absorption of light across different frequencies or wavelengths, a spectrum is generated, offering a detailed portrayal of the molecular interactions at play.

The practical application of UV-Vis spectroscopy typically involves the dissolution of the target molecules in a transparent solvent, such as aqueous buffers. The technique's strength lies in its linearity; the absorbance of a solute is directly proportional to its concentration, making UV-Vis spectroscopy an ideal tool for quantitative analysis. Moreover, the specific wavelength of absorption and the intensity of absorbance are not only dictated by the chemical nature of the molecules but also by the surrounding molecular environment of their chromophores. This sensitivity to environmental changes renders absorption spectroscopy an excellent method for monitoring various biochemical processes, including ligand-binding reactions. The UV-Vis spectrometer (Scheme 2.4) typically features two light sources: a deuterium lamp for the ultraviolet region and a tungsten-halogen lamp for the visible spectrum. The light from these sources is directed through a monochromator or optical filters to isolate specific wavelengths. It then travels through a cuvette containing the sample. The amount of light that passes through the sample, and consequently the light absorbed by the sample, is detected by a sensitive detector such as a photomultiplier or a photodiode.



Scheme 2.4 A schematic diagram of a UV-visible spectrometer

2.2.2 Beer-Lambert law

The process of determining the concentrations of substance in a solution can be efficiently and precisely achieved through absorbance measurements. This method hinges on the relationship between the absorbance (A) and the intensity of light before (I_0) and after (I) it passes through the sample (Eq. 2.1). Furthermore, the principle of the Beer-Lambert law, represented by Eq. 2.2, establishes that the absorbance is directly proportional to the concentration of the solute.

$$A = -\log_{10} (I/I_0) \quad \text{Eq. 2.1}$$

$$A = \varepsilon cl \quad \text{Eq. 2.2}$$

In Eq. 2.2, A stands for absorbance, ε stands for molar absorption coefficient, c stands for molar concentration, and l stands for optical path length. It can be seen that there is a linear connection between solution concentration and absorbance at absorbance values between 0.1 and 1, allowing the concentration of a solution to be estimated by measuring its absorbance (Eq. 2.3).

$$c = \frac{A}{\varepsilon l} \quad \text{Eq. 2.3}$$

2.2.3 UV-visible spectroscopy of proteins

UV-Vis spectroscopy serves as a critical tool in analysing the structural and functional aspects of metallo-proteins, including those containing FeS clusters. [145] The UV-Vis spectra of proteins are typically categorized into "near" and "far" UV regions. The near UV region, spanning 250–300 nm, is often referred to as the aromatic region. This region includes the absorption of aromatic amino acids like tryptophan, tyrosine, and phenylalanine, along with disulfide bonds. Tryptophan, with its indole ring, exhibits the most intense absorption in this region, with a maximum extinction coefficient at 279 nm. [146] Tyrosine and phenylalanine also contribute to the absorption in the near UV, though with lower extinction coefficients. The far UV region, below 250 nm, is dominated by the peptide backbone's transitions, with contributions from some side chains. [147] The peptide chromophore, responsible for absorption in the far-UV region, involves σ -bonding electrons, nonbonding electrons on O and N atoms, and π -electrons. The lowest energy transition in the peptide chromophore is from a nonbonding orbital to an anti-bonding π orbital, an n to π^* transition, followed by a π to π^* transition. [146]

Proteins with FeS clusters exhibit distinct colouration and spectral characteristics. These clusters display characteristic absorption bands in the 300–600 nm range, attributed to the ligand to metal charge transfer (LMCT) processes. A protein containing only an $[2\text{Fe-2S}]^{2+}$ cluster appears brown showing broad maxima near 330, 420, and 460 nm. In contrast, proteins with $[3\text{Fe-4S}]^{1+}$ or $[4\text{Fe-4S}]^{2+}$ clusters display very broad spectra with notable shoulders in the 380–430 nm range. [148] The absorption changes in redox clusters are key to assessing protein redox processes. For instance, the UV-Vis spectroscopy of IsoC, which is a Rieske-type ferredoxin with a $[2\text{Fe-2S}]$ cluster, shows distinct peaks at 323 and 454 nm, with an additional shoulder peak at 575 nm in

its oxidised, 2+ state. When IsoC is reduced to its 1+ state using sodium dithionite, the new maxima are observed at 382, 431, and 515 nm. [149]

2.3 Electron paramagnetic resonance

2.3.1 Introduction to EPR

Electron paramagnetic resonance (EPR) spectroscopy, also known as electron spin resonance (ESR), was marked by its unique ability to explore paramagnetic molecules, a feature that has since been extensively applied in the study of biological systems. EPR spectroscopy is adept at observing organic free radicals, which typically arise from chemical oxidation-reduction reactions or through exposure to irradiation. Additionally, EPR is instrumental in studying transition-metal ions like Mn, Fe, Co, Cu, and Mo, in their paramagnetic oxidation states. The ability of EPR to provide detailed information about the oxidation states of these metal centres makes it an invaluable tool in metalloproteins, where these paramagnetic centres frequently constitute the active sites.

2.3.2 EPR study of metalloproteins and FeS proteins in particular

Metalloproteins

In metalloproteins, EPR spectroscopy is instrumental in studying the behaviour of transition metal ions. These ions often form covalently bonded complexes or clusters, exhibiting unique EPR spectra due to strong exchange interactions. [150] For instance, the Cu^I-Cu^{II} dimeric Cu_A centres in enzymes like nitrous oxide reductase and cytochrome oxidase show complex EPR splitting due to interactions with two Cu nuclei, as revealed by multifrequency EPR studies which demonstrates the sensitivity of EPR to intricate metal cluster structures. [151] In oxidised ferredoxin and methemerythrin, two Fe^{III} ions

are strongly antiferromagnetically coupled. [152, 153] This coupling results in a "ladder" of energy levels with a ground state $S = 0$, leading to no EPR signal at liquid helium temperatures. However, at higher temperatures, excited states with $S = 1, 2, \dots, 10$ become populated, but still eluding EPR detection due to rapid electron-spin relaxation. In contrast, in the mixed-valence state $\text{Fe}^{\text{II}}\text{-Fe}^{\text{III}}$, the coupling leads to a detectable ground state $S = \frac{1}{2}$ at low temperatures. [154]

FeS protein

FeS proteins, a diverse group of metalloproteins discovered in the 1970s primarily through EPR spectroscopy, play a pivotal role in various biological processes. [155] These proteins are characterised by their FeS clusters, typically bound to cysteine residues within the protein structure. The unique electronic properties of these clusters, particularly their strong exchange coupling between the Fe atoms, make EPR an ideal technique for their study.

The EPR spectra of FeS proteins are highly informative. The total number of d electrons on the Fe atoms in these clusters determines their EPR detectability. In their oxidised states, neither $[\text{2Fe-2S}]^{2+}$ nor $[\text{4Fe-4S}]^{2+}$ clusters are detectable with standard perpendicular mode EPR spectrometers. However, upon reduction, such as with sodium dithionite ($\text{Na}_2\text{S}_2\text{O}_4$), the reduced $[\text{2Fe-2S}]^{1+}$ and $[\text{4Fe-4S}]^{1+}$ clusters exhibit characteristic axial EPR spectra, with $g_{\parallel} \approx 2.02$ and $g_{\perp} \approx 1.94$. [156, 157] The $[\text{3Fe-4S}]^{1+}$ cluster presents a sharp, nearly isotropic EPR signal centred at $g \approx 2.01$, which disappears upon reduction. [158] Additionally, the high-potential iron-sulfur protein (HiPIP) $[\text{4Fe-4S}]^{3+}$ cluster typically exhibits an axial spectrum with $g_{\parallel} \approx 2.14$ and $g_{\perp} \approx 2.03$. [159]

A notable application of EPR is in the study of the Fe protein of nitrogenase. This protein, essential in nitrogen fixation, undergoes significant changes in its oxidation state during its function. In its reduced ($[4\text{Fe-4S}]^{1+}$) state, the Fe protein exhibits a $S = \frac{1}{2}$ state, detectable by EPR. Upon oxidation to a $[4\text{Fe-4S}]^{2+}$ state, the spin state changes to $S = 0$, rendering it EPR-silent with standard perpendicular mode. [36, 112] The ability of EPR to detect these changes is crucial for understanding the electron transfer mechanisms in nitrogenase, providing insight into how this enzyme facilitates the conversion of atmospheric N_2 into NH_3 .

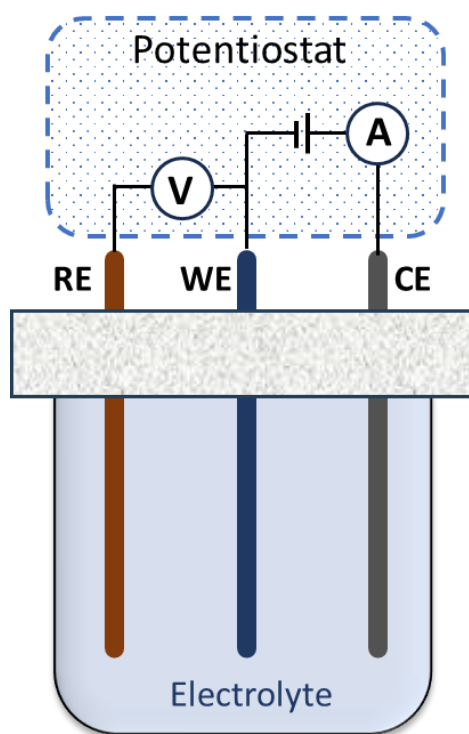
The combination of UV-Vis and EPR spectroscopy is often employed to establish the predominant cluster type present in these proteins. This dual approach enhances the understanding of the electronic structure and redox properties of FeS clusters, providing valuable insights into their roles in biological systems, which has been used in Chapter 3 for the study of the Fe protein of nitrogenase.

2.4 Electrochemistry

Electrochemical techniques such as cyclic voltammetry and chronoamperometry are commonly employed for the study of redox proteins. Beyond determining reduction potentials, these methods are crucial in exploring the thermodynamics and kinetics of reactions associated with redox proteins or small molecules, including aspects like protonation and substrate binding. Electrochemistry has been applied to a broad range of catalytic processes, including electron transfer, substrate diffusion, and interactions with inhibitors. [160]

2.4.1 The three-electrode system

A three-electrode system in electrochemistry is used for precise electrochemical measurements. It consists of a working electrode (WE), a reference electrode (RE), providing a stable reference potential, and a counter (or auxiliary) electrode (CE), controlled via a potentiostat (Scheme 2.5). The WE is where the redox processes of interest take place, while the CE serves as the site for the opposite half-cell reaction. It complements the WE by ensuring that the electrical circuit is completed, allowing current to flow through the electrochemical cell. The RE is crucial for maintaining a stable and known potential against which the potential of the WE is measured.



Scheme 2.5 The three-electrode electrochemical system with reference (RE), working (WE), and counter (CE) connected to a potentiostat.

In the three-electrode arrangement, the setup includes a voltmeter, which is connected in parallel with the RE and WE (as depicted in Scheme 2.5). This configuration allows the potential of the WE to be monitored relative to that of the RE. The current, which is measurable by an ammeter, flows predominantly between the WE and CE, and

is limited by the reaction in the circuit. To facilitate efficient electron transfer, it is essential to use a CE with a significantly larger surface area than that of the WE.

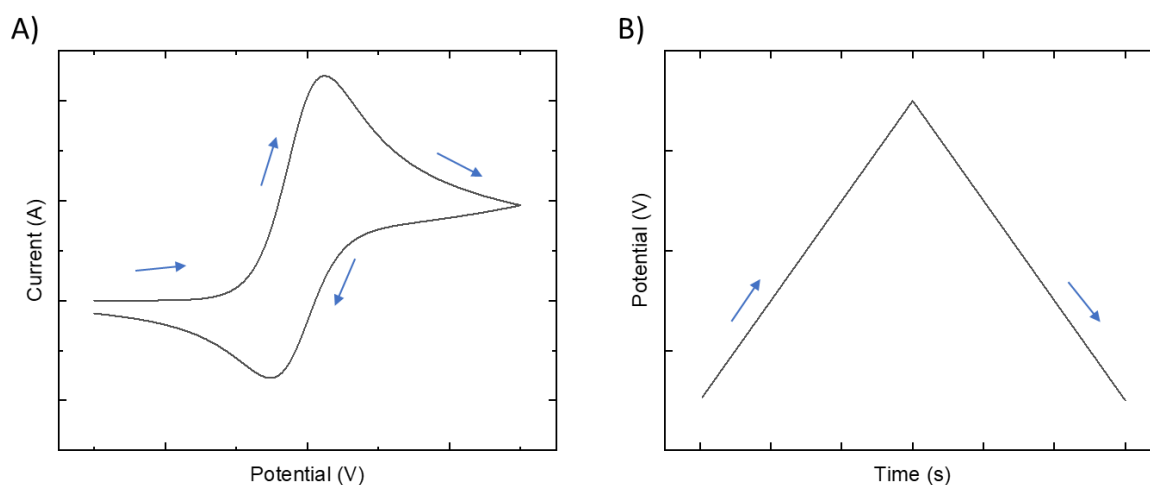
In a three-electrode system, cyclic voltammetry (CV) and chronoamperometry (CA) are key techniques used to study electrochemical properties. CV involves varying the electrode potential cyclically to observe redox behaviours, while CA measures the current response over time at a fixed potential. Both CV and CA have been extensively applied in the study of redox proteins, including FeS proteins. [161, 162] In this thesis CV and CA will be employed to investigate the properties of FeS proteins such as the Fe protein of nitrogenase (Chapter 3), nitrogenase homologue (Chapter 4), and FeFe hydrogenase (Chapter 5).

2.4.2 Cyclic voltammetry

Cyclic voltammetry (CV) is commonly one of the initial techniques used in electrochemical experiments due to its simplicity and quick provision of data about redox potentials and electrocatalysis rates. In this method, a triangular waveform potential is applied to the WE, and the current is recorded. The potential applied at the WE is swept between two set values at a constant rate, and the responsive current is plotted against applied potential (Scheme 2.6). Characteristic of reversible redox reactions, two peaks (E_{pc} , E_{pa}) typically appear in the cyclic voltammogram, with their average indicating the midpoint potential, E_m . This technique, crucial in this thesis, helps determine reference electrode offsets and mediators' midpoint potentials.

Redox potential and reversibility obtained by CV have been proved to be useful in studying redox proteins. Protein film electrochemistry (PFE) involves adsorbing a protein onto an electrode surface, allowing for the monitoring of the protein's redox features.

[163] Initially applied to small redox proteins in the 1970s and later to larger redox enzymes, PFE has been extensively used over the past 20 years to investigate various aspects of redox proteins and enzymes [164], including proton transfer [165], electron transfer ET [166, 167], and diffusion along substrate channels [168, 169] etc.



Scheme 2.6 A) A typical cyclic voltammogram for a reversible process in solution, with arrows indicating the direction of the scan over time; B) the potential waveform used to carry out the cyclic voltammetry. The CV and potential waveform were simulated using a CV simulator. [170]

2.4.3 Chronoamperometry

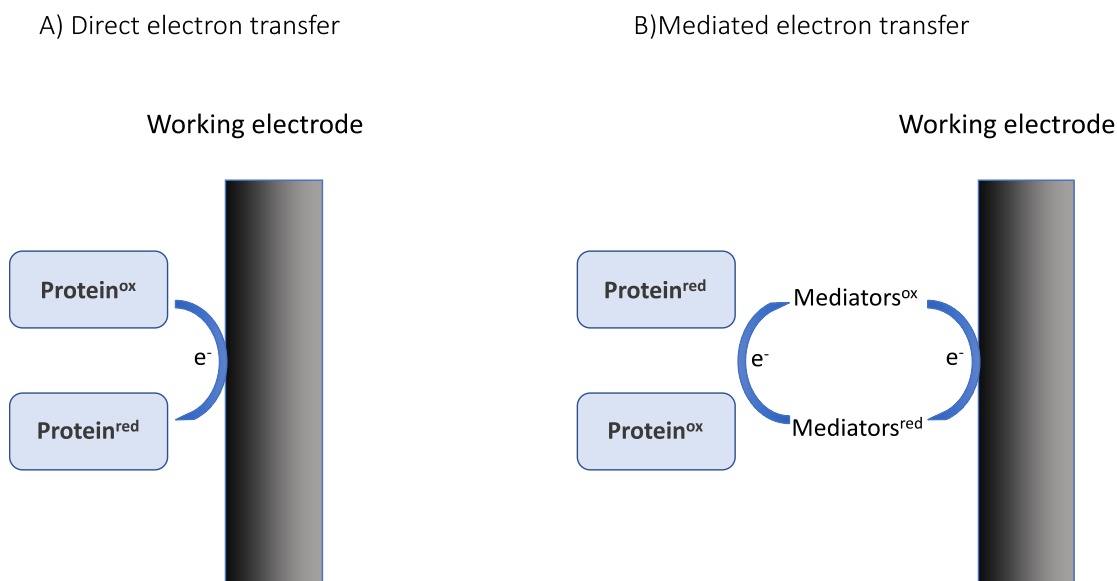
Chronoamperometry (CA) is an established electrochemical technique where a potential pulse is applied to a WE, and the resulting electrochemical current is then measured as a function of time following a single or double potential step. This method detects changes in current due to the variation (reduction or oxidation) in the diffusion layers of the analyte at the electrode surface. Complementary to CV, CA has been instrumental in studying redox proteins. For instance, Chen *et al.* utilised CA to investigate the behaviour of MoFe nitrogenase, particularly focusing on the protein's intrinsic changes and its interaction with various substrates and inhibitors. [135]

Additionally Léger *et al.* employed CA experiments with hydrogenase to quantitatively characterise the kinetics of inhibition by CO, as well as by O₂. [171]

2.4.4 Electron transfer

In protein electrochemistry, electron transfer can happen in two ways. Direct electron transfer processes involve the protein in direct contact with the electrode, so electrons interchange rapidly between the protein and the electrode (Scheme 2.7 A). More often sluggish heterogeneous electron transport occurs between protein and an electrode surface. The fact that the bulk of the protein matrix insulates the redox-active site is primarily responsible for the sluggish rates of electron transfer. [172] Mediated electron transfer processes use small redox molecules, which diffuse very quickly due to their small size, to transfer electrons between the electrode and the protein in a reversible manner (Scheme 2.7 B).

The metalloproteins studied in this thesis undergo slow electron exchange with the electrode surface. Therefore, redox mediators will be used in this thesis to ensure efficient electron transfer between the electrode and redox-active FeS clusters within the proteins or crystals.



Scheme 2.7 Illustrations of the electron transfer processes between working electrode and protein A) direct electron transfer, and B) mediated electron transfer with the aid of redox mediators.

2.5 Spectroelectrochemistry

Spectroelectrochemistry is an analytical technique that combines spectroscopy and electrochemistry to study the behaviours of molecules under various electrical potentials. It provides insights into the changes in molecular structure, composition, and electronic properties as a result of redox reactions. This approach is particularly useful for understanding the mechanisms of complex chemical and biological systems, where the interaction between light and matter is influenced by changes in the redox state. Spectroelectrochemistry can employ different types of spectroscopy, such as UV-Vis, IR or Raman spectroscopy, depending on the specific application. UV-Vis spectroelectrochemistry and electrochemical IR microspectroscopy have been employed to study FeS cluster proteins in this thesis.

2.5.1 Ultraviolet-visible spectroelectrochemistry

Ultraviolet-visible spectroelectrochemistry (UV-Vis SEC) method involves the simultaneous control and measurement of electrochemical properties and

measurement of optical absorbance, allowing for a detailed investigation of electron transfer processes and the associated changes in the electronic structure of the analyte.

For the general procedure of UV-Vis SEC experiment conducted with a protein, redox mediators were utilised to facilitate rapid electron transfer between the protein and the electrode. The three electrodes were inserted into the UV-Vis cuvette (as depicted in Scheme 3.2, Section 3.1.2), which contained a total volume of 150-400 μL of protein and a mediator cocktail (final concentration of 5-15 μM for each mediator). The electrodes were then connected to the potentiostat. To initiate the titration, different potentials were applied in 25-100 mV increments, allowing equilibration for 10 minutes at each level UV-Vis spectra were subsequently recorded at each potential once equilibrium had been reached.

This thesis extensively employs UV-Vis SEC for investigating the redox potential of FeS cluster proteins. A detailed exploration and elaboration of this technique, focusing on its development and practical implementation, will be presented in Section 3.1.

2.5.2 Electrochemical IR microspectroscopy

Infrared (IR) microscopy method has been introduced in Section 2.1.3, which combines an IR spectrometer with a microscope, a technique known as IR microscopy, allows for the detailed study of very small samples. Electrochemical IR microspectroscopy (ECIRM) has emerged as a powerful tool for studying protein crystals. [173-178] Ash *et al.* developed a method to precisely create and verify specific redox states in single metalloprotein crystals, using electrochemical control and synchrotron IR microspectroscopy, demonstrating a fully reversible and uniform electrochemical reduction from the oxidised inactive to the fully reduced state in NiFe hydrogenase 1 from

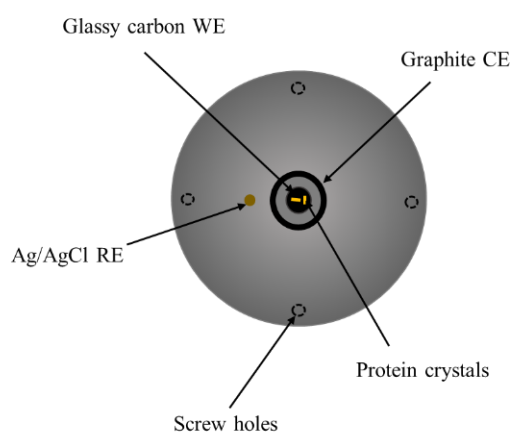
Escherichia coli. [177] Morra *et al.* successfully generated and identified the crucial catalytic redox states of prototypical [FeFe]-hydrogenase I from *Clostridium pasteurianum* (Cpl) within a protein crystal using ECIRM. [179]

This technique synergises the sensitivity of IR spectroscopy with the precision of electrochemical methods, enabling detailed investigations of protein structures and their dynamic redox states. The study of protein crystals is pivotal in understanding the structural and functional aspects of proteins. Traditional methods like X-ray diffraction offer structural insights but lack dynamic information regarding the redox states of proteins. The ECIRM method fills this gap by providing a unique way to probe the reactivity in protein crystals under various redox conditions. ECIRM involves the use of an IR microscope to focus an IR beam onto a single crystal for spectroscopic data collection. The high concentration of protein in crystals amplifies the intensity of IR bands, thereby enhancing the signal-to-noise ratio. This improvement aids in the identification of otherwise undetectable bands and ensures the authenticity of the spectral bands observed.

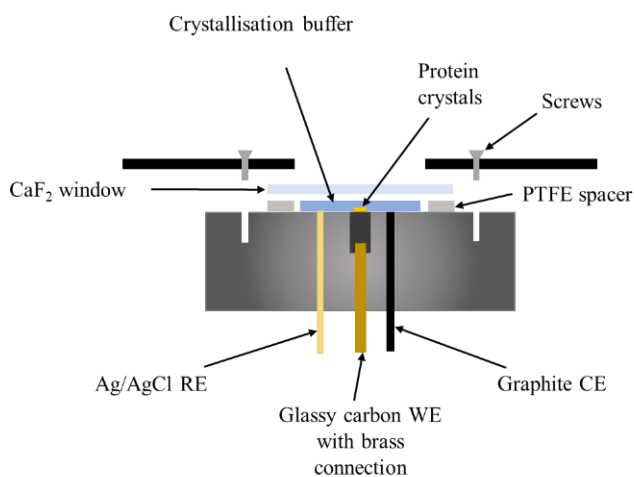
In the cell for ECIRM experiments, a 4 mm diameter working electrode (WE) made of glassy carbon is used, which serves both as an electrochemical interface and a reflective surface for IR spectroscopy. The construction of the electrochemical cell includes a 2 mm diameter Ag/AgCl reference electrode (RE), and a graphite counter electrode (CE) in a ring formation that encircles the WE (Scheme 2.8). The crystal, which is in contact with a buffer solution containing redox mediators that cover the full potential range used in the electrochemical experiments, is placed atop the working electrode. By varying the potential applied to the WE, different redox states of the protein's active site

can be probed. This is akin to conducting a redox titration, where IR spectra are recorded at varying potentials until equilibrium is reached. The ECIRM method is primarily utilised to investigate the redox states of single [FeFe] hydrogenase crystals in Chapter 5.

A) Top view



B) Cross-section view



Scheme 2.8 The ECIRM cell includes: A) A top view of the cell illustrates the working electrode (WE) constructed from glassy carbon, a counter electrode (CE) crafted from a graphite carbon ring, and the Ag/AgCl reference electrode (RE); B) a detailed cross-sectional view highlights the placement of the spacer gasket and the CaF₂ window. [178]

2.6 Over-expression of DdHydAB in *E. coli*

In native organisms, three maturase proteins are required to co-express for the native production of [FeFe] hydrogenases; HydE and HydG are involved in the synthesis of the [2Fe]_H cluster; HydF acts as the scaffold protein and delivers the [2Fe]_H cluster to the vacant active site of the hydrogenase. [180-183] However, the low yield of the [FeFe] hydrogenases from the native organisms has long been hindering researchers from better understanding this enzyme. [184] In recent years, several recombinant expression strategies have been explored for a higher yield of [FeFe] hydrogenases. A feasible way is to co-express maturases of hydrogenases in an alternative host *e.g.* *Escherichia coli* (*E. coli*). [185] Significant progress was made on this matter in 2013, when it was found that

decomposition of the cofactor during the lengthy maturation. The holo *DdHydAB* is primarily a CO-inhibited state, namely the H_{ox}-CO state. [190, 191] A step to release CO (marked with a red circle in Scheme 5.1) under a N₂ atmosphere is followed to produce an active enzyme at the H_{ox} state. The recombinant expression of *DdHydAB* in *E. coli* is described below and characterised with SDS-PAGE, UV-Vis and IR spectroscopy.

Cell growth and *DdHydAB* expression

A single colony was first inoculated into a small volume (50 mL) of sterile media to grow *E. coli* in a liquid preculture. The Luria Bertani media (LB, 10 g L⁻¹ tryptone, 5 g L⁻¹ yeast extract) is dissolved in a phosphate buffer (5 g L⁻¹ Na₂HPO₄, 10 g L⁻¹ K₂HPO₄) containing antibiotics kanamycin (50 µg mL⁻¹) and chloramphenicol (34 µg mL⁻¹). The precultures were incubated overnight at 37 °C with a speed of 200-300 rpm gentle shaking for aeration. On the following day, 10 mL of the preculture was transferred to 1 L of the same LB media containing the same antibiotics as in the preculture. 2 mM cysteine (the source of sulfur), 0.5% w/v glucose, and 4 mM ferric ammonium citrate (the source of iron) were added in the LB media as supplements for cell growth. The *E. coli* cells were inoculated to an optical density at 600 nm of 0.6 at 37 °C and 200-300 rpm.

Then the culture was purged with nitrogen for 1 h in an air-tight glass bottle to reach an anaerobic condition before the induction of the *DdHydAB* expression. The protein production was induced with 1 mM IPTG, with an additional 3 mM cysteine as a supplement, and the culture was incubated overnight at room temperature under agitation.

DdHydAB purification

All of the subsequent procedures were completed in an anaerobic environment, and all glass and plastic labware was kept in the glovebox for at least 24 h before use. Centrifugation was used to anaerobically harvest the cells (6,500 x g for 30 min at 4 °C) as a pellet. The pellet was then resuspended in buffer W (100 mM Tris-HCl, 150 mM NaCl, pH 8.0), with the addition of lysozyme to rupture the bacterial cell wall and deoxyribonuclease I (DNase I) to cleave bacterial DNA. The resuspended cells were sonicated with Fisherbrand™ Q500 Sonicator for 15 min (every 2-second sonication with a 5-second interval) to release the expressed apo-protein (containing the [4Fe-4S] clusters but lacking the [2Fe] subcluster). Insoluble debris was separated and removed by ultrafast centrifugation (45, 000 xg for 60 min). The supernatant containing the apo-protein was purified with a 20 mL Streptactin Superflow high-capacity column (IBA) pre-equilibrated with buffer W. The purified apo-protein was eluted with buffer W containing 2.5 mM desthiobiotin as the eluent after washed with buffer W. The soluble apo-protein was concentrated to c.a. 0.5 mM using centrifugal concentrators (30 kDa MWCO), and stored in a -80 °C freezer.

Artificial maturation and CO release

The steps for artificial maturation were performed in a dark anaerobic glovebox considering the oxygen and light sensitivity of the *DdHydAB*. [192] In a 50 mL Falcon tube, apo-*DdHydAB* was diluted to c.a. 200 μM in buffer W before [2Fe]^{adt} was added to 1 mM from a 50 mM stock (also in buffer W). To self-assemble the [2Fe]^{adt} cofactor at the vacant site in the apo-*DdHydAB*, this mixture was incubated at 35°C and at 300 rpm for 50 h. The excess [2Fe]^{adt} cofactor was separated by eluting the activated hydrogenase on a 10 mL PD-10 column with 25 mM Tris-HCl, 20 mM NaCl pH 8 buffer. After this artificial

maturation of the apo *DdHydAB*, the protein bearing the $[2Fe]_H$ cluster called holo *DdHydAB* is generated.

The holo *DdHydAB* is incubated in the anaerobic glovebox to release CO, in the dark, incubated with gentle shaking at 15 °C and 300 rpm for 48 h.

2.7 General methods, reagents and equipment

2.7.1 Protein source and handling

The sample of NifH and AnfH from nitrogenases were both provided by Prof Lance Seefeldt (Utah State University, USA). The NifH (2.6 mM) and AnfH (1.7 mM) samples were received in a Tris buffer (pH 8.0, 50 mM), with NaCl (500 mM) and sodium dithionite (2 mM). The samples of N_2B_2 and L_2 protein from dark-operative protochlorophyllide oxidoreductase DPOR were both provided by Prof Jürgen Moser (Institut für Mikrobiologie, Technische Universität Braunschweig, Germany). The N_2B_2 (119 μ M) and L_2 protein samples (143 μ M) were received in a Tris buffer (pH 7.5, 40 mM), with $MgCl_2$ (10 mM) and NaCl (150 mM). Additionally, the *DdHydAB* sample in solution was prepared in this lab and was crystallised with help from Dr Stephen Carr (Research Complex at Harwell) in a crystallisation buffer (100 mM Tris, 900 mM LiCl and 32% (w/v) PEG 6000).

The protein samples were all stored in a liquid N_2 dewar because due to their O_2 sensitivity. Prior to experiments, the buffer of the sample was exchanged to desired buffer using Amicon Ultra 8 (0.5 centrifugal filter unit, membrane NMWL, 30 kDa). Additionally, dithionite in the NifH and AnfH samples was removed during the buffer exchange process.

2.7.2 Anaerobic handling

For anaerobic sample handling, all preparation of samples took place within N₂-filled gloveboxes (Glove Box Technology) with O₂ levels maintained below 1 ppm. Prior to storage in the glovebox, all solutions were thoroughly saturated with N₂.

2.7.3 Buffer preparation

The buffer was degassed extensively before being taken into the Glovebox (O₂ content < 1 ppm). It was then stirred overnight with the lid loosely open in the Glovebox to further remove the residual O₂ prior to usage.

2.7.4 Reference electrode potential conversion

If a saturated calomel electrode (SCE) is used as a reference electrode, the potential relative to the standard hydrogen reference electrode (SHE) will be calculated as $E_{SHE} = E_{SCE} + 0.242 \text{ V}$; if an Ag/AgCl electrode is used as a reference electrode, the potential relative to SHE will be calculated as $E_{SHE} = E_{Ag/AgCl} + 0.222 \text{ V}$.

2.7.5 MgATP/MgADP solution preparation

MgCl₂, ATP and ADP were stored overnight in a Glovebox to remove O₂. They were dissolved in degassed buffer separately to obtain 200 mM stocks. The 100 mM MgATP/MgADP solution was then prepared by stoichiometrically mixing MgCl₂ and ATP/ADP stocks in a 1:1 ratio.

2.7.6 Other instrumentations

Electrochemical measurements were regulated using an AutoLab 128N potentiostat from Metrohm, operated through Nova 1.10 software. Additionally, UV-Vis spectra were measured using a Cary 60 UV-vis spectrometer.

Chapter 3 Spectroelectrochemical studies of the [4Fe-4S] cluster in the Fe protein of nitrogenase: defining redox midpoint potentials

Nitrogenases are pivotal enzymes in the biological nitrogen/nutrient cycle, catalysing the reduction of dinitrogen (N_2) to ammonia (NH_3). Broadly, there are three types of nitrogenases, classified based on the metal present in their active site: MoFe, VFe, and FeFe nitrogenases. Despite structural and phylogenetic similarities among these types each variant plays a unique role in nitrogen fixation.[30, 31] A core component of these enzymes is the Fe protein, a roughly 60 kDa homodimer, acting as the reductase in the nitrogenase complex. The Fe proteins in MoFe, VFe, and FeFe nitrogenases are encoded by the genes *nifH*, *vnfH*, and *anfH*, respectively. They are integral to both the biosynthesis and catalytic functions of nitrogenases. In the process of nitrogenase action, the Fe protein not only transfers electrons to the catalytic component but also facilitates critical steps in enzyme maturation and function. Specifically, the product of the *nifH* gene is essential for incorporating Mo (Molybdenum) and homocitrate into the MoFe cofactor. The MoFe cofactor, often referred to as the FeMo-cofactor, is a [Mo:7Fe:9S:C]:homocitrate cluster that forms the heart of the MoFe nitrogenase. It is where the actual reduction of N_2 to NH_3 takes place. Similarly, the biosynthesis of the P-cluster, a complex [8Fe-7S] cluster integral to electron transfer within the enzyme, is also influenced by the Fe protein. [26, 32]

The [4Fe-4S] clusters of NifH and VnfH have been found to cycle between three different redox states: the most oxidised state [4Fe-4S]²⁺, the one-electron reduced [4Fe-

$4S]^{1+}$, and the two-electron reduced $[4Fe-4S]^0$ (also called the all-ferrous or super-reduced state). To facilitate a one-electron transfer event during nitrogenase catalysis, the $[4Fe-4S]$ cluster of NifH is thought to cycle between the $[4Fe-4S]^{2+}$ and $[4Fe-4S]^{1+}$ states in vivo, with flavodoxins or ferredoxins used as physiological electron donors to achieve the $[4Fe-4S]^{1+}$ state. [193-195] However, it remains unclear whether the all-ferrous state participates in native catalysis. Coupling the all-ferrous $[4Fe-4S]^0$ cluster with the oxidised $[4Fe-4S]^{2+}$ cluster would be highly advantageous from the standpoint of cellular energy conservation, lowering the expenditure of MgATP by half. It is suggested that the reaction might use one MgATP per electron transfer if the electrons are transferred from the all-ferrous state of the Fe protein, rather than the observed two MgATPs when only the $[4Fe-4S]^{1+}$ and $[4Fe-4S]^{2+}$ states are involved. [196] A recent study showed that Eu(II)–DTPA-reduced NifH and VnfH (i.e., the all-ferrous state, $[4Fe-4S]^0$) can reduce CO_2 to CO, as confirmed by gas chromatography-mass spectrometry (GC–MS). [41] This non-native reactivity of the $[4Fe-4S]^0$ state of the Fe protein is particularly interesting, but perhaps not surprising, given that the potential of the $S = 4$ all-ferrous state is very low, approximately -790 mV vs SHE, [10] and it contains the two electrons necessary to reduce CO_2 to CO. [40] Comparatively, the reduction potential of CODH for CO_2 reduction is around -520 mV vs SHE. [197] However, CODH is typically a more complex oligomer (e.g., a dimer or a larger multimeric complex) and contains multiple metal clusters, such as Ni-Fe-S and Fe-S clusters, intricately involved in its catalytic mechanism.[198]

The redox midpoint potential of the $[4Fe-4S]^{2+/1+}$ couple in NifH has been observed to decrease by more than 100 mV when nucleotides are bound to NifH. [199] Thus, it

would be interesting to study how nucleotide binding (MgATP and MgADP) affects the potential for the formation of the $[4\text{Fe-4S}]^0$ state of NifH. In order to study this, potentiometric titrations were also attempted in the presence of MgATP and MgADP.

AnfH is the reductase component of FeFe nitrogenase and is less studied compared to NifH and VnfH. Structural comparisons show that AnfH from the diazotroph *Azotobacter vinelandii* has a similar structure to its counterparts NifH and VnfH in the ADP-bound state. [200] Although it is not yet confirmed whether AnfH can adopt the same oxidation states as NifH and VnfH, a similar redox behaviour is anticipated due to the structural and electronic similarities of these three homologous proteins. Consequently, the ability of AnfH to form an all-ferrous state is investigated.

As previously mentioned, the iron-sulfur clusters in the Fe protein of nitrogenase (NifH) exhibit distinct oxidation states that can be identified using UV-Vis spectroscopy. The all-ferrous state ($S = 4$), often recognized by a peak around 520 nm, represents a fully reduced form of the protein. As the oxidation state shifts to a mixed-valent or $1+$ state, the UV-Vis spectrum may show a peak at around 380-400 nm, reflecting the unique electronic structure of this state. Finally, the $2+$ state, indicative of a fully oxidised protein, is typically marked by a peak around 410 nm. These characteristic peaks are influenced by various experimental factors, such as pH and temperature, allowing for a detailed exploration of the redox behaviour of this complex enzyme. The ability to distinguish between these specific oxidation states is the reason UV-Vis spectroscopy is frequently used to study the redox properties of NifH and other FeS proteins.

The techniques employed in these studies on the Fe protein include ultraviolet-visible spectroelectrochemistry (UV-Vis SEC) and electron paramagnetic resonance

(EPR) spectroscopy, in collaboration with Dr. William Myers, CAESR, as introduced in Chapter 2. Due to the limited availability of commercial cells for small sample volumes, a specialized electrochemical cell has been developed in this work to facilitate the UV-Vis SEC experiments.

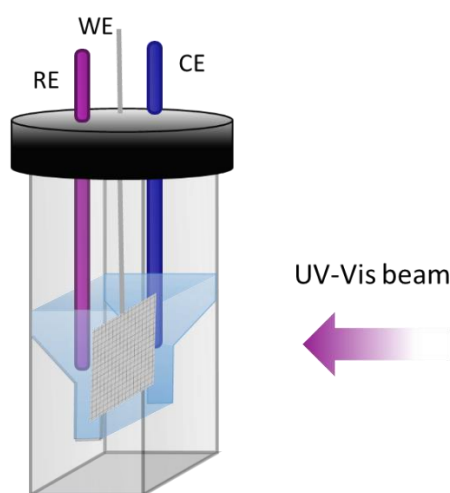
3.1 Cell development for the UV-vis spectroelectrochemistry

3.1.1 A review of the existing UV-Vis spectroelectrochemistry cells

Electrochemistry is a particularly valuable tool for the investigation of complex redox systems, such as enzymes, where it offers dynamic insight into the underlying reactions. Utilising controlled external voltages within an electrochemical cell, redox reactions can be manipulated and observed by measuring corresponding electric currents. In this project, electrochemistry will serve as the central technique for manipulating and controlling protein behaviour, offering a potent means of directing catalysis and unravelling the potentials governing specific reactions.[70] The integration of UV-Vis spectroscopy with electrochemical control allows for simultaneous observation of electronic and structural changes within the system, bridging the gap between electrochemical behaviour and molecular characteristics. The synergistic combination of these techniques can provide crucial insights into the mechanistic and kinetic details of redox processes, making it an indispensable tool in contemporary chemical research.

The application of electrochemistry in this context requires a UV-Vis spectroelectrochemical (UV-Vis SEC) cell compatible with standard UV-Vis spectrometers. In the field of spectroelectrochemistry, the design of the UV-Vis SEC cell is crucial for achieving accurate and efficient experimental results. There are

commercial options available from companies such as Gamry Instruments, BASI Research Products, Pine Research, and ALS Co. Ltd, which typically feature a quartz cuvette capped with holders for three essential electrodes (Scheme 3.1).

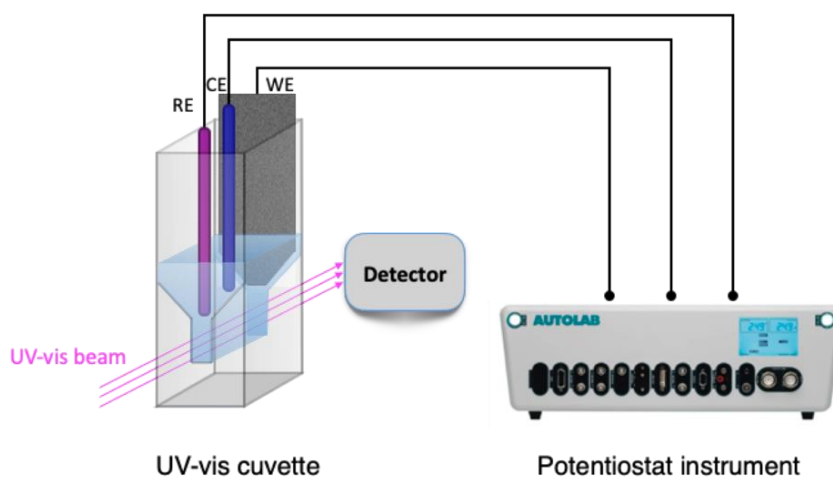


Scheme 3. 1 Common design of a commercial UV-Vis SEC cell

The commercially available cell from Gamry Instruments, with a standard cuvette path length of 1 cm, requires a large sample volume (at least 2 mL), making it potentially unsuitable for limited-sample applications. Alternative providers offer thin-layer cuvettes, demanding less sample volume, but the shorter optical path lengths ranging from 0.5 mm to 1.7 mm present challenges for low-absorbing samples. According to the Beer-Lambert law (Eq 2.2), shorter path lengths result in decreased absorbance for the same sample concentration, which will compromise the sensitivity of the experiment. Additionally, the commonly used platinum or gold grid working electrodes restrict the operative potential range at negative values due to hydrogen evolution. This limitation underscores the necessity of creating a specialized UV-Vis SEC cell that combines both a small volume requirement with a broad operative potential range. Such a design is pivotal for the redox study of proteins in this thesis, accommodating the unique needs of the experimental system and ensuring that accurate, actionable insights are obtained.

3.1.2 The design of the UV-Vis spectroelectrochemistry cell

The integration of UV-Vis spectroscopy with electrochemistry culminates in the UV-Vis Spectroelectrochemistry (UV-Vis SEC) method, a robust approach that enables the simultaneous acquisition of electrochemical (current, potential) and spectroscopic responses. Specifically tailored for the study of FeS cluster redox proteins, a specialized three-electrode UV-Vis cuvette cell has been designed for this project. This design facilitates the simultaneous execution of electrochemistry and monitoring of the UV-Vis spectrum, rendering it a highly sensitive and direct method to observe the redox processes, particularly for [4Fe-4S] clusters within Fe protein and L₂ protein, whose UV-Vis absorption spectrum undergoes significant alterations during redox reactions.



Scheme 3. 2 A schematic diagram of the UV-Vis spectroelectrochemistry (UV-Vis SEC) set-up

The UV-Vis SEC cuvette features a standard path length of 1 cm and is designed to be wider at the top while narrowing towards the bottom, thus enabling operation with small volumes of protein sample (minimum 50-100 μ L). The cuvette accommodates a large surface carbon working electrode, a carbon counter electrode, and a homemade saturated calomel electrode (SCE) as a reference. The choice of a home-built counter electrode and SCE stems from specific requirements, including the need for frit separation and a lack of suitable commercial miniature SCE options. Furthermore, the

production of Fe protein and its homologues presents significant challenges due to its O₂ sensitivity, rendering the protein a valuable and limited resource. Accordingly, all procedures are meticulously optimized to conserve protein usage.

The expansive surface area of the working electrode ensures maximal solution contact and facilitates electron transfer between the electrode and solution. Redox titrations are meticulously conducted by applying varying potentials in incremental steps via a potentiostat, while monitoring the consequential changes in the UV-Vis spectra with a spectrophotometer.[37] More details on these design elements, including specific dimensions, materials, and configurations, along with schematic diagrams will be comprehensively elucidated in the subsection that follows.

Carbon electrodes are available in various types and configurations. While glassy carbon stands as the most common type, its high cost and difficulty in shaping make it less appealing for some applications. Carbon in the shapes of paper, felt, and mesh has been evaluated as a potential material for the working electrode, primarily due to ease of manipulating and abundant surface area for redox reactions (Figure 3.1). However, these forms have their limitations.

Despite their apparent advantages, paper, felt, and mesh carbon materials are not ideal choices for the construction of a UV-Vis spectrochemical cell. A working electrode must exhibit consistent function across repeated uses, but restoring the cleanliness of these porous carbon forms is a challenge. Moreover, the extended duration of redox titrations, often exceeding five hours, demands a robust material. Carbon cloth and similar materials are found to be quite fragile; their performance deteriorates over the course of an experiment, evidenced by small carbon pieces and

particles released into the cell. This debris can cause scattering across the UV-Vis spectrum, complicating the interpretation of the absorption from the species of interest.

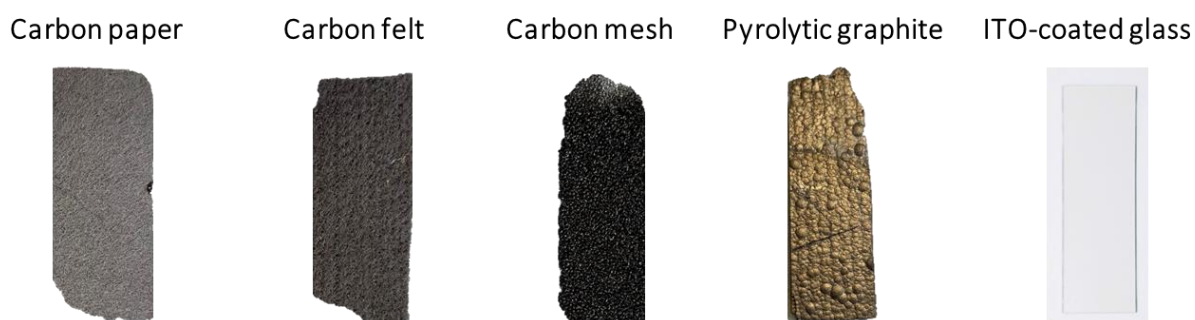


Figure 3. 1 Different forms of considered electrode materials

Indium tin oxide (ITO)-coated glass is another common material used in spectroelectrochemistry (SEC). The ITO electrode has been widely used in the research of proteins such as Decaheme cytochrome and Ferredoxin-NADP⁺ reductase, owing to its unique combination of optical transparency and conductive properties. [201-203] However, it has been observed herein that the ITO-coated glass electrode exhibits an oxidation peak at approximately -0.62 V vs SHE, and a reductive peak below approximately -0.84 V versus SHE in its cyclic voltammetry. (Figure 3.2 A). These peaks can interfere with the observation and interpretation of the electrochemical phenomena under investigation, especially when the redox processes of interest are occurring in the same potential range as the ITO's redox peaks.

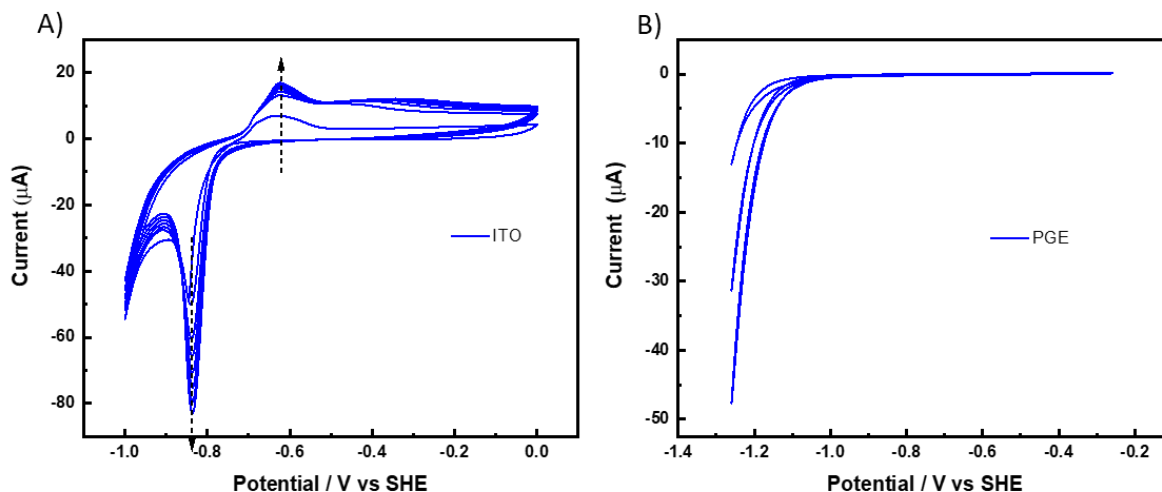
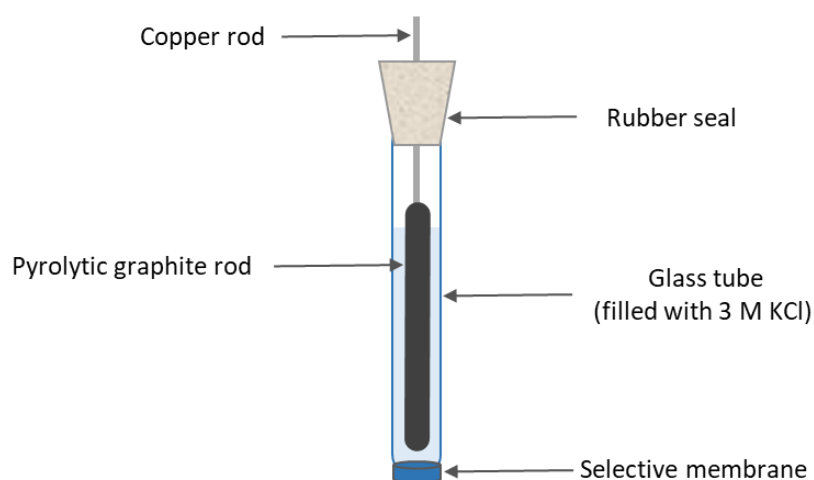


Figure 3.2 Cyclic voltammetry of 5 mM KCl solution using A) ITO-coated glass and B) pyrolytic graphite as working electrode, pyrolytic graphite as counter electrode and calomel electrode as reference electrode

After careful examination, pyrolytic graphite emerges as the optimal material for the UV-Vis spectroelectrochemical cell. Comparable to graphite but with covalent bonding between its graphene sheets, pyrolytic graphite offers a unique blend of characteristics. It is manufactured through the heating of a hydrocarbon to near its decomposition temperature, allowing graphite to crystallise in a process known as pyrolysis. This material provides benefits such as mechanical reproducibility through polishing, ease of machining, and resistance to degradation. Additionally, pyrolytic graphite displays no redox activity over an extensive potential range from -0.2 V to -1.1 V vs SHE, as illustrated in Figure 3.2 B. This characteristic ensures its operation within the potential range corresponding to the desired redox reactions, presenting an additional benefit when compared to an ITO electrode.

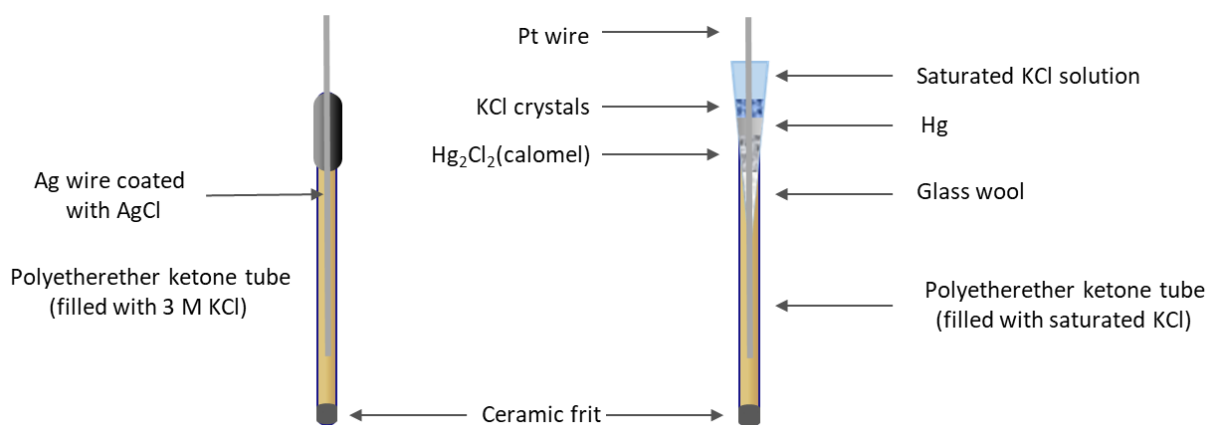
Platinum has frequently been used as a counter electrode (CE) for various electrochemical experiments; however, the cost can be high if a large surface area is to be achieved. Pyrolytic graphite is also used as a counter electrode because of its stability and large surface area (Scheme 3.3). To prevent the products formed at the surface of

the counter electrode from affecting the desired reaction at the working electrode, the pyrolytic graphite is installed in a fritted glass tube. This tube separates the liquid of the counter electrode from the working electrode by a selective membrane and is filled with 3 M KCl to ensure good conductivity. On top of the pyrolytic graphite rod, there is a copper rod for connection to the potentiostat instrument, and it is sealed with a rubber cap.



Scheme 3.3 Homemade counter electrode in a fritted glass tube

A miniature reference electrode (RE) is necessary due to the restricted space in the cell. A commercial leak-free Ag/AgCl reference electrode with a 2 mm diameter (Warner instrument) was initially used (as shown in Scheme 3.4, left). Its construction consists of a polyether etherketone (PEEK) tube with a frit at one end, filled with 3 M KCl electrolyte, and a silver wire with an AgCl coating immersed in it. Although the leak-free Ag/AgCl electrode is designed to eliminate problems associated with electrolyte loss and sample contamination, a significant potential drift was observed during electrochemical experiments. A possible reason for this drift is that Tris buffer, used in the experiment, may leak into the Ag/AgCl electrode, causing potential drift as Tris interacts with the silver.



Scheme 3.4 Comparison of a commercial leak-free Ag/AgCl reference electrode (left) with a homemade SCE reference electrode (right)

Hence, a homemade saturated calomel electrode (SCE) RE was crafted to fit in the cell as the reference electrode (as shown in Scheme 3.4, right). The advantage of SCE is that the concentration of KCl and the potential of the electrode remain constant, even if the KCl solution is partially evaporated. The components of a homemade saturated calomel electrode (SCE) are shown in Scheme 3.4. Within a micro-point pipette tip, the components are layered from bottom to top with glass wool, Hg_2Cl_2 paste made with saturated KCl solution, Hg drops, and KCl crystals. This pipette tip is installed on top of a PEEK tube, which is filled with saturated KCl solution and fitted with a frit that contacts the solution. This PEEK tube with ceramic frit was acquired from an inoperative commercial leak-free Ag/AgCl reference electrode mentioned previously. The pipette tip and the tube are connected by a platinum wire running through the center, and saturated KCl solution permeates the entirety of the electrode.

3.1.3 Redox mediators

For the studies of the redox properties of the Fe protein, Eu-complexes will be used either as redox mediators or as strong reductants for the potentiometric titrations. The redox potential of the $\text{Eu}^{\text{III}}/\text{Eu}^{\text{II}}$ couple in aqueous solution is commonly reported as

around -0.35 V at neutral pH, while chelating with a series of polyaminocarboxylate ligands makes the midpoint potential shift in the negative direction, stabilising Eu(III). A study by Vincent et al. demonstrated that the Eu(II) form can be generated in situ, and that Eu(II)-polyaminocarboxylate complexes form instantaneously in aqueous solution as low-potential reductants. It was found that some Eu(II)-polyaminocarboxylate complexes, including Eu(II)-DTPA (diethylenetriamine pentaacetic acid) complexes, have lower reduction potentials than common reducing agents like sodium dithionite (ca. -0.66 V) and deazaflavin (ca. -0.650 V). [204] These Eu(II) complexes are able to reduce nitrogenase Fe protein to its super-reduced state $[4\text{Fe}-4\text{S}]^0$ (c.a. -0.8 V). [37]

The following Eu-complexes will be used as redox mediators in the negative potential range: 1,2-bis(o-aminophenoxy)ethane-N,N,N',N'-tetraacetic acid (BAPTA), ethylene glycol-bis(2-aminoethylether)-N,N,N',N'-tetraacetic acid (EGTA), and diethylenetriamine-N,N,N',N'',N''-pentaacetate (DTPA). All Eu(III)-ligand complexes were formed by adding each ligand to Eu(III) solution at a 1:1 molar ratio. Cyclic voltammetry was employed to study the electrochemical properties of the selected Eu-ligand complexes. Experiments were conducted under anaerobic conditions using a three-electrode electrochemical system, comprising a glassy carbon working electrode, Pt wire counter electrode, and SCE reference electrode.

The ligands are dissolved in 0.25 mM NaOH to yield a 25 mM stock solution, while a 50 mM Eu(III) stock solution was prepared by dissolving EuCl_3 in Milli Q water, or Eu_2O_3 in 0.25 mM HCl. As mentioned previously, the Eu(III)-ligand complexes were formed by adding each ligand to Eu(III) solution at a molar ratio of 1:1. Then these Eu(III)-ligand complexes (EuCl_3 , Eu-BAPTA, Eu-EGTA, and Eu-DTPA) were diluted to a concentration

of 2.0 mM each in Tris-HCl buffer (50 mM, pH 8, with 50 mM NaCl) for the cyclic voltammetry measurements. Figure 3.3 illustrates the result of a cyclic voltammetry experiment on EuCl_3 and Eu(III) -ligand complexes (Eu-BAPTA , Eu-EGTA , and Eu-DTPA). The redox potential of $\text{Eu}_{(\text{aq})}^{\text{II/III}}$ couple stands at -0.45 at pH 8, and it is lowered to -0.63 , -0.87 and -1.09 V vs SHE, respectively, when Eu is chelated with BAPTA, EGTA and DTPA. These redox potentials span a wide potential range, effectively covering the region where the redox transformations of the proteins of interest are anticipated to occur.

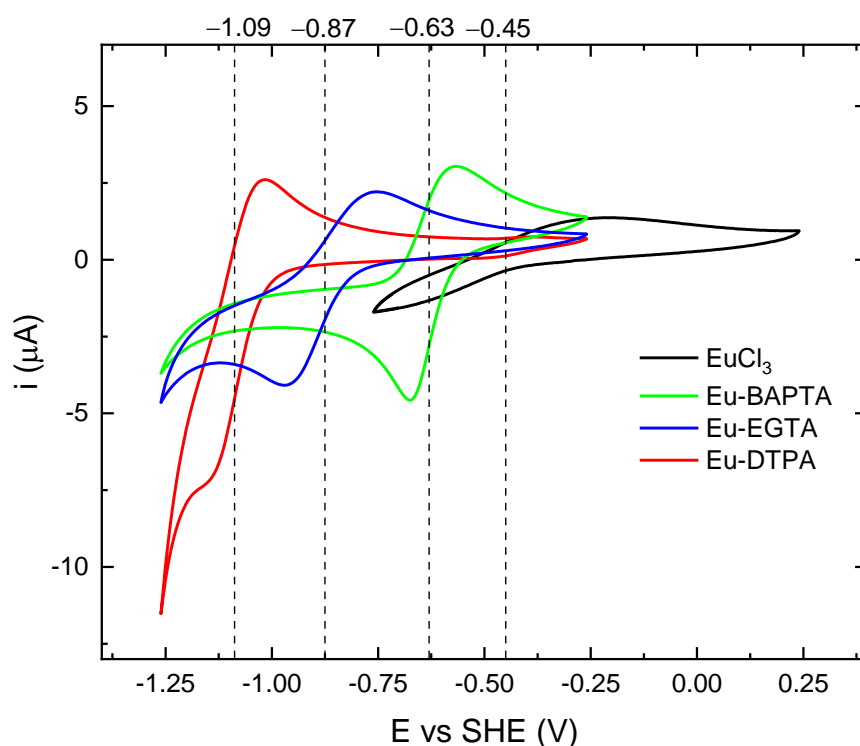


Figure 3. 3 A) cyclic voltammetry of EuCl_3 (black line), Eu-BAPTA (green line), Eu-EGTA (blue line), and Eu-DTPA (red line) at a concentration of 2.0 mM each in Tris-HCl buffer (50 mM, pH 8, with 50 mM NaCl).

It is intriguing to observe that the source of Eu(III) ion has an impact on the formation of the Eu -ligand complex. To illustrate this impact, the cyclic voltammetry of two mixtures is presented in Figure 3.4. When EuCl_3 or Eu_2O_3 is dissolved in the corresponding solvent and mixed with BAPTA solution, a redox species Eu-BAPTA is

formed as evidenced by the redox current (blue line in Figure 3.4). However, $\text{Eu}_2(\text{SO}_4)_3$ does not show redox activity dissolved in HCl, nor when mixed with BAPTA (red line in Figure 3.4).

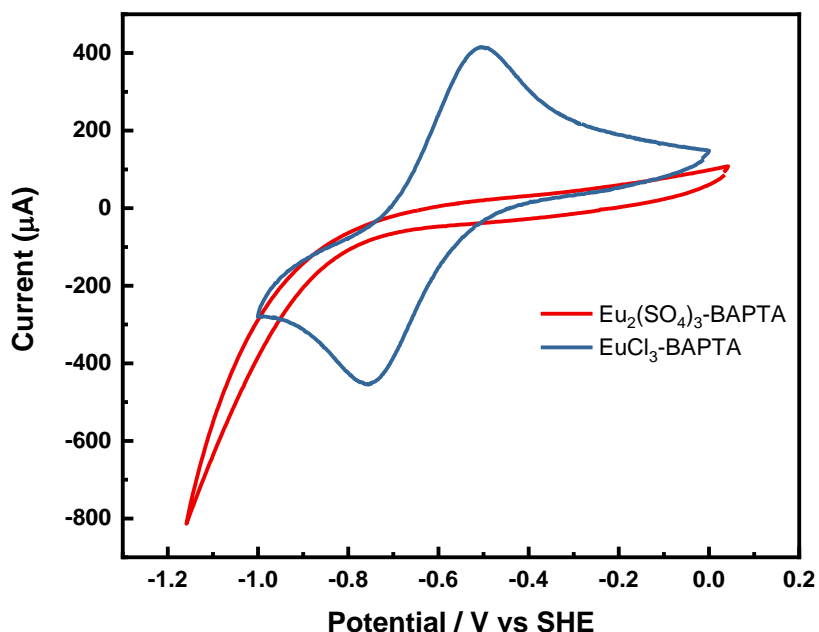


Figure 3. 4 Cyclic voltammetry of $\text{EuCl}_3\text{-BAPTA}$ (blue) and $\text{Eu}_2(\text{SO}_4)_3\text{-BAPTA}$.

A significant advantage of Eu-ligand complexes as redox mediators is their very weak absorption in the ultraviolet and visible spectral range, allowing them not to interfere with peaks arising from the protein. Commonly, redox mediators with a more positive potential (in this case, > -500 mV vs SHE), such as methyl viologen, are organic molecules that can be reversibly oxidised and reduced.[205] Incorporating phenosafranine ($E_m = -252$ mV), benzyl viologen ($E_m = -359$ mV) and methyl viologen ($E_m = -446$ mV) in the cell was explored to mediate electron transfer with the Fe protein from nitrogenase.

Phenosafranine, benzyl viologen, and methyl viologen were dissolved in MilliQ water to create three 5 mM stock solutions. Within a SEC cuvette featuring a pathlength of 1 cm, a 1 mL mixture of these redox mediators was prepared at a concentration of 25 μ M by diluting the stock solutions with a 50 mM HEPES pH 8 buffer containing 0.1 M NaCl. The UV-Vis SEC setup and three electrodes described in section 3.1.2 were employed to monitor the changes in the UV-Vis spectra while a continuous potential of -600 mV vs SHE was applied over the course of 1 hour. Figure 3.5 depicts the UV-Vis absorption of the mixture of the aforementioned redox mediators.

At a concentration as low as 25 μ M, there is strong absorption at 520 nm due to phenosafranine (red trace, Figure 3.5), which further complicates upon reduction at -600 mV vs SHE, manifesting as two sharp peaks around 400 nm and broad absorption from 500 nm to 700 nm. This strong UV-Vis absorption complicates data analysis and may compromise the quantitative determination of redox states in the protein of interest. Thus, these mediators were excluded during redox titration with the UV-Vis electrochemical cell. Later studies of the Fe protein of nitrogenase revealed that while redox mediators are not mandatory for the transition between the 1+/2+ states of the [4Fe-4S] cluster (occurring between approximately -500 mV to -200 mV), Eu-ligand complexes are essential for the transition between the 0/1+ states.

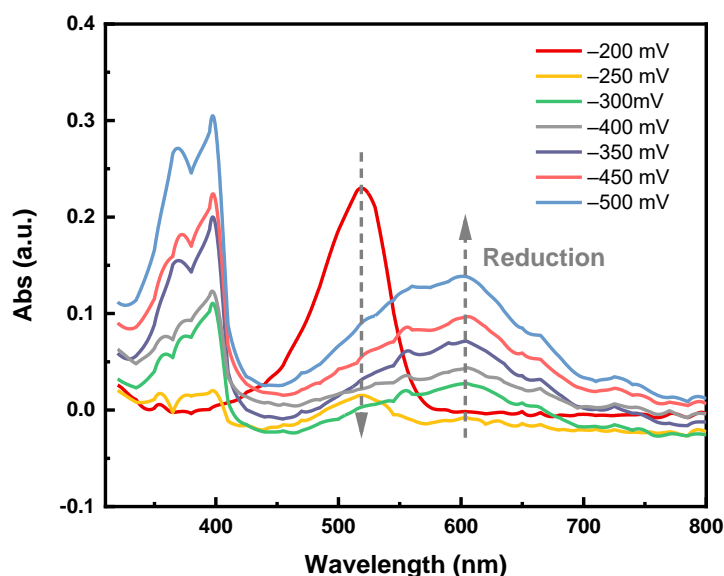


Figure 3. 5 The UV-Vis absorption of a mixture of phenosafranine, benzyl viologen and methyl viologen (25 μM each) during reduction.

3.1.4 Preliminary UV-Vis SEC experiment with Azurin

The UV-visible spectroelectrochemical cell (UV-Vis SEC cell) was initially tested using azurin, an easily-prepared blue copper protein. Azurin is a small protein (approximately 14 kDa) that functions as an electron transfer protein by interconverting the Cu^{III} couple. [206] In its oxidised form, azurin has a characteristic absorption at around 630 nm, arising from the ligand-metal charge transfer (LMCT) transition. This 630 nm band vanishes when the protein is reduced, since the fully-occupied d^{10} orbital of Cu^{I} cannot accept any charge from the ligand. By monitoring changes in the absorption peak at 630 nm, the redox state of the protein can be determined. Meanwhile, azurin's ability to be relatively easily overexpressed in *E. coli*, along with its high yields and purity, make it a practical choice for this application. [207, 208] The azurin from *Pseudomonas aeruginosa* used in this study was produced in our laboratory by Wangzhe Li and Tin Lai.

For the UV-Vis SEC experiment conducted with azurin, redox mediators were utilised to facilitate rapid electron transfer between the protein and the electrode.

Specifically, 2,6-dichloroindophenol sodium salt hydrate (DCIP) and potassium ferricyanide were employed, dissolved in a 50 mM HEPES pH 8 buffer to create a 0.5 mM stock solution. Azurin was subsequently diluted in the same buffer, containing NaCl at a 0.1 M concentration. The three electrodes were inserted into the UV-Vis cuvette (as depicted in Scheme 3.2, Section 3.1.2), which contained a total volume of 400 μL of azurin (final concentration of 50 μM) and a mediator cocktail (final concentration of 5 μM for each mediator). The electrodes were then connected to the potentiostat.

To initiate the titration, different potentials were applied in 100 mV increments, allowing equilibration for 10 minutes at each level (+450, +350, and +250 mV vs SHE). UV-Vis spectra were subsequently recorded at each potential once equilibrium had been reached (further details in Figure 3.6 and the associated explanation). Equilibrium is considered to be reached when there is no change between the subsequent spectrum and the preceding one.

Figure 3.6 illustrates the UV-Vis spectra obtained at the three distinct applied potentials, clearly showing that the 630 nm peak diminishes as the potential is lowered, eventually vanishing at +250 mV vs SHE. This change indicates the reduction of azurin to Cu^{I} . Selecting mediators for the positive potential range can be challenging, as many exhibit colour. Nevertheless, the UV-Vis absorption of both DCIP and potassium ferrocyanide falls below 550 nm, and thus does not interfere with the region where the azurin peak (630 nm) is expected. These mediators cause only negligible changes to the UV-Vis spectra within the applied potential range. From this experiment, the estimated midpoint potential of the Cu^{III} couple in azurin was found to be approximately +300 mV vs SHE, aligning with values reported in existing literature +292 mV at pH 8.[206, 209]

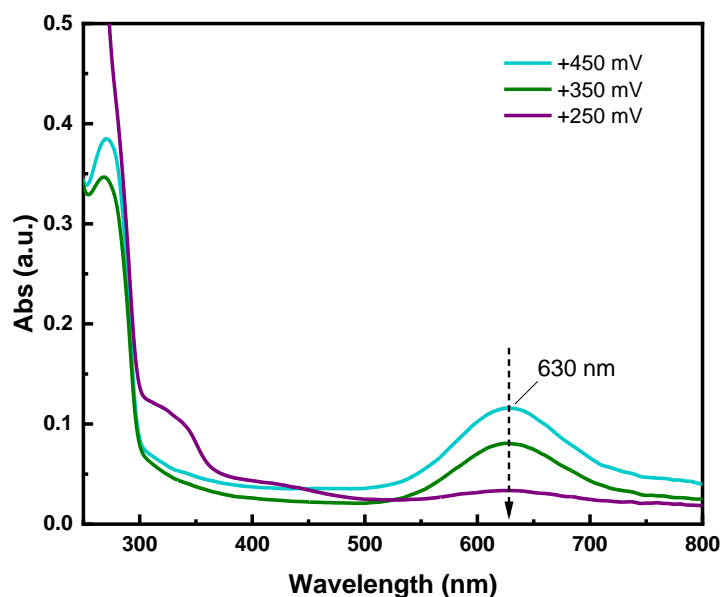


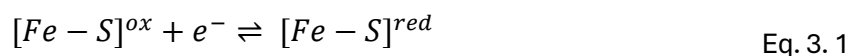
Figure 3.6 UV-Vis spectra of the redox titration of 50 μM azurin in the presence of redox mediators (2,6-Dichloroindophenol sodium salt hydrate and potassium ferricyanide, 5 μM each). The applied potentials are indicated on the plot. Azurin is in HEPES buffer (50 mM, pH 8) with 100 mM NaCl as supporting electrolyte.

This preliminary test with azurin demonstrates that the developed UV-Vis SEC cell is capable of performing redox titration with a small amount of protein. The UV-Vis SEC cell, designed for protein electrochemistry, includes a working electrode made of pyrolytic graphite (PGE) known for its mechanical stability and wide potential range without redox activity (-0.2 V to -1.1 V vs SHE). It also features a PGE counter electrode with a large surface area and a homemade saturated calomel electrode (SCE) as a stable reference electrode. The cell's cuvette accommodates small volumes (50-100 μL) for sample efficiency. Together, these components ensure the cell's effectiveness and stability for redox potential studies of proteins. This UV-Vis SEC cell will be utilised for the redox studies of Fe protein in the later sections of this chapter.

3.1.5 Data analysis with Nernst equation

Herein how the Nernst equation is applied in the analysis of experimental data in this thesis will be demonstrated. In the case of [4Fe-4S] cluster of the Fe protein, the

redox process is a simple one-electron reduction process without the protonation of the cluster, the redox process happening on the working electrode for the [Fe-S] cluster is



Three-electrode cells enable the evaluation of one half reaction independent of the other. The Nernst equation relates a cell's potential to the concentration of the redox species present and the standard reduction potential.

$$E = E^0 - \frac{RT}{nF} \ln \frac{[RED]}{[OX]} \quad \text{Eq. 3. 2}$$

In Equation 3.2, E is the potential applied, E^0 is the standard redox potential of the ox/red couple vs SHE, R is the universal gas constant ($8.314 \text{ J}\cdot\text{K}^{-1}\cdot\text{mol}^{-1}$), T is the temperature in K, F is the Faraday constant ($96,500 \text{ C/mol}$), and n is the number of electrons transferred in the reaction. Usually, the $[RED]$ and $[OX]$ are the activities of the reduced and oxidised species respectively. The concentration of the redox species is proportional to the intensity of absorbance according to the Beer-Lambert law. Assume the concentration is equal to the activity of the species as the solution is diluted, then the activity is proportional to the intensity of absorbance. So here we define the $[red]$ and $[ox]$ as the relative concentrations determined from UV-Vis absorbance intensities (relative intensities) of the reduced and oxidised [Fe-S] cluster individually. For a reversible process where there is no degradation of the [Fe-S] cluster, the sum of the relative intensity of the involved species will be defined as 1.

$$[red] + [ox] = 1 \quad \text{Eq. 3. 3}$$

Therefore:

$$[ox] = 1 - [red] \quad \text{Eq. 3. 4}$$

The relative intensity of a species will be defined as

$$[red] = \frac{A}{A_{total}} \times 100\% \quad \text{Eq. 3.5}$$

where A is the absorbance of the UV-Vis beam by the reduced species, and A_{total} is the maximum absorbance of this species at the concentration relevant to the experiment.

Rearranging the Nernst equation (Eq. 3.2), the $[ox]$ and $[red]$ are shown as:

$$[ox] = \frac{1}{1 + \exp \frac{nF}{RT} (E^0 - E)} \quad \text{Eq. 3.6}$$

or:

$$[red] = 1 - \frac{1}{1 + \exp \frac{nF}{RT} (E^0 - E)} \quad \text{Eq. 3.7}$$

Setting the E^0 value as -0.5 V vs SHE, n value as 1 (a single-electron transfer), and T as 25°C (298.15 K) the curve of the $[ox]$ and $[red]$ against the potential is shown in Figure 3.7. It is shown that at a low potential (-0.7 V vs SHE), the dominant species is the reduced state. When the applied potential increases, the proportion of the oxidised species gradually increases, attaining 50% at -0.5 V vs SHE (the redox midpoint potential). As the applied potential continues increasing, the reduced species keeps converting to the oxidised state.

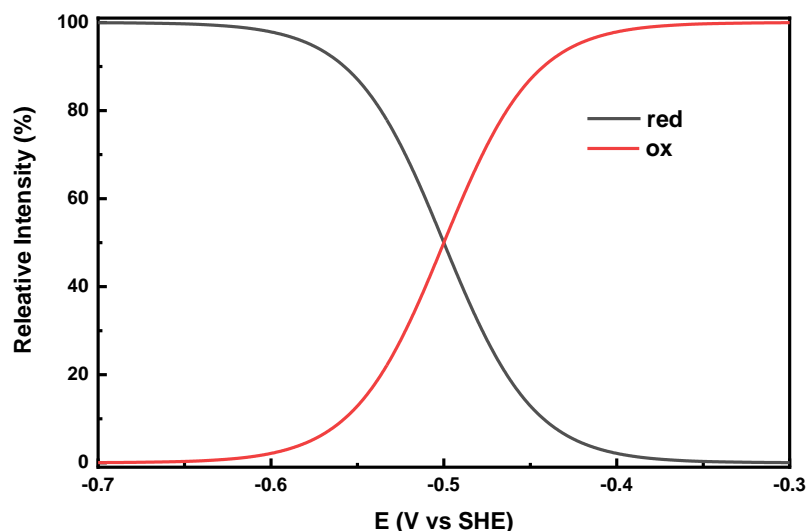


Figure 3.7 Change of $[ox]$ and $[red]$ against the applied potential. The curve is simulated with Eq. 3.6 and Eq. 3.7, with $E^0 = -0.5$ V vs SHE, and $n = 1$.

At the redox midpoint potential (E_m), there is an equal concentration of oxidised and reduced species. If E_m is obtained under standard conditions, (total relative intensity of all components is 1, 298.15 K, 1 bar), it is the standard redox potential (E^0). The E_m is an important intrinsic property of a redox species, which represents how easily a species can be reduced by accepting electrons. A lower redox potential means that the species is harder to reduce. The UV-Vis SEC cell developed in the earlier section will be used to determine the redox potentials of the Fe protein of nitrogenase and the L₂ protein of nitrogenase homologues.

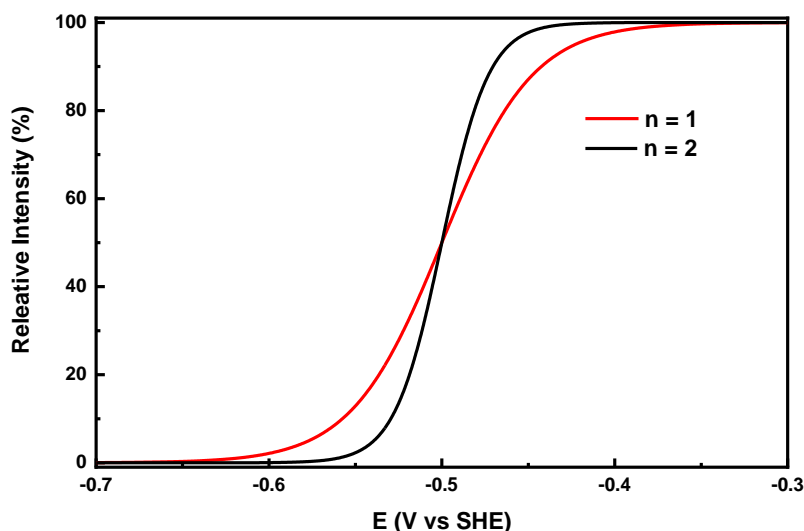


Figure 3. 8 Change of $[ox]$ against the applied potential. The curve is simulated with Eq. 3.6, with $E^0 = -0.5$ V vs SHE, and $n = 1$ (red trace) or 2 separately (black trace).

The value of n is the number of electrons transferred in a redox reaction. It affects the shape of the curve. As in Figure 3.8, with the E^0 value as -0.5 V vs SHE, (a single-electron transfer) and T as 25 °C, the curve of the $[ox]$ and $[red]$ against the potential is plotted, with n set as 1 (red trace) or 2 (black trace) individually. When $n = 2$, the curve is steeper, meaning that the concentration of species changes more sharply with applied potential than when $n = 1$. Therefore, the Nernst equation could be used to determine the number of electrons transferred during a redox reaction by simulating the curve with various n values until it fits the measured one the best. In this thesis, the n values of protein's redox processes will be determined by this simulation method with OriginLab.

3.2 Formation and characterisation of the all-ferrous state of the NifH

3.2.1 Formation of the all-ferrous state of the NifH

The all-ferrous state of NifH represents the oxidation state of interest for this work, so the formation of this state was initially experimented with. The formation of the all-ferrous state of NifH was carried out similarly as described by Vincent *et al.*. [40]

Generally, [4Fe-4S] cluster proteins show a broad peak around 410 nm in the 2+ state and this peak vanishes upon one-electron reduction to the 1+ state. [210-212]

The NifH samples (2.6 mM) were received in Tris buffer (pH 8.0, 50 mM), with NaCl (500 mM) and sodium dithionite (2 mM). As NifH is sensitive to the presence of O₂, the sample tubes were stored by submerging them in liquid N₂ within a cryogenic dewar. The inclusion of dithionite not only prevents the self-oxidation of NifH but also shields it from potential O₂ damage. Before proceeding with a redox titration, the sample's buffer was exchanged for CHES buffer (pH 9, 100 mM), containing NaCl (150 mM), utilising an Amicon Ultra 8 (0.5 centrifugal filter unit, membrane NMWL, 30 kDa). During this buffer exchange process, the dithionite is also effectively removed.

NifH was subsequently diluted to a concentration of 0.03 mM with the same CHES buffer, and a UV-Vis spectrum was recorded (depicted as the black line in Figure 3.9 A). The emergence of a peak at 380 nm indicates that the NifH is in a partially oxidised state. Eu(II), though a mild reducing agent in solution, gains greater reductive potency when complexed with polyamino carboxylate ligands such as DTPA, which stabilises the Eu(II) form. However, since Eu(II)-DTPA can be oxidised to Eu(III)-DTPA in the presence of proton reduction, it is crucial to generate it *in situ*.

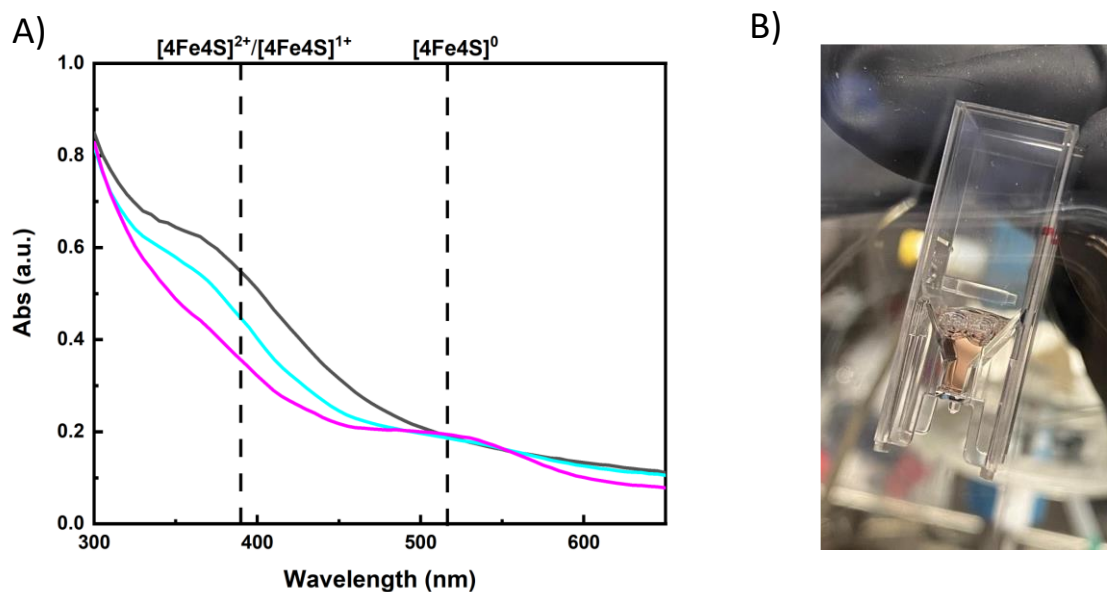


Figure 3.9 **A)** The UV-Vis spectra indicating the formation of the all-ferrous state NifH ($[4Fe-4S]^0$) at pH 8. The black line is the UV-Vis spectrum of 0.03 mM NifH in its partially oxidised ($[4Fe-4S]^{2+}/[4Fe-4S]^{1+}$) state, the cyan line shows the UV-Vis spectrum of NifH upon the addition of 1 molar equivalent of $Eu(II)$ -DTPA, and the magenta line shows the UV-Vis spectrum of the $[4Fe-4S]^0$ state generated upon addition of 2 molar equivalent of $Eu(II)$ -DTPA. **B)** the light pink colour of NifH in the cuvette when the $[4Fe-4S]^0$ state is generated at pH 8.

Firstly, to initiate the formation of the all-ferrous state, one molar equivalent of $Eu(II)$ was added to the UV-Vis cuvette containing NifH. Subsequently, one molar equivalent of DTPA was also introduced, and another UV-Vis spectrum was measured (as represented by the cyan line in Figure 3.9 A). As evident in the cyan line, the intensity of the 380 nm peak has diminished, indicating that the protein is undergoing reduction. To complete the reduction, one more molar equivalent of both $Eu(II)$ and DTPA were added, resulting in the magenta line of the UV-Vis spectrum in Figure 3.9 A. Upon the subsequent addition of $Eu(II)$ and DTPA, no change in the spectrum was observed. Thus, a total of 2 molar equivalents of electrons were introduced to achieve the all-ferrous state. Following the addition of two equivalents of $Eu(II)$ and DTPA, the 380 nm peak completely disappeared, and a 520 nm peak emerged, along with a change in the colour of the protein to light pink (Figure 3.9 B). This 520 nm peak has been previously identified as corresponding to the $S = 4$ all-ferrous state of NifH.[37]

3.2.2 Stability of the all-ferrous state of NifH

In Section 3.2.1, the all-ferrous state of Fe protein was successfully formed by the addition of two molar equivalents of Eu(II)-DTPA. After the generation of this state, when the cuvette was left inside the UV-Vis spectrophotometer under the N₂ atmosphere of the glovebox, it was observed that the pink colour faded gradually with time and the 380 nm peak reappeared, indicating reoxidation of the all-ferrous state. The all-ferrous state has been suggested to be stabilised in the Fe protein compared with small synthetic clusters, where this state could be reached but was found to be highly unstable.[34, 35] Probably the all-ferrous state is reoxidised by protons in the solution since it is formed at a potential much more negative than the H⁺/H₂ potential. As the redox titration process to explore the potential of the [4Fe-4S] cluster spans several hours, the stability of this state is of great importance. To thoroughly investigate the stability of the all-ferrous state in NifH under the given experimental conditions, UV-Vis spectra were collected at one-minute intervals immediately following the formation of the all-ferrous state. This allowed for continuous monitoring of its stability at 25°C and pH 8.

The reoxidation of the [4Fe-4S]⁰ state of NifH could be monitored by following the changes in the UV-Vis spectra over time. Figure 3.10 A shows consecutive UV-Vis spectra of the NifH measured immediately after the formation of the all-ferrous state over 30 minutes. The absorbance of the peaks at 380 and 520 nm represent the [4Fe-4S]²⁺/[4Fe-4S]¹⁺ and [4Fe-4S]⁰ states of NifH, respectively. It can be seen that while the absorbance at 520 nm (the [4Fe-4S]⁰ state) decreases, the absorbance at 380 nm increases (the [4Fe-4S]²⁺/[4Fe-4S]¹⁺ state). This is consistent with the all-ferrous state being re-oxidised by the protons in the solution slowly over time. In Figure 3.10 B, the relative absorbance intensity for the all-ferrous state (band at 520 nm) and [4Fe-4S]²⁺/[4Fe-4S]¹⁺ (band at 380

nm), is plotted against time. The curve shows a half-life of around 7.5 minutes for the all-ferrous state at 25°C in 50 mM HEPES pH 8 buffer. It can be clearly seen that after 30 min the all-ferrous state is completely gone.

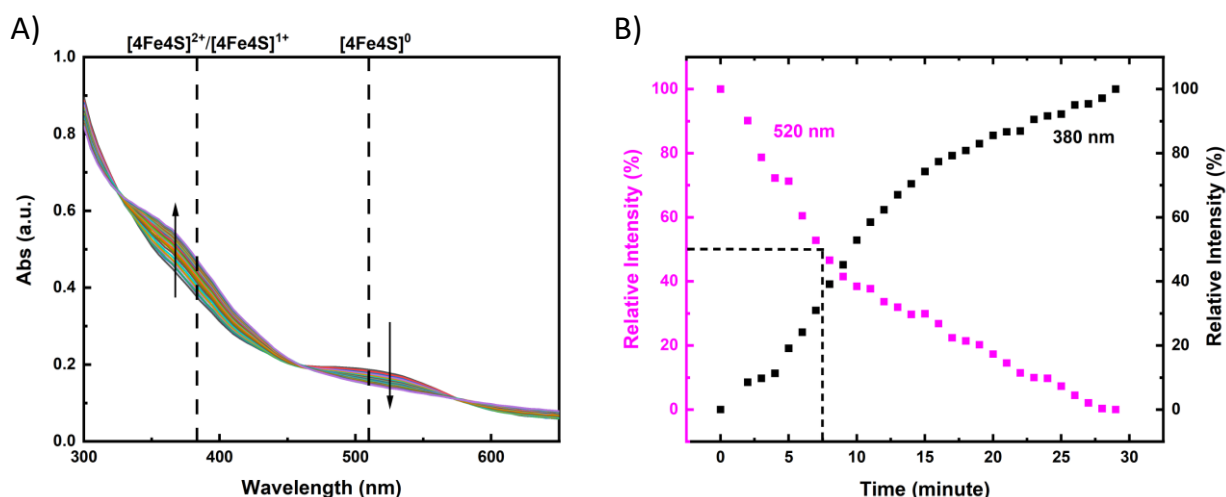


Figure 3.10 **A)** Consecutive UV-Vis spectra measure to check the stability of the all-ferrous state at pH 8. **B)** Absorbance at 520 nm (magenta points, all-ferrous state) and 380 nm (black points, partially oxidised state) plotted against time at pH 8 and 25 °C; the dashed lines indicate the time when the relative intensity at 520 nm decreased to 50% (the half-life of the all-ferrous state).

Next, the stability of the all-ferrous state was examined under various conditions. The half-life values were determined by monitoring the absorbance at 520 nm until it reached 50% of its original value. Table 3.1 below summarises the results. The stability of the all-ferrous state at pH 8 was compared to that at pH 9. Studies were also performed in the presence of MgATP to investigate whether the all-ferrous state can be formed in the presence of MgATP and how the stability is affected by MgATP binding. The effect of temperature on the formation and stability of the all-ferrous state was also studied by performing experiments at 10°C and 25°C.

Table 3. 1 Stability of the all-ferrous state of NifH under various conditions and in the presence and absence of MgATP.

Temperature/°C	pH	MgATP presence	$t_{1/2}$ /min
10	9	No	338
		Yes	326
	8	No	47
		Yes	43
25	9	No	226
		Yes	102
	8	No	7.5
		Yes	13

These results show the all-ferrous state to be more stable at the higher pH (longer half-life time), supporting the hypothesis that the all-ferrous state gets re-oxidised by proton reduction. Furthermore, the half-life of the all-ferrous state at pH 8 is over 40 minutes at 10°C compared to around 10 minutes at 25°C for the same pH. Hence, lower temperature is also beneficial to stabilise the all-ferrous state. The all-ferrous state can also be formed in the presence of MgATP, though it seems to have relatively little influence on its stability. More experiments are explored to shed light on how MgATP is involved in the formation of the all-ferrous state and how it affects the midpoint potential of the $[4\text{Fe-4S}]^{2+}/[4\text{Fe-4S}]^{1+}$ and the $[4\text{Fe-4S}]^{1+}/[4\text{Fe-4S}]^0$ couples.

3.2.3 Reversibility of formation of the all-ferrous state

Reversibility of formation of the all-ferrous state seems an important feature to consider when discussing its possible relevance *in vivo*. Following the stability experiment performed at pH 8 and 25°C in Section 3.2.2, when NifH was totally re-

oxidised, the reversibility of the formation of the all-ferrous state was studied by adding aliquots of Eu(II)-DTPA to the re-oxidised Fe protein and see whether the all-ferrous state could be formed again. UV-Vis spectra were collected after adding each molar equivalent of Eu(II)-DTPA, as shown in Figure 3.11.

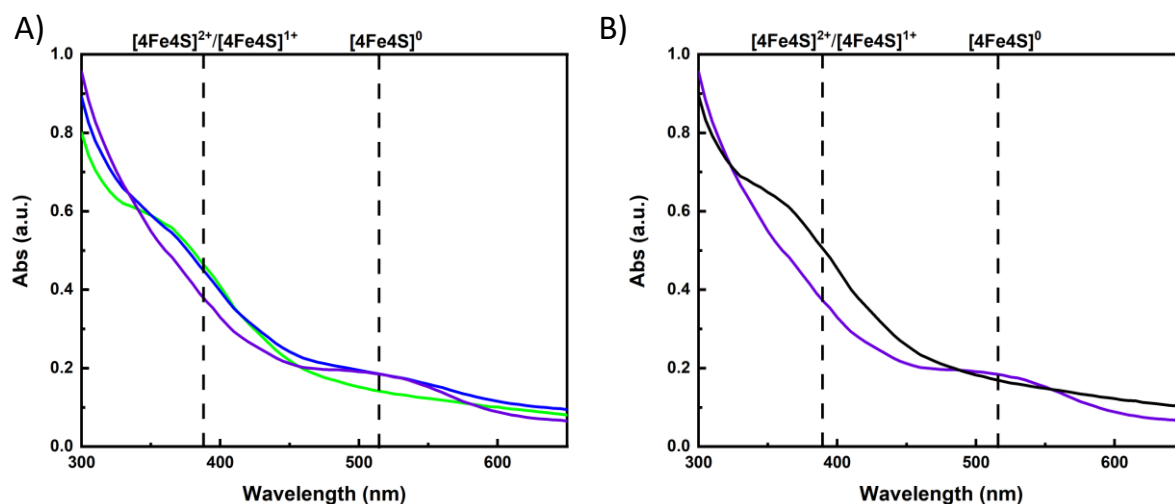


Figure 3. 11 **A)** green line: the UV-Vis spectrum of the re-oxidised Fe protein at pH 8. Blue and purple lines: the UV-Vis spectra collected after adding 1 and 2 molar equivalents of Eu(II)-DTPA to the re-oxidised Fe protein respectively, to form the all-ferrous state at pH 8. **B)** UV-Vis spectra showing the all-ferrous state formed the second time (purple line) and left to re-oxidise again with time (black trace) at pH 8.

The green line in Figure 3.11 A is the re-oxidised Fe protein, which has the characteristic peak around 380 nm arising from $[4\text{Fe-4S}]^{2+}/[4\text{Fe-4S}]^{1+}$. Then, the blue line was collected after adding 1 molar equivalent of Eu(II)-DTPA. It can be seen that the intensity of the peak around 380 nm decreased a bit, but the peak at 520 nm was still not observed. Hence, as observed in Section 3.2.1, one molar equivalent of Eu(II)-DTPA is not sufficient to produce the pink super-reduced species. However, after adding another molar equivalent of Eu(II)-DTPA (two equivalents in total), the peak at 520 nm appeared again (see the purple line, Figure 3.11 A). Thus, it can be concluded that the all-ferrous state of Fe protein could be formed again after re-oxidising and re-reducing the protein, indicating that its formation is indeed reversible. The UV-Vis spectra of Figure 3.11 A show how after the all-ferrous state was formed for the second time (purple line, Figure

3.11 A), it was also left to re-oxidise with time (black line, Figure 3.11 B). The black line does not exhibit the peak at 520 nm and instead has a peak at around 380 nm, thus showing that the protein has again been re-oxidised probably by the protons in the solution. To conclude, under the experimental conditions tested (N_2 atmosphere at pH 8 and 25°C) the all-ferrous state can be formed reversibly. The full reversibility of the all-ferrous state was also observed at pH 9.

3.3 Redox states of Fe protein controlled by electrochemistry

In preliminary tests with azurin, the UV-Vis SEC cell demonstrated its ability to perform *in-situ* redox titration on this small protein, effectively determining azurin's midpoint potential. As the Fe protein is three times larger than azurin, redox mediators are helpful to facilitate electron transfer between the electrode surface and the protein. Therefore, it becomes vital to assess whether the UV-Vis SEC cell can control the Fe protein's oxidation states with the selected redox mediators outlined in section 3.1.3. This evaluation aims to establish the potentials of the redox couples under various conditions. As detailed in section 3.2.1, the all-ferrous state can be created by adding two equivalents of Eu(II)-DTPA to NifH. However, it remains a point of interest to explore whether this all-ferrous state can also be generated electrochemically.

3.3.1 Attempt to form all-ferrous state electrochemically

A UV-Vis SEC experiment was undertaken to investigate the electrochemical reduction of NifH to the all-ferrous state, as illustrated in Figure 3.12. Within the UV-Vis SEC cell, 150 μ L of NifH (33 μ M) was positioned in pH 9 CHES buffer at 10 °C. Subsequently, Eu(III)-L mediators were introduced to achieve a final concentration of 5 μ M for each Eu(III)-L species. The cell was subjected to a negative potential of -1000 mV

vs SHE, and UV-Vis spectra were recorded after equilibrium was reached within the cell. Over the course of the experiment, the concentration of Eu(III)-L mediators was progressively increased to 30 μM to investigate whether the all-ferrous state could be formed at a higher concentration in the presence of the redox mediators. A UV-Vis spectrum was collected following every addition of the redox mediators after the cell reached equilibrium.

The NifH is at a mixed oxidation state of 1+ and 2+ state when it is combined with the Eu(III)-L mediators as indicated by the absorbance at around 380 nm (the black trace in Figure 3.12 A). After the application of the negative potential at -1000 mV vs SHE for an hour, the absorbance at ca 400 nm slightly decreased consistent with elimination of the 2+ state (the purple trace in Figure 3.12 A). The pause time of the potential was lengthened to see if the all-ferrous could be formed. After 2 hours, no peak was evident at 520 nm in the spectra, suggesting the all-ferrous state could not be formed under these conditions or was reoxidised too rapidly (the green trace in Figure 3.12). The original concentration of the Eu(III)-L mediator is 5 μM of each, including Eu(III)-DTPA. More Eu(III)-L mediator stock was added to achieve a higher final concentration of 15 μM and 30 μM sequentially (the blue and red trace separately in Figure 3.12 A). However, the optical feature of the all-ferrous state was still not observed, regardless of the concentration of the mediators or the duration of the potential application. This may be due to the all-ferrous state re-oxidising more rapidly than it forms.

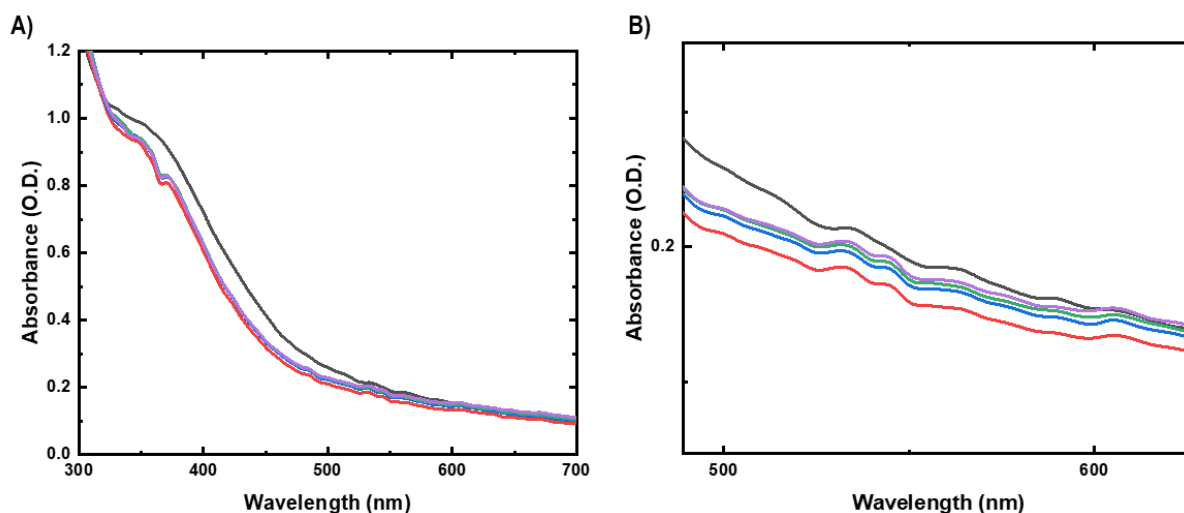


Figure 3. 12 A) Black trace: the UV-Vis spectra of NifH (33 μM) with the Eu(III)-L mediators (5 μM each) at open circuit potential. Purple and green traces: the spectra of NifH after applying -1000 mV for 1 h and 2 h separately. Blue and red traces: at -1000 mV, the NifH spectra with higher concentration of Eu(III)-L mediators, 15 μM and 30 μM individually. Figure B is the enlarged graph of Figure A from 500 – 600 nm.

Based on the above experiments, it can be concluded that the all-ferrous state could not be formed electrochemically in the UV-Vis SEC cell, probably due to the rapid re-oxidation. As the redox titration could not be performed reductively due to this conclusion, the possibility of conducting an oxidative titration is explored in the next step.

3.3.2 Determining the potential range for redox titration

To determine the redox potentials of NifH, the potential range of NifH was initially established using the UV-Vis SEC technique. A similar NifH solution was prepared in a UV-Vis cuvette, but two equivalents of Eu(II)-DTPA were added to the NifH to form the all-ferrous state. The potential of the cell was sequentially held at -1000 mV, -600 mV, and -200 mV until the UV-Vis spectrum did not change at each potential (Figure 3.13).

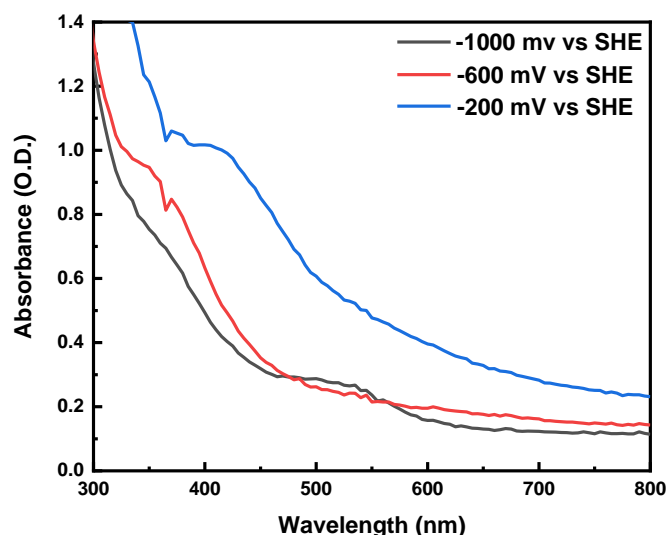


Figure 3. 13 The UV-Vis spectra of the NifH (33 μM) at different potentials. The potentials were applied at -1000 mV, -600 mV and -200 mV sequentially. The CHES buffer (pH 9, 100 mM) contains 150 mM NaCl and redox mediators with a final concentration of $5 \mu\text{M}$ of each Eu(III)-L species.

At -1000 mV, the all-ferrous state is now stabilised as shown in Figure 3.13 (the black trace). When the potential was increased to -600 mV, the all-ferrous state completely disappeared, and the $1+$ appeared instead (the red trace in Figure 3.13). When the potential was taken more positive, to -200 mV, the $1+$ state was oxidised to the $2+$ state indicated by the absorption at 410 nm (the blue trace in Figure 3.13). It can be concluded that NifH could be oxidised in the UV-Vis SEC cell stepwise from the all-ferrous to $1+$ and $2+$ state. The all-ferrous and $1+$ states exist between -1000 mV and -600 mV, while the $1+$ and $2+$ states prevail at -600 mV to -200 mV above. This experiment demonstrated the feasibility for an oxidative redox titration and defined the potential range required. This finding provided the necessary foundation for further redox titration experiments.

3.4 Determination of the redox potentials of the NifH

To assess the redox potential of the $[4\text{Fe-4S}]^{1+/0}$ couple, UV-Vis SEC experiments were conducted. Initial UV-Vis SEC experiments with NifH were done in the presence and

absence of redox mediators to determine the potential of the $[4\text{Fe-4S}]^0$ formation. However, difficulties were encountered as the electrochemical control was perturbed by the large background current generated by proton reduction at pH 8, which quickly re-oxidised the all-ferrous state.

As stated in section 3.2.2, it was discovered that the all-ferrous state of NifH is substantially more stable at pH 9 and 10 °C. Thus, the redox titration of NifH was done under these conditions. Eu-complexes (Eu-BAPTA, Eu-EGTA, Eu-DTPA, 10 μM each) were used as redox mediators for the low potential range, with the different polyamino carboxylate ligands giving $\text{Eu}^{\text{III/II}}$ midpoint potentials from -630 mV to -1090 mV, vs SHE, spanning the range where the redox chemistry of the $[4\text{Fe-4S}]^{1+/0}$ couple is likely to happen. The redox midpoint potential of the $[4\text{Fe-4S}]^{2+/1+}$ couple in NifH has been reported to be around -300 mV, vs SHE in the absence of nucleotides, and this potential has been observed to decrease by around 120 mV when MgATP is bound to NifH.[199] Thus, it would be interesting to study how nucleotide binding (MgATP and MgADP) affects the potential for formation of the $[4\text{Fe-4S}]^0$ state of NifH. In order to study this, potentiometric titrations were also performed in the presence of MgATP and MgADP.

3.4.1 Redox titration of NifH in the absence of nucleotides

In Section 3.3.2, the UV-Vis SEC technique was employed to ascertain the potential range necessary for the redox titration of NifH. This investigation specifically centred on the transitions among its various oxidation states: the all-ferrous state, the 1+ state, and the 2+ state. The determined potential range spanned from -1000 mV to -200 mV vs SHE. Notably, the redox titration of NifH was initially carried out without nucleotides, setting a foundation for subsequent, more intricate studies that incorporate nucleotide binding.

Prior to the redox titration, 350 μL of NifH (33 μM) was mixed with redox mediators (10 μM each) in the SEC cell as shown in section 3.1.2, and treated with two molar equivalents of Eu(II)-DTPA to form the all-ferrous state to start the titration from there. Subsequently, an oxidative redox titration was performed by applying potentials from -1000 to -150 mV vs SHE by the potentiostat at 25 mV potential using chronoamperometry (Figure 3.14 A). Simultaneously, alterations in the UV-Vis spectra were monitored *in situ* using a UV-Vis spectrophotometer (Figure 3.14 B). Within the -1000 to -150 mV range, the oxidation state of the [4Fe-4S] cluster transitions first to 1+ and then to 2+ as the potential is increased. The absorbance of the all-ferrous state ([4Fe-4S]⁰) was tracked via the 520 nm peak, whereas the oxidised state ([4Fe-4S]²⁺) was observed through the 410 nm peak in the UV-Vis spectra. This redox titration procedure for NifH was carried out thrice, with the findings illustrated in Figure 3.14. Data points of the same hue (be it black, blue, or red) denote a single dataset, underscoring the experiment's consistency and repeatability.

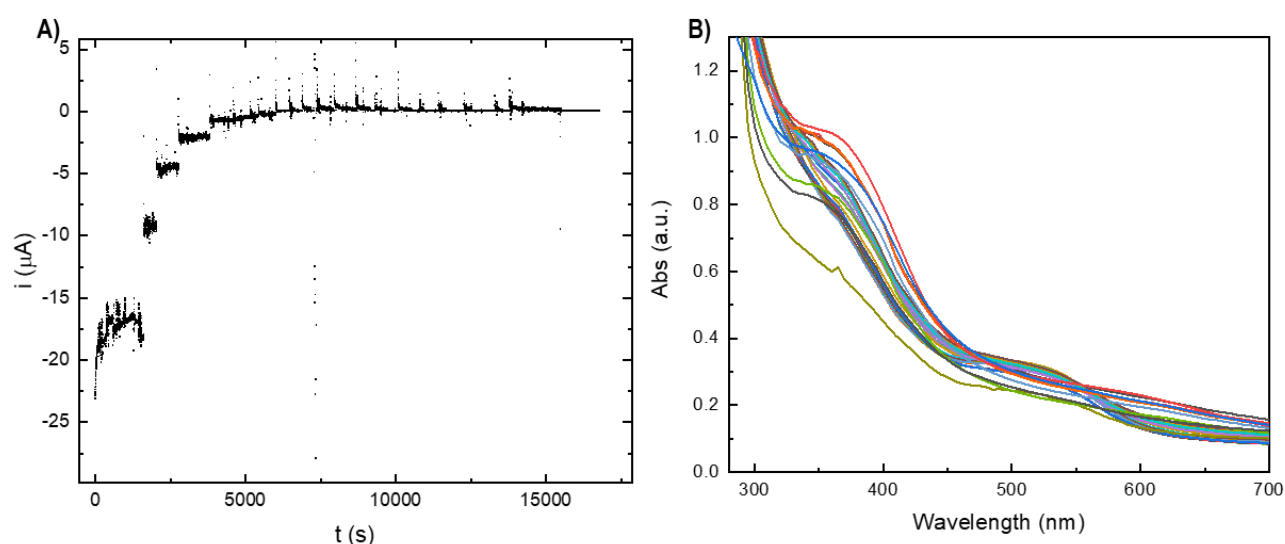


Figure 3.14 A) Chronoamperometric response of NifH (33 μM) during oxidative titration from -1000 to -150 mV vs SHE. The current (i) is plotted against time (t); B) UV-Vis spectra of NifH recorded at various potentials during its oxidative titration. Each curve corresponds to a specific potential, illustrating the changes in absorption characteristics of NifH as it undergoes redox transformations.

Figure 3.15 displays the results of the analysis, where the relative intensity of the all-ferrous state and the 2+ state are plotted against the applied potential (represented in plots A and B respectively) and fitted using the Nernst equation (Eq. 3.6). This oxidative titration can be distinctly categorized into two regions.

Specifically, plot A (Figure 3.15) reveals the oxidation progression of the [4Fe-4S] cluster from its 0 to 1+ state, spanning potentials from -1000 to -600 mV. Within this range, there is a noticeable decrease in absorbance at 520 nm. The midpoint potential, indicative of an equilibrium between 50% oxidised and 50% reduced species, was found by fitting the data with the Nernst equation (Eq. 3.7). In the absence of nucleotides, the midpoint potential for the [4Fe-4S]^{1+/0} couple was determined to be -790 mV vs SHE, with a $n = 0.74$ and a correlation coefficient $R^2 = 0.9329$.

In plot B (Figure 3.15), the oxidation transition from the 1+ to the 2+ state is depicted, corresponding to potentials ranging from -600 to -150 mV. This transition is marked by an increasing absorbance at 410 nm. By fitting the data in Figure 3.15 B using the Nernst equation (Eq. 3.6), we deduced a midpoint potential of -284 mV vs SHE with a $n = 0.72$ and a correlation coefficient $R^2 = 0.9783$ for the [4Fe-4S]^{2+/1+} couple, again in the absence of nucleotides. When these findings are juxtaposed against the literature, they display good alignment: previously reported midpoint potentials are -790 mV [40] and -300 mV [199], both vs SHE, for these respective couples. This similarity shows that the experimental values are in close agreement with established literature.

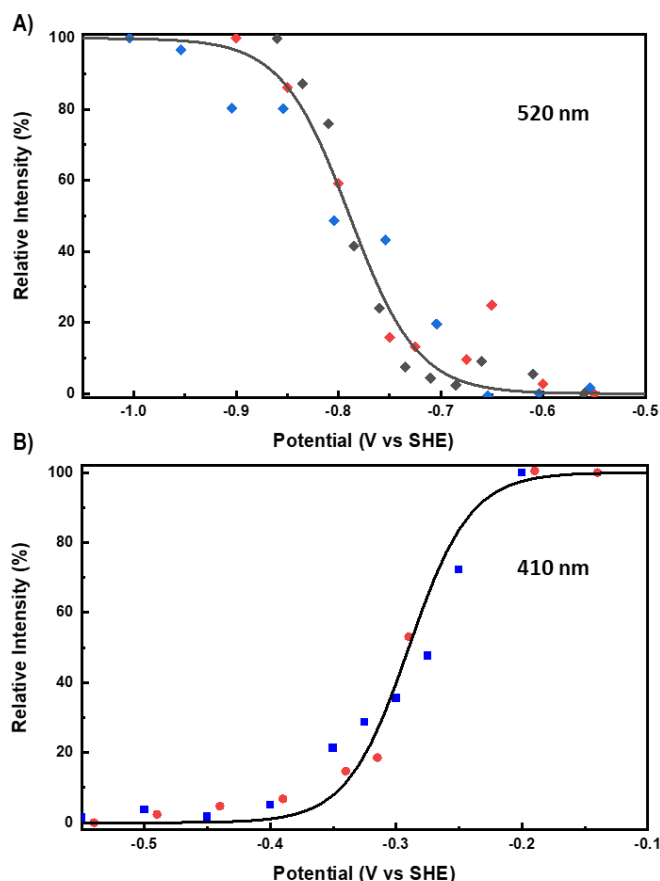


Figure 3.15 Redox titration of the [4Fe-4S] cluster in NifH of nitrogenase in the absence of nucleotides. NifH, in CHES buffer (100 mM, pH 9) with 150 mM NaCl as supporting electrolyte. The [4Fe-4S]⁰ state was formed adding two equivalents of Eu(II)-(DTPA) at pH 9 and 10 °C. It was oxidatively titrated with electrochemistry in the presence of a cocktail of redox mediators. The applied potential ranges from -1000 to -250 mV vs SHE with 25 mV steps. UV-Vis spectra were taken *in situ* after reaching redox equilibrium at each potential, to monitor the peaks at 520 nm (the [4Fe-4S]⁰ state) and 410 nm ([4Fe-4S]^{2+/1+}). Black traces are fitted with the Nernst equation. The data points in the same colour (black, blue, or red) represent one distinct set of data.

3.4.2 Redox titration of NifH in the presence of MgATP

In section 3.4.1, the UV-Vis SEC method was used to determine the redox potential of NifH in the absence of nucleotide, and the experiment outcome exhibited observable consistency with reported values, underlining the accuracy and reliability of the adopted methodology. While these findings provide valuable insights into the inherent redox properties of NifH, biological systems often present a more intricate matrix of interactions. Among these, the role of nucleotides, particularly MgATP, can significantly modulate the redox behaviour of proteins, thereby influencing their functions. Thus, understanding how MgATP affects the redox potential of NifH is pivotal

for a comprehensive understanding of its biochemical activity. In this section, the effects of MgATP on the redox potential of NifH is investigated.

Cyclic voltammetry was conducted in the presence of MgATP/MgADP and Eu-L mediators as a control experiment to assess whether nucleotides influence the mediating capability of the Eu-L complexes (Figure 3.16). The solution comprised 10 mM MgCl₂, 10 mM ATP/ADP, 6 mM EuCl₃, 2 mM DTPA, 2 mM BATPA, and 2 mM EGTA. These compounds were dissolved in a CHES buffer (100 mM, pH 9) with 150 mM NaCl serving as the supporting electrolyte.

In Figure 3.16, the cyclic voltammograms (CVs) of the Eu-L alone and those in the presence of MgATP and MgADP are represented by black, red, and blue lines, respectively. The CV of Eu-L alone exhibits redox peaks in the range from -0.6 to -1.2 V vs SHE. Interestingly, in the presence of MgADP and MgATP, these redox peaks are notably absent, indicating that the Eu-L is not able to mediate electron transfer when MgADP or MgATP are present. One possible explanation for this observation could be that MgADP and MgATP interact with the Eu-L complex, altering its electron transfer capabilities, perhaps through direct binding or causing a change in its local environment. Given this interference with electron mediation, it was attempted to remove excess MgADP and MgATP after binding to NifH.

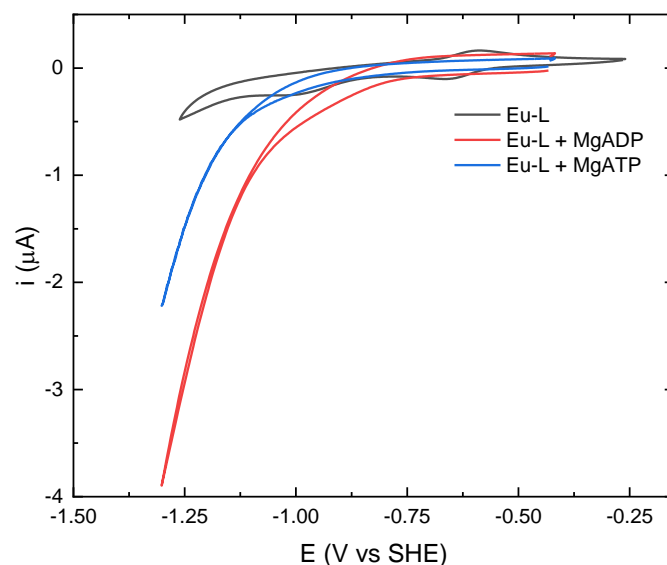


Figure 3.16 Cyclic voltammograms (CVs) showing the electrochemical behaviour of the Eu-L mediators. The black trace represents the CV of Eu-L alone, while the red and blue traces illustrate the CV in the presence of MgATP and MgADP, respectively. The measurements were performed in a CHES buffer (100 mM, pH 9) with 150 mM NaCl as the supporting electrolyte.

To generate MgATP-bound NifH, a mixture was prepared by combining a ten-fold excess of MgATP (350 μM) compared to NifH (35 μM). This blend was then transferred to an anaerobic glovebox and kept inside an icebox for a 2-hour binding period. Subsequently, the mixture was reduced using two molar equivalents of Eu(II)-DTPA. The corresponding UV-Vis spectra for this process can be found in Figure 3.17. Excess MgATP was subsequently removed via a buffer exchange using an Amicon Ultra 8 filter (0.5 centrifugal filter unit, membrane NMWL, 30 kDa). This step was essential since it was observed that the Eu-L mediators could not function as electron mediators in the presence of an excessive amount of nucleotide. Once the surplus ATP was eliminated, a redox titration was performed as detailed in section 3.4.1.

Upon inspecting the UV-Vis spectra of NifH, a noticeable change wasn't immediately evident post the 2-hour MgATP binding period (as depicted by the red line in Figure 3.17). The only identifiable shift was a 6% decrease in absorbance at 380 nm.

However, after the reduction using Eu(II)-DTPA, a distinct absorption peak emerged at 418 nm. This feature differentiates it from the spectra of nucleotide-free NifH (indicated by the blue line in Figure 3.17).

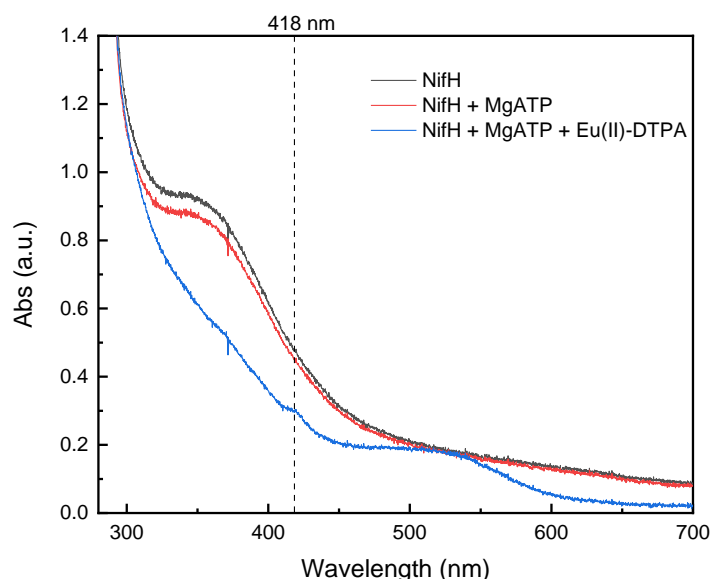


Figure 3.17 UV-Vis spectra comparing NifH before (black line) and after binding (red line) with MgATP and subsequent reduction with Eu(II)-DTPA (blue line). NifH, in CHES buffer (100 mM, pH 9) with 150 mM NaCl as supporting electrolyte.

The midpoint potential of the $[4\text{Fe-4S}]^{1+/0}$ couple in the presence of MgATP was determined to be -820 mV vs SHE with $n = 0.66$ ($R^2 = 0.9435$). This value was derived from fitting the relative intensity at 520 nm, representing the all-ferrous state, in Figure 3.18 A using the Nernst equation (Eq. 3.7). Notably, this is the inaugural measurement of the midpoint potential of the $[4\text{Fe-4S}]^{1+/0}$ couple in the presence of MgATP. As discussed in section 3.4.1, the midpoint potential of the $[4\text{Fe-4S}]^{1+/0}$ couple under the same conditions, but in the absence of MgATP, was found to be -790 mV. This is 43 mV more negative than its counterpart in the nucleotide-free form.

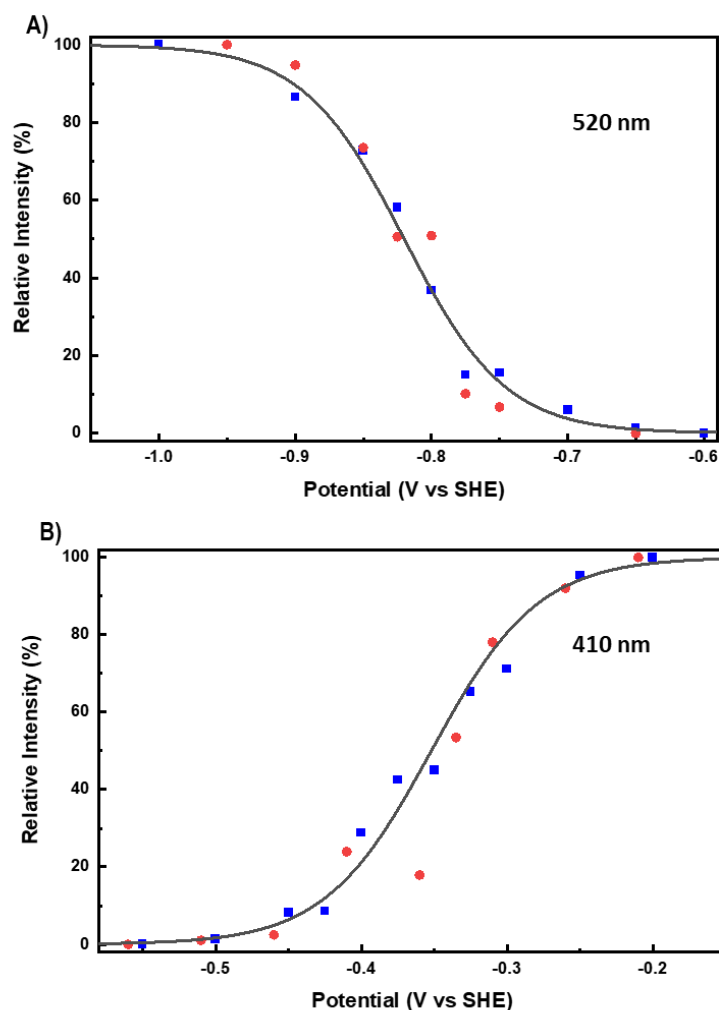


Figure 3.18 Redox titration of the [4Fe-4S] cluster in NifH of nitrogenase in the presence of MgATP. NifH, in CHES buffer (100 mM, pH 9) with 150 mM NaCl as supporting electrolyte. The [4Fe-4S]⁰ state was formed adding two equivalents of Eu(II)-DTPA at pH 9 and 10°C. It was oxidatively titrated with electrochemistry in the presence of a cocktail of redox mediators. The applied potential ranges from -1000 to -250 mV vs SHE with 25 mV intervals. After reaching redox equilibrium at each potential, UV-Vis spectra were taken *in situ* to monitor the band at 520 nm (the [4Fe-4S]⁰ state, Figure A) and 410 nm (the [4Fe-4S]²⁺ state). Black traces are fitted with the Nernst equation. The data points in the same colour (blue, or red) represent one distinct set of data.

Subsequently, as the +1 state progressed to the +2 state, evident from the relative intensity at 410 nm (indicating the 2+ state in Figure 3.18 B), the data were fitted using the Nernst equation (Eq. 3.6). The resulting midpoint potential for the [4Fe-4S]^{2+/1+} couple in the presence of MgATP was -352 mV vs SHE with $n = 0.67$ ($R^2 = 0.9138$). This is 62 mV higher than the -430 mV value reported by Watt *et al.* [199] It's worth mentioning that Watt *et al.* achieved the MgATP-bound state of NifH through equilibrium dialysis. In

contrast, in this study, the MgATP-bound state was formed by adding an excessive amount of MgATP to the system followed with buffer exchange. This difference in methodology could explain the observed variation in results, as there is a possibility that MgATP may dissociate from NifH during the buffer exchange process.

The measured midpoint potential of the 0/1+ couple of NifH during this redox titration in the presence of MgATP is -820 mV vs SHE. A key point of ambiguity arises regarding whether MgATP binds to the all-ferrous state of NifH when Eu(II)-DTPA is present. Nevertheless, a small peak at 418 nm is observable upon reduction by Eu(II)-DTPA. Although UV-Vis or CD spectra of the all-ferrous state don't exhibit noticeable changes upon the addition of MgATP, Angove *et al.* demonstrated that MgATP does bind to the all-ferrous state of NifH when excess Ti(III)-citrate is present. [196] Given the reduction potential of <-800 mV for the Ti^{IV/III} citrate couple, it is suggested that Ti(III)-citrate donates electrons to the [4Fe-4S]¹⁺ cluster, thus producing the all-ferrous state of NifH. This could provide indirect evidence that the all-ferrous state NifH forms a relatively stable binding complex. [40]

Rebelein *et al.* conducted EPR analysis of Eu(II)-DTPA-reduced NifH both in the absence and presence of MgATP. They did not explicitly address whether the all-ferrous state of NifH is bound with MgATP. Instead, they assumed it is formed by default. [41] Notably, the EPR feature and the reduction activity of CO₂ to CO in NifH under these two conditions were indistinguishable. After reducing NifH with Eu(II)-DTPA in the presence of MgATP, four potential NifH forms emerge: nucleotide-free, Mg-bound, ATP-bound, or MgATP-bound. Given the observed negative shift in the midpoint potential of the 0/1+

couple compared to the nucleotide-free state, this potential might be indicative of a partially MgATP-bound NifH.

3.4.3 Redox titration of NifH in the presence of MgADP

In previous analyses, it was discerned that the redox potential of NifH most likely undergoes modulation upon binding with MgATP. This shift in redox potential exhibits the impact that nucleotide binding can have on the redox properties of proteins. Apart from MgATP, MgADP, another key nucleotide, has been documented in literature to influence the redox potential of certain proteins. Drawing on this knowledge, this section delves into the effects of MgADP on the redox potential of NifH. Through this investigation, we aim to deepen our understanding of how MgADP interaction modulates the redox behaviour of NifH.

The procedure to obtain MgADP-bound NifH mirrored the method described in the MgATP section. Afterward, reduction was accomplished using two molar equivalents of Eu(II)-DTPA. The UV-Vis spectra of this process are presented in Figure 3.19. The subsequent redox titration was performed in alignment with the protocol detailed in section 3.4.1.

Upon examining the UV-Vis spectra of NifH, no significant change was apparent after the 2-hour MgADP binding (as represented by the red line in Figure 3.19). The only minor alteration observed was a 3% decrease in absorbance at 380 nm. Furthermore, after reduction with Eu(II)-DTPA, the peak at 418 nm, which was evident in the MgATP-bound NifH at its all-ferrous state, was absent (as indicated by the blue line in Figure 3.19).

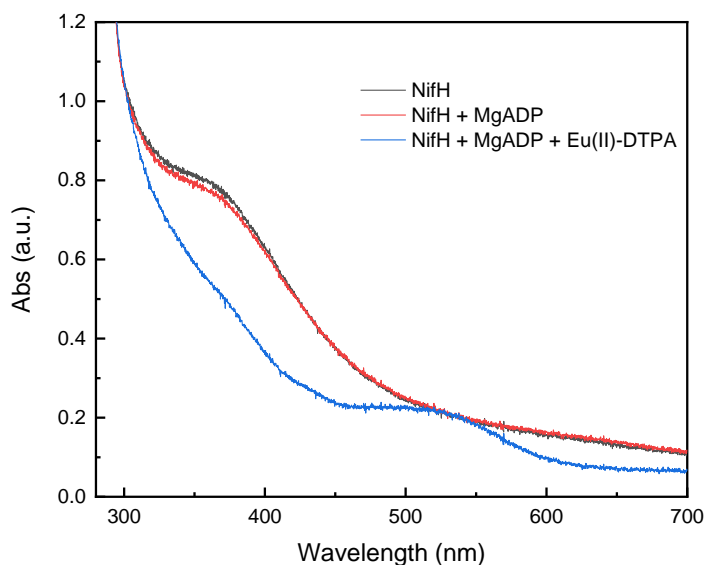


Figure 3.19 UV-Vis spectra comparing NifH before (black line) and after binding (red line) with MgADP and subsequent reduction with Eu(II)-DTPA (blue line). NifH, in CHES buffer (100 mM, pH 9) with 150 mM NaCl as supporting electrolyte.

The midpoint potential of the $[4\text{Fe-4S}]^{1+/0}$ couple in the presence of MgADP was determined to be -822 mV vs SHE with $n = 0.45$ ($R^2 = 0.9685$). This value was derived from fitting the relative intensity at 520 nm, representing the all-ferrous state, in Figure 3.20 A using the Nernst equation (Eq. 3.7). This value is 32 mV more negative than the midpoint potential observed in the absence of nucleotide at pH 9 and 10 °C.

Subsequently, as the 1+ state progressed to the 2+ state, evident from the relative intensity at 420 nm (indicating the 2+ state in Figure 3.20 B), the data were fitted using the Nernst equation (Eq. 3.6). The resulting midpoint potential for the $[4\text{Fe-4S}]^{2+/1+}$ couple in the presence of MgADP was -413 mV vs SHE with $n = 0.82$ ($R^2 = 0.9773$). [199]

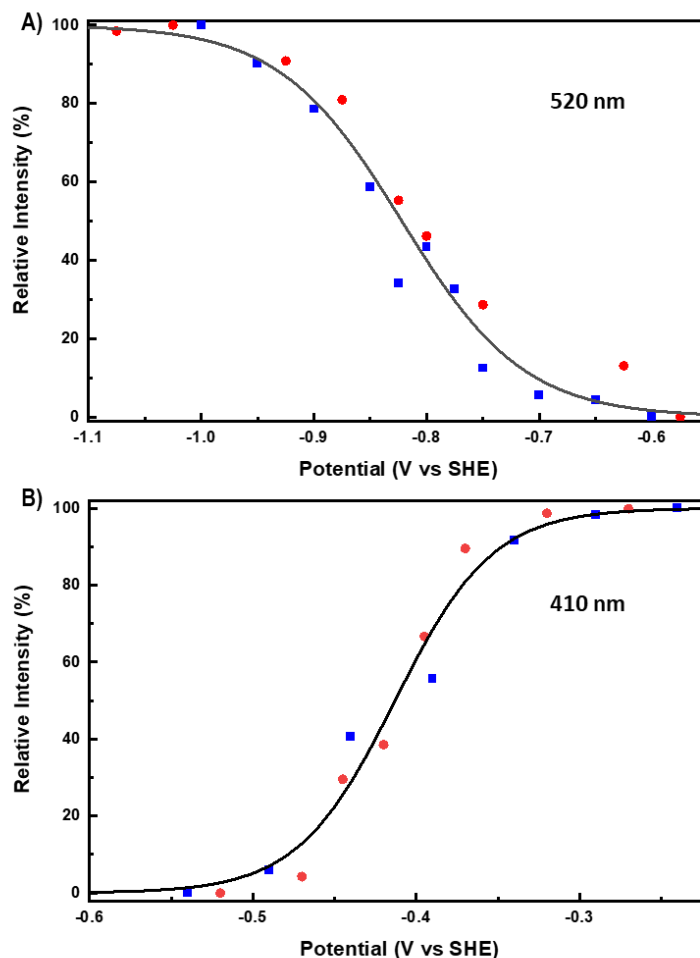


Figure 3.20 Redox titration of the [4Fe-4S] cluster in NifH of nitrogenase in the presence of MgADP. NifH, in CHES buffer (100 mM, pH 9) with 150 mM NaCl as supporting electrolyte. The [4Fe-4S]⁰ state was formed adding two equivalents of Eu(II)-(DTPA) at pH 9 and 10°C. It was oxidatively titrated with electrochemistry in the presence of a cocktail of redox mediators. The applied potential ranges from -1000 to -6000 mV vs SHE with a 25 mV interval. After reaching redox equilibrium at each potential, UV-Vis spectra were taken *in situ* to monitor the band at 520 nm (the [4Fe-4S]⁰ state, Figure A) and 410 nm (the [4Fe-4S]²⁺ state). Black traces are fitted with the Nernst equation. The data points in the same colour (blue, or red) represent one distinct set of data.

In the study by Watt *et al.*, the midpoint potentials of the [4Fe-4S]^{2+/1+} couple were recorded as -430 mV and -490 mV for NifH in the presence of MgATP and MgADP, respectively. In contrast, in this experiment, the measured values were -352 mV and -413 mV, when Eu(II)-DPTA was also present.[199] The discrepancy from the literature values can be attributed to the use of Eu-L in this methodology and the subsequent removal of excess MgATP and MgADP after their binding with NifH. This procedure might have inadvertently removed some nucleotides bound to NifH, potentially yielding a state

of NifH that is only partially bound to nucleotides. For future studies aimed at measuring the redox potential of NifH, a more suitable redox mediator is required, especially since the presence of nucleotides appears to impair the electron mediating capability of the Eu-L complexes.

Table 3.2 below presents the midpoint potentials reported in the literature compared to those obtained from this work. The midpoint potentials for both the $[4\text{Fe-}4\text{S}]^{2+/1+}$ and $[4\text{Fe-}4\text{S}]^{1+/0}$ couples have been examined, both in the absence and presence of nucleotides (MgATP/MgADP).

Table 3. 2 Comparison of the midpoint potential of NifH reported previously and obtained from this work

Mid potential of NifH	Nucleotide-free		MgATP presence		MgADP presence	
	Literature	Experimental	Literature	Experimental (partially bound)	Literature	Experimental (partially bound)
$E_m(2+/1+)$	-300 mV	-284±4 mV	-430 mV	-352±3 mV	-490 mV	-413±3 mV
$E_m(1+/0)$	-790 mV	-790±5 mV	N/A	-820±4 mV	N/A	-822±5 mV

3.5 EPR studies of the NifH

To support the UV-Vis data, the oxidation states of the $[4\text{Fe-}4\text{S}]$ clusters were also studied by EPR spectroscopy in collaboration with Dr William Myers in the Centre for Advanced Electron Spin Resonance (CAESR).

Three NifH samples were treated separately with: a) 1.5 molar equivalents of methylene blue, b) 1 molar equivalent of NaDT and c) 2 molar equivalents of Eu(II)-DTPA, in order to form the $[4\text{Fe-}4\text{S}]^{2+}$, $[4\text{Fe-}4\text{S}]^{1+}$ and $[4\text{Fe-}4\text{S}]^0$ states respectively. The UV-Vis spectra of these three individual samples were collected to check that the corresponding states have been formed (Figure 3.21 A). Then the samples were transferred to EPR tubes (Figure 3.21 B) and frozen in liquid nitrogen to be measured by EPR.

The EPR spectra of the control samples (methylene blue (green line) and Eu(II)-DTPA (grey line)) look like the cavity background, thus the features seen in the EPR spectra of the protein samples can be attributed to the Fe protein. The $[4\text{Fe-4S}]^{2+}$ state (blue lines in C and D, Figure 3.21) looks as expected, [213] it is EPR silent, (no EPR signal, $S = 0$). The EPR spectrum of the $[4\text{Fe-4S}]^{1+}$ state (red lines in C and D, Figure 3.21), shows an EPR signal around $g = 2$, but looks different from what has been published for this state, suggesting some O_2 -damage during freezing.[213]

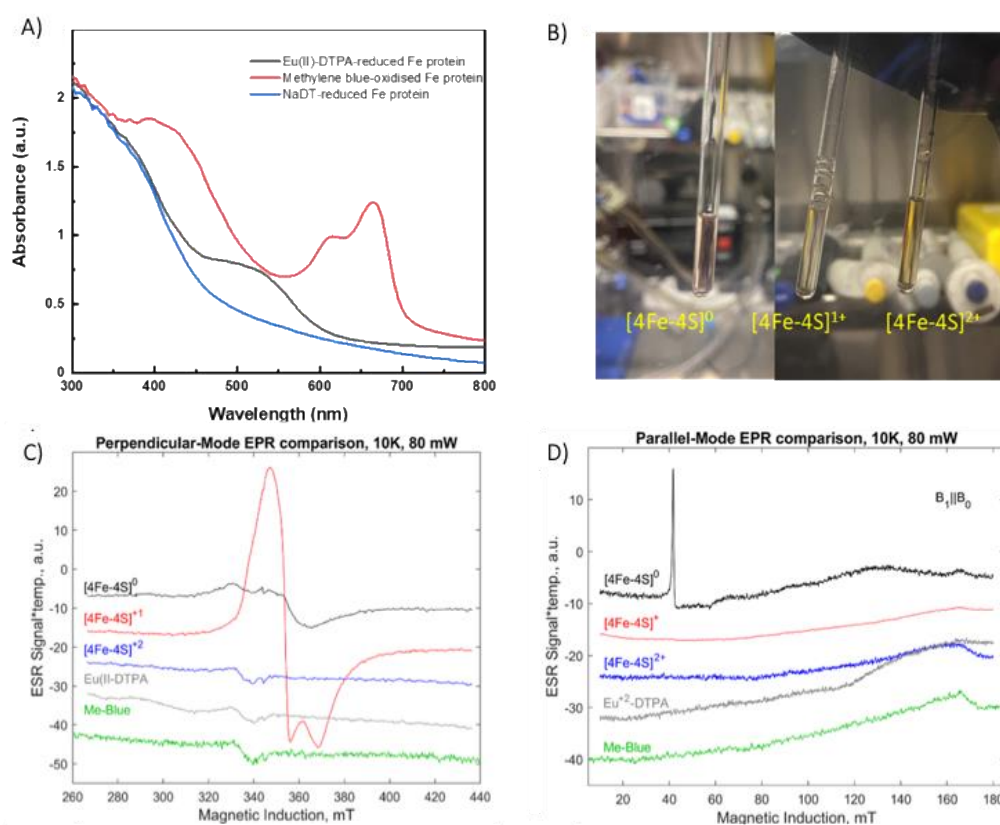
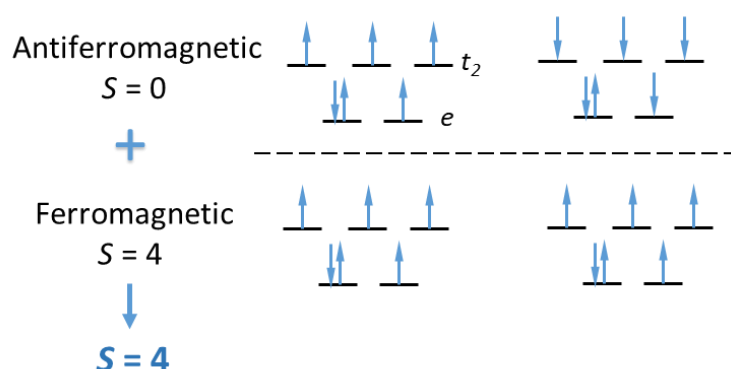


Figure 3.21 **A)** UV-Vis spectra of NifH at pH 9 and 10 °C : the $[4\text{Fe-4S}]^{2+}$ state (formed adding 1.5 equivalents of methylene blue, red line), the $[4\text{Fe-4S}]^{1+}$ state (formed adding 1 equivalent of NaDT, blue line), and the all-ferrous $[4\text{Fe-4S}]^0$ state (formed adding two equivalents of Eu(II)-DTPA, black line). The UV-Vis spectra were collected separately on each individual sample. **B)** Photos of each state in the EPR tube previous freezing them in liquid nitrogen. **C)** Perpendicular mode EPR spectra of NifH at 10 K of the $[4\text{Fe-4S}]^{2+}$ state (formed adding 1.5 equivalents of methylene blue, blue line), the $[4\text{Fe-4S}]^{1+}$ state (formed adding 1 equivalent of NaDT, red line), and the $[4\text{Fe-4S}]^0$ state (formed adding two equivalents of Eu(II)-DTPA, black line). **D)** The same than C) but measured in parallel mode. The EPR spectra of methylene blue (green line) and Eu(II)-DTPA (grey line) are also shown in C) and D).

In the perpendicular EPR spectrum of the $[4\text{Fe-4S}]^0$ state (black trace in C, Figure 3.21), the $[4\text{Fe-4S}]^0$ cluster is silent as expected. [36, 214] Use of the parallel mode allows detection of integer spin systems, and the parallel mode spectrum (black trace in D, Figure 3.21) shows clear evidence of the $S = 4$ EPR signal. The $S = 4$ state arises when two Fe(II) pairs align antiferromagnetically and two Fe(II) pairs align ferromagnetically as illustrated in Scheme 3.5. Each Fe(II) is high spin, tetrahedral with $S = 2$ and so the antiferromagnetic pair gives $S = 2 - 2 = 0$ and the ferromagnetic pair gives $S = 2 + 2 = 4$.



Scheme 3.5 The spin state of the all-ferrous state of NifH

Figure 3.22 A shows four additional samples measured by EPR. NifH samples at $1+$ state were treated separately with: a) 1.5 molar equivalents of methylene blue, b) 1 molar equivalent of reduced-methyl viologen, c) 2 molar equivalents of reduced-methyl viologen and d) 1 molar equivalent of Eu(II)-DTPA . The EPR spectra of NifH containing methyl viologen (Figure 3.22 A, blue and cyan) clearly show the rhombic Fe(III) signal from the $[4\text{Fe-4S}]^{1+}$ cluster, which is not in agreement with the previously reported data by Watt *et al.* where it was suggested that the EPR signal intensity initially diminishes upon reduction of the $[4\text{Fe-4S}]^{1+}$ state by MV. [38] Interestingly, one equivalent of Eu(II)-DTPA leaves a smaller proportion of $[4\text{Fe-4S}]^{1+}$ and gives some $[4\text{Fe-4S}]^0$, which is observable in parallel mode EPR, as shown in Figure 3.22 (A, red trace). [36] A best-fit simulation of

the EPR signal from NifH reduced with one equivalent Eu(II)-DTPA is shown in Figure 3.22 (B, red trace), containing two components of g -matrices of principle components of $a = [1.9978 \ 1.954 \ 1.8561]$, $b = [2.0160 \ 1.944 \ 1.828]$, with broadenings of $\sigma_a = [0.062 \ 0.021 \ 0.023]$, $\sigma_b = [0.076 \ 0.01274 \ 0.114]$.

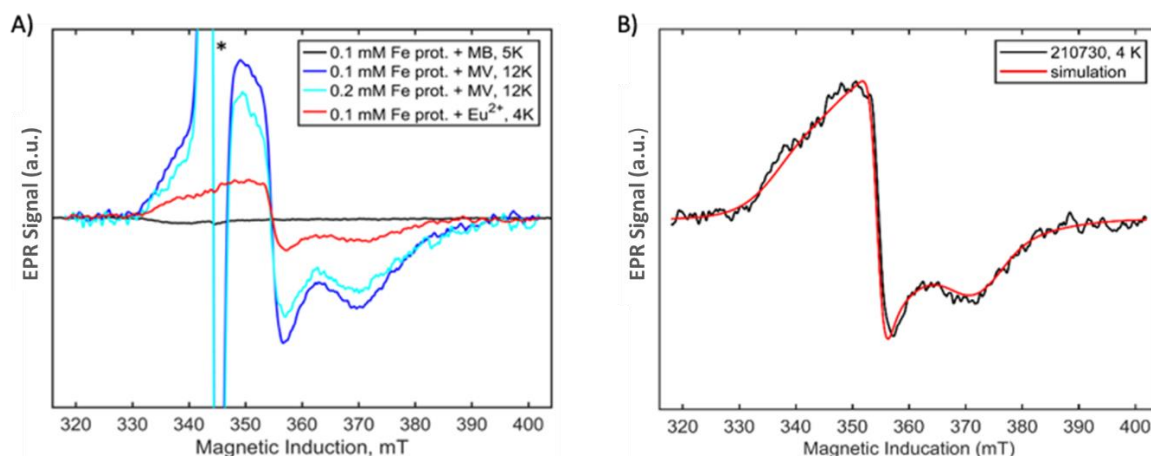


Figure 3.22 NifH EPR data collected at X-band with the microwave field perpendicular to the DC magnetic field. A) EPR spectra of NifH samples including redox agents methylene blue (MB, black), methyl viologen (MV, blue and cyan) and Eu(II)-DTPA (red) were measured as indicated in the figure legend. The asterisk (*) indicated the signal from MV. The microwave frequency was 9.6426 GHz, while microwave powers were 10 mW for the first trace and 0.05 mW for the remainder. A best-fit simulation of the Eu(II)-DTPA-reduced NifH is shown as the red trace in B.

The correlation between the EPR and UV-Vis spectroscopic data provides a robust verification of the redox states of the [4Fe-4S] cluster in NifH. To conclude, the study revealed that the use of a single equivalent of Eu(II)-DTPA in the reduction of NifH leads to only a partial reduction of the [4Fe-4S]¹⁺ cluster. This partial reduction is characterised by a smaller proportion of the rhombic Fe(III) signal, as corroborated by the UV-Vis data. However, the introduction of an additional equivalent of Eu(II)-DTPA results in the full reduction to the all-ferrous state. Furthermore, the EPR spectra of NifH containing methyl viologen also distinctly show the rhombic Fe(III) signal from the [4Fe-4S]¹⁺ cluster, contradicting expectations from previous literature and suggesting the inadequacy of methyl viologen in fully reducing the [4Fe-4S] cluster to the all-ferrous state despite its reducing capability.

3.6 Redox behaviour of the AnfH

Having established the UV-Vis SEC method with NifH, this method will now be extended to investigate its counterpart AnfH. AnfH is the reductase component of the FeFe nitrogenase. Recent advancements in the structural analysis have provided more clarity to this protein's properties. Specifically, Trncik *et al.* recently elucidated the crystal structure of the ADP-bound reductase component AnfH to a resolution of 2.0 Å. [200] An inspection of the overall structures reveals that AnfH, originating from the diazotroph *Azotobacter vinelandii*, aligns structurally with its counterparts NifH and VnfH, particularly when in the ADP-bound state. Moreover, the configuration assumed by the $[4\text{Fe-4S}]^{1+}$ clusters of AnfH parallels those of NifH and VnfH. Such structural resemblances are further reinforced by the consistent $S = 3/2$ and $S = 1/2$ EPR resonances in the dithionite-reduced $1+$ state across these proteins, with X-ray absorption spectroscopy (XAS)/ Extended X-ray Absorption Fine Structure (EXAFS) analysis providing additional support. [215]

The resemblance doesn't just halt at structural properties; it extends to the redox behaviours of these Fe proteins. For instance, VnfH and NifH can transition between three oxidation states: the oxidised $[4\text{Fe-4S}]^{2+}$, the reduced $[4\text{Fe-4S}]^{1+}$, and the super-reduced, all-ferrous $[4\text{Fe-4S}]^0$ states.[38] Although it remains uncertain whether AnfH exhibits similar oxidation behaviours as NifH and VnfH, their shared structural and electronic characteristics suggest a parallel redox behaviour. [216] Therefore, the possibility of the formation of the all-ferrous state in AnfH is explored, alongside understanding the electrochemical control over its redox behaviour. This investigation builds upon the SEC UV-Vis method that has been established from previous work with NifH.

3.6.1 Formation of the three oxidation states of the AnfH

Initially, the feasibility of forming the all-ferrous state in AnfH was determined. The procedure to generate this state of the [4Fe-4S] cluster in AnfH followed that outlined in Section 3.2.1, which involved the addition of Eu(II)-DTPA to the AnfH sample.

To characterise the different oxidation states of AnfH, UV-Vis spectroscopy was employed. Three distinct samples of AnfH were individually treated with different agents: 1.5 molar equivalents of methylene blue (MB) to form the [4Fe-4S]²⁺ state, 1 molar equivalent of sodium dithionite (NaDT) to form the [4Fe-4S]¹⁺ state, and 4 molar equivalents of Eu(II)-DTPA to form the [4Fe-4S]⁰ (all-ferrous) state. UV-Vis spectra were subsequently recorded for each of these samples to monitor the oxidation states were achieved, as illustrated in Figure 3.23 A.

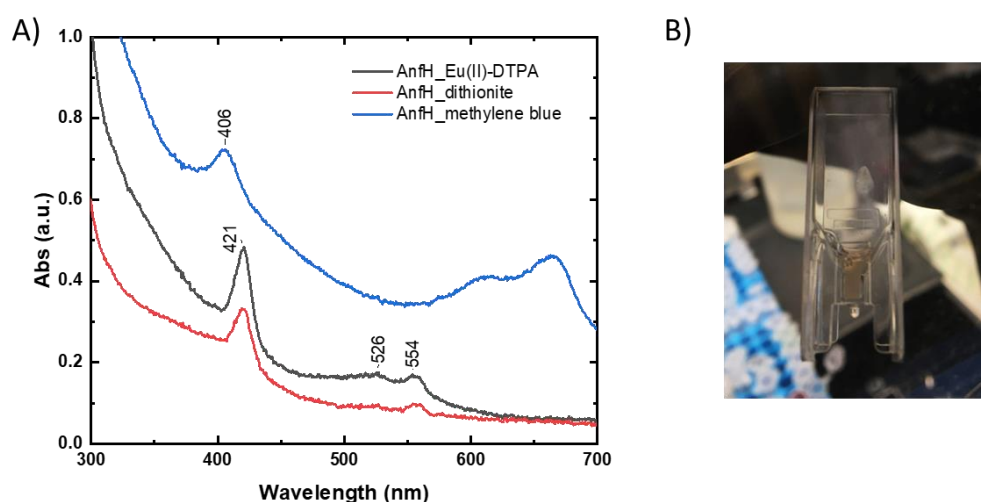


Figure 3.23 A) The UV-Vis spectra of AnfH at three oxidation states. The 2+ (blue), 1+ (red) and all-ferrous (black) states are formed by the addition of methylene blue, sodium dithionite and Eu(II)-DTPA individually; B) The picture of the all-ferrous state AnfH

The UV-Vis spectral characteristics of the methylene blue-oxidised AnfH (depicted by the blue trace in Figure 3.23 A exhibit a pronounced absorption peak at 406 nm. This is distinct from the broad absorption observed for NifH under similar conditions.

Absorptions seen beyond 600 nm can be attributed to the presence of methylene blue. Upon reduction of AnfH with sodium dithionite, there's a notable shift of the peak to 421 nm, and two new absorption peaks emerge at 526 nm and 554 nm, as seen in the red trace of Figure 3.23 A. These three peaks persist even after the addition of Eu(II)-DTPA. However, the characteristic broad absorption peak associated with the all-ferrous state cluster emerges around 520 nm (indicated by the black trace in Figure 3.23 A). Accompanying this broad peak, the solution turns a pale pink upon reduction with Eu(II)-DTPA (Figure 3.23 B), further validating the formation of the all-ferrous state in AnfH. Consequently, this evidence confirms that AnfH can indeed transition through the same oxidation states as its NifH and VnfH counterparts, inclusive of the distinctive all-ferrous state.

3.6.2 Redox titration attempt on AnfH

It has been established that AnfH also accommodates the same three oxidation states as its counterpart, NifH. Building on this understanding, the subsequent section will delve into the measurement of the redox potential of AnfH. Utilising the UV-Vis SEC methodology previously applied to NifH, efforts were made to elucidate the redox characteristics of AnfH.

At 10 °C, 350 μ L of AnfH (139 μ M) in pH 9 CHES buffer was introduced into UV-Vis SEC cell. Eu(III)-L mediators were then added to achieve a final concentration of 30 μ M for each Eu(III)-L species. Subsequently, four molar equivalents of Eu(II)-DTPA were introduced to the AnfH to form the all-ferrous state. The potential of the UV-Vis SEC cell was sequentially set from -940 mV to -140 mV vs SHE with a 50 mV interval. At each potential, the UV-Vis spectrum was monitored until it remained unchanged, after which a final UV-Vis spectrum was recorded (Figure 3.24).

At a potential of -940 mV, the all-ferrous state is stabilised, as depicted in Figure 3.24 (shown by the lightest yellow trace). As the potential increased to -140 mV, the UV-Vis spectra exhibited no noticeable alterations (as shown by the red and blue traces in Figure 3.24). Absorptions at 526 nm and 554 nm, characteristic of the all-ferrous state, persisted even at potentials typically considered positive for $[4\text{Fe-4S}]$ clusters. Notably, the broad peak diminished as the potential increased. However, the absorption at 406 nm, indicative of the $2+$ state, was absent even at -140 mV. These observations suggest that while AnfH is resistant to electrochemical oxidation to its $2+$ state, it can be oxidised to the $1+$ state from the all-ferrous state.

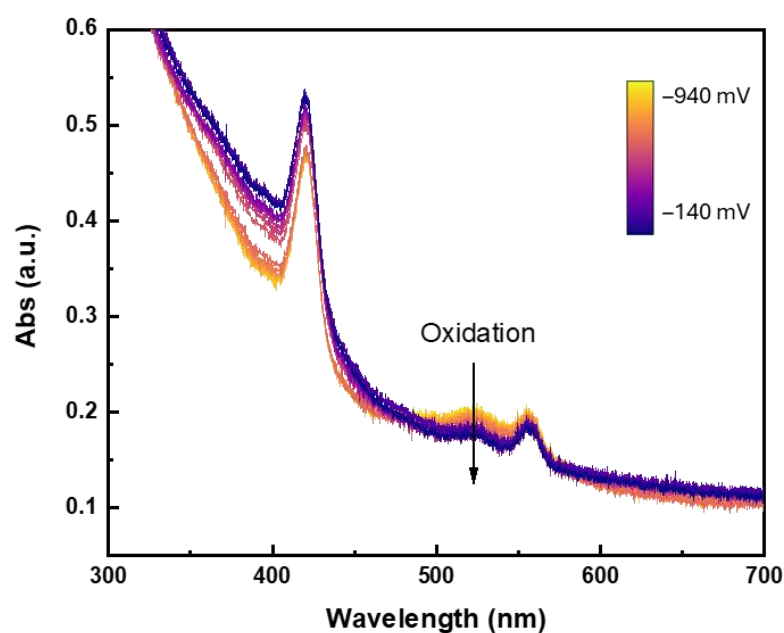


Figure 3.24 The UV-Vis spectra of the AnfH ($139 \mu\text{M}$) at different potentials. A series of potentials were applied from -940 mV to -140 mV sequentially with an interval of 50 mV. The CHES buffer (pH 9, 100mM) contains 150 mM NaCl and redox mediators with a final concentration of $30 \mu\text{M}$ of each Eu(III)-L species.

The midpoint potential of the $[4\text{Fe-4S}]^{1+/0}$ couple of AnfH was determined to be -613mV vs SHE with $n = 0.28$. This value was derived from fitting the relative intensity at 520 nm, representing the all-ferrous state, in Figure 3.25 using the Nernst equation (Eq.

3.7). However, the fit was not satisfactory as a challenge emerged when the absorption of AnfH in its all-ferrous state was found to be significantly weaker than that of NifH. Even at a relatively high concentration of 139 μM , the absorption remained below 0.2, which casts doubt on the reliability of the derived redox potential values. Further exploration of this phenomenon is warranted in future studies, potentially focusing on aspects such as the stability and EPR characteristics of AnfH.

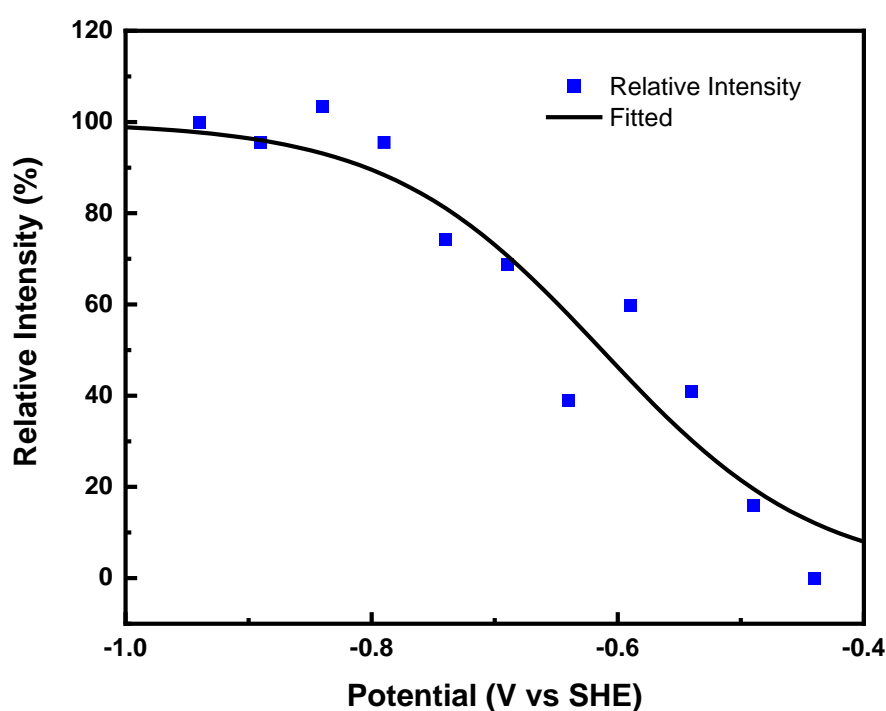


Figure 3.25 Redox titration of the $[4\text{Fe-4S}]$ cluster in AnfH of nitrogenase. AnfH, in CHES buffer (100 mM, pH 9) with 150 mM NaCl as supporting electrolyte. The $[4\text{Fe-4S}]^0$ state was formed adding two equivalents of Eu(II)-(DTPA) at pH 9 and 10°C. It was oxidatively titrated with electrochemistry in the presence of a cocktail of redox mediators. The applied potential ranges from -940 to -140 mV vs SHE with a 50 mV interval. After reaching redox equilibrium at each potential, UV-Vis spectra were taken *in situ* to monitor the band at 520 nm (the $[4\text{Fe-4S}]^0$ state). Black traces are fitted with the Nernst equation.

3.7 Conclusion

In this chapter, a novel three-electrode UV-Vis spectroelectrochemical cell (UV-Vis SEC) was developed for studying the redox chemistry of FeS clusters, allowing for in

situ UV-Vis spectral analysis. This UV-Vis SEC cell comprises a PGE working electrode, a fritted PGE counter electrode, and a homemade SCE reference electrode. Initially tested on azurin, the cell was then employed to investigate the Fe protein. Using this setup, the redox potentials of the [4Fe-4S] clusters in NifH and AnfH proteins were studied under various conditions. The research also focused on the formation of the all-ferrous states in both NifH and AnfH. Additionally, EPR measurements were conducted on NifH to corroborate findings from the UV-Vis spectroscopy, offering a comprehensive view of the redox behaviours of these clusters.

The stability of the all-ferrous state of NifH has been studied under various conditions. These results indicate that this state is more stable at higher pH and lower temperature, while MgATP has relatively little impact on its stability. In the tested experimental conditions, the all-ferrous state can be reversibly formed after oxidation. It has been well established that the all-ferrous state can be formed using Eu(II)-DTPA as the reductant. However, attempts to form the all-ferrous state NifH electrochemically in the UV-Vis SEC cell were unsuccessful. UV-Vis SEC experiments were conducted to assess the redox potential of the [4Fe-4S]^{1+/0} couple by an oxidative titration. The midpoint potentials of the [4Fe-4S]^{2+/1+} couple in NifH were measured at -284 mV, -352 mV, and -413 mV for NifH in the absence of nucleotide, in the presence of MgATP, and in the presence of MgADP, respectively, with the additional presence of Eu(III)-DTPA. Similarly, the midpoint potentials of -790 mV, -820 mV, and -822 mV were obtained for the [4Fe-4S]^{1+/0} couple under these respective conditions.

However, due to the potential binding of Eu(II) to nucleotides, the observed redox potentials of the [4Fe-4S] cluster in NifH might be influenced by nucleotide-bound

clusters. Therefore, Eu-L redox mediators are not suitable for titration in the presence of nucleotides. A new, colourless redox mediator needs to be explored to reassess the redox potential of the $[4\text{Fe-4S}]^{1+/0}$ couple in the presence of nucleotide.

The correlation between EPR and UV-Vis spectroscopic data provides robust verification of the redox states of the $[4\text{Fe-4S}]$ cluster in NifH. The study revealed that using a single equivalent of Eu(II)-DTPA for the reduction of NifH leads to only a partial reduction of the $[4\text{Fe-4S}]^{1+}$ cluster. However, the introduction of an additional equivalent of Eu(II)-DTPA results in the full reduction to the all-ferrous state. Furthermore, the EPR spectra of NifH containing methyl viologen contradict previous literature, suggesting that methyl viologen is inadequate for fully reducing the $[4\text{Fe-4S}]$ cluster to the all-ferrous state despite its reducing capability.

The redox behaviours of AnfH from the FeFe nitrogenase were also studied. It was shown that AnfH could adopt the all-ferrous state in the $[4\text{Fe-4S}]$ cluster, similar to NifH. Utilising the UV-Vis SEC methodology previously applied to NifH, efforts were made to elucidate the redox characteristics of AnfH. Observations indicate that while AnfH is resistant to electrochemical oxidation to its 2+ state, it can be oxidised to the 1+ state from the all-ferrous state.

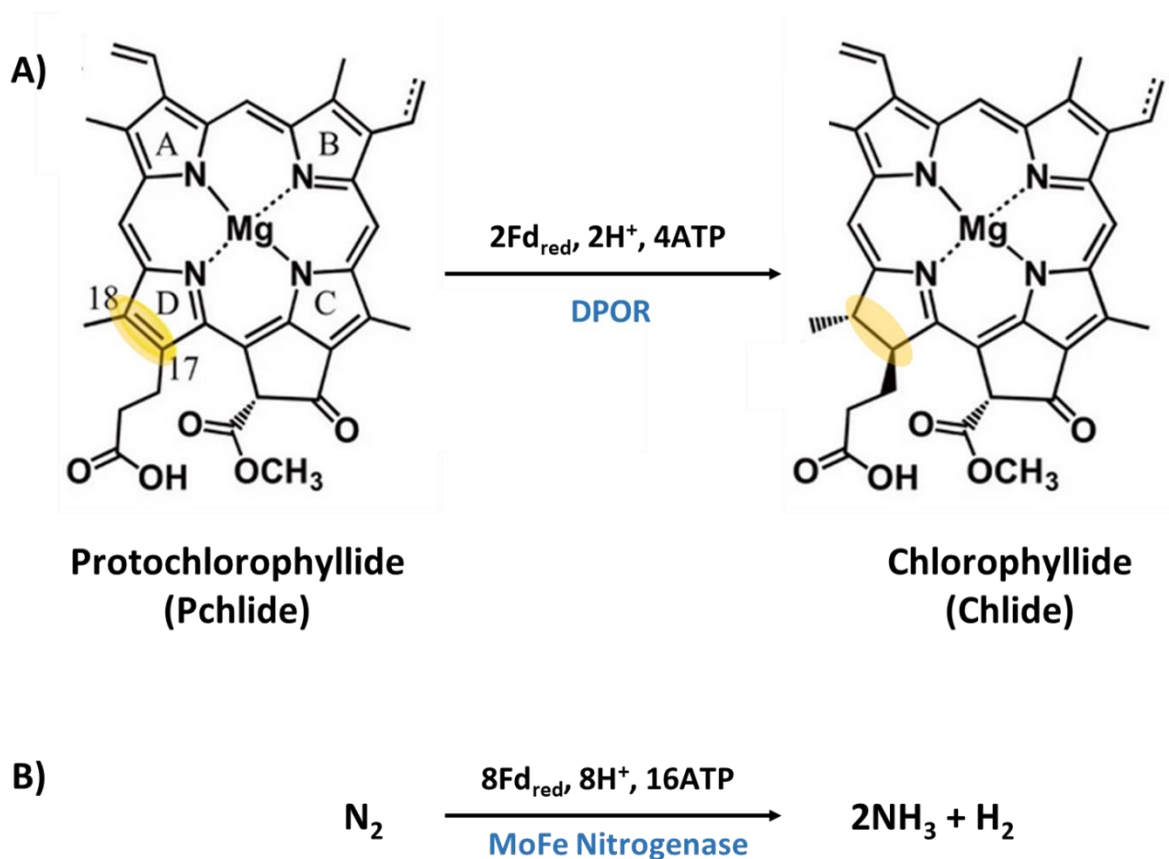
In future studies, it will be crucial to explore a new, colourless redox mediator to reassess the redox potential of the $[4\text{Fe-4S}]^{1+/0}$ couple in the presence of nucleotides. Then a detailed investigation of MgATP and MgADP-bound NifH redox titration will be planned. This will involve examining the redox potentials in the context of these nucleotide-bound states, providing insights into how ATP and ADP binding influences the redox behaviour of NifH. Additionally, the exploration of AnfH will be extended, focusing

not only on its redox potentials in the presence/absence of nucleotide, but also on studying its stability and characterising its EPR features. These investigations are crucial for a deeper understanding of the redox properties and biological functions of these proteins.

Chapter 4 Redox behaviour of the Fe protein homologues

The recent identification of dark-operative protochlorophyllide oxidoreductase (DPOR), a homologue to nitrogenases, has expanded our understanding of enzyme-catalysed reductions. [66] DPOR, like nitrogenases, is a two-component metalloprotein comprising an electron transfer (reductase) component and a catalytic component. This enzyme plays a crucial role in chlorophyll and bacteriochlorophyll synthesis by reducing protochlorophyllide (Pchl_{id}) to chlorophyllide (Chl_{id}). During catalysis, the components of DPOR form a functional complex, facilitating electron transfer for Pchl_{id} reduction in the N₂B₂ protein. The redox potentials of the L₂ and N₂B₂ proteins remain unknown, and it is unclear if they can achieve an all-ferrous state similar to the Fe protein in nitrogenase.

The process of reduction Protochlorophyllide (Pchl_{id}) to Chlorophyllide (Chl_{id}) in a light-independent manner involves the L₂ protein transferring two electrons from an electron donor, such as reduced ferredoxin (Fd_{red}) *in vivo* or dithionite *in vitro*, to the N₂B₂ protein complex (Scheme 4.1 A). This electron transfer is facilitated through the [4Fe-4S] centre in L₂ protein which aids in electron transport. Simultaneously, the energy required for this process is provided by the hydrolysis of two ATP molecules. [71, 75] Similarly, in the nitrogenase system, the Fe protein is initially reduced by ferredoxin or its functional analogue flavodoxin (Scheme 4.1 B). Post-reduction, electrons are passed from the [4Fe-4S] cluster in the Fe protein to the FeMo cofactor of the MoFe protein, this time utilising the P-cluster as an intermediary in the electron transfer process. [217]



Scheme 4.1 Comparisons of the reduction process of Pchl and N_2 *in vivo*. A) DPOR facilitates the trans addition of hydrogen across the C-17–C-18 double bond in protochlorophyllide (Pchl), leading to the formation of chlorophyllide (Chl). This process utilises reduced ferredoxin (Fd_{red}) as an electron donor *in vivo* and consumes 2 H^+ and 4 ATP molecules. B) MoFe nitrogenase reduces N_2 to NH_3 , which requires 8 molecules of Fd_{red} for electron donation *in vivo*, along with the consumption of 8 H^+ and 16 ATP molecules.

Nitrogenases have been shown to exhibit catalytic activity without the presence of its electron transfer partner (Fe protein) and ATP. For instance, a study by Milton *et al.* demonstrated the immobilisation of MoFe protein of nitrogenase on an electrode surface, using cobaltocene as an electron mediator for real-time monitoring, which allows the MoFe protein to reduce 2 H^+ to H_2 , N_3^- to NH_3 and NO_2^- to NH_3 , independent of the Fe protein and ATP hydrolysis.[218] It is also reported that β -98^{Tyr→His} MoFe protein can effectively reduce nitrogenous substrate hydrazine (N_2H_4) to two NH_3 molecules using a low-potential reductant Eu^{II} -DPTA ($E_m = -1.1$ V vs SHE), in the absence of the Fe protein or ATP. [219] To date, light-driven N_2 reduction without the Fe-protein has been noted in

instances where the MoFe protein is immobilised on CdS quantum dots.[220] DPOR is also capable of catalysing the two-electron reduction of N_3^- or N_2H_4 to NH_3 , a function that parallels the activity of nitrogenase in reducing the same substrates. [69, 221] Considering the structural and functional similarities between DPOR and nitrogenase, it is meaningful to study the activity of DPOR in the absence of its reductase component (L_2 protein). This approach could provide valuable insights into the mechanism of the enzyme and its potential dependence or reliance on the L_2 protein for catalytic activity.

Overall, this chapter concentrates on investigating the redox properties and electrochemical catalytic activities of dark-operative protochlorophyllide oxidoreductase (DPOR). Beyond the UV-Vis SEC method developed in Chapter 3, a potentiometric titration method was established in Section 4.1, using ferredoxin as a model. Section 4.2 delves into the potential of L_2 and N_2B_2 proteins to reach an all-ferrous state. The subsequent sections, 4.3 and 4.4, focus on determining the specific redox potentials of L_2 and N_2B_2 proteins, respectively. Finally, Section 4.5 presents an electrochemical analysis of DPOR's activity, examining the influence of the L_2 protein's presence or absence. This cohesive approach provides a comprehensive understanding of the redox behaviour of these proteins in the context of nitrogenase-like activity.

4.1 Development of the potentiometric titration method

4.1.1 Preliminary test with ferredoxin

Experiments to determine the redox potentials (E_m) of L_2 protein and N_2B_2 protein have been carried out using UV-Vis SEC method that developed in Chapter 3. These experiments will be described in Sections 4.3 and 4.4. However, efforts to ascertain the redox potential of N_2B_2 protein using UV-Vis SEC have encountered challenges. It has

been observed that N_2B_2 protein cannot be reduced or oxidised, even in the presence of redox mediators. Therefore, a new method is required for the determination of redox potentials. Potentiometric titration represents a frequently used method for measuring the redox potential of redox enzymes. It is typically paired with a quantitative measurement instrument, such as Electron Paramagnetic Resonance (EPR). For instance, the redox potential of the cofactors of *Saccharomyces cerevisiae* Nar1 was determined using an EPR-coupled potentiometric method. [139]

Ferredoxin I (Fd I) from *Spinacia oleracea* is a small protein with molecular weight of 6 kDa exhibiting a known E_m around -400 mV vs SHE. [162, 222] The proximity of the [2Fe-2S] cluster to the surface, as depicted in Figure 4.1, facilitates direct electron transfer to the electrode. This short distance from the [2Fe-2S] cluster to the surface eliminates the need for a redox mediator during the redox process by the electrode. [222, 223] The E_m of azurin is $+292$ mV vs SHE, and that of FdI is -400 mV. [162, 209, 222] The E_m of Fd I is closer to that of the [4Fe-4S] cluster, [11] making it a better model. In Chapter 3, azurin was used as a model because FdI was not available at the time of the development of the UV-Vis SEC method. Hence it serves herein as a model for testing and refining the potentiometric titration method when coupled with *in situ* UV-Vis spectroscopy. This pairing significantly reduces the amount of enzyme required. For instance, potentiometric titration coupled with Electron Paramagnetic Resonance (EPR) requires approximately 75 nmol protein per sample, necessitating this amount for each of the 10 samples. However, when coupled with *in situ* UV-Vis, the requirement drops dramatically to around 20 nmol protein for a single titration.

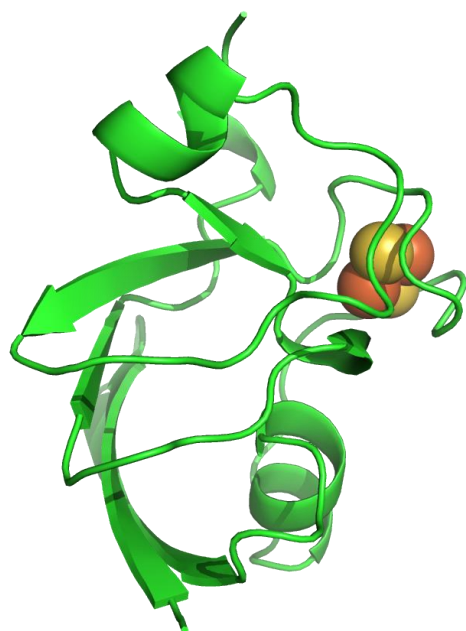


Figure 4.1 The crystal structure of ferredoxin I from *Spinacia oleracea*. PDB: 1A70

A potentiometric titration method has been developed, in which sodium dithionite (NaDT) is used as a titrant, for the determination of the redox potential of the ferredoxin protein. A platinum (Pt) wire and an Ag/AgCl reference electrode were utilised as the working electrode and the reference electrode, respectively. A set of NaDT solutions with concentration from 0.01 to 1 mM were prepared as titrant. Ferredoxin, prepared at a concentration of 40 μM within a 400 μL volume, was subjected to incremental additions of NaDT. The protein was in a pH 8.5 HEPES buffer (50 mM) containing 50 mM of NaCl as the electrolyte. A set of NaDT solutions with concentration from 0.01 to 1 mM were prepared as titrant. A small aliquot, ranging from 0.1-2 μL , of the NaDT solution was added to the mixture in the titration vessel to decrease the potential of the protein solution. The addition of NaDT started with the lowest concentration, 0.01 mM. Notably, if more than 10 μL of was necessarily need to decrease the potential by – 50 mV, a more concentrated NaDT stock solution was added instead. After each NaDT addition, the open circuit potential of the ferredoxin solution was measured using an

AutoLab electrochemistry potentiostat. UV-Vis spectra of the sample were also obtained following each NaDT increment.

With the incremental addition of NaDT, the UV absorption of ferredoxin, as illustrated in Figure 4.2 A, gradually diminishes at 465 nm. This suggests an ongoing reduction of ferredoxin by NaDT. The changes over time in the open circuit potential (OCP) of the ferredoxin solution after the addition of NaDT are represented in Figure 4.2 B. Each distinct step on the graph corresponds to an individual NaDT addition. Additions of NaDT continued until the OCP no longer displayed significant changes, even when an excessive amount of NaDT was introduced. Equilibrium was reached at -199 mV vs SHE after a duration of 2686 s. The first step on the graph represents the introduction of a small aliquot of NaDT solution (0.01 mM) to the protein solution, which promptly led to a decrease in the OCP. Further additions of NaDT caused the OCP of the protein solution to continue stepping down to lower values. After 5570 seconds, the OCP after equilibration remained static, showing no further changes despite the introduction of an excess amount of NaDT.

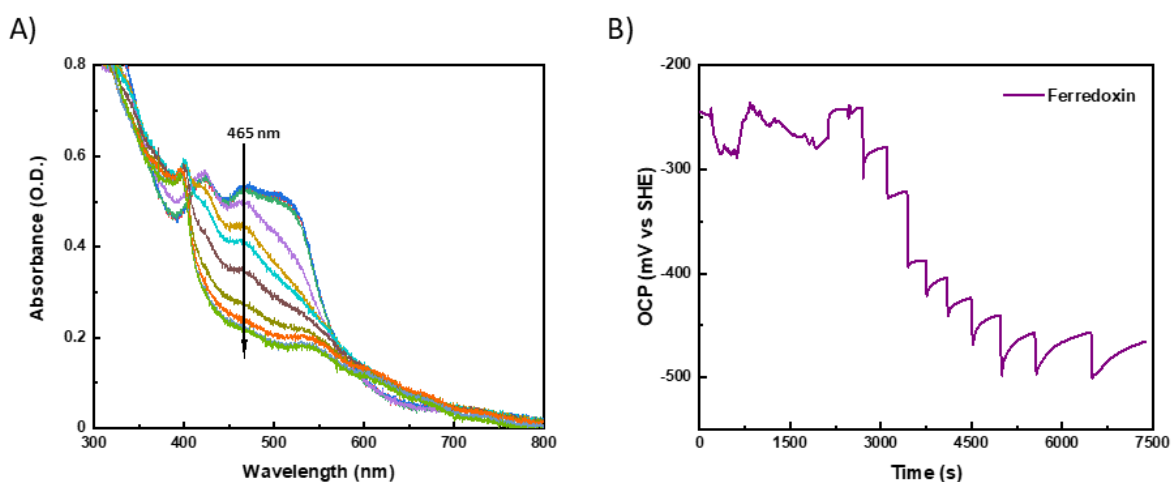


Figure 4.2 A) The changes in the UV-Vis absorption of ferredoxin with the gradual addition of sodium dithionite (NaDT) during the potentiometric titration; B) The temporal variations in the open circuit potential (OCP) of the ferredoxin solution following the introduction of sodium dithionite (NaDT).

The absorbance of UV-Vis light at 465 nm was graphed in relation to the OCP (Figure 4.3 A), and the first derivative of this plot was subsequently drawn (Figure 4.3 B). This approach facilitated the construction of a titration curve, connecting the open circuit potential to the UV-Vis absorption. The redox potential of ferredoxin was inferred from the inflection point on the titration curve, measuring at -422 mV vs SHE. Notably, the redox potential of spinach ferredoxin has been documented at approximately -405 mV vs SHE in earlier literature. [162] Other investigations have reported a similar value, around -420 mV. [222] The measured redox potential in this study closely aligns with these previously reported values, thereby confirming the validity of this approach.

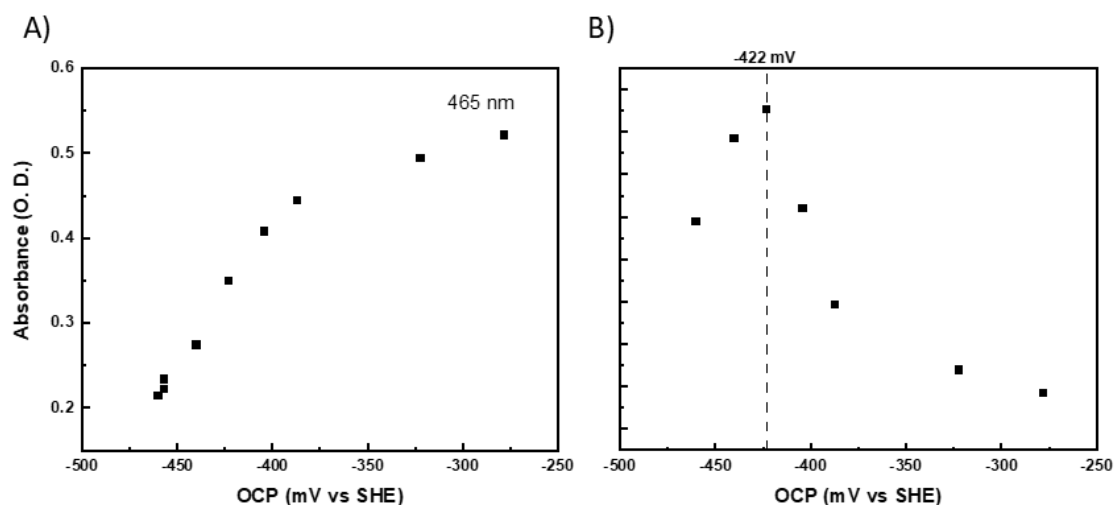


Figure 4.3 A) The relationship between the UV-Vis light absorbance at 465 nm and the open circuit potential (OCP) of the solution; B) The first derivative of plot A, highlighting the rate of change in absorbance with respect to the OCP.

This method is considered to provide valuable insight into the redox properties of proteins, supporting their characterisation, and encouraging applications to other metalloprotein. This potentiometric method is used in parallel with UV-Vis SEC for the

attempts of determining the redox potentials of L₂ protein and N₂B₂ protein in section 4.3 and section 4.4.

4.2 Exploration of the all-ferrous state in DPOR

The involvement of the all-ferrous state of the Fe protein in the reduction of N₂ by nitrogenase is a subject of debate. [224] However, experiments have shown that the L₂ protein of DPOR is capable of engaging in chimeric interactions with the MoFe protein, and this interaction, particularly with the Y127S mutant of the L₂ protein, is significantly enhanced in the presence of ATP. [225] If the L₂ protein cannot form an all-ferrous state, but still manages to reduce some nitrogenase substrates like N₃⁻ or N₂H₄ when combined with the MoFe protein, it could indirectly suggest that the all-ferrous state is not essential in the catalytic cycle of nitrogenase. Furthermore, since the N₂B₂ protein is a tetramer containing two [4Fe-4S] clusters, it might also be capable of forming an all-ferrous state. Therefore, this section primarily investigates the possibility of the all-ferrous state formation within DPOR.

4.2.1 Exploration of the all-ferrous state in L₂ protein

As introduced in section 1.4, the gene coding the L₂ protein shares 33% identity of that of the Fe protein. In addition, they both perform as the reductase for their relative catalytic enzyme. Due to these structural and the functional similarities of L₂ protein to the Fe protein in nitrogenase, the question arises whether the all-ferrous state can also be accommodated in the L₂ protein from this nitrogenase homologue? Hence, the possibility of forming the all-ferrous state in L₂ protein is explored in this section. The same method is used to reduce the L₂ protein, with Eu(II)-DTPA as the reductant. UV-vis

spectroscopy was used to monitor the state of L₂ protein, to check if the characteristic UV-vis absorption is also observed.

The L₂ protein was diluted to 32 μM in 300 μL buffer. The HEPES (40 mM, pH 7.5) buffer contains 10 mM MgCl₂, 150 mM NaCl. The protein solution was placed in the UV-vis SEC cell, then a UV-vis spectrum was taken; and then Eu(II)-DTPA from a 25 mM stock was added to reach a 1 molar equivalent of the L₂ protein. 1 molar more equivalent was added to the L₂ protein. UV-Vis spectra was taken once equilibrium was reached after the addition of every molar equivalent of Eu(II)-DTPA. The UV-Vis spectra are shown as in Figure 4.4 A, with a picture (Figure 4.4 B) of the L₂ protein after the addition of two equivalents of Eu(II)-DTPA. Since the L₂ protein is a homodimer featuring a single [4Fe–4S] cluster, one molar equivalent in reference to the L₂ protein means one molar equivalent of the cluster. [217]

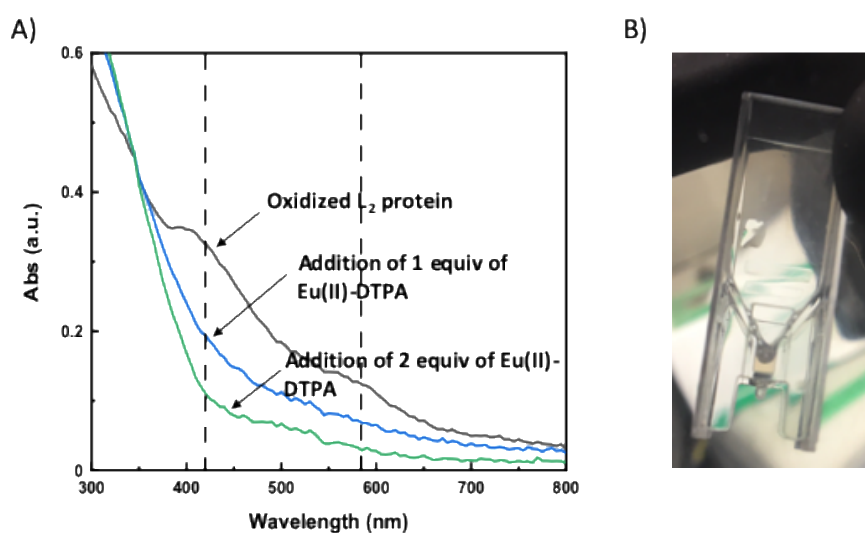


Figure 4.4 A) The UV-Vis spectra of the oxidised L₂ protein (black trace), and the spectra following the addition of 1 molar equivalent (blue trace) and 2 molar equivalents (green trace) of Eu(II)-DTPA; B) a picture of the L₂ protein after the addition of two equivalents of Eu(II)-DTPA.

Figure 4.1, black trace shows the oxidised L₂ protein has an absorption around 420 nm and 580 nm. The absorption at 420 nm is commonly from the ligand metal charge

transfer (LMCT) in the $[4\text{Fe-4S}]^{2+}$ cluster in as other FeS cluster containing proteins. [226] After the addition of 1 molar equivalent of Eu(II)-DTPA (Figure 4.4 A, blue trace), the absorption at 420 nm disappeared, meaning the $[4\text{Fe-4S}]$ cluster has been reduced to 1+ state, which does not have absorption at 420 nm. [226] Upon the addition of 2 molar equivalents of Eu(II)-DTPA in total (Figure 4.4 A, green trace), there is no sign of a new raising peak at around 520 nm, neither at other wavelength. The colour is pale yellow (Figure 4.4 B), which is commonly from the $[4\text{Fe-4S}]^{1+}$ in the protein, rather than pink which is from the $[4\text{Fe-4S}]^0$ cluster in the Fe protein. It seems like the all-ferrous state could not be formed in the wild-type L_2 protein at the presence of excessive amount of strong reductant as Eu(II)-DTPA. There is a dual interest in the study of the L_2 protein: firstly, in exploring whether the L_2 protein ite can form an all-ferrous state, and secondly, in using research on the L_2 protein to indirectly investigate the redox states that might be involved in the Fe protein during the nitrogenase-catalysed reduction of N_2 . The functioning of the Fe protein involves a dynamic mechanism where ATP hydrolysis is linked to the conformational alterations of MoFe protein. [227-230] It was reported that Y127S variant of the L_2 protein shows enhanced nucleotide-dependent interaction with MoFe compared to wild-type L_2 protein and initiates ATPase activity in relation to the chimeric protein-protein interaction. [231] Future research could further investigate the all-ferrous state in the Y127S variant of the L_2 protein or other alternative reductase of nitrogenase, expanding our understanding on the necessity of the all-ferrous state in the catalytic cycle.

4.2.2 Exploration of the all-ferrous state in N_2B_2 protein

The N_2B_2 protein only has one $[4\text{Fe-4S}]$ cluster as in the Fe protein of nitrogenase, and we were curious about the whether it can be super reduced to the all-ferrous state.

Hence, the N_2B_2 protein was investigated with its oxidation states monitored by UV-vis spectroscopy. [67]

The N_2B_2 protein was diluted to 18 μM in 300 μL buffer. The HEPES (40 mM, pH 7.5) buffer contains 10 mM MgCl_2 , 150 mM NaCl . The protein solution was placed in the UV-vis SEC cell, then a UV-vis spectrum was taken; and then Eu(II)-DTPA from a 25 mM stock was added to reach a 1 to 4 molar equivalents with respect to the N_2B_2 protein in the solution. Data shown in Figure 4.5. Given that the N_2B_2 protein is an $\alpha_2\beta_2$ heterotetramer with two $[4\text{Fe-4S}]$ clusters, the term '1 molar equivalent' in relation to N_2B_2 protein denotes one molar equivalent of the entire N_2B_2 protein.

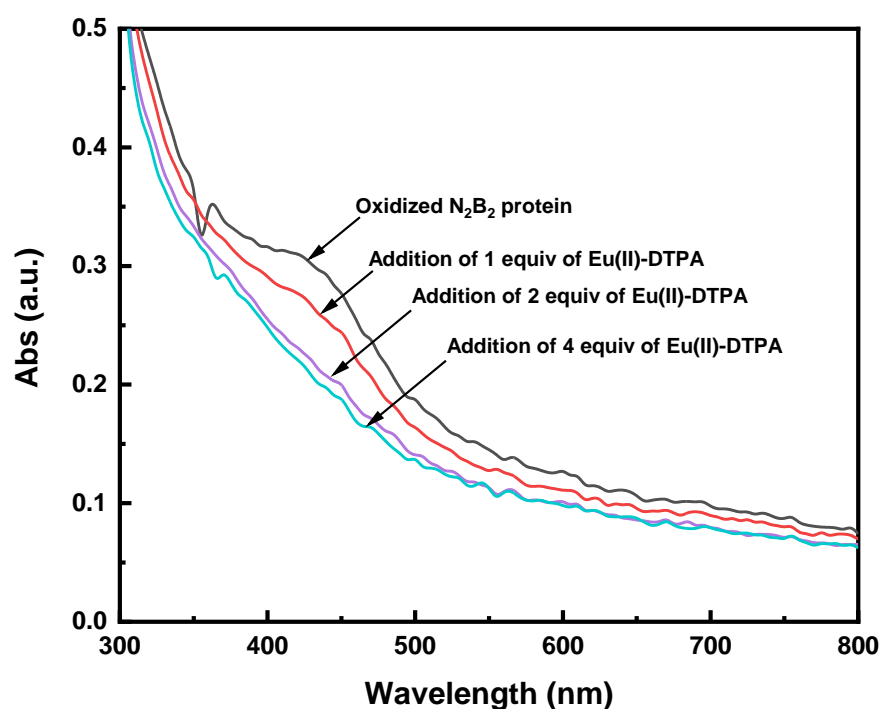


Figure 4.5 The UV-Vis spectra of the oxidised N_2B_2 protein (black trace), and the spectra following the addition of 1 molar equivalent (red trace), 2 molar equivalents (purple trace) and 4 molar equivalents (cyan trace) of Eu(II)-DTPA

The broad absorption at 420 nm indicates the oxidised state of N_2B_2 protein (black trace Figure 4.5). It can be observed that with the addition of 1 molar equivalent of Eu(II)-DTPA the absorption at 420 nm decreased (red trace, Figure 4.5) meaning that the N_2B_2 protein is getting reduced. Upon the addition of another molar equivalent of Eu(II)-DTPA, the absorbance further decreased (purple trace, Figure 4.5). With the addition of 4 molar equivalents of Eu(II)-DTPA (cyan trace, Figure 4.5), the further change of the UV-Vis spectrum is negligible. Eu(II)-DTPA is capable of reducing the N_2B_2 protein indicated by the absorbance decrease at 420 nm, however the pink colour and absorption at 520 nm was missing. It can be preliminarily concluded that the all-ferrous state could not be formed in the N_2B_2 protein.

It is observed that neither of the two proteins in DPOR can produce an all-ferrous state, yet they are capable of catalysing the reduction of Pchlide to Chlide. Drawing a parallel with nitrogenases, this might suggest that an all-ferrous state is not necessarily formed during the N_2 reduction process. Further work is required to substantiate this hypothesis.

4.3 Redox titration of the L_2 protein

In section 3.1 the UV-Visible Spectroelectrochemistry (UV-Vis SEC) method has been established, which was validated on Fe proteins NifH and AnfH. Additionally, the potentiometric titration method was confirmed using ferredoxin. However, the redox potential of the L_2 protein, an analogue of the Fe protein, remains unknown. Therefore, it is crucial to test the redox potential of the L_2 protein and compare it with that of the Fe protein. Both the UV-Vis SEC and potentiometric titration methods have been employed to assess the redox potential of the L_2 protein.

4.3.1 UV-Vis SEC titration on L₂ protein

The UV-Vis SEC method is initially utilised to access the redox potential of the L₂ protein.

In the setup of a UV-Vis SEC cell, 400 μL of L₂ protein at a concentration of 40 μM was introduced. The L₂ protein solution was maintained in a HEPES buffer with a pH of 7.5, comprising 40 mM HEPES, 150 mM NaCl, and 10 mM MgCl₂. The cell was equipped with three electrodes, including a pyrolytic graphite working electrode. This electrode was prepared by polishing with sandpaper for three minutes and then sonicating in Milli-Q water to create a clean surface. For the experiment, redox mediators such as methylene blue, methyl viologen, benzyl viologen, and Eu-L mediators were added, each at a concentration of 15 μM . The procedure involved a reductive redox titration, applying potentials stepwise from -200 to -700 mV vs SHE, in -25 mV increments. Following the achievement of equilibrium at each potential, a UV-Vis spectrum was recorded and is displayed in Figure 4.6.

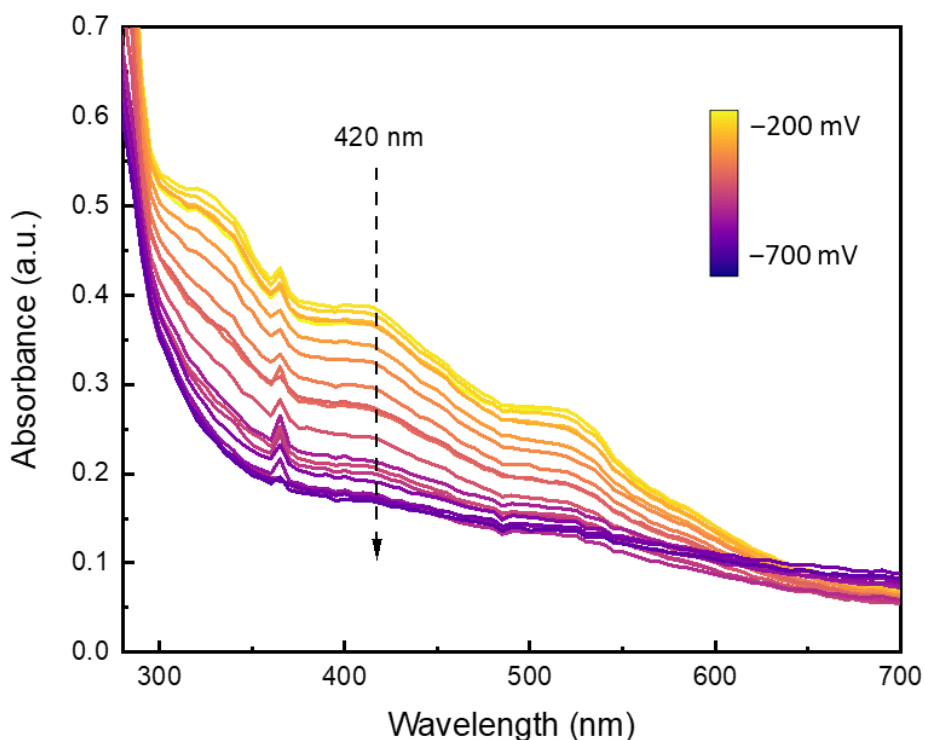


Figure 4.6 UV-Vis spectra of L_2 protein recorded at various potentials during its reductive titration. Each curve corresponds to a specific potential, illustrating the changes in absorption characteristics of L_2 protein as it undergoes redox transformations.

In Figure 4.6, it is observed that as the applied potential progressively becomes more negative, the absorbance at 420 nm gradually decreases. This indicates that, similar to the Fe protein, the L_2 protein is progressively reduced under reducing potentials. Furthermore, the relative intensity of the absorbance at 420 nm was plotted against the applied potentials, as depicted in Figure 4.7. These data were analysed as described in section 3.1.5. The plot was fitted using the Nernst equation (Eq 3.6), resulting in $n = 0.36$, $E_m = -431 \pm 5$ mV, and $R^2 = 0.9867$. This can be compared to the NifH (Fe protein), whose redox potential of the $2+/1+$ couple is -284 mV. As observed before during the titration on NifH, the n value is a fraction that is much smaller than 1, and the fitting is quite off if the n value is set as 1; the reason for the small n value is possibly due to a slow electron transfer process.

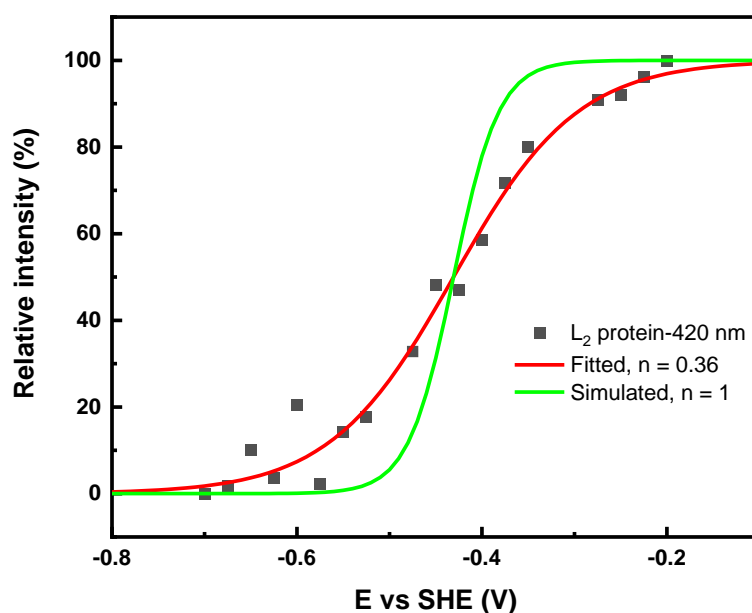


Figure 4.7 The relative intensity of the absorbance at 420 nm as a function of the applied potentials during UV-Vis SEC titration on the L₂ protein, depicted by a dotted line, along with the fitted result of the analysis shown by a red line (n = 0.36) and a simulated result by a green line (n = 1).

4.3.2 Potentiometric titration on L₂ protein

In section 4.3.1 of the study, the redox potential of the L₂ protein was successfully determined through the application of the UV-Vis SEC method. To corroborate these findings, a potentiometric titration was additionally conducted on the L₂ protein. This subsequent titration employed sodium dithionite (NaDT) as the titrant.

In this experiment, the buffer and redox mediators matched those utilised in the UV-Vis SEC titration, as outlined in section 4.3.1. A solution of the L₂ protein was prepared at a concentration of 35 μM. To maintain consistent mixing throughout the process, the solution was agitated continuously at 800 rpm using a magnetic stir bar. Furthermore, sodium dithionite (NaDT), with a concentration of 100 μM, was added to the solution in sequential aliquots. After each addition of NaDT, the open circuit potential (OCP) of the protein solution was measured using an AutoLab electrochemistry

potentiostat. Additionally, UV-Vis spectra of the sample were obtained following each NaDT addition. The obtained data allowed the construction of a titration curve, correlating the open circuit potential with the UV-Vis absorption. The redox potential of the protein was determined based on the inflection point of the titration curve.

In Figure 4.8 A, there is a notable change in the solution's OCP of the solution. At 2000 seconds, under stirring conditions of 800 rpm, the OCP measured -440 mV vs SHE, but a complete equilibrium had not been reached. Corresponding to this point, the UV-Vis spectrum is represented by the red line in Figure 4.8 B. Upon adding one aliquot of NaDT solution, a rapid decrease in OCP was observed, yet equilibrium was still not achieved after 1000 seconds. This phase was marked by alterations in the UV-Vis spectrum (blue trace, Figure 4.8 B) and the emergence of slight white precipitate in the solution. Subsequent additions of NaDT aliquots continued to show a similar pattern of OCP decline and UV-Vis background changes. Even after the fourth aliquot of NaDT and a waiting period of 4000 seconds, equilibrium remained elusive, and more precipitate was evident, suggesting the denaturation of the L₂ protein. To determine whether this denaturation was a reaction condition-dependent phenomenon, the experiment was replicated under various conditions, including different temperatures and pH levels. Despite these modifications, the denaturation of L₂ protein persisted and could not be prevented. This observation and its implications will be further elaborated in section 4.4.2.

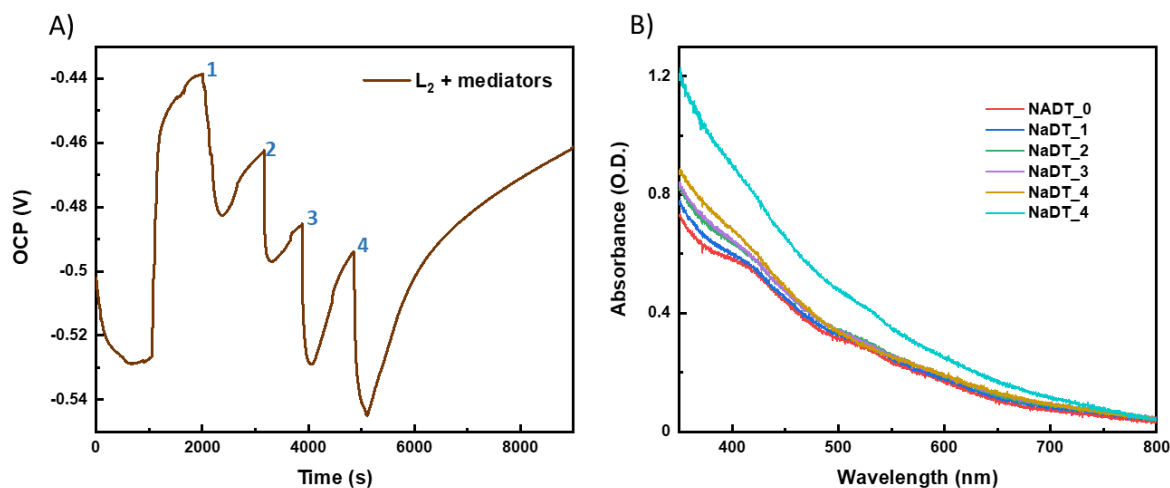


Figure 4.8 A) The temporal variations in the open circuit potential (OCP) of the L₂ protein solution following the introduction of sodium dithionite (NaDT); B) The changes in the UV-Vis absorption of L₂ protein with the gradual addition of sodium dithionite (NaDT) during the potentiometric titration

In Section 4.3, two different methods were employed to measure the redox potential of the L₂ protein. The first method, UV-Vis SEC method, yielded an E_m value of -431 ± 5 mV vs SHE. The second approach, the potentiometric method, did not produce corresponding data. This was due to the irreversible precipitation of the L₂ protein occurring during the titration process.

4.4 Attempted redox titration of the N₂B₂ protein

The N₂B₂ protein serves as the catalytic subunit of the Dissimilatory Pyridine Nucleotide Oxidoreductase (DPOR) complex, playing a crucial role in the reduction of chlorophyll precursors. Since its initial purification, the interest typically focuses on understanding its structure, function, and role in biochemical processes. [75, 225, 232-234] However, the redox potential of the N₂B₂ protein has remained an unresolved mystery. To date, this vital parameter has not been conclusively determined, marking a notable gap in our understanding of the protein's biochemical role and function.

In Section 4.3, the redox potential of the L₂ protein, which is the electron transfer partner of N₂B₂, was successfully assessed using the UV-Vis SEC method. For the N₂B₂ protein, two methods have been employed to carry out redox titration. These include the UV-Vis SEC method developed in Chapter 3, and the potentiometric titration method introduced in section 4.1.

4.4.1 UV-Vis SEC titration on N₂B₂ protein

As detailed in section 4.3, the redox potential of the L₂ protein was successfully evaluated using the UV-Vis SEC method. Therefore, this method has also been applied initially to evaluate the redox potential of the N₂B₂ protein.

In a UV-Vis SEC cell, 400 µL of N₂B₂ protein solution at a concentration of 22 µM was added. To set up a UV-Vis SEC cell, three electrodes were inserted, among which the working electrode (pyrolytic graphite electrode) was polished with sandpaper for three minutes and subsequently sonicated in Milli-Q water to ensure a fresh surface before use. The N₂B₂ protein was preserved in a pH 7.5 HEPES buffer solution. This buffer consisted of 40 mM HEPES, 150 mM NaCl, and 10 mM MgCl₂. Additionally, to stabilise the N₂B₂ protein, 1% v/v glycerol was added. [235, 236] Mediators, including methylene blue, methyl viologen, benzyl viologen and Eu-L mediators, were introduced at a concentration of 15 µM each. A UV-Vis spectrum was then taken following the addition of these mediators (black trace, Figure 4.9). Reductive redox titration was performed by applying potentials in a stepwise manner from positive to negative, ranging from –100 to –600 mV vs SHE, with increments of –100 mV. At each potential step, once the potential reached equilibrium, a UV-Vis spectrum was recorded as shown in Figure 4.9.

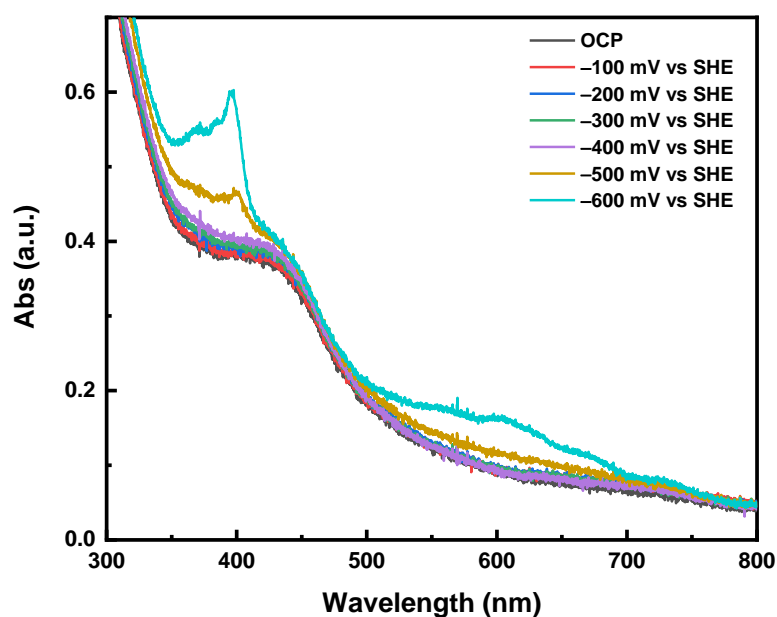


Figure 4.9 UV-Vis spectra of N_2B_2 protein recorded at various potentials during its reductive titration. Each curve corresponds to a specific potential, illustrating the changes in absorption characteristics of N_2B_2 protein as it undergoes redox transformations.

After adding mediators to the solution, the open circuit potential (OCP) was measured at -15 mV vs SHE, indicating the solution was in a relatively oxidised state. The mediators, at a concentration of $15 \mu\text{M}$, did not exhibit significant absorption, as shown by the black trace in Figure 4.9. As the applied potential was gradually decreased from -100 mV to -600 mV, a sharp peak at 400 nm and a broad peak at 600 nm were observed, typically associated with the absorption of the reduced methyl viologen. [237] These absorption properties are crucial for interpreting the actual absorption of the N_2B_2 protein. Despite variations in the absorption spectrum, the slope between 450 - 550 nm remained relatively constant, suggesting that the absorption of the N_2B_2 protein did not undergo significant changes. This observation indicates that the redox mediators underwent a gradual reduction process. However, the N_2B_2 protein could not be reduced, despite the presence of redox mediators.

In the previous experiment, glycerol was added due to its potential to stabilise the N_2B_2 protein. [235, 236] However, glycerol could also increase the solution's viscosity. Since viscosity significantly influences electron transfer rates in biological systems by affecting the protein's internal dynamics and the transition between nonadiabatic and apparent adiabatic transfer mechanisms, [238] additional experiments were conducted without glycerol to observe if the N_2B_2 protein could be reduced in a less viscous solution. The results showed that the oxidation state of the N_2B_2 protein could not be altered, regardless of the presence or absence of glycerol. Furthermore, an oxidative titration was performed on the N_2B_2 protein after reduction with sodium dithionite (NaDT). The results showed the N_2B_2 protein could not be re-oxidised electrochemically. This inability to revert to the original oxidation state electrochemically after reduction or oxidation might be attributed to the protein's large molecular weight (210 kDa). [69, 75] The substantial size of the N_2B_2 protein could be causing the electron transfer process to be exceptionally slow. This slow electron transfer rate might be the reason why the electrochemical redox titration was ineffective.

4.4.2 Potentiometric titration on N_2B_2 protein

In section 4.4.1 of the study, it was demonstrated that the N_2B_2 protein could not be reduced or oxidised using the UV-Visible Spectroelectrochemistry (UV-Vis SEC) method. This finding indicated that the electrochemical approaches employed were not effective for studying the redox behaviour of the N_2B_2 protein. Due to this limitation, the study pivots to an alternative approach outlined in section 4.1, which involves the use of potentiometric titration. The potentiometric titration for the N_2B_2 protein will utilise sodium dithionite (NaDT) as the titrant.

For this experiment, both the buffer and the redox mediators were consistent with those used in the UV-Vis SEC titration detailed in section 4.4.1. The N_2B_2 protein was prepared at a concentration of 35 μM . During the procedure, the solution was continuously stirred using a stir bar at a speed of 800 rpm to ensure uniform mixing. Additionally, aliquots of sodium dithionite (NaDT), at a concentration of 100 μM , were introduced into the solution sequentially. The open circuit potentials (OCP) and UV-Vis spectra were recorded at various stages throughout the experiment, as depicted in Figure 4.10.

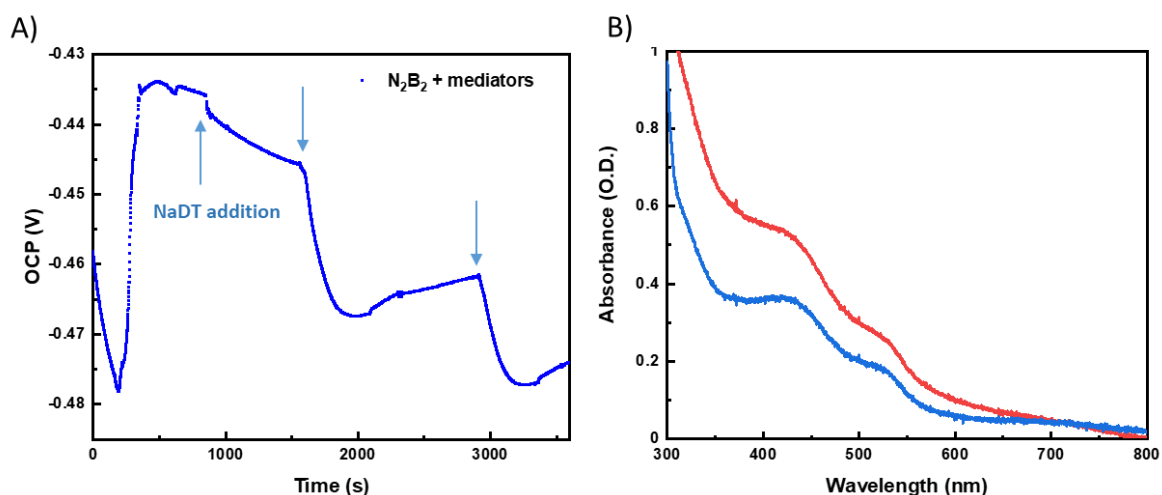


Figure 4.10 A) The temporal variations in the open circuit potential (OCP) of the N_2B_2 protein solution following the addition of sodium dithionite (NaDT); B) The changes in the UV-Vis absorbance of N_2B_2 protein with the gradual addition of sodium dithionite (NaDT) during the potentiometric titration

Observations from Figure 4.10 A reveal that, despite prolonged waiting periods extending up to 1800 seconds, equilibrium was not attained in the potentiometric titration of the N_2B_2 protein solution. This was the case even after the addition of NaDT. Subsequently, the solution became cloudy, indicating the denaturation of the N_2B_2 protein. This was further confirmed by a UV-Vis spectrum analysis performed after centrifugation, which showed a 38% decrease in absorbance at 420 nm (Figure 4.10 B).

This decrease was attributed to both the reduction by NaDT (the amount of NaDT being 2.5% molar equivalent of N_2B_2 protein) and the protein's denaturation. Notably, a similar phenomenon was observed during the potentiometric titration of the L_2 protein.

Interestingly, this denaturation of N_2B_2 and L_2 protein was not observed during the UV-Vis SEC titration. The primary difference between the two experimental setups was that the potentiometric titration involved agitation at 800 rpm. Mechanical forces such as stirring or agitation are known to cause protein denaturation. Stirring increases the kinetic energy, potentially disrupting the interactions between amino acids and leading to protein unfolding. [239] However, stirring is an essential component of potentiometric titration, making this method unsuitable for the redox titration of N_2B_2 protein, despite its successful application in the study of ferredoxin. This is also likely the underlying cause for the denaturation of the L_2 protein observed during the potentiometric titration in section 4.3.2. Further attempts were conducted in the absence of glycerol, as described in section 4.4.1. Nevertheless, these adjustments did not overcome the inherent instability of N_2B_2 under agitation, which continued to hinder the redox titration process.

The efforts to determine the redox potential of the N_2B_2 protein using UV-Vis SEC and potentiometric titration methods have faced significant challenges. One primary issue using UV-Vis SEC method is that the N_2B_2 protein could not be reduced or oxidised, even in the presence of redox mediators. This may be attributed to the protein's substantial size, which likely leads to slow electron transfer. Additionally, the N_2B_2 protein demonstrates insufficient stability under the conditions required for potentiometric titration. These factors – the large size of the protein and its instability

under agitation – are probable reasons why the redox potential of N_2B_2 has remained unreported to date.

However, an alternative approach, such as Electron Paramagnetic Resonance (EPR), might offer a solution. EPR allows for the assessment of the redox state while the samples are maintained in a frozen state, potentially circumventing the stability issues faced in other methods. The drawback of this technique is its requirement for a significantly larger amount of protein, approximately 33 mg, compared to just 1 mg needed for the methods currently employed. Despite this limitation, EPR could provide a viable pathway for advancing our understanding of the N_2B_2 protein's redox potential.[240]

4.5 Electrochemical reduction catalysis of Pchlide with N_2B_2 protein

As a homologue of nitrogenase, the possibility of DPOR to accept electrons from an electrode and achieve Pchlide reduction, either solely through its catalytic domain (N_2B_2 protein) or in the combined presence of L_2 and N_2B_2 proteins, is the focal point of this investigation. The study explores the possibility of reducing Pchlide under an applied negative voltage, independent of conventional chemical reductants such as sodium dithionite (NaDT) or Eu(II)-DTPA. Section 4.4 highlighted the challenges in facilitating electrochemical redox changes in the N_2B_2 protein. Consequently, this section examines whether the inclusion of L_2 protein can assist in these redox processes. Although UV-Visible spectroscopy may not distinctly identify which protein undergoes oxidation or reduction, the unique spectral characteristics of Pchlide and Chlide offer a means to detect the formation of Chlide. Thus, if the electrode effectively transfers electrons to the N_2B_2 protein, the synthesis of Chlide should be observable. This section presents an

exploration into the electrochemical reduction of Pchl_{id}e within a UV-Vis SEC cell, undertaken in the absence of NaDT.

Assays to test the catalytic reduction of Pchl_{id}e were conducted in a UV-Vis SEC cell. The working electrode was made of pyrolytic graphite, the counter electrode was a pyrolytic graphite rod in a compartment separated by a frit, and the reference electrode was a homemade Saturated Calomel Electrode (SCE). The applied potential was set at –700 mV vs SHE. A total of four reaction assays were prepared, each with a volume of 150 μ L and containing 13 μ M Pchl_{id}e as the substrate. The reaction buffer consisted of 40 mM HEPES, 150 mM NaCl, and 10 mM MgCl₂, with a pH of 7.5. Reactions were carried out at 25 degrees Celsius in dark, anaerobic conditions at –700 mV vs SHE for 60 minutes.

After incubation, the reaction was quenched with an equal volume of acetone, and UV-Visible spectra were taken to assess the changes induced by the reaction. The composition of each assay was as listed in the table below:

Assay	N₂B₂ protein	L₂ protein	ATP	Redox mediators
1	1 μ M	×	×	×
2	1 μ M	×	×	5 μ M
3	1 μ M	4 μ M	10 mM	×
4	1 μ M	4 μ M	10 mM	5 μ M

The redox mediators included methylene blue, methyl viologen, benzyl viologen, and Eu-L mediators, each added at a concentration of 5 μ M. These assays were

quenched after 60 minutes of turnover at 25 °C by the addition of acetone to 50 % v/v final concentration. The UV-Vis spectra of each assay are depicted in Figure 4.11.

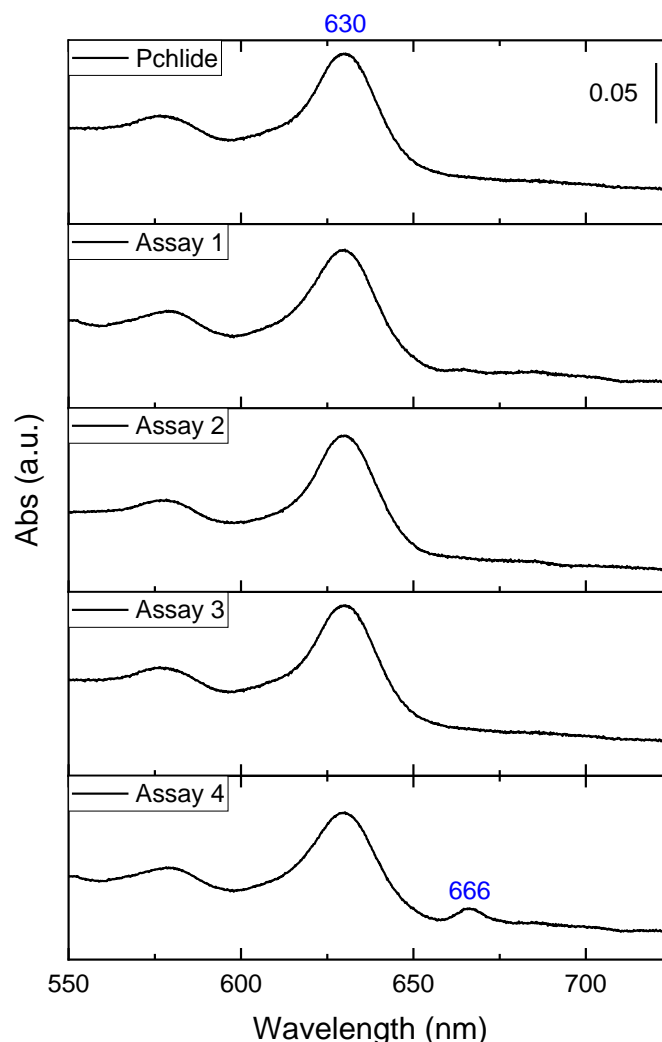


Figure 4.11 UV-Vis spectra comparison of four reaction assays conducted in a UV-Vis SEC cell, each with a 150 μL volume and containing 13 μM Pchlde. Assay 1: 1 μM N_2B_2 protein; assay 2: 1 μM N_2B_2 protein with redox mediators (methylene blue, methyl viologen, benzyl viologen, and Eu-L mediators at 5 μM each); assay 3: 1 μM N_2B_2 protein, 4 μM L_2 protein, and 10 mM ATP; assay 4: 1 μM N_2B_2 protein, 4 μM L_2 protein, 10 mM ATP, and redox mediators. Common conditions for all assays included a reaction buffer of 40 mM HEPES, 150 mM NaCl, 10 mM MgCl_2 (pH 7.5), carried out at 25°C in dark, anaerobic conditions at -700 mV vs SHE for 60 minutes. Reactions were quenched after 60 minutes with acetone to a final concentration of 50% v/v.

In this series of assays, the catalytic activity of N_2B_2 protein in the reduction of Pchlde was investigated under various conditions. Assays 1 and 2 exclusively featured N_2B_2 protein without its electron transfer counterpart, the L_2 protein. Assay 2 differed

from assay 1 by the addition of redox mediators. In both assays, even under an applied potential of -700 mV vs SHE, the UV-Visible spectra showed no absorption peak at 666 nm, the characteristic wavelength for Chlide, suggesting that Pchlide remained unreduced. [232, 233]

Conversely, assays 3 and 4 included both L₂ and N₂B₂ proteins in a 2:1 ratio. These setups mirrored the standard assay but without sodium dithionite. Assay 4 additionally incorporated redox mediators. The UV-Vis spectrum of assay 3 revealed that, even after an hour at -700 mV vs SHE, Pchlide was not reduced. In contrast, assay 4 exhibited an absorption peak at 666 nm, indicating the successful formation of Chlide. Although the Chlide absorbance was weak, by applying an extinction coefficient of $42,181 \text{ M}^{-1} \text{ cm}^{-1}$ for Chlide in these conditions, [241] it was possible to calculate a specific activity of the N₂B₂ protein, approximately $0.23 \text{ nmol Chlide min}^{-1} \text{ mg}^{-1}$.

These results elucidate that in a UV-Vis SEC cell, N₂B₂ protein alone is insufficient for the electrocatalytic reduction of Pchlide under an applied voltage. The reduction process necessitates the presence of the L₂ protein. Furthermore, it is evident that the electron transfer from the electrode to the L₂ protein is not a direct pathway but involves an indirect mechanism mediated by redox mediators. These mediators initially convey electrons from the electrode to the L₂ protein, which, upon reduction and interaction with ATP, subsequently transfers electrons to N₂B₂ for Pchlide reduction.

Bedendi *et al.* demonstrated the utilisation of three mediators—Ti(III) citrate, methyl viologen, and triquat—as alternative electron donor to DPOR. [241] While Bedendi *et al.* observed DPOR functioning without dithionite utilising electrochemically reduced triquat as the mediator, this work involved the use of a range of redox mediators,

including methylene blue, benzyl viologen, methyl viologen, and Eu-L mediators, as alternative electron donors. In the referenced research, the observed threefold higher activity of the N_2B_2 protein compared to this study could be attributed to two key factors. Firstly, a significantly higher concentration of the mediator was used, specifically 400 μM in contrast to the 5 μM employed here. Secondly, a different mediator, triquat, was utilised in the experiment. [241] These variations in mediator concentration and type are likely to have contributed to the enhanced activity of the N_2B_2 protein observed in the research. Overall, we both have confirmed that redox mediators, in conjunction with the electrode, can substitute for dithionite as a reductant.

In addition to employing the UV-Vis SEC method for assessing the N_2B_2 protein's reactivity, protein film electrochemistry (PFE) has also been utilised to evaluate the catalytic activity of immobilised N_2B_2 . The rationale behind this approach is that immobilisation on an electrode can potentially enhance electron exchange efficiency, and often can reach a higher local concentration of the protein on the electrode surface. [242] Moreover, immobilised proteins generally exhibit greater stability than those in free solution. [243]

Chen's study showcased the interaction of substrates and inhibitors with the MoFe protein in the absence of the Fe protein, facilitated by redox mediators. This was achieved using protein film electrochemistry (PFE) combined with infrared spectroscopy, specifically Protein Film Infrared Electrochemistry (PFIRE). [135, 244] In this process, 1-ethyl-3-(3-dimethylaminopropyl) carbodiimide (EDC) and *N*-hydroxysulfosuccinimide (NHSS) were used as crosslinkers to attach the MoFe protein to carboxylated BP2000 particles. Importantly, PFIRE allows for the *in situ* verification of

enzyme immobilisation. Building upon this concept, this technique was applied to explore if the N₂B₂ protein, once immobilised, could electrocatalytically reduce Pchl_{id}e. The approach aimed to discern whether confining N₂B₂ protein on the electrode surface alters its reduction activity and whether it can facilitate Pchl_{id}e reduction using electrons from the electrode rather than its natural reductase partner, the L₂ protein.

It was discovered that N₂B₂ protein could be successfully immobilised onto BP2000 using EDC and NHSS as crosslinkers. However, due to significant adsorption of Pchl_{id}e onto BP2000, likely resulting from π - π stacking interactions, it was challenging to confirm the reduction of Pchl_{id}e. Consequently, in the absence of clear evidence of N₂B₂ protein's catalytic activity, only the experiment's conclusions are presented here rather than detailed experimental data. For those interested in the topic of PFE, the research conducted by Vincent, Armstrong, and other leading scientists in this field offers valuable insights. [164, 245-249]

4.6 Conclusion

In this chapter, we have explored various aspects of redox behaviours in DPOR, particularly focusing on its potential to form an all-ferrous state, its redox potential, and its reduction activity in an electrochemical cell. It was discovered that neither the L₂ protein nor the N₂B₂ protein could be reduced to the all-ferrous state by Eu(II)-DPTA. Additionally, a potentiometric titration method was successfully developed and validated for ferredoxin, which was used to measure the redox potential of DPOR alongside the UV-Vis SEC method. The exploration of the L₂ protein's redox potential through two different methods yielded mixed results. The UV-Vis SEC method effectively determined an E_m value of -431 ± 5 mV vs SHE, yet the potentiometric method faced

obstacles due to the irreversible precipitation of the L₂ protein during titration. Regarding the N₂B₂ protein, both UV-Vis SEC and potentiometric titration methods faced significant challenges. The primary issue with the UV-Vis SEC method was the inability to either reduce or oxidise the N₂B₂ protein, even in the presence of redox mediators. This difficulty was attributed to the protein's substantial size, which likely led to a slower rate of electron transfer, coupled with its instability under the required conditions for potentiometric titration. As a result, the redox potential of the N₂B₂ protein remains elusive. Further investigations within the UV-Vis SEC cell reactions revealed that under homogenous catalysis conditions, the reduction of Pchlide solely by the N₂B₂ protein was challenging. Conversely, under heterogeneous catalysis conditions, the outcome was inconclusive due to the strong adsorption of Pchlide on BP2000, which prevented the use of UV techniques to confirm its reduction to Chlide. However, the presence of both N₂B₂ protein and L₂ protein in the system allowed for the utilisation of electrons from the electrode to catalyse the reduction of Pchlide.

For future work, it is proposed to investigate the all-ferrous state of the L₂ protein mutant Y127S or other alternative reductases of nitrogenases, as well as their complexes with the MoFe protein, VFe protein or FeFe protein of nitrogenases, to evaluate their catalytic activity against various substrates. This approach aims to indirectly verify the necessity of the all-ferrous state for the catalytic activity of the MoFe protein. Additionally, implementing an EPR-coupled potentiometric method is suggested to accurately measure the redox potential of the N₂B₂ protein. These methods could provide deeper insights into the redox characteristics of N₂B₂ protein, which is crucial for understanding its function in its mechanism.

Chapter 5 Studies on *DdHydAB* via IR microspectroscopy on single crystals

Hydrogen (H₂) gas, a compelling potential energy carrier, has spurred efforts to engineer biologically-based systems for renewable H₂ synthesis. [FeFe] hydrogenases like *Desulfovibrio desulfuricans* HydAB (*DdHydAB*) stand as the most efficient enzyme for proton reduction and hydrogen oxidation, functioning at approximately the thermodynamic potential of the H₂/H⁺ couple. Studying the mechanism of this enzyme's active centre could prove invaluable for designing catalysts that employ earth-abundant metals, such as iron.

In terms of catalytic efficiency, *DdHydAB* is among the most efficient [FeFe] hydrogenases known. Its turnover frequency for hydrogen production can be on par with or even surpass other [FeFe] hydrogenases.[250] Its robust performance, even under challenging conditions, makes *DdHydAB* a particularly intriguing model for studies aiming to unravel the mechanisms of biological hydrogen conversion. Furthermore, *DdHydAB* exhibits unique properties at the molecular level. For instance, *DdHydAB* and *CpHydA1* [FeFe] hydrogenase, feature accessory clusters known as F-clusters along with the H cluster (more details could be found in section 1.5, chapter 1).[251] These F-clusters may play a crucial role in electron transfer, influencing the redox states of the active site, and are not found in all [FeFe] hydrogenases.

The iron atoms in the active site H cluster of [FeFe] hydrogenases are coordinated by physiologically unusual CO and CN⁻ ligands. These ligands serve as superb probes for Fourier Transform Infrared (FTIR) spectroscopy, given that the vibrational stretching bands arising in the infrared spectrum are highly responsive to electron density changes

caused by alterations in the oxidation state of the cluster or protonation. Consequently, various redox states of the H cluster have been identified using IR spectroscopy on enzyme in solution. [252]

It has been demonstrated that transitioning between redox states electrochemically is feasible within a NiFe hydrogenase single crystal. [178] The slowed reactivity of the crystal permits resolution of the production kinetics of individual sub-states that would typically coexist simultaneously in solution. The crystalline form also retards protein dynamics, making possible the detection of FTIR bands of bridging CO in the $H_{red}H^+$ and $H_{sred}H^+$ states of [FeFe] hydrogenases, which are challenging to discern in protein solution at room temperature (section 5.3). This discovery resolves long-standing confusion, given that such slowed protein dynamics are usually observed only at low temperatures. [253]

Additionally, the high protein concentration within the crystal allows for recording spectra with elevated signal-to-noise ratios, facilitating the identification of the bands corresponding to each active site state. This microspectroscopic-electrochemical method, previously employed in the study of NiFe hydrogenase crystals and single crystal of prototypical [FeFe]-hydrogenase I from *Clostridium pasteurianum* (Cpl), [178, 179] will be extended to the investigation of *DdHydAB* [FeFe] hydrogenase in this chapter.

The feasibility of electrochemical control over the *DdHydAB* crystal is explored in this chapter, with FTIR spectroscopy serving as a monitoring tool for tracking the transformation of oxidation states. The enzyme *DdHydAB* was produced by reconstructing an apo-protein, overexpressed in *E. coli*, with an artificially synthesised $[Fe_2(adp)(CO)_4(CN)_2]^{2-}$ ($[2Fe]^{adt}$) cofactor, thereby achieving high yields. As *DdHydAB* is

sensitive to O₂, the overexpressed *DdHydAB* was converted to a stable H_{inact} state for protection against O₂ and subsequently crystallised in the lab.

The states of the *DdHydAB* crystal upon electrochemical reduction were tracked using an electrochemical IR microspectroscopic (ECIRM) cell. Within this cell, the pH dependence of the redox potentials of various states was assessed by titration from pH 5 to pH 8. Furthermore, the impact of pH on the protonation of the states was explored using the same cell. Potential applications of this cell for studying nitrogenase and other redox enzymes will be discussed at the conclusion of this chapter.

5.1 Characterization of *DdHydAB* after Production and Artificial Maturation

As described in Section 2.6, apo-*DhHydAB* was overexpressed and purified. The apo-*DdHydAB* was then artificially matured to form holo-*DdHydAB*, which was subsequently incubated in an anaerobic glovebox. These processes were validated and monitored using SDS-PAGE (sodium dodecyl sulfate-polyacrylamide gel electrophoresis), UV-Vis, and IR spectroscopy. SDS-PAGE was used to estimate the purity of the protein, and to identify the protein by measuring the molecular weight of the peptide. The supernatant of the lysate after sonication and the eluate that ran through the IBA column were analysed with SDS-PAGE. The sample was denatured at 95 °C for 3 minutes prior to being loaded onto an SDS gel (Invitrogen) and electrophoresed for 45 minutes at 200 V for 45 min. An instant blue (Expedeon) was used to dye the gel allowing the display of the protein bands (Figure 5.1).

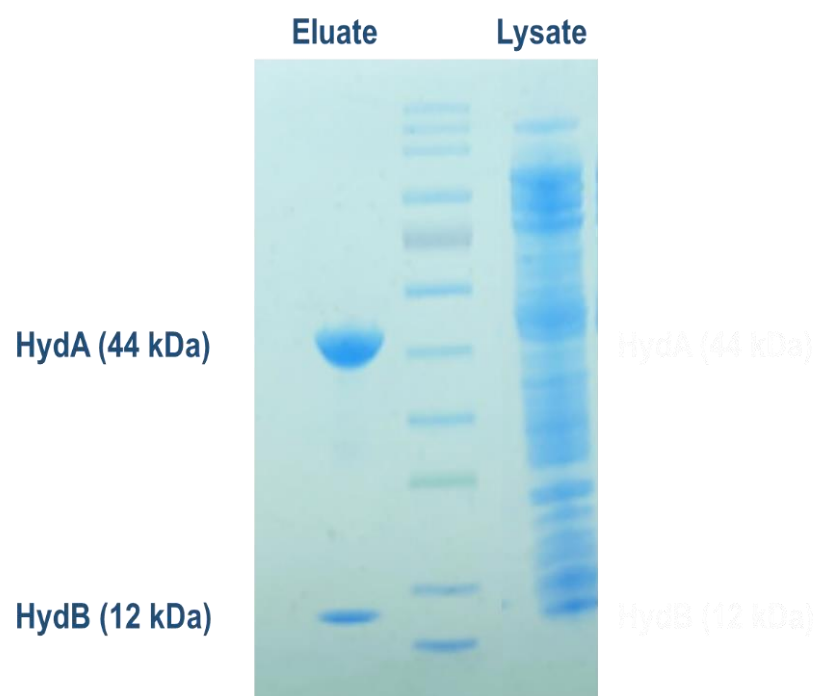


Figure 5.1 The SDS-PAGE of the apo-*DdHydAB* [FeFe] hydrogenase after strep-tactin affinity chromatography. The two bands for apo-*DdHydAB* were identified in the eluate at 44 kDa (large subunit HydA) and 12 kDa (small subunit HydB). Lysate is the supernatant after sonication, and eluate was the purified fraction after eluting the supernatant on a Streptactin Superflow high capacity column (IBA) with 2.5 mM desthiobiotin. The band in the middle is a pre-stained protein ladder for the determination of molecular weight of the protein bands.

The lane on the right in Figure 5.1 shows fractions of the supernatant of the lysate after disruption, which shows a great mixture of peptides. This supernatant was purified with a 20 mL IBA column pre-equilibrated with buffer W. There were only two bands shown from the eluate (the left lane in Figure 5.1), which indicates the high purity of the protein. If taking the pre-stained protein ladder (NEB, the middle lane in Figure 5.1) as a reference for the protein molecular weight, the two bands indicate molecular weights of 44 kDa and 12 kDa, corresponding to the HydA and HydB of the *DdHydAB* respectively.

During the expression of *DdHydAB*, cysteine and ferric ammonium citrate are supplemented as the sources of sulfur and iron separately for the synthesis of the [4Fe-4S] clusters in apo *DdHydAB*. The expression and purity of the protein were confirmed by the SDS-PAGE. The remaining the concern is whether the [4Fe-4S] clusters were

successfully synthesised in the protein. UV-Vis spectroscopy is a rapid means of inspecting the existence of the [4Fe-4S] cluster and determining the concentration of the apo protein. As seen in the UV-Vis spectrum of the apo protein in Figure 5.2, it shows a broad absorption around 400 nm, which confirms the integrity of the [4Fe-4S] cluster. In addition, the molar extinction coefficient of *DdHydAB* is known to be $52500 \text{ M}^{-1} \text{ cm}^{-1}$ at 412 nm. [254] The concentration of the apo protein is calculated accordingly based on the Beer-Lambert law (Eq. 2.2).

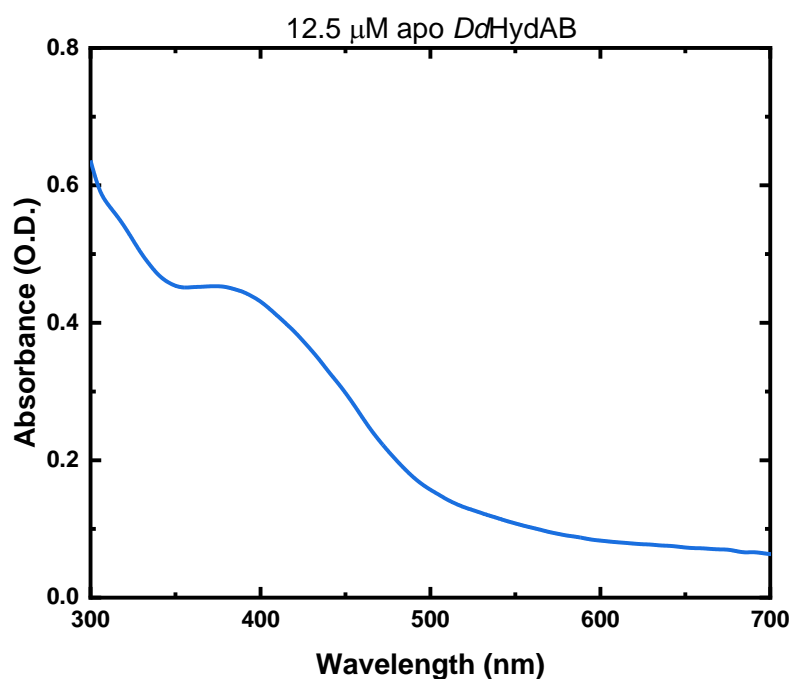


Figure 5.2 The UV-Visible absorption spectrum of purified apo-*DdHydAB*. The apo-*DdHydAB* (12.5 μM) is in a pH 8 buffer containing 100 mM Tris-HCl and 150 mM NaCl. The spectrum is measured aerobically in a Cary 60 spectrophotometer using a 1 cm pathlength UV-Vis cuvette.

Once the expression of the apo *DdHydAB* is confirmed with UV-Vis spectroscopy, it is followed by the process of artificially maturing the apo protein with a synthetic $[\text{2Fe}]^{\text{adt}}$ cofactor to generate CO-inhibited holo *DdHydAB* ($\text{H}_{\text{ox}}\text{-CO}$). The inhibiting CO was released under a nitrogen atmosphere to produce a putative active enzyme. The IR spectrum of the sample after CO release is shown as Figure 5.3.

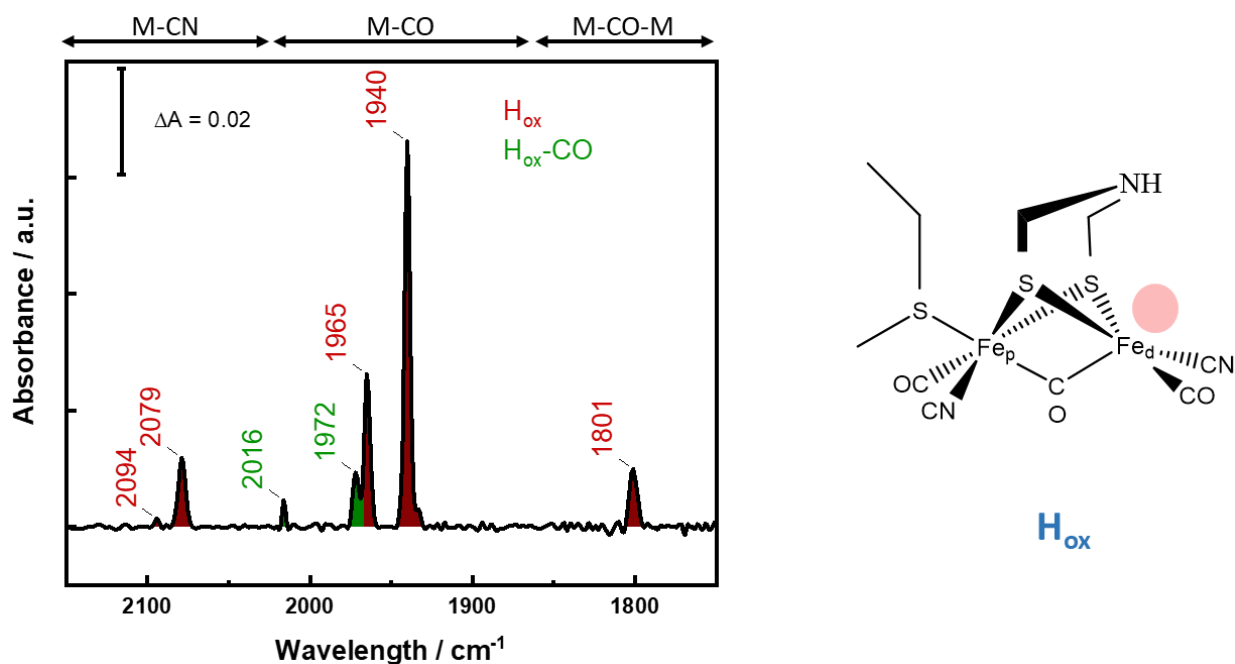


Figure 5.3 FTIR spectra of putative active *DdHydAB* (H_{ox}) after holo *DdHydAB* (H_{ox} -CO) was incubated under N_2 atmosphere for 48 h at 15 °C for 48 h. Peak values corresponding to the H_{ox} , and H_{ox} -CO states are coloured in red and green respectively. The protein is in a 25 mM Tris-HCl, 25 mM KCl, pH 8 buffer. The CO ligand on Fe_d in holo *DdHydAB* (H_{ox} -CO) was released after the incubation and led to the H_{ox} state (structure on the right side).

The structure of the $[2Fe]_H$ at the H_{ox} state is shown in Figure 5.3, where the red circle is a vacant coordinating site for substrates. When an extrinsic CO binds to this vacant site, the H_{ox} -CO state is formed. The predominant features are identical to the previously reported H_{ox} state, mixed with a lesser absorbance from the H_{ox} -CO state. [190, 255] The bands labelled with red number in Figure 5.3 arise from the H_{ox} state, and green are corresponding to the H_{ox} -CO state. The three strong stretching bands at 1801, 1940 and 1965 cm^{-1} are assigned to the CO in the H_{ox} state cluster. They are arisen respectively from the Fe-Fe bridging carbonyl (μCO , 1801 cm^{-1}), the terminal CO ligand at Fe_d (dCO , 1940 cm^{-1}) and the terminal CO at Fe_p (pCO , 1964 cm^{-1}). The bands at 2094 cm^{-1} and 2079 cm^{-1} are from the stretching of terminal CN^- ligand of the H_{ox} state. The terminal binding of extrinsic CO to the cluster at the distal Fe_d gives rise to a new peak at 2016 cm^{-1} , and

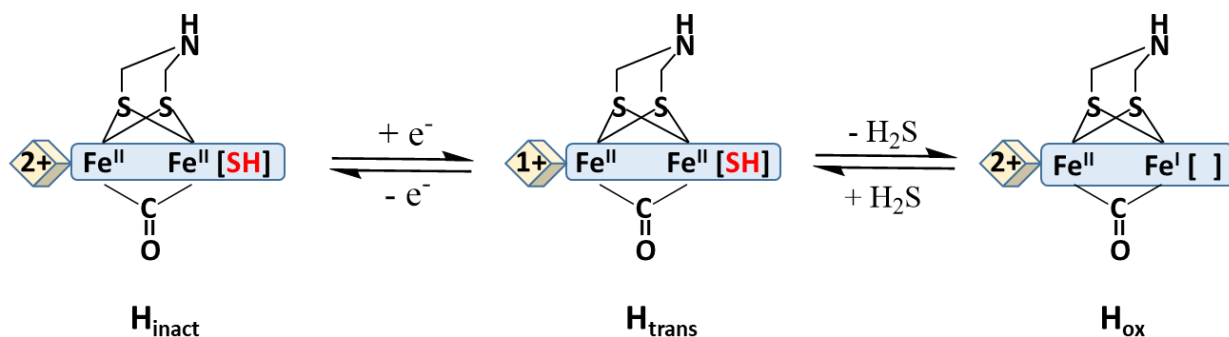
also causes a positive shift of the band of the δ CO ligand to 1972 cm^{-1} due to a decrease of the π -back-bonding capability of this atom.

It can be concluded that using the recombinant expression method the complete *DdHydAB* hydrogenase is successfully produced. It is spectroscopically identical to the native enzyme, with a predominant H_{ox} state and small portion of H_{ox} -CO state.

5.2 Protection of *DdHydAB* with oxygen-stable H_{inact} state and reactivation

Though [FeFe] hydrogenases are highly active for both H_2 oxidation and proton reduction, they are too oxygen-sensitive to have broad applications. Multiple ways have been explored for the protection of [FeFe] hydrogenases from oxygen damage. Interestingly, in the native host, *DdHydAB* is produced aerobically, which persists in an inactive oxygen-stable form known as the H_{inact} state. Both Fe atoms of the $[\text{2Fe}]_{\text{H}}$ cluster adopt Fe(II) configuration with an additional ligand attached to Fe_{d} . [192] This H_{inact} state can be reduced to active states with the release of the putative ligand from Fe_{d} (Scheme 5.2). [184] The nature of this additional ligand remained unclear until recently when Rodríguez-Maciá *et al.* reproduced this H_{inact} state *in vitro* in the presence of Na_2S upon oxidation of *DdHydAB*. This finding suggested that the additional ligand bound to Fe_{d} could be a sulfur species, likely SH^- . [256] Later the sulfur ligand was confirmed with a 1.65 Å crystal structure of this state along with other spectroscopic analyses, e.g. X-ray absorption spectroscopy (XAS), and nuclear resonance vibrational spectroscopy (NRVS). [257] In this H_{inact} state, the sample may be taken from the glovebox and exposed to air for three days, with half of the $[\text{2Fe}]_{\text{H}}$ cluster retained intact. Hence, for ease of handling and storage, the *DdHydAB* used in this chapter was first converted to this state based on the protocol reported by Rodríguez-Maciá *et al* (section 5.2.1). [256] It was

investigated whether the electrochemical method could be employed to reactivate *DdHydAB* from the H_{inact} state *in crystallo* (5.2.2).



Scheme 5.2 Schematic structures of the H-cluster in H_{inact} , H_{trans} and H_{ox} states from *DdHydAB*. The yellow diamond represents the $[4\text{Fe}-4\text{S}]_{\text{H}}$ cluster with the oxidation state labelled. The H_{inact} state is reactivated upon reduction and the release of the $-\text{SH}^-$ ligand.

5.2.1 Preparation of the H_{inact} -state *DdHydAB*

The H_{inact} state of *DdHydAB* was prepared by further oxidising the H_{ox} state with Hexaammineruthenium (III) chloride (HAR) and then treating it with Na_2S . [256]

In section 5.1, the holo *DdHydAB* was overexpressed in *E. coli*, and converted to H_{ox} state by incubating in a N_2 atmosphere glovebox. In an anaerobic glovebox, the *DdHydAB* produced in section 5.1 was diluted to 0.2 mM with pH 8 buffer (25mM Tris and 25 mM KCl). Hexaammineruthenium (III) chloride (HAR) was added to the dilute protein to 1 mM from a 100 mM stock, ensuring a full conversion at the H_{ox} state. Then 10 mM of Na_2S was added from a 1 M stock, followed by further addition of 10 mM HAR.

The sample was removed from the glovebox and exposed to air. The separation and purification were performed on a benchtop with the presence of oxygen in the air. The aggregates were removed by centrifugation for 10 min at 4 °C, 4000 rpm. The supernatant was eluted through a desalting column that was pre-equilibrated with 25 mM Tris buffer (pH 8) containing 25 mM KCl. The eluant was concentrated to ca 2 mM using centrifugal concentrators (30 kDa MWCO). The concentrated sample was examined by FTIR in a transmission cell.

After treatment with HAR, then Na₂S and HAR, the FTIR spectrum of the *DdHydAB* (orange integration in Figure 5.4) shows a trend of blue shift towards higher energy, compared with the FTIR spectrum of the H_{ox} state (red integration in Figure 5.4). From the higher wavenumber to the lower, five distinctive peaks, 2106, 2086, 2007, 1983, and 1847 cm⁻¹, correspond respectively to the two terminal CN⁻ ligands, two terminal CO ligands and the bridging carbonyl μCO of the [2Fe]_H cluster. The FTIR features of the sample are identical to that of the previously reported H_{inact} state. [256] Thus, the success of the conversion of the H_{ox} to H_{inact} state in the *DdHydAB* sample is confirmed spectroscopically.

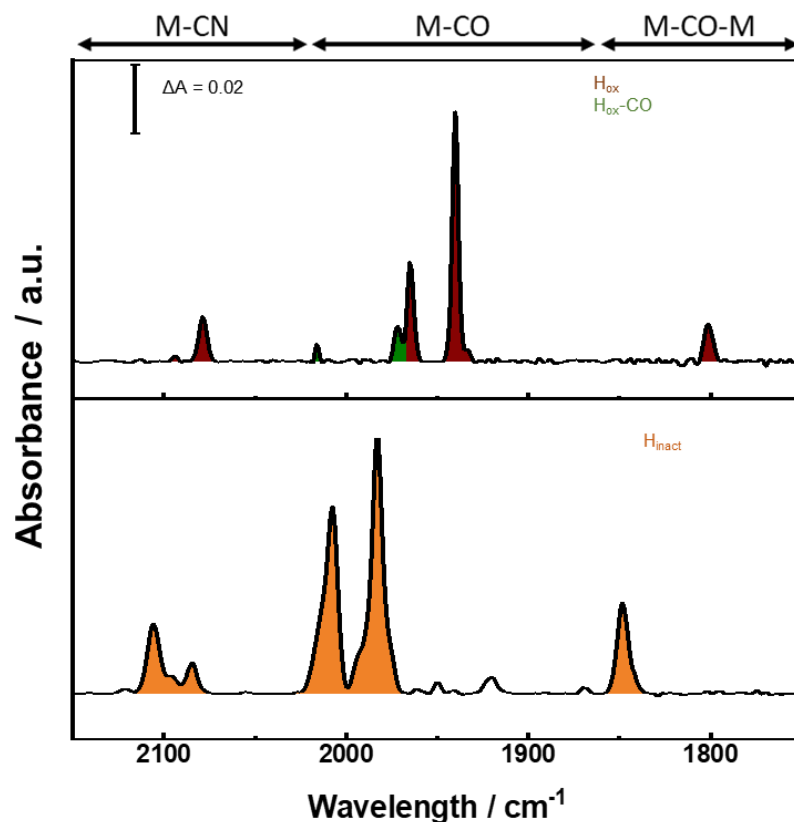


Figure 5.4 The FTIR spectrum of *DdHydAB* at the H_{ox} state (spectrum at the top); and the spectrum of the H_{ox} -state *DdHydAB* being treated with Hexaammineruthenium (III) chloride (1 mM), Na₂S (10 mM) and Hexaammineruthenium (III) chloride (1 mM) sequentially, which is dominated by H_{inact} state (spectrum at the bottom).

5.2.2 Reactivation of *DdHydAB* from the H_{inact} state with electrochemistry

In *DdHydAB*, the H_{inact} state is known as the inactive state because it is not part of the catalytic cycle of proton reduction. It is important to investigate whether this state can be reactivated. This exploration is conducted electrochemically using the SEC IR cell for an *in crystallo* sample.

The *DdHydAB* sample was firstly crystallised with help from Dr Stephen Carr (Research Complex at Harwell) in a crystallisation buffer (0.1 M Tris, 0.9 M LiCl and 32% (w/v) PEG 6000). The crystals were studied in crystallisation buffer (pH 8), mixed with 0.5 mM of the redox mediators anthraquinone-2-sulfonate ($E_m = -277$ mV), benzyl viologen ($E_m = -358$ mV), methyl viologen ($E_m = -449$ mV), and Eu(III)-BAPTA ($E_m = -630$ mV). The

mixture suspending the *DdHydAB* crystal was placed on the 4 mm diameter working electrode in a ECIRM cell for manipulation by electrochemistry. It was ensured that the buffer solution adequately covered the surfaces of all three electrodes. The cell was sealed with a 25 μm PTFE spacer and an IR-transparent CaF_2 window. This assembly was done in a N_2 -purged, anaerobic Glovebox. Silicone sealant was used to make the cell gas tight. IR spectra were obtained by averaging 512 scans at a resolution of 2 cm^{-1} . For this purpose, a Bruker Vertex 80V IR spectrometer and a Hyperion 3000 IR microscope were employed. A FTIR spectrum was collected *in situ* after potential application at -400 mV vs SHE for 2 h.

The FTIR spectrum of *DdHydAB* crystal after potential poise at -400 mV vs SHE is shown in Figure 5.5. The absorption from the H_{inact} state shown in Figure 5.4 (orange integration) has completely disappeared and is replaced by three new sets of peaks. The strongest absorption at 1940 and 1965 cm^{-1} (red integration in Figure 5.5) indicates that H_{ox} is the predominant state. The peaks at 2100 , 2075 , 1988 , 1975 and 1835 cm^{-1} (grey integration in Figure 5.5) are identical to those observed previously for H_{trans} from the native enzyme. [192] Another distinct absorption is at 1894 cm^{-1} (blue integration in Figure 5.5), it is assigned to the terminal CO bound to Fe_d of the $[\text{2Fe}]_{\text{H}}$ cluster at the $\text{H}_{\text{red}}\text{H}^+$ state. [258]

From the FTIR spectra, it is observed that at -400 mV , the H_{inact} state is reactivated and reduced to a mixture of H_{trans} , H_{ox} and $\text{H}_{\text{red}}\text{H}^+$ states *in crystallo*. The midpoint potential previously reported for the $\text{H}_{\text{inact}}/\text{H}_{\text{ox}}$ at pH 8 is -350 mV , which is consistent with the much weaker absorption from the H_{trans} state than that from the H_{ox} state. A small fraction of the H_{ox} was further reduced to the $\text{H}_{\text{red}}\text{H}^+$ state.

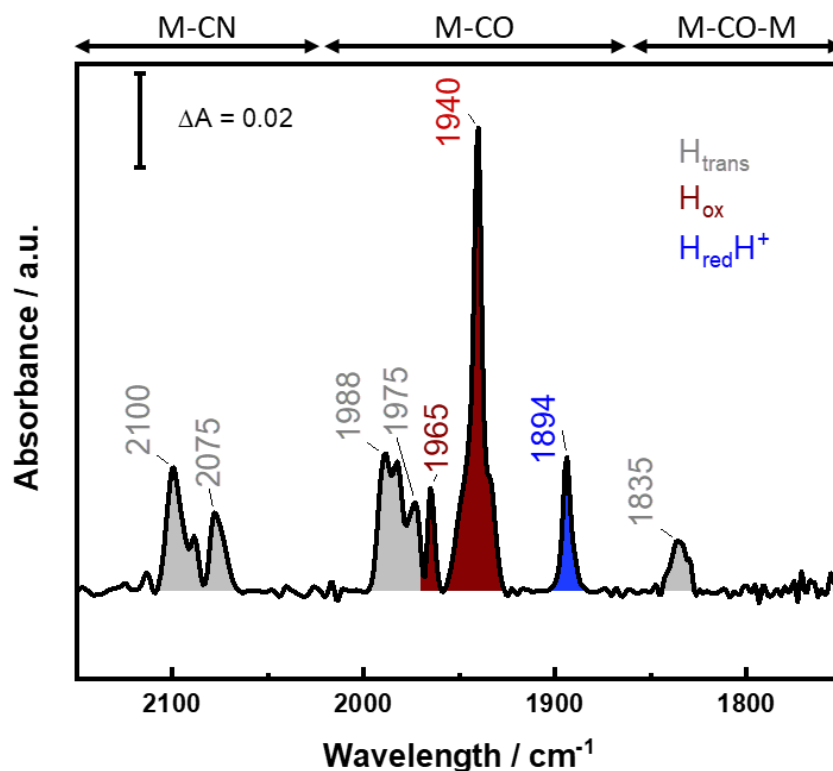


Figure 5.5 The FTIR spectrum of *DdHydAB* crystal after potential poise at -400 mV vs SHE in the presence of 0.5 mM of the redox mediators (anthraquinone-2-sulfonate, benzyl viologen, methyl viologen, and Eu(III)-BAPTA). The absorption bands from H_{trans} , H_{ox} and $H_{\text{red}}H^+$ are coloured grey, red and blue respectively.

In this section, the oxygen-stable state of *DdHydAB*, H_{inact} state is reproduced *in vitro* in the presence of sulphide and oxidant, which is confirmed by FTIR spectroscopy. It is shown that this state *in crystallo* can be reactivated upon reduction in an IR SEC cell.

5.3 Probing the redox states of *DdHydAB* in crystallo via IR microspectroscopy

During the catalytic cycle, there are several intermediates involved, of which the H_{ox} state is the most oxidised state. For the easy recollection of their proposed structure, the catalytic cycle will be presented again here. The terminal CN^- ligand and CO are excluded from the structure in the scheme for simplicity (Scheme 5.3). For the oxidised state, the H_{inact} , H_{trans} and H_{ox} states (introduced in previous Section 1.5), there is a general arrangement on their spectroscopic features, while the reduced states, H_{red} , $H_{\text{red}}H^+$, H_{sred} ,

process, where it binds protons and facilitates their reduction. As electrons are transferred to the active site through the FeS clusters, the H_{ox} state undergoes a series of reductions and protonations. This leads to the eventual production of hydrogen gas. In this section the reduction of the H_{ox} state is studied using an electrochemical IR microspectroscopic cell, to gain insights into the intricate mechanisms of electron and proton transfer within the enzyme.

The *DdHydAB* crystals were in crystallisation buffer ((pH 5, 0.1 M sodium acetate, 0.9 M LiCl and 32% (w/v) PEG 6000), mixed with 0.5 mM of the redox mediators anthraquinone-2-sulfonate ($E_m = -277$ mV), benzyl viologen ($E_m = -358$ mV), methyl viologen ($E_m = -449$ mV), and Eu(III)-BAPTA ($E_m = -630$ mV). The suspension of *DdHydAB* crystals was placed on the working electrode in a SEC IR cell for manipulation by electrochemistry. The method to assemble this cell has been described in section 2.6. FTIR spectra were collected *in situ* after potential application at -589 mV (Figure 5.6) and -669 mV (Figure 5.7) vs SHE.

At -589 mV, the FTIR spectrum of the *DdHydAB* crystal is noticeably complicated and shows a mix of several states. There are peaks arising from the H_{ox} -CO state, but for simplicity, the peaks from H_{ox} -CO are not labelled in the spectrum.

The $H_{red}H^+$ state is identified by the absorption at 2079, 2040, 1916 and 1984 cm^{-1} (blue integration in Figure 5.6), as they are identical to that reported by Mebs *et al* [260] and by Sommer *et al* in *CrHydA1*. [261] In both of their analyse, the 1964 cm^{-1} band was also assigned to $H_{red}H^+$; but a different state $H_{hyd:ox}$ appears to be responsible for this absorbance. [259] The fifth band arising from the bridging CO stretching of $H_{red}H^+$ appears

at 1817 cm^{-1} , which is not easy to detect at room temperature, but is revealed at low temperature. [262]

For the case here, the absorbance at 1964 cm^{-1} is too intense to be from the $\text{H}_{\text{hyd:red}}$ state which is identified by a weak absorption at 1850 cm^{-1} . [259] Along with the bands at 2089 , 1964 , 1940 and 1801 cm^{-1} , it is assigned to the H_{ox} state, which is the second predominant state. The IR spectra of artificially matured *DdHydAB* frequently exhibit a band at 1985 cm^{-1} , which has been challenging to attribute to any known state of the H-cluster. [188] Martini *et al.* have demonstrated that the H_{trans} -like states are formed upon the reaction of [FeFe] hydrogenases with exogenous CN^- and have assigned this band to the terminal CO ligands in the CN^- -dependent H_{trans} -like state found in the *DdHydAB* C178A mutant. Additionally, Martini *et al.* proposed that a small amount of the CN^- -dependent H_{trans} -like state might form during the artificial maturation of the enzyme, potentially causing the 1985 cm^{-1} band. [263] However, observations during maturation, as depicted in Figure 5.3, suggest otherwise. In this context, the peak at 1985 cm^{-1} has been assigned to the $\text{H}_{\text{hyd:ox}}$ state, based on the work by Lorent *et al.*, where it is detected following a one-electron reduction from the H_{ox} state in *CrHydA1*. [259] Given that the potential applied was -589 mV vs SHE , resulting in *DdHydAB* predominantly taking the one-electron reduced form (H_{red} or $\text{H}_{\text{red}}\text{H}^+$), it is more probable that this intense band originates from the $\text{H}_{\text{hyd:ox}}$ state.

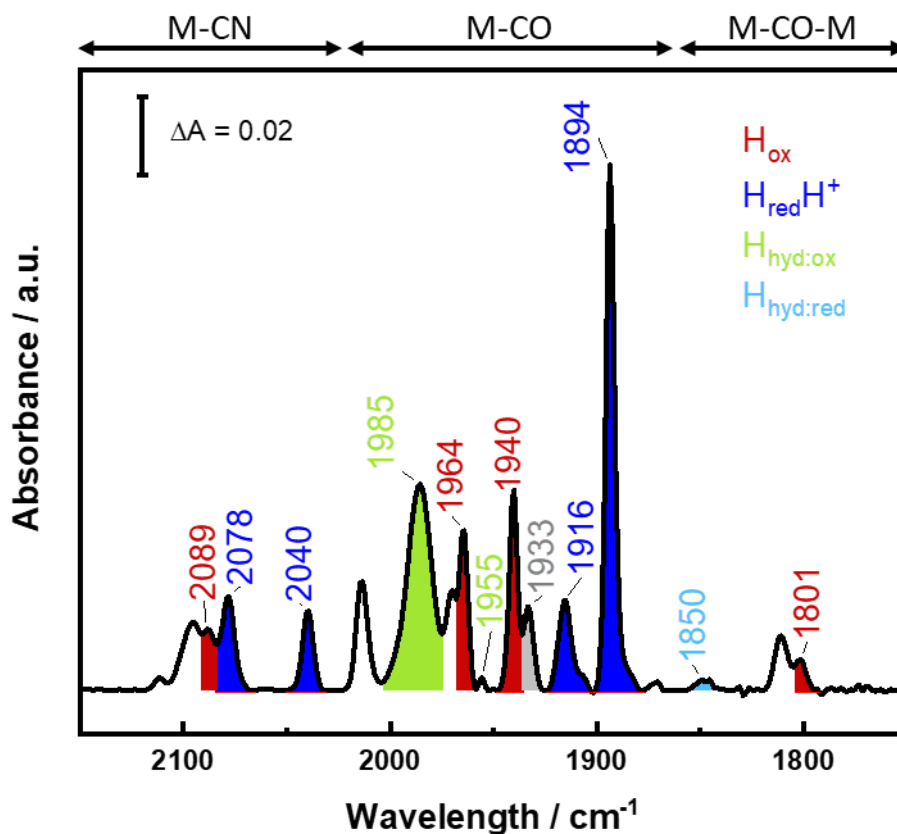


Figure 5.6 The FTIR spectrum of *DdHydAB* crystal after potential poise at -589 mV vs SHE in the presence of 0.5 mM of the redox mediators (anthraquinone-2-sulfonate, benzyl viologen, methyl viologen, and Eu(III)-BAPTA). The FTIR bands from H_{ox} , $H_{red}H^+$, $H_{hyd:ox}$ and $H_{hyd:red}$ are coloured red, blue, light green and cyan respectively.

At -669 mV, the FTIR spectrum gets more complicated (Figure 5.7): a new state $H_{sred}H^+$ appeared (purple peak fitting in Figure 5.7). There are also peaks arising from the H_{ox-CO} state, but for simplicity the peaks from H_{ox-CO} are not marked in the original spectrum. At this potential, the predominant state is still the $H_{red}H^+$ state, shown by the peaks at 2079 , 2040 , 1916 and 1984 cm^{-1} (blue integration in Figure 5.7). The bands from the $H_{hyd:red}$ state are not easy to be individually identified as they overlap with other more intense bands. For example, 1972 cm^{-1} from $H_{hyd:red}$ overlaps with 1970 cm^{-1} of H_{ox-CO} , and the absorption at 2078 cm^{-1} overlaps with the 2079 cm^{-1} band of $H_{red}H^+$ state (which is still the predominate state at -669 mV). Also both $H_{hyd:red}$ and $H_{hyd:ox}$ have absorption at 1956 cm^{-1} , so this band cannot be used to distinguish them. However, the $H_{hyd:red}$ can be

identified by the absorption at 1850 cm^{-1} , while 1985 cm^{-1} is the signature feature of the $H_{\text{hyd:ox}}$ state.

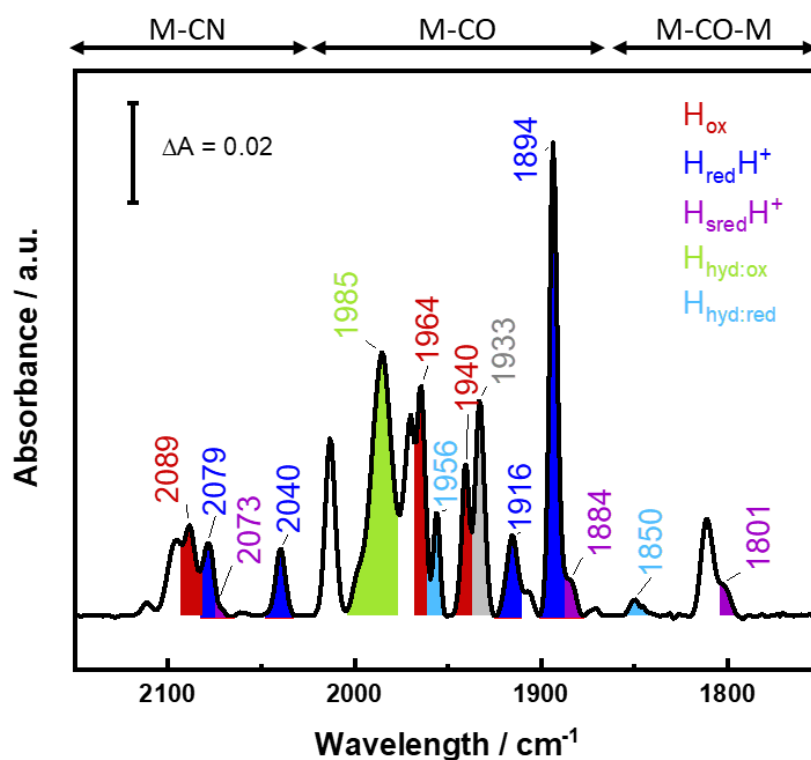


Figure 5.7 The FTIR spectrum of *DdHydAB* crystal after potential poise at -669 mV vs SHE in the presence of 0.5 mM of the redox mediators (anthraquinone-2-sulfonate, benzyl viologen, methyl viologen, and Eu(III)-BAPTA). The FTIR bands from H_{ox} , $H_{\text{red}}H^+$, $H_{\text{sred}}H^+$, $H_{\text{hyd:ox}}$ and $H_{\text{hyd:red}}$ are coloured red, blue, purple, light green and cyan respectively.

For more visible presence of how the state changes at a more negative applied potential, the spectrum taken at -669 mV is subtracted using the spectrum taken at -589 mV as a reference (Figure 5.8). The positive bands at 1850 cm^{-1} and 1985 cm^{-1} show that the population of both $H_{\text{hyd:red}}$ and $H_{\text{hyd:ox}}$ state increases slightly at -669 mV .

From the difference spectrum, a strong peak is shown at 1932 cm^{-1} (grey integration in Figure 5.8). The band at 1932 cm^{-1} was assigned to the $H_{\text{sred}}H^+$ state by Roseboom *et al* in 2006. [192] But later the five peaks of this state were identified in 2020,

as not including the band at 1932 cm^{-1} . [259] It is also present at -589 mV , and co-exists with $\text{H}_{\text{red}}\text{H}^+$. In CrHydA1 at pH 10, the dominant species is the H_{red} state which is identified by this 1933 cm^{-1} band. [264] This raises the question of whether the pH could turn more alkaline in the cell due to the proton reduction at such low potential, resulting in the generation of the non-protonated H_{red} state? However, other bands arising from the H_{red} state are not seen, such as 2083 , 2067 , 1962 and 1791 cm^{-1} .

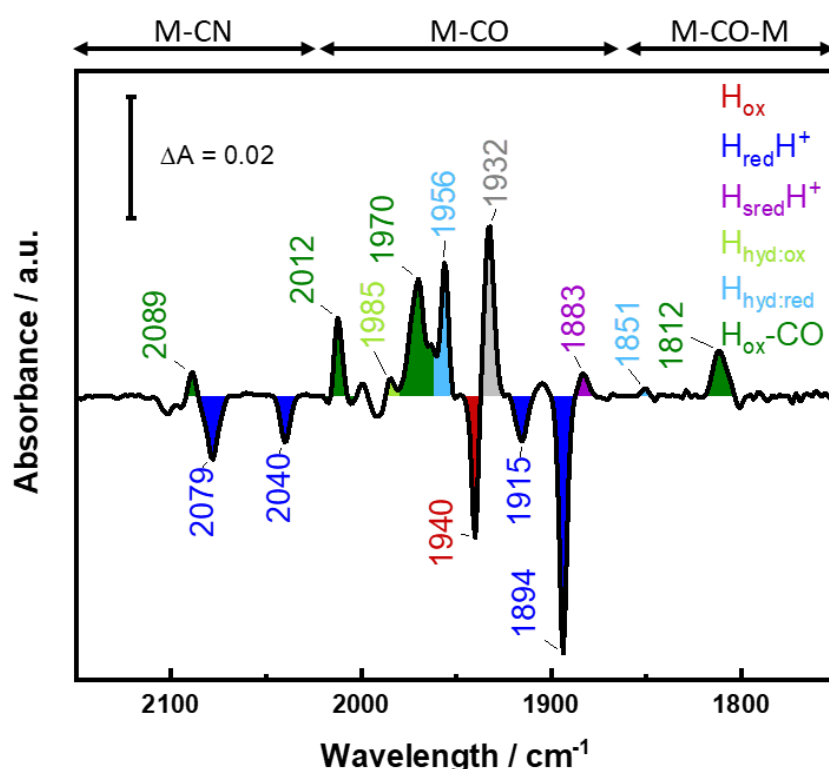


Figure 5.8 The FTIR difference spectrum of *DdHydAB* at -669 mV subtracted using the spectrum taken at -579 mV as a reference. The new bands and existing bands with a stronger absorption are shown with positive absorbances, and *vice versa*. The FTIR bands from H_{ox} , $\text{H}_{\text{red}}\text{H}^+$, $\text{H}_{\text{sred}}\text{H}^+$, $\text{H}_{\text{hyd:ox}}$, $\text{H}_{\text{hyd:red}}$ and $\text{H}_{\text{ox}}\text{-CO}$ states are coloured red, blue, purple, light green, cyan and dark green respectively. A band at 1932 cm^{-1} with an uncertain origin is coloured grey.

The absorption at 1918 cm^{-1} was assigned to the $\text{H}_{\text{sred}}\text{H}^+$ state by Stripp *et al* 2018, but it does not appear in the FTIR spectra here, which could be because that it overlaps the 1916 cm^{-1} peak of the $\text{H}_{\text{red}}\text{H}^+$ state. [253] Hence, the 2nd derivative of the original spectrum collected at -669 mV was processed (Figure 5.9). However, it is still invisible in

the 2nd derivative spectrum. In the 2nd derivative spectrum, there is a shoulder peak at 1925 cm⁻¹, it might be from the H_{sred}H⁺ state, as it is relatively close to the 1922 cm⁻¹ peak that is assigned to H_{sred}H⁺ of CrHydA1 by Lorent. [259] Other features from this two-electron reduced state are shown by the weak absorption at 2070 and 2029 and 1801 cm⁻¹.

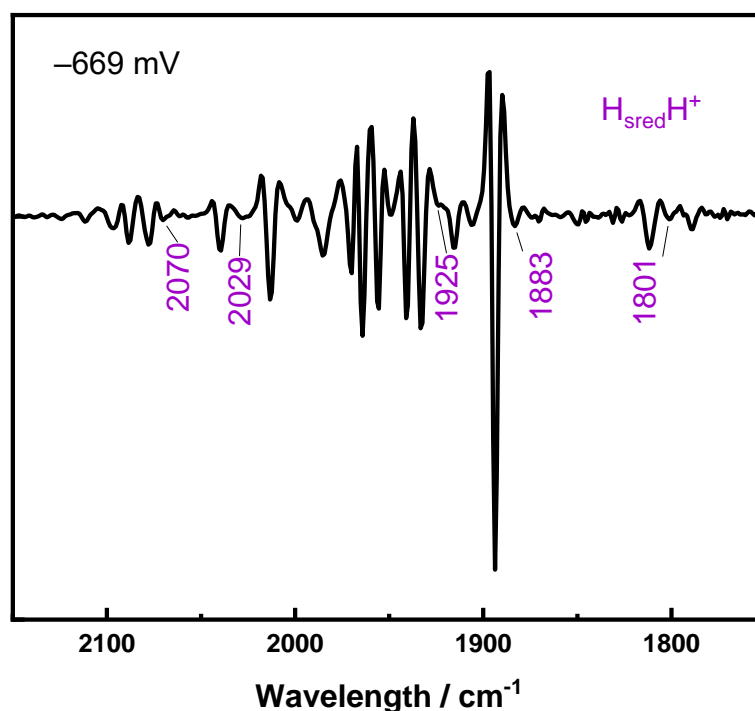


Figure 5.9 The second derivative of the FTIR spectrum of *DdHydAB* crystal after potential poise at -669 mV vs SHE in the presence of 0.5 mM of the redox mediators (anthraquinone-2-sulfonate, benzyl viologen, methyl viologen, and Eu(III)-BAPTA). The FTIR bands from H_{sred}H⁺ state are coloured purple.

The bridging CO in the H_{red}H⁺ and H_{sred}H⁺ states are difficult to perceive at ambient temperature. The bridging CO band of H_{red}H⁺ was not observed at all, while a very weak band at 1801 was observed in the 2nd derivative figure, which is possibly from the H_{sred}H⁺ state. This might be due to a combination of two effects: 1) The bridging CO ligand's coordination geometry is more susceptible to protein dynamics, causing the 1800 cm⁻¹ band to broaden; and 2) the geometry of the bridging CO ligand and the protein surrounding it changes the transition dipole moment, and decreases the probability of

infrared absorption and thus the overall decreased intensity. Protein dynamics are delayed at low temperatures, and a glass transition occurs in the protein revealing the bridging CO band at 1817 and 1801 cm^{-1} of the $\text{H}_{\text{red}}\text{H}^+$ and $\text{H}_{\text{sred}}\text{H}^+$ states respectively. [252, 253]

A noteworthy phenomenon is the appearance of H_{ox} state at -669 mV. The presence of this oxidised state at such negative potential does not seem to make sense. (red peak, 1964 and 1940 cm^{-1}). [262] Referring back to the proposed catalytic cycle, the H-cluster in the $\text{H}_{\text{sred}}\text{H}^+$ state forms a hydride at Fe_d , which, after protonation and H_2 production, returns to the H_{ox} state, completing the catalytic cycle and preparing for another round of electron and proton transfer. [252] The H cluster is regenerated to the H_{ox} state after turnover, which hence is coherent with the presence of the FTIR feature of this state.

From the presence of the H_{ox} state at low potential, a common issue of handling hydrogenase comes into sight. Since protons, the substrate of hydrogenases, are constantly available in aqueous solution, the electrons that enter the enzyme from the working electrode may be employed right away to produce H_2 . If the spectroelectrochemical cell is sealed and gas tight, H_2 will build up until the applied potential equals the H_2/H^+ potential. High H_2 pressure built up at extremely negative potentials, however, might cause deviations from equilibrium according to Eq. 5. 1, where $[\text{H}_2]$ represents for the pressure of H_2 .

$$E = E^0 - \frac{RT}{2F} \ln \frac{[\text{H}_2]}{[\text{H}^+]^2} \quad \text{Eq. 5. 1}$$

It is also observed that the bands from the H_{ox} -CO state increased a lot at lower potential, suggesting that the H clusters were deconstructed, releasing CO which damaged other active sites.

5.3.2 Myoglobin protection of the H cluster

From our observations in the above section, it is apparent that the H_{ox} -CO state can be generated at low potentials, but it may also originate from oxygen damage. Therefore, it is crucial to mitigate such oxygen damage during the experiment. During prolonged experiments, more H clusters can be compromised. Myoglobin, known for its oxygen-binding capacity, was incorporated as a protective measure against possible oxygen damage, providing an opportunity to evaluate its effectiveness in preserving the H cluster integrity over the course of the experiment. In the following section, we demonstrate the impact of protective measures against such damage using myoglobin.

Two overnight redox titrations were performed on *DdHydAB* crystals within the IR Spectroelectrochemical (SEC) cell. The assembly of the cell, along with the buffer and mediators, remained the same as in the previous section. The distinguishing factor in this setup was the addition of 0.4 mM myoglobin in solution to one of the experiment setups.

The comprehensive analysis of the redox titration will be discussed in the subsequent section. In this part, the focus is on the differences between the initial and final spectra of the redox titration process. To this end, the final spectrum of the *DdHydAB* crystal was subtracted from the initial spectrum, resulting in the FTIR difference spectrum presented in Figure 5.10.

This difference spectrum features four negative CN^- and CO stretching bands (depicted as orange integrations in Figure 5.10) at 2106, 2007, 1983, and 1847 cm^{-1} ,

suggesting a single initial H_{inact} state. Following the overnight redox titration, a new dominant species is observed, as evidenced by the strong absorption at 1812 cm^{-1} and the complete disappearance of the CO stretching band at 1847 cm^{-1} . This new state, identified as $H_{\text{ox}}\text{-CO}$, is further signified by five positive peaks at 2096, 2089, 2016, 1972, and 1963 cm^{-1} (indicated as green peak fitting in Figure 5.10). [192]

The $H_{\text{ox}}\text{-CO}$ state shares the same electronic structure as the H_{ox} state, with the addition of an exogenous CO ligand terminally attached to the Fe_d (Figure 5.10 B) [265] Despite strict measures to maintain an anaerobic environment during the experiment, a small amount of oxygen may still infiltrate the cell. Upon exposure to O_2 , the H-cluster in certain enzyme molecules can decompose, liberating free CO ligands. This CO ligand is released once both bonds of the bridging CO with the two Fe atoms are cleaved. Furthermore, aside from oxygen-induced damage, the inevitable prolonged application of potential could also lead to H-cluster disintegration. The freed CO, subsequently, acts as an inhibitor to the remaining active sites, prompting the formation of the $H_{\text{ox}}\text{-CO}$ state. [266, 267] Thus, both oxygen presence and extended potential application times contribute to the generation of this modified H_{ox} state, underscoring the need for careful experimental conditions and effective protective strategies.

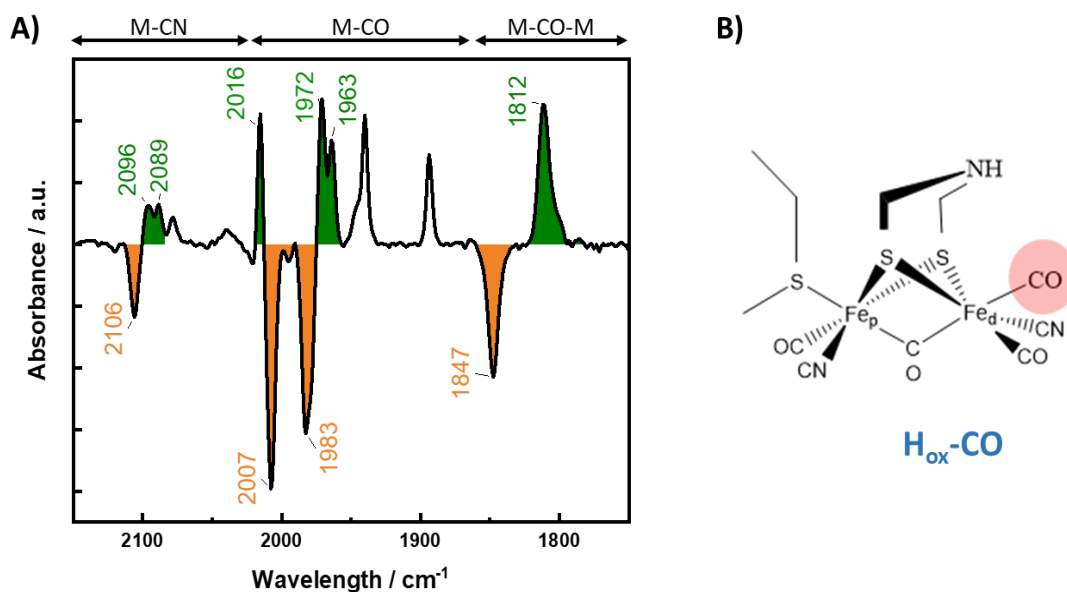


Figure 5.10 A) The FTIR difference spectrum of *DdHydAB* after redox titration subtracted using the first spectrum taken as a reference in the absence of myoglobin. The new bands and existing bands with a stronger absorption are shown with positive absorbances, and *vice versa*. The positive FTIR bands from the H_{ox} -CO state are coloured dark green; and the negative FTIR bands from the H_{inact} state are coloured orange. B) The structure of H_{ox} -CO with an extra exogenous CO ligand terminally attached to Fe_d .

In order to mitigate the formation of this inactive H_{ox} -CO state, myoglobin was incorporated during the redox titration of *DdHydAB* crystals. The binding of carbon monoxide (CO) to myoglobin occurs at a significantly higher rate than its binding to [FeFe] hydrogenase. At pH 7 and 20°C, the rate of CO binding to myoglobin is remarkably fast, with a second-order rate constant of $5 \times 10^5 \text{ M}^{-1} \text{ s}^{-1}$. [268] In contrast, the formation of the [FeFe] hydrogenase-CO complex, within a pH range of 6.5 to 8.5 and 25°C, exhibits a substantially lower rate constant of $5.7 \text{ mM}^{-1} \text{ s}^{-1}$. [269] This indicates that myoglobin binds CO at a rate that is over eight orders of magnitude greater than that of [FeFe] hydrogenase, highlighting the exceptional affinity of myoglobin for CO under these conditions. Damage to some H clusters due to the application of potential is an unavoidable outcome. However, by introducing myoglobin into the cell, the liberated CO is more likely to be captured by myoglobin, rather than the remaining H clusters. This process protects the active sites from inactivation by the CO ligand. Furthermore,

reduced myoglobin (Fe^{II}) potentially acts as an oxygen scavenger, preventing oxygen-induced damage to H clusters.

The FTIR spectra illustrated in Figure 5.11 compares the difference between the starting and ending spectra of the redox titration process in the presence of 0.4 mM myoglobin. The positive peak at 1812 cm^{-1} exhibits an absorbance that is approximately 25% of the intensity of the negative peak at 1847 cm^{-1} . This implies that about a quarter of the H cluster is in the inhibited $\text{H}_{\text{ox-CO}}$ state. Compared to the redox titration conducted without myoglobin, where the H clusters are predominantly in the $\text{H}_{\text{ox-CO}}$ state, the H clusters are better preserved when myoglobin is present. The addition of myoglobin did not result in the appearance of any extra bands in the IR spectra. Consequently, myoglobin will be added as a protective measure in subsequent redox titration experiments with *DdHydAB* crystals.

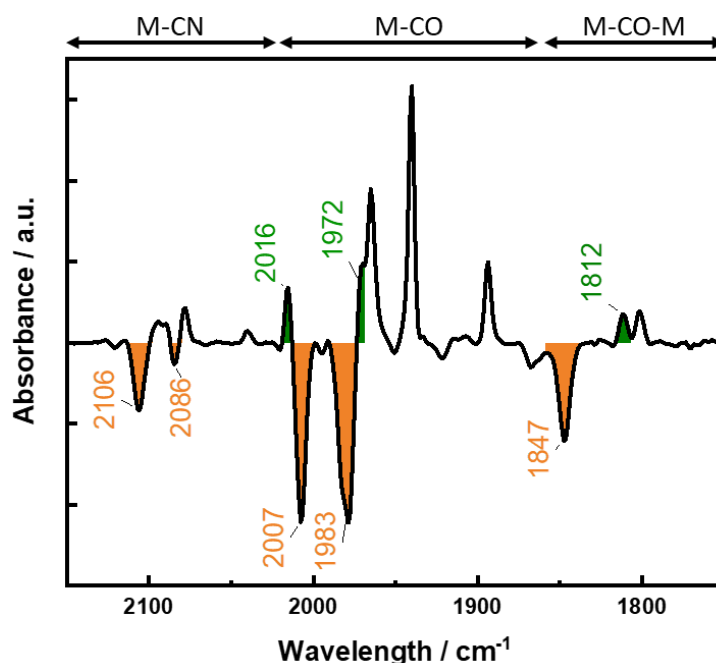


Figure 5.11 The FTIR difference spectrum of *DdHydAB* after redox titration subtracted using the first spectrum taken as a reference *in the presence of myoglobin*. The new bands and existing bands with a stronger absorption are shown with positive absorbances, and *vice versa*. The positive FTIR bands from the $\text{H}_{\text{ox-CO}}$ state are coloured dark green; and the negative FTIR bands from the H_{inact} state are coloured orange.

5.3.3 Conclusion

In this section 5.3, the *DdHydAB* crystals undergo reduction within the IR SEC cell, and their states are analysed using distinctive FTIR features. The presence of $H_{\text{hyd:ox}}$ and $H_{\text{hyd:red}}$ states can be observed at room temperature under dark conditions. At a potential of -589 mV, four states from the catalytic cycle are detected, namely, H_{ox} , $H_{\text{red}}H^+$, $H_{\text{hyd:ox}}$, and $H_{\text{hyd:red}}$, with the $H_{\text{red}}H^+$ state being dominant. When a more negative potential of -669 mV is applied, the $H_{\text{sred}}H^+$ state appears, albeit with the persistence of the H_{ox} state. The population of both $H_{\text{hyd:red}}$ and $H_{\text{hyd:ox}}$ states show a minor increase at -669 mV. Even though the intensity of the $H_{\text{red}}H^+$ state decreases, it remains the dominant species. There is some uncertainty regarding the origin of the band at 1933 cm^{-1} , which might be attributed to the non-protonated H_{red} state.

Additionally, it has been noted that H clusters get damaged at lower potentials, leading to the formation of the CO-inhibited $H_{\text{ox}}\text{-CO}$ state. NaDT-reduced myoglobin was incorporated to bind O_2 or the CO released from the damaged H clusters due to the application of extreme potentials. This method has proven to be effective.

Determining the potentials at which $H_{\text{hyd:ox}}$ and $H_{\text{hyd:red}}$ states begin to appear could be intriguing. If they prevail, it might be possible to estimate their redox potentials. In situ or *in crystallo* redox titration of *DdHydAB* has not been performed before. Therefore, the next section will focus on conducting in situ redox titration of *DdHydAB* crystals within the IR SEC cell.

5.4 Probing the redox states of *DdHydAB* *in crystallo* via IR microspectroscopy Electrochemical IR microspectroscopy of *DdHydAB* crystals under various conditions

Several redox states of the H cluster have been identified using IR spectroscopy or spectroelectrochemistry on enzymes in solution. [252] In this section, the transition between these states will be controlled electrochemically in a single crystal for the first time on *DdHydAB* crystals. The slowed protein dynamics *in crystallo* allows the detection of some bands that are only visible at low temperature, and with the high protein concentrations *in crystallo*, we may record spectra with high signal-to-noise ratios, making it easier to identify the bands of each active site state.

The redox potential of the H_2/H^+ couple is pH-dependent as the proton concentration decreases ten folds when pH increases by 1. According to the Nernst equation, the redox potential decreases by 59 mV at 25 °C with the increase of one pH unit. Proton-coupled electron transfer (PCET) is a crucial process for [FeFe] hydrogenases to catalyse the reversible activation of molecular H_2 . The concerted PCET lowers the kinetic barrier and facilitates the operation of hydrogenase near equilibrium at high turnover rate. [270] How the pH affects the intermediates of the *DdHydAB* catalytic cycle, and the redox potentials of redox couples at the active site, would be interesting to investigate. In this section a redox titration is carried out on a *DdHydAB* single crystal using the electrochemical IR microspectroscopical method (introduced in section 2.6). The challenges and possibility of extending this method to the study of nitrogenases will also be discussed.

5.4.1 Spectroscopic Analysis of Redox-Dependent Changes in *DdHydAB* Crystals

This section focuses on the redox titration of *DdHydAB*, and its spectroscopic response under varying electrochemical potentials. Using chronoamperometry, the potential of a *DdHydAB* single crystal is systematically varied, and the corresponding changes in its FTIR spectra are observed. This approach aims to correlate specific potential levels, ranging from 34 to -566 mV vs SHE, with shifts in the IR absorption peaks.

A redox titration was carried out a *DdHydAB* single crystal, during which the solution potential was determined using chronoamperometry and the IR spectra were taken once the cell had equilibrated. Potentials were sequentially applied to the cell, from 34 to -566 mV vs SHE for a reductive titration, while IR spectra were taken after equilibrium at each potential step. The procedure to assemble the cell and the composition of solution is stated in section 2.6.

The effect of the applied potential of the *DdHydAB* crystal on its FTIR spectra is demonstrated in Figure 5.12. Ten spectra collected from 34 to -566 mV vs SHE are plotted in a 3D representation. It shows that the most intense peak shifts from 1983 to 1940 and then 1894 cm^{-1} as the applied potential is stepped more negative. This is in line with the conversion of the oxidation states in the H cluster. The corresponding states of these absorptions are H_{inact} , H_{ox} and $H_{\text{red}}H^+$ individually, of which the electronic configurations have been demonstrated in scheme 5.3. As the H cluster is reduced, the number of electrons in the d orbital increases, thus the π -backbond is stronger. The strong π -back bonding weakens the CO and CN^- bonds, causing the absorption arising from the CN and CO stretching to be shifted towards the lower wavenumber. The larger redshift of peaks from CO than that from CN^- is on account of CO being a better π -

acceptor. For instance, the two terminal CO ligands at the H_{ox} state have bands at 1964 and 1940 cm^{-1} , which are shifted to 1916 and 1894 cm^{-1} upon one-electron reduction to the $H_{red}H^+$ state. Compared to the *ca* 50 cm^{-1} redshift of CO peaks, the two terminal CN^- peaks only shift *c.a.* 9 and 29 cm^{-1} respectively upon reduction. Hence, the absorbance change of the CO peaks is a practical measurement to detect the variation of the oxidation states of the H cluster.

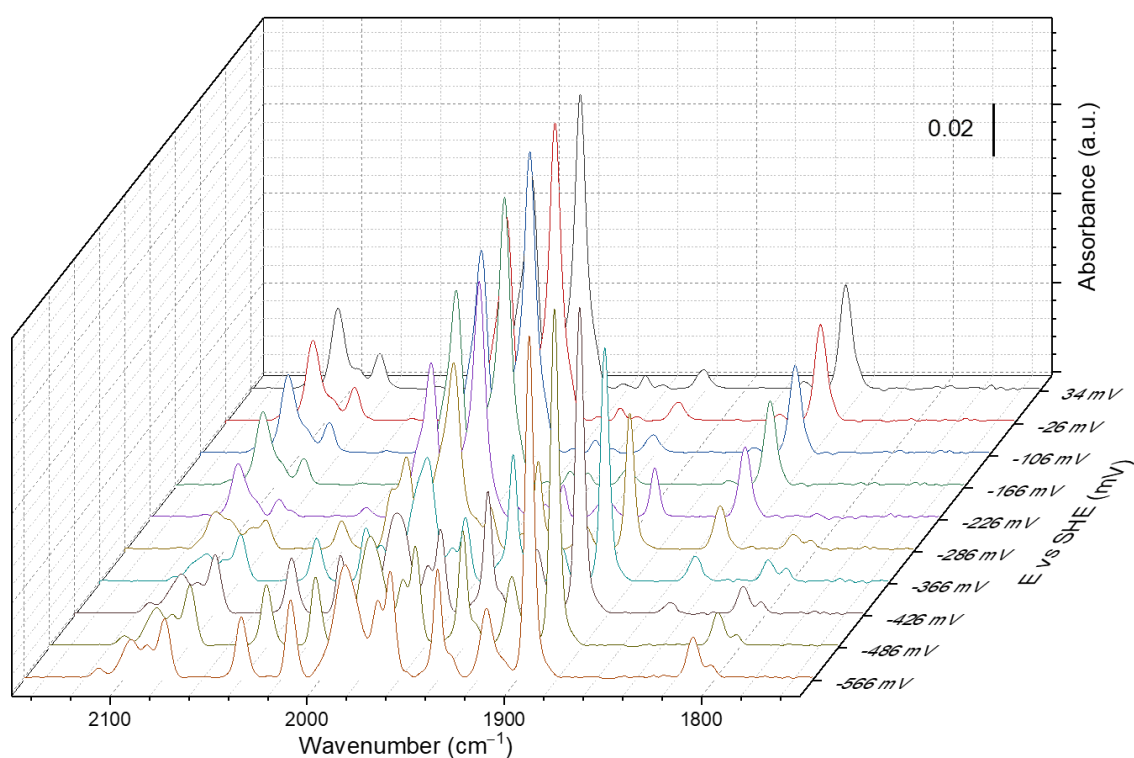


Figure 5.12 A 3D representation of FTIR spectra of *DdHydAB* single crystal. These ten spectra were collected from 34 to -566 mV vs SHE using the electrochemical IR microspectroscopic cell.

5.4.2 The nature of 1933 cm^{-1} band

This section examines the origin of the absorption band at 1933 cm^{-1} . While this band has been previously attributed to the H_{red} state in *CrHydA1* at pH 10, its applicability to *DdHydAB* remains uncertain. The analysis aims to determine if the 1933 cm^{-1} band is indicative of the same state in *DdHydAB*.^[261]

The change of the 1933 cm^{-1} band is compared with the 1894 cm^{-1} band from the $\text{H}_{\text{red}}\text{H}^+$ state. The absorbance of these bands is plotted against potential (Figure 5.13). A reductive titration was carried out on the *DdHydAB* crystal from -79 mV to -639 mV with 20 mV intervals, at pH 8 (blue area in Figure 5.13), followed with an oxidative titration that reversed the applied potentials on the same single crystal (purple area in Figure 5.13). During the reductive titration, the 1933 cm^{-1} band starts to show at -519 mV after the first appearance of $\text{H}_{\text{red}}\text{H}^+$ at -379 mV. During the following oxidative titration, the intensity of the 1933 cm^{-1} and 1894 cm^{-1} bands shows a discernibly similar trend.

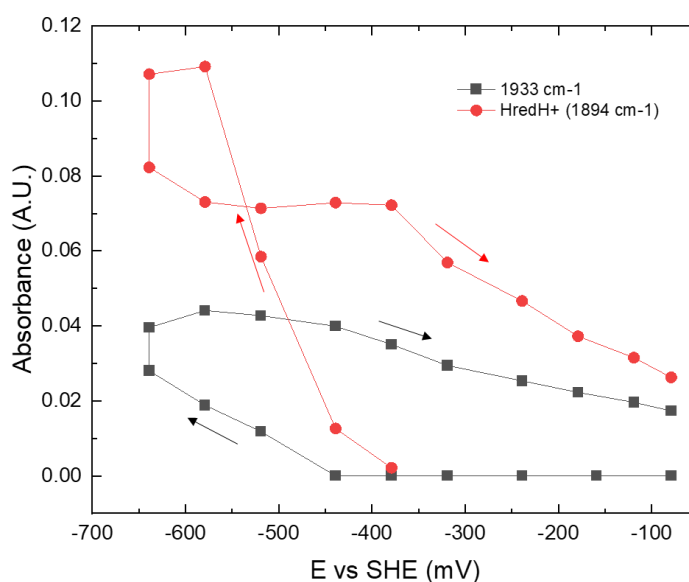


Figure 5.13 The variations of the absorbance at 1894 cm^{-1} and 1933 cm^{-1} against potential. The band at 1894 cm^{-1} represents the $\text{H}_{\text{red}}\text{H}^+$ state, while the origin of the 1933 cm^{-1} will be discussed in later text. A reductive redox titration is conducted over the first 12 h from -79 to -639 mV, followed by an oxidative titration on the same crystal from -639 mV to -79 mV.

The 1933 cm^{-1} band was previously assigned to the H_{red} state which is the unprotonated form of the $\text{H}_{\text{red}}\text{H}^+$ state and populates at high pH. [261] With a pK_a of $\text{H}_{\text{red}}\text{H}^+$ at *ca* 9.5, the H_{red} state is expected to be observed at this pH unless the pH has increased during the titration. [252] The 1933 and 1891 cm^{-1} bands at pH 10 in CrHydA1 show

identical behaviour as a function of the electrochemical potential, which is also observed here. [261] At this stage, the 1933 cm^{-1} is assigned to the H_{red} state hypothetically. The $H_{\text{red}}H^+$ and H_{red} states together constitute the one-electron reduced cluster from the H_{ox} state. The contribution from the hypothesised H_{red} state to the one-electron reduced form is 15% at -579 mV during the reductive titration and increased to 40% during the subsequent oxidation at the same potential. As [FeFe] hydrogenases are well-known for their extremely high efficiency in proton reduction (1000 s^{-1})[184], the pH could potentially increase in this small volume of solution ($5\text{ }\mu\text{L}$ on the working electrode) due to the rapid proton reduction. Besides, the 1933 cm^{-1} band is more intense at pH 8 than at pH 7 at the same applied potential, while not present at pH 5 and 6. Thus, the band at 1933 cm^{-1} is assigned safely to CO stretching of the H cluster at the H_{red} state.

5.4.3 The reversibility of H-cluster states

The reversibility of formation of the oxidation states of the *DdHydAB* H-cluster *in crystallo* was examined by re-oxidising the H-cluster that was reduced during the reductive redox titration. A potential of -650 mV vs SHE was applied to the *DdHydAB* crystal in the cell for about 1 h to reduce the H cluster in *DdHydAB*. Then potentials were applied gradually from -639 mV to -79 mV vs SHE to reoxidise the crystal, while IR spectra were taken after equilibrium at each potential step. The absorbances at 1940 cm^{-1} and 1984 cm^{-1} were plotted against applied potential to track the population of H_{ox} state and the $H_{\text{red}}H^+$ state separately. Figure 5.14 shows the variation of the H_{ox} and the $H_{\text{red}}H^+$ states during the oxidative process.

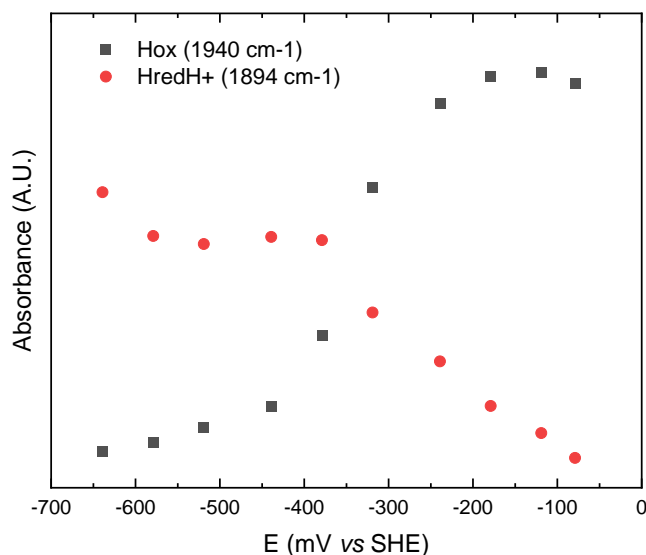
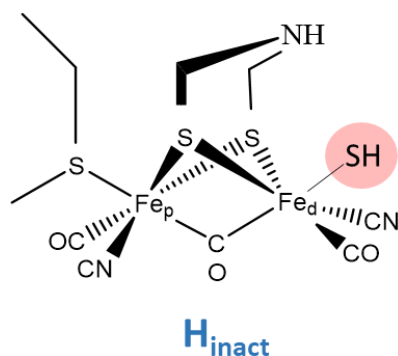


Figure 5.14 The variation of the H_{ox} and the H_{red}H⁺ states during the oxidative titration on the DdHydAB crystal. It is illustrated by the plot of FTIR absorbance at 1940 cm⁻¹ (H_{ox}) and 1894 cm⁻¹ (H_{red}H⁺) respectively against applied potential.

The H_{red}H⁺ and H_{ox} states are reversibly interconverted: they both recovered their concentrations after the gradual application of positive potentials. The midpoint potential for the H_{ox}/H_{red}H⁺ couple measured during this reoxidation is -350 mV. This is much more positive than the potential measured during the reductive titration, -516 mV. This suggests a kinetically slow step in the re-formation of the H_{ox} state *in crystallo*.

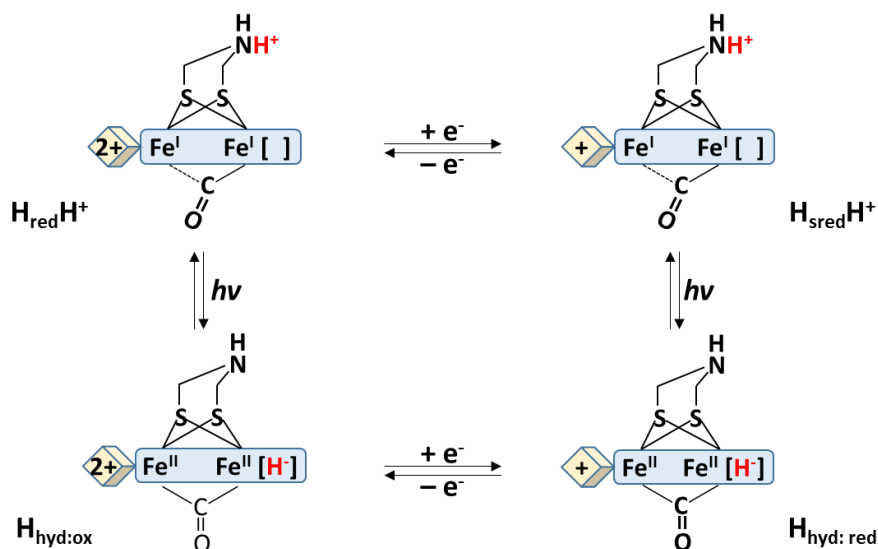
In solution the H_{trans} and H_{inact} states cannot be recovered once the cluster is activated to the H_{ox} state. [256, 271] This is consistent with the irreversible release of HS- bound to the distal Fe_d (Scheme 5.4). [257] Since *in crystallo* diffusion may be slowed and the lost HS- ligand could be trapped in the crystal, it raises the possibility of a reversibility of the H_{trans} and H_{inact} states. However, it is also observed that H_{trans} and H_{inact} states were not recovered during the oxidative titration *in crystallo* even with an applied potential as positive as -80 mV, which is the same as in the solution. [256, 271]



Scheme 5.4 SH- ligand (red circle) of the H_{inact} releases upon the formation of the H_{ox} state

5.4.4 Detecting the $H_{\text{hyd:ox}}$ and $H_{\text{hyd:red}}$ states of *DdHydAB in crystallo*

$H_{\text{hyd:ox}}$ and $H_{\text{hyd:red}}$ states are the photo-enriched tautomers of the $H_{\text{red}}H^+$ and $H_{\text{sred}}H^+$ states; the conversion of these four states is shown in Scheme 5.5. Upon one-electron reduction on the H cluster at the $H_{\text{red}}H^+$ state, it is reduced to the $H_{\text{sred}}H^+$ state. The hydride forms are enriched at low temperatures (110 K) and illumination (460 nm), and the parent states ($H_{\text{red}}H^+$ and $H_{\text{sred}}H^+$) can be regained by relaxation in the dark. [90] The experiment in this section is carried out in the dark, and portions of the states with hydride are also observed.



Scheme 5.5 The photoreaction between the $H_{\text{red}}H^+ / H_{\text{hyd:ox}}$ and $H_{\text{sred}}H^+ / H_{\text{hyd:red}}$ couples, and the redox reaction between the $H_{\text{red}}H^+ / H_{\text{sred}}H^+$ and the $H_{\text{hyd:ox}} / H_{\text{hyd:red}}$ couples

The $H_{\text{hyd:red}}$ and $H_{\text{hyd:ox}}$ states are individually identified with the absorption at 1850 and 1985 cm^{-1} according to the work by Lorent *et al.*, and the reasons for the assignment of these peaks has been illustrated in section 5.3. [259] Both $H_{\text{hyd:red}}$ and $H_{\text{hyd:ox}}$ have absorption at 1956 cm^{-1} , so normally this band cannot be used to distinguish them. However, during the titration, it is found that the $H_{\text{sred}}H^+$ state has a very negative formation potential and did not accumulate in the applied potential range. This is observed in *DdHydAB* as a result of the redox anticooperativity between clusters while not in *CrHydA1*. [258] Thus *DdHydAB* may not be a good candidate to study the $H_{\text{hyd:red}}$ and $H_{\text{sred}}H^+$. As $H_{\text{hyd:red}}$ is the tautomer of the $H_{\text{sred}}H^+$ state that is only enriched at low temperatures and with illumination, it is barely observed at the experimental conditions (room temperature and in the dark). Because of the extremely low contribution from the $H_{\text{hyd:red}}$ state, the 1956 cm^{-1} band is primarily from the $H_{\text{hyd:ox}}$ state.

The variations of the $H_{\text{hyd:ox}}$ and $H_{\text{red}}H^+$ states against time are drawn in Figure 5.15. A reductive redox titration was conducted from -79 to -639 mV , followed by an oxidative titration on the same crystal. The $H_{\text{hyd:ox}}$ state exists in a more negative potential range, from -519 mV to -639 mV during the reductive titration, which is -379 mV to -639 mV for $H_{\text{red}}H^+$. During the oxidative titration, the $H_{\text{hyd:ox}}$ state exists from -639 mV to -319 mV , while there the $H_{\text{red}}H^+$ state remained at -79 mV . The appearance of the $H_{\text{red}}H^+$ state at a relatively positive potential might account for a more sluggish oxidative titration process than the initial reductive titration.

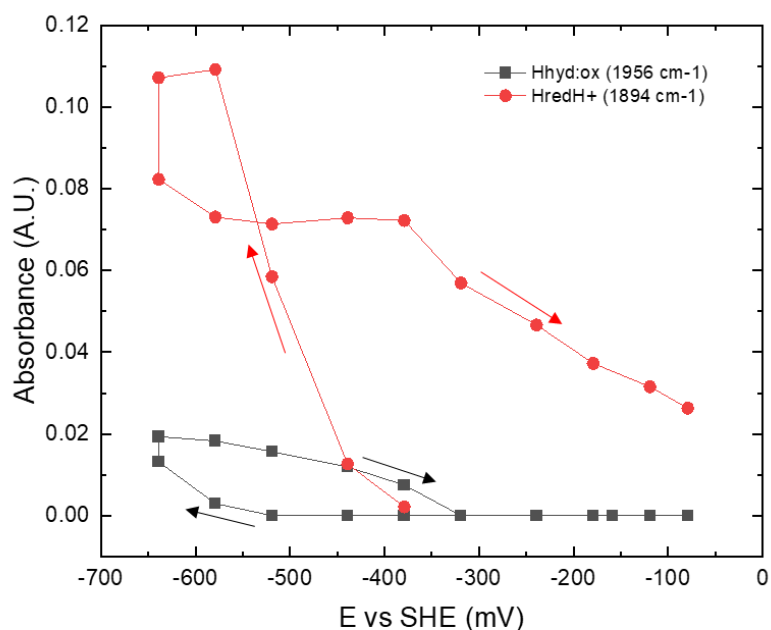


Figure 5.15 The variations of the $H_{\text{hyd:ox}}$ and $H_{\text{red}}H^+$ states against potential, which are determined based on the FTIR absorbance at 1956 and 1894 cm^{-1} respectively. A reductive redox titration was conducted over the first 12 h from -79 to -639 mV, followed by an oxidative titration on the same crystal from -639 mV to -79 mV.

5.4.5 The pH dependency of the midpoint potentials of the *DdHydAB in crystallo*

The proton serves as the fundamental agent in the reduction catalysis performed by *DdHydAB*. This is because of proton coupled electron transfer, a mechanism that forms the core of many bioenergetic processes. This specific process allows the proton and electron to transfer together, thereby leading to reactions that would otherwise be energetically unfavourable. Consequently, the redox potential, which is critical for driving these reactions, is intrinsically dependent on the pH. To understand the impact of pH on the redox potential, and subsequently, on the catalytic performance of *DdHydAB*, it is important to conduct a redox titration under a variety of pH conditions. This can reveal valuable insight into how pH influences the redox potential for different oxidation states of *DdHydAB*.

The pH of the environment could also affect the intermediates generated during the catalytic cycle. These intermediates play a crucial role in the overall reaction mechanism. Their stability, form, and function could vary significantly with pH, leading to a shift in the reaction kinetics and mechanism. This makes pH a crucial factor to consider when examining reduction catalysis by *DdHydAB*. It can fundamentally shape the redox reactions, the catalytic cycle, and the behaviour of intermediates. Therefore, gaining a deeper understanding of the interplay between pH and these biochemical processes could provide critical insights into the behaviour and optimisation of such catalytic systems. Consequently, a redox titration was conducted under various pH conditions to assess the influence of pH on the redox potential of *DdHydAB* in its different oxidation states. This investigation also sought to determine whether pH has any effect on the intermediates present during the catalytic cycle of *DdHydAB*.

Redox titration was performed on *DdHydAB* crystals at various pH values (pH 5, 6, 7, and 8) in the IR microspectroscopy electrochemical cell. The *DdHydAB* crystal, in the H_{inact} state, was subjected to a reductive titration ranging from -79 mV to -639 mV, with intervals of 20 mV. This was followed by an oxidative titration, which reversed the applied potentials on the same single crystal. Details regarding cell assembly and solution composition can be found in Section 2.6. At each pH level, the IR absorbances corresponding to each oxidation state of the H cluster were plotted against the applied potential, as depicted in Figure 5.16. This was done to illustrate the correlation between the population of a specific oxidation state and the applied potential. The oxidation states H_{inact} , H_{ox} , H_{red} , $H_{\text{red}}H^+$, and $H_{\text{sred}}H^+$ are distinguishable through absorbances at 1983 cm^{-1} , 1940 cm^{-1} , 1933 cm^{-1} , 1894 cm^{-1} , and 1883 cm^{-1} , respectively, unless otherwise stated.

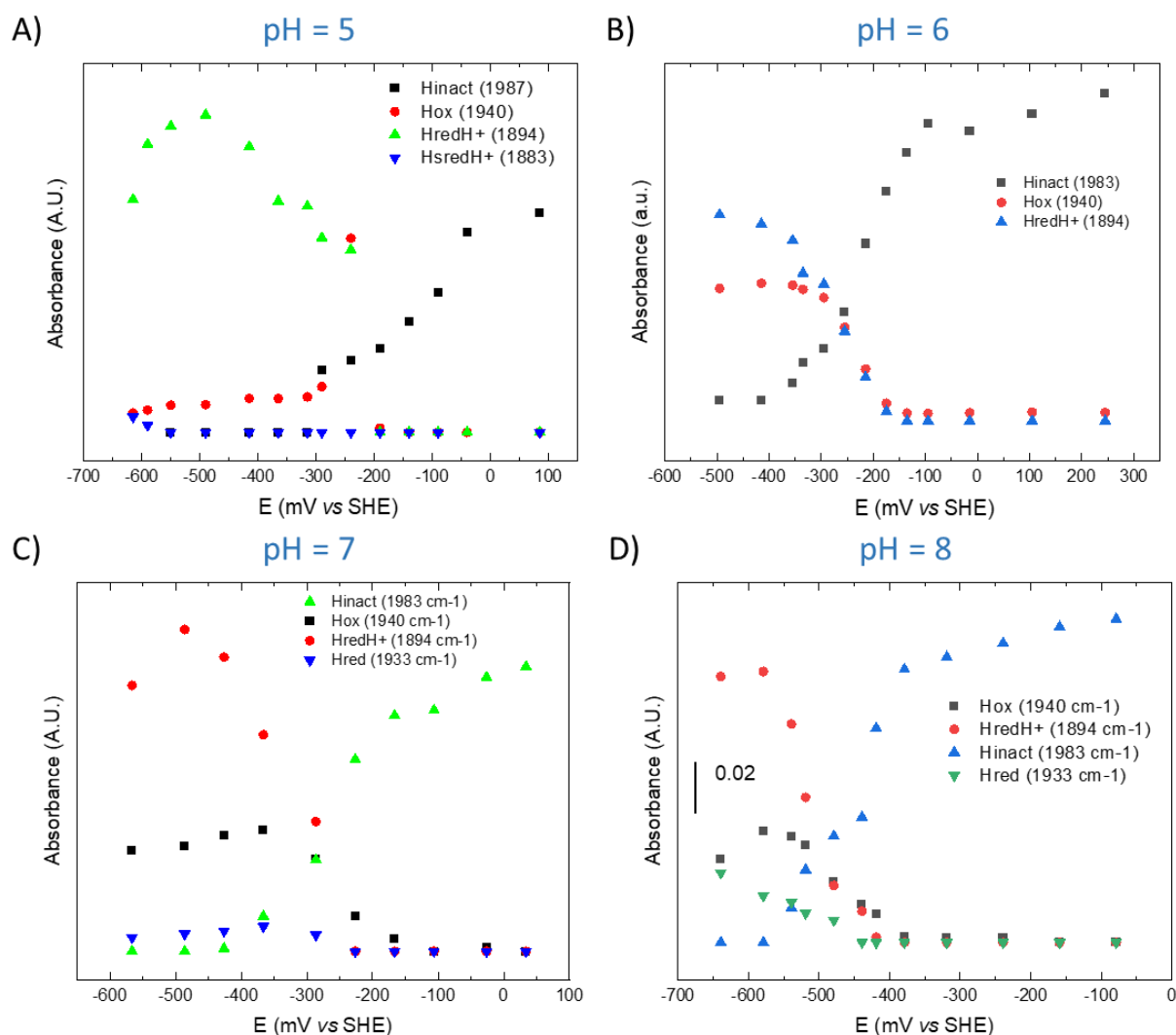


Figure 5.16 Correlation between IR absorbance and applied potential at various pH levels for different oxidation states of the H Cluster in *DdHydAB* in crystallo. The distinct oxidation states H_{inact} , H_{ox} , H_{red} , H_{redH^+} , and H_{sredH^+} are identified by their characteristic absorbance peaks at 1983 cm^{-1} , 1940 cm^{-1} , 1933 cm^{-1} , 1894 cm^{-1} , and 1883 cm^{-1} , respectively.

The H_{ox} state refers to the active state of *DdHydAB* after the H_{inact} state has been reduced by one electron. This state was extensively examined by Senger *et al.*, who discovered that when enzyme samples are subjected to acidic conditions ($pH < 4$) and a high concentration of the reductant dithionite (at least 10 mM), the IR spectra of $H_{ox}H$ shows the emergence of a unique species. This species is characterised by an up-shift of 4-6 cm^{-1} for all terminal ligand bands and up to 10 cm^{-1} higher values for the bridging CO ligand. [272] The production of this species is notably pH-dependent and can be fully

reversed when the pH is increased to alkaline conditions, leading to its designation as $H_{ox}H$.

In the current experiment, however, the $H_{ox}H$ state was not observed. This section involved a redox titration performed at a lower pH boundary of 5, and the concentration of dithionite was kept low (< 1 mM). These experimental conditions likely account for the absence of the up-shift characteristic of the $H_{ox}H$ state within the pH range where the redox titration was conducted.

At pH 5, the H_{ox} state exhibits a rapid rise in concentration at -240 mV and a sudden decrease in concentration from -290 mV when the accumulation of $H_{red}H^+$ commences, as depicted in Figure 5.16 A. Besides this unique behaviour at pH 5, the H_{ox} state gradually starts to emerge with the decreasing applied potential at pH levels of 6, 7, and 8. Thus, it appears that the manifestation and characteristics of the H_{ox} state are profoundly influenced by the pH and the concentration of the applied reductant.

At pH 5 and pH 6, the 1933 cm^{-1} band indicative of the H_{red} state is not prominently observed. However, a significant change is noted at pH 7 and pH 8. Here, the 1933 cm^{-1} band characteristic for the H_{red} state begins to emerge at the same potential as the 1894 cm^{-1} band that is distinctive of the $H_{red}H^+$ state. Despite this simultaneous emergence, the protonated $H_{red}H^+$ state is notably less populated than the H_{red} state at pH 7 and 8.

At pH 7, the 1933 cm^{-1} band characteristic of the H_{red} state emerges at -275 mV. This applied potential shifts to -415 mV at pH 8, marking a significant difference. Additionally, at pH 8, the maximum absorbance of the $H_{red}H^+$ state reaches -580 mV, a considerably more negative potential compared to -500 mV at pH 7.

Investigation across the entire pH range reveals that the absorbance originating from the $H_{\text{sred}}H^+$ state is notably weak, a factor that hinders the identification of a distinct pattern of change. Despite this limitation, a general trend emerges upon close observation: the necessity for more negative potentials for the $H_{\text{sred}}H^+$ state to accumulate becomes evident under increasingly alkaline conditions.

This implies that as the environmental pH increases, the energy requirement for transitioning into the $H_{\text{sred}}H^+$ state also increases, thus necessitating the application of more negative potentials. This interplay between pH and applied potential, and their influence on the dominance of specific states within the H-cluster of *DdHydAB*, indicates the criticality of both factors in these biochemical processes.

Adding to this complexity is the role of the proximal F-cluster and the [4Fe-4S] site of the H-cluster. The interaction between these two elements appears to have destabilising effects on states where both are reduced, specifically, the $H_{\text{sred}}H^+$ and $H_{\text{hyd:red}}$ states. This destabilisation prompts a shift in the balance of states. Irrespective of the pH, the $H_{\text{red}}H^+$ state assumes dominance near the equilibrium H_2/H^+ potential.

Interestingly, this behaviour seems to be unique to *DdHydAB* and *CpHydA1*, as indicated by reference, [258] which both possess accessory F-clusters. This fact suggests the pivotal role of these F-clusters in the mechanism of the enzyme, further solidifying their importance in understanding the intricacies of the system's redox chemistry.

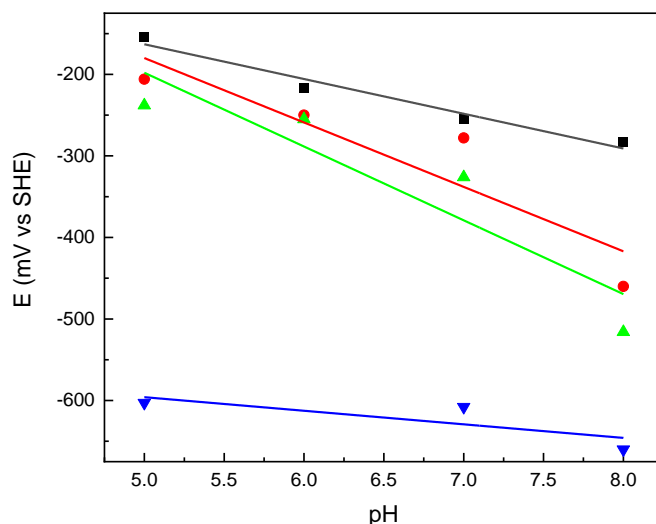


Figure 5.17 The pH dependency of the midpoint potentials of the *DdHydAB in crystallo*

The pH dependence of the midpoint potentials, spanning from pH 5 to 8, has been charted based on the absorbance observed from different states. Due to the difficulty in discerning the H_{trans} state in the collected spectra, the midpoint potentials of the $H_{\text{inact}}/H_{\text{trans}}$ (represented by black squares) and $H_{\text{trans}}/H_{\text{ox}}$ (represented by red circles) couples were gauged by the changes in absorbance of the H_{inact} and H_{ox} states, respectively.

Across all examined pH values, the absorbance from the $H_{\text{sred}}H^+$ state remains notably weak. This state only begins to appear at -669 mV at pH 8, and even then, the absorption remains minimal. The midpoint potential of the $H_{\text{sred}}H^+$ state is challenging to estimate; the blue line in the Figure 5.17 illustrates the pH-dependent potential where the 1883 cm^{-1} band, characteristic of the $H_{\text{sred}}H^+$ state, first emerges.

The midpoint potentials of the H cluster states display a marked dependence on pH. As the pH escalates, the midpoint potentials correspondingly decrease. The midpoint potential of the $H_{\text{inact}}/H_{\text{trans}}$ couple drops by 43 mV per pH unit. Meanwhile, the dependencies for the $H_{\text{trans}}/H_{\text{ox}}$ and $H_{\text{ox}}/H_{\text{red}}H^+$ couples are -79 mV and -90 mV per pH unit,

respectively. Also, the potential at which the $H_{\text{red}}H^+$ state is first observed decreases at a rate of 17 mV per pH unit. These findings demonstrate the interplay between pH and the electrochemical properties of the enzyme states, ultimately impacting the catalytic behaviour of the system.

5.5 Conclusion

In this chapter, the O_2 -stable H_{inact} state of *DdHydAB* was successfully reproduced *in vitro* using a combination of sulfide and oxidant, a finding confirmed by FTIR spectroscopy. This state, when formed *in crystallo* (crystalline form), was shown to be reactivatable upon reduction in an IR SEC cell. The chapter further delves into the investigation of the reduced states of *DdHydAB* using IR spectroelectrochemical methods, with a focus on their distinct FTIR features.

Additionally, a methodology to shield the H cluster from oxygen damage and prevent the formation of the $H_{\text{ox}}\text{-CO}$ state is explored. The effects of pH on the intermediates of the *DdHydAB* catalytic cycle, and the redox potentials of the redox couple, present intriguing areas of study. Redox titration of *DdHydAB* single crystal, employing electrochemical IR microspectroscopy, identified the band at 1933 cm^{-1} as corresponding to CO stretching of the H cluster in the H_{red} state.

A key observation was the reversibility of the oxidation states of the *DdHydAB* H-cluster *in crystallo*. Following reductive redox titration, the transitions involving the $H_{\text{red}}H^+$ and H_{ox} states were found to be reversible, regaining their original concentration upon the gradual application of positive potentials. In contrast, the H_{trans} and H_{inact} states did not revert to their original form during oxidative titration *in crystallo*, even under conditions similar to those in solution, indicating a unique aspect of these states.

The study also covered the photo-enriched tautomers $H_{\text{hyd:ox}}$ and $H_{\text{hyd:red}}$ states of *DdHydAB in crystallo*. It was found that the $H_{\text{hyd:red}}$ state does not accumulate significantly, and the $H_{\text{hyd:ox}}$ state appears at a more negative potential than the $H_{\text{red}}H^+$ state. Notably, the $H_{\text{ox}}H$ state was not observed, even at pH 5.

The formation of $H_{\text{red}}H^+$ and $H_{\text{hyd:red}}$ states of *DdHydAB* in solution is challenging, but these states were observable in crystal due to slower dynamics and higher protein concentration. Applying a sufficiently negative potential, given the high concentration and slower dynamics, resulted in the enrichment of these states, facilitating more intensive study. This approach shows promise particularly for studying hydrogenases with accessory [4Fe-4S] clusters, where such states are less enriched due to redox anticooperativity. Moreover, it could also aid in the observation of catalytic intermediates with short lifetimes, formed during the reduction of N_2 by nitrogenase.

Finally, the impact of pH on the redox states and potentials of *DdHydAB* was studied through redox titration under different pH values. This revealed that proton reduction leads to a mixture of states, also causing a pH increase in a small volume cell. Identifying ways to suppress proton reduction and integrating a flow system to maintain stable pH during experiments could offer valuable insights, particularly for studies on hydrogenases and nitrogenase in the future.

Looking to the future, the possibility of IR spectro-electrochemical experiments becomes even more significant. These experiments can be tailored to specific conditions, such as varying pH values, the addition of external inhibitors, or using altered forms of the enzyme. Such modifications, particularly those affecting the active site metal cofactor or nearby amino acids, open new avenues for investigation. [139, 273] A

key example is the substitution of propane-1,3-dithiolate (PDT) for the natural ADT ligand. This change, which prevents protonation at the bridgehead atom of the PDT ligand, effectively renders the $[2\text{Fe}]_{\text{H}}$ subcluster redox quiet. [139] As a result, focus can be shifted more towards understanding the electron transfer activities at the $[4\text{Fe-4S}]_{\text{H}}$ subcluster.

Chapter 6 Conclusion

The present thesis has developed and refined spectroelectrochemical methodologies that have expanded our capacity to study redox-active proteins, particularly those containing iron-sulfur (FeS) clusters. The development of the UV-Vis spectroelectrochemical cell (UV-Vis SEC) and the subsequent refinement to electrochemical infrared microspectroscopy (ECIRM) have been instrumental in dissecting the complex redox dynamics of proteins such as nitrogenases, nitrogenase homologues, and [FeFe] hydrogenase.

In Chapter 3, the development of the UV-Vis spectroelectrochemical cell (UV-Vis SEC) marked an advancement in the study of FeS proteins. This UV-Vis cell facilitated *in situ* UV-Vis spectral analysis of small volume samples, enabling the detailed examination of redox states in proteins such as NifH and AnfH. It was shown that AnfH, like NifH, could adopt the all-ferrous state in the [4Fe-4S] cluster, a finding of significant importance for understanding the redox properties of these proteins. The research elucidated the stability of the all-ferrous state under various conditions, including the influence of pH, temperature, and nucleotides like MgATP and MgADP. The findings also highlighted the limitations of traditional redox mediators like Eu(II)-DTPA in the presence of nucleotides, underscoring the need for the development of new, colourless mediators for accurate redox potential measurements in a low potential range.

Chapter 4 expanded the scope of the research to include the redox behaviours of nitrogenase homologues, dark operative protochlorophyllide oxidoreductase (DPOR), specifically the L₂ and N₂B₂ proteins. The chapter detailed the challenges encountered in reducing these proteins to the all-ferrous state using Eu(II)-DTPA and the development of a potentiometric titration method for ferredoxin. The mixed results obtained from the UV-

Vis SEC and potentiometric methods for the L₂ protein highlighted the complexity of dissecting redox potentials in these systems. The redox potential of the N₂B₂ protein remained elusive due to its size and instability, emphasising the need for innovative approaches such as an EPR-coupled potentiometric method. The research also explored the catalytic activity of the N₂B₂ protein in solution phase or surface immobilised conditions, providing insight into the reduction of Pchlide and the role of the L₂ protein in this process.

Chapter 5 studied the [FeFe] hydrogenase from *Desulfovibrio desulfuricans* (*DdHydAB*) using ECIRM. The O₂-stable H_{inact} state of *DdHydAB*, was successfully reproduced *in vitro* and its reduced states was examined using IR spectroelectrochemical methods. The research identified the reversibility of the oxidation states of H-cluster *in crystallo* and the impact of pH on the redox states and potentials of *DdHydAB*. The study also explored the formation of photo-enriched tautomers H_{hyd:ox} and H_{hyd:red} states of *DdHydAB in crystallo*, revealing unusual aspects of these states. As has been noted for NiFe hydrogenases previously in the group, the research highlighted the potential for enriching certain states in crystals of FeFe hydrogenase, due to slower dynamics and higher protein concentration, which could be particularly useful for studying hydrogenases with accessory [4Fe--4S] clusters. The impact of pH on proton reduction and the development of strategies to maintain stable pH during experiments were also discussed, offering valuable insight for future studies on hydrogenases and nitrogenase.

In summary, this thesis has made contributions to the understanding of redox properties and mechanisms in metalloproteins. The development of UV-Vis SEC and ECIRM methodologies has opened improved avenues for probing complex redox systems. The research has not only enriched our understanding of the redox

characteristics of FeS proteins but also emphasised the critical need for innovative tools to accurately dissect these mechanisms. The findings have implications for understanding the role of redox states in the catalytic activity and catalytic mechanisms of metalloproteins.

Looking to the future, the research presented in this thesis lays the foundation for further investigations into the redox properties of metalloproteins. The development of novel redox mediators, detailed investigations of nucleotide-bound redox titrations, and the exploration of proteins like AnfH and *DdHydAB* under various conditions will be crucial for gaining deeper insight into their redox properties and biological functions. The integration of advanced spectroelectrochemical techniques with tailored experimental conditions will continue to be a powerful approach for studying the intricate mechanisms of redox proteins, paving the way for future discoveries in biocatalysis.

References

1. Pandelia, M.E., N.D. Lanz, S.J. Booker, and C. Krebs, *Mossbauer spectroscopy of Fe/S proteins*. *Biochim Biophys Acta*, 2015. **1853**(6): p. 1395-405.
2. Cammack, R., *Iron—sulfur clusters in enzymes: Themes and variations*. *Advances in Inorganic Chemistry*, 1992. **38**(C): p. 281-322.
3. Johnson, D.C., D.R. Dean, A.D. Smith, and M.K. Johnson, *Structure, function, and formation of biological iron-sulfur clusters*. *Annual Review of Biochemistry*, 2005. **74**: p. 247-281.
4. Beinert, H., J. Meyer, and R. Lill, *Iron–Sulfur Proteins*, in *Encyclopedia of Biological Chemistry*, W.J. Lennarz and M.D. Lane, Editors. 2004, Elsevier: New York. p. 482-489.
5. Weiss, M.C., et al., *The physiology and habitat of the last universal common ancestor*. *Nature Microbiology*, 2016. **1**(9): p. 16116.
6. Raanan, H., et al., *Small protein folds at the root of an ancient metabolic network*. *Proceedings of the National Academy of Sciences*, 2020. **117**(13): p. 7193-7199.
7. Nitschke, W., S.E. McGlynn, E.J. Milner-White, and M.J. Russell, *On the antiquity of metalloenzymes and their substrates in bioenergetics*. *Biochimica et Biophysica Acta (BBA) - Bioenergetics*, 2013. **1827**(8): p. 871-881.
8. Mortenson, L., R. Valentine, and J. Carnahan, *An electron transport factor from Clostridium pasteurianum*. *Biochemical and biophysical research communications*, 1962. **7**(6): p. 448-452.
9. Beinert, H. and R.H. Sands, *Studies on succinic and DPNH dehydrogenase preparations by paramagnetic resonance (EPR) spectroscopy*. 1960.
10. Tagawa, K. and D.I. Arnon, *Ferredoxins as electron carriers in photosynthesis and in the biological production and consumption of hydrogen gas*. *Nature*, 1962. **195**(4841): p. 537-543.
11. Liu, J., et al., *Metalloproteins containing cytochrome, iron-sulfur, or copper redox centers*. *Chemical Reviews*, 2014. **114**(8): p. 4366-4369.
12. Johnson, D. and D. Dr, *smith aD, Johnson mK, annu. rev. Biochem*, 2005. **74**: p. 247-281.
13. Flint, D.H. and R.M. Allen, *Iron– sulfur proteins with nonredox functions*. *Chemical reviews*, 1996. **96**(7): p. 2315-2334.
14. Bian, S. and J. Cowan, *Protein-bound iron–sulfur centers. Form, function, and assembly*. *Coordination chemistry reviews*, 1999. **190**: p. 1049-1066.
15. Lill, R., *Function and biogenesis of iron–sulphur proteins*. *Nature*, 2009. **460**(7257): p. 831-838.
16. Broderick, J.B., 8.27 - *Iron–Sulfur Clusters in Enzyme Catalysis*, in *Comprehensive Coordination Chemistry II*, J.A. McCleverty and T.J. Meyer, Editors. 2003, Pergamon: Oxford. p. 739-757.
17. Py, B., P.L. Moreau, and F. Barras, *Fe–S clusters, fragile sentinels of the cell*. *Current opinion in microbiology*, 2011. **14**(2): p. 218-223.
18. Beinert, H. and P.J. Kiley, *Fe-S proteins in sensing and regulatory functions*. *Current opinion in chemical biology*, 1999. **3**(2): p. 152-157.
19. Liebecq, C., *IUPAC-IUBMB Joint Commission on Biochemical Nomenclature (JCBN) and Nomenclature Committee of IUBMB (NC-IUBMB). Newsletter 1996*. *European journal of biochemistry*, 1997. **247**(2): p. 733-739.
20. Stephens, P., D. Jollie, and A. Warshel, *Protein control of redox potentials of iron–sulfur proteins*. *Chemical Reviews*, 1996. **96**(7): p. 2491-2514.

21. Noodleman, L., M. Pique, and V. Roberts, *Wiley Encyclopedia of Chemical Biology*. 2009, John Wiley & Sons, Inc.: Hoboken, NJ.
22. Bill, E., *Iron-sulfur clusters—new features in enzymes and synthetic models*. *Hyperfine Interactions*, 2012. **205**(1): p. 139-147.
23. Orme-Johnson, W., *Iron-sulfur proteins: structure and function*. *Annual Review of Biochemistry*, 1973. **42**(1): p. 159-204.
24. Tsibris, J.C. and R.W. Woody, *Structural studies of iron-sulfur proteins*. *Coordination Chemistry Reviews*, 1970. **5**(4): p. 417-458.
25. Claudia Binda, A.C., Alessandro Aliverti, Giuliana Zanetti, Andrea Mattevia, *Structure of the Mutant E92K of [2Fe–2S] Ferredoxin I from Spinacia oleracea at 1.7 Å Resolution*. *Structural Biology*, 1998. **54**: p. 1353-1358.
26. Hu, Y., et al., *Nitrogenase Fe protein: A molybdate/homocitrate insertase*. *Proceedings of the National Academy of Sciences of the United States of America*, 2006. **103**(46): p. 17125-17130.
27. Kirn, J. and D.C. Rees, *Crystallographic structure and functional implications of the nitrogenase molybdenum-iron protein from Azotobacter vinelandii*. *Nature*, 1992. **360**(6404): p. 553-560.
28. Howard, J.B. and D.C. Rees, *Structural basis of biological nitrogen fixation*. *Chemical Reviews*, 1996. **96**(7): p. 2965-2982.
29. Peters, J.W., et al., *Redox-dependent structural changes in the nitrogenase P-cluster*. *Biochemistry*, 1997. **36**(6): p. 1181-1187.
30. Barney, B.M., et al., *Breaking the N₂ triple bond: Insights into the nitrogenase mechanism*. *Dalton Transactions*, 2006(19): p. 2277-2284.
31. Dos Santos, P.C., et al., *Substrate interactions with the nitrogenase active site*. *Accounts of Chemical Research*, 2005. **38**(3): p. 208-214.
32. Hu, Y., A.W. Fay, C.L. Chi, and M.W. Ribbe, *P-cluster maturation on nitrogenase MoFe protein*. *Proceedings of the National Academy of Sciences of the United States of America*, 2007. **104**(25): p. 10424-10429.
33. Seefeldt, L.C., B.M. Hoffman, and D.R. Dean, *Mechanism of mo-dependent nitrogenase*. *Annual Review of Biochemistry*, 2009. **78**: p. 701-722.
34. Chakrabarti, M., et al., *Mössbauer, electron paramagnetic resonance, and theoretical studies of a carbene-based all-ferrous Fe₄S₄ cluster: Electronic origin and structural identification of the unique spectroscopic site*. *Inorganic Chemistry*, 2009. **48**(7): p. 2735-2747.
35. Scott, T.A., C.P. Berlinguette, R.H. Holm, and H.C. Zhou, *Initial synthesis and structure of an all-ferrous analogue of the fully reduced [Fe₄S₄]⁰ cluster of the nitrogenase iron protein*. *Proceedings of the National Academy of Sciences of the United States of America*, 2005. **102**(28): p. 9741-9744.
36. Angove, H.C., S.J. Yoo, B.K. Burgess, and E. Münck, *Mössbauer and EPR evidence for an all-ferrous Fe₄S₄ cluster with S = 4 in the Fe protein of nitrogenase*. *Journal of the American Chemical Society*, 1997. **119**(37): p. 8730-8731.
37. Vincent, K.A., et al., *Instantaneous, stoichiometric generation of powerfully reducing states of protein active sites using Eu(II) and polyaminocarboxylate ligands*. *Chemical Communications*, 2003. **3**(20): p. 2590-2591.
38. Watt, G.e.D. and K.R.N. Reddy, *Formation of an all ferrous Fe₄S₄ cluster in the iron protein component of Azotobacter vinelandii nitrogenase*. *Journal of Inorganic Biochemistry*, 1994. **53**(4): p. 281-294.
39. Lowery, T.J., et al., *Flavodoxin hydroquinone reduces Azotobacter vinelandii Fe protein to the all-ferrous redox state with a S = 0 spin state*. *Proceedings of the National Academy of Sciences of the United States of America*, 2006. **103**(46): p. 17131-17136.

40. Guo, M., et al., *Direct assessment of the reduction potential of the [4Fe-4S]^{1+/0} couple of the Fe protein from Azotobacter vinelandii*. Journal of the American Chemical Society, 2002. **124**(41): p. 12100-12101.
41. Rebelein, J.G., M.T. Stiebritz, C.C. Lee, and Y. Hu, *Activation and reduction of carbon dioxide by nitrogenase iron proteins*. Nature Chemical Biology, 2017. **13**(2): p. 147-149.
42. Van Stappen, C., et al., *The Spectroscopy of Nitrogenases*. Chemical Reviews, 2020.
43. Howard, J.B. and D.C. Rees, *NITROGENASE : A Nucleotide-Dependent Molecular Switch*. Annu. Rev. Biochem, 1994. **63**: p. 235-64.
44. Hageman, R.V., *Nitrogenase and nitrogenase reductase associate and dissociate with each catalytic cycle*. Biochemistry, 1978. **75**(6): p. 2699-2702.
45. Reinbothe, C., et al., *Chlorophyll biosynthesis: Spotlight on protochlorophyllide reduction*. Trends in Plant Science, 2010. **15**(11): p. 614-624.
46. Moser, J. and M.J. Bröcker, *Enzymatic Systems with Homology to Nitrogenase*. 2011. p. 326-326.
47. Seefeldt, L.C. and D.R. Dean, *Role of Nucleotides in Nitrogenase Catalysis*. Accounts of Chemical Research, 1997. **30**(6): p. 260-266.
48. Vansuch, G.E., et al., *Cryo-annealing of Photoreduced CdS Quantum Dot–Nitrogenase MoFe Protein Complexes Reveals the Kinetic Stability of the E4(2N2H) Intermediate*. Journal of the American Chemical Society, 2023. **145**(39): p. 21165-21169.
49. Müller, A., et al., *Characterization of the [iron only] nitrogenase from rhodobacter capsulatus*. Journal of Inorganic Biochemistry, 1995. **59**(2-3): p. 551-551.
50. Dilworth, M.J., R.R. Eady, R.L. Robson, and R.W. Miller, *Ethane formation from acetylene as a potential test for vanadium nitrogenase in vivo*. Nature, 1987. **327**(6118): p. 167-168.
51. Hu, Y., *Extending the Carbon Chain : Hydrocarbon Formation Catalyzed by Vanadium / Molybdenum Nitrogenases*. Science, 2011. **333**(2011): p. 753-756.
52. Hwang, J., C. Chen, and R. Burris, *Inhibition of nitrogenase-catalyzed reductions*. Biochimica et Biophysica Acta (BBA)-Bioenergetics, 1973. **292**(1): p. 256-270.
53. Walmsley, J., A. Toukdarian, and C. Kennedy, *The role of regulatory genes nifA, vnfA, anfA, nfrX, ntrC, and rpoN in expression of genes encoding the three nitrogenases of Azotobacter vinelandii*. Archives of microbiology, 1994. **162**(6): p. 422-429.
54. Kennedy, C., et al., *Regulation of expression of genes for three nitrogenases in Azotobacter vinelandii*, in *Nitrogen Fixation*. 1991, Springer. p. 13-23.
55. Rohde, M., et al., *Crystal structure of VnfH, the iron protein component of vanadium nitrogenase*. J Biol Inorg Chem, 2018. **23**(7): p. 1049-1056.
56. Sippel, D. and O. Einsle, *The structure of vanadium nitrogenase reveals an unusual bridging ligand*. Nature Chemical Biology, 2017. **13**(9): p. 956-960.
57. Eady, R., et al., *The vanadium nitrogenase of Azotobacter chroococcum. Purification and properties of the Fe protein*. Biochemical Journal, 1988. **256**(1): p. 189-196.
58. Smith, B.E., R.R. Eady, D. Lowe, and C. Gormal, *The vanadium-iron protein of vanadium nitrogenase from Azotobacter chroococcum contains an iron-vanadium cofactor*. Biochemical journal, 1988. **250**(1): p. 299-302.
59. Chisnell, J.R., R. Premakumar, and P.E. Bishop, *Purification of a second alternative nitrogenase from a nifHDK deletion strain of Azotobacter vinelandii*. Journal of bacteriology, 1988. **170**(1): p. 27-33.
60. Ezzaher, S., et al., *Evidence for the formation of terminal hydrides by protonation of an asymmetric iron hydrogenase active site mimic*. Inorganic chemistry, 2007. **46**(9): p. 3426-3428.

61. van der Vlugt, J.I., T.B. Rauchfuss, C.M. Whaley, and S.R. Wilson, *Characterization of a Diferrous Terminal Hydride Mechanistically Relevant to the Fe-Only Hydrogenases*. Journal of the American Chemical Society, 2005. **127**(46): p. 16012-16013.
62. Trncik, C., T. Müller, P. Franke, and O. Einsle, *Structural analysis of the reductase component AnfH of iron-only nitrogenase from Azotobacter vinelandii*. Journal of Inorganic Biochemistry, 2022. **227**: p. 111690.
63. R Davis, L.L., R Petrovich, V K Shah, G P Roberts, P W Ludden, *Purification and Characterization of the Alternative Nitrogenase from the Photosynthetic Bacterium Rhodospirillum rubrum*. J Bacteriol, 1996. **178**: p. 1445-50.
64. Trncik, C., F. Detemple, and O. Einsle, *Iron-only Fe-nitrogenase underscores common catalytic principles in biological nitrogen fixation*. Nature Catalysis, 2023. **6**(5): p. 415-424.
65. Schmidt, F.V., et al., *Structural insights into the iron nitrogenase complex*. Nature Structural & Molecular Biology, 2024. **31**(1): p. 150-158.
66. Sarma, R., et al., *Crystal structure of the L protein of Rhodobacter sphaeroides light-independent protochlorophyllide reductase with MgADP bound: A homologue of the nitrogenase Fe protein*. Biochemistry, 2008. **47**(49): p. 13004-13015.
67. Brocker, M.J., et al., *ATP-driven reduction by dark-operative protochlorophyllide oxidoreductase from Chlorobium tepidum mechanistically resembles nitrogenase catalysis*. J Biol Chem, 2008. **283**(16): p. 10559-67.
68. Moser, J., et al., *Structure of ADP-aluminium fluoride-stabilized protochlorophyllide oxidoreductase complex*. Proceedings of the National Academy of Sciences of the United States of America, 2013. **110**(6): p. 2094-2098.
69. Hu, Y. and M.W. Ribbe, *Nitrogenase and homologs*. Journal of Biological Inorganic Chemistry, 2015. **20**(2): p. 435-445.
70. Bard, A.J. and L.R. Faulkner, *ELECTROCHEMICAL METHODS Fundamentals and Applications*. Vol. 8. 2001.
71. Muraki, N., et al., *X-ray crystal structure of the light-independent protochlorophyllide reductase*. Nature, 2010. **465**(7294): p. 110-4.
72. Brocker, M.J., et al., *Crystal structure of the nitrogenase-like dark operative protochlorophyllide oxidoreductase catalytic complex (ChIN/ChIB)₂*. J Biol Chem, 2010. **285**(35): p. 27336-27345.
73. Luigi Calzolari; Carol M. Gors; Zhi-Hao Zhao; Quincy Teng; Michael W. W. Adams, G.N.L.M., *¹H NMR investigation of the electronic and molecular structure of the four-iron cluster ferredoxin from the hyperthermophile Pyrococcus furiosus. Identification of Asp 14 as a cluster ligand in each of the four redox states*. biochemistry, 1995. **34**: p. 11373—11384.
74. Page, C.C., C.C. Moser, X. Chen, and P.L. Dutton, *Natural engineering principles of electron tunnelling in biological oxidation–reduction*. Nature, 1999. **402**(6757): p. 47-52.
75. Bröcker, M.J., et al., *Crystal Structure of the Nitrogenase-like Dark Operative Protochlorophyllide Oxidoreductase Catalytic Complex (ChIN/ChIB)₂*. Journal of Biological Chemistry, 2010. **285**(35): p. 27336-27345.
76. Chiu, H.-J., et al., *MgATP-Bound and Nucleotide-Free Structures of a Nitrogenase Protein Complex between the Leu 127Δ-Fe-Protein and the MoFe-Protein*. Biochemistry, 2001. **40**(3): p. 641-650.
77. Einsle, O. and D.C. Rees, *Structural Enzymology of Nitrogenase Enzymes*. Chemical Reviews, 2020. **120**(12): p. 4969-5004.
78. Moser, J., et al., *Structure of ADP-aluminium fluoride-stabilized protochlorophyllide oxidoreductase complex*. Proc Natl Acad Sci U S A, 2013. **110**(6): p. 2094-8.

79. Stephenson, M. and L.H. Stickland, *Hydrogenase: a bacterial enzyme activating molecular hydrogen: The properties of the enzyme*. Biochem J, 1931. **25**(1): p. 205-14.
80. Lubitz, W., H. Ogata, O. Rudiger, and E. Reijerse, *Hydrogenases*. Chem Rev, 2014. **114**(8): p. 4081-148.
81. Sven T. Stripp, T.H., *How algae produce hydrogen—news from the photosynthetic hydrogenase*. Dalton Trans, 2009(45): p. 9960–9969.
82. Berggren, G., et al., *Biomimetic assembly and activation of [FeFe]-hydrogenases*. Nature, 2013. **499**(7456): p. 66-69.
83. Greening, C., et al., *Genomic and metagenomic surveys of hydrogenase distribution indicate H₂ is a widely utilised energy source for microbial growth and survival*. ISME J, 2016. **10**(3): p. 761-77.
84. Wegelius, A., H. Land, G. Berggren, and P. Lindblad, *Semisynthetic [FeFe]-hydrogenase with stable expression and H₂ production capacity in a photosynthetic microbe*. Cell Reports Physical Science, 2021. **2**(3).
85. Billoud, P.M.V.a.B., *Occurrence, classification, and biological function of hydrogenases: an overview*. Chemical Reviews, 2007. **107**(10): p. 4206-4265.
86. Happe, T. and J.D. Naber, *Isolation, characterization and N-terminal amino acid sequence of hydrogenase from the green alga Chlamydomonas reinhardtii*. Eur J Biochem, 1993. **214**(2): p. 475-81.
87. Land, H., M. Senger, G. Berggren, and S.T. Stripp, *Current State of [FeFe]-Hydrogenase Research: Biodiversity and Spectroscopic Investigations*. ACS Catalysis, 2020. **10**(13): p. 7069-7086.
88. Lampret, O., et al., *Interplay between CN– Ligands and the Secondary Coordination Sphere of the H-Cluster in [FeFe]-Hydrogenases*. Journal of the American Chemical Society, 2017. **139**(50): p. 18222-18230.
89. Duan, J., et al., *Geometry of the Catalytic Active Site in [FeFe]-Hydrogenase Is Determined by Hydrogen Bonding and Proton Transfer*. ACS Catalysis, 2019. **9**(10): p. 9140-9149.
90. Lorent, C., et al., *Shedding Light on Proton and Electron Dynamics in [FeFe] Hydrogenases*. J Am Chem Soc, 2020. **142**(12): p. 5493-5497.
91. Rumpel, S., et al., *Direct Detection of the Terminal Hydride Intermediate in [FeFe] Hydrogenase by NMR Spectroscopy*. Journal of the American Chemical Society, 2018. **140**(11): p. 3863-3866.
92. Meyer, J., *[FeFe] hydrogenases and their evolution: a genomic perspective*. Cell Mol Life Sci, 2007. **64**(9): p. 1063-84.
93. Mortenson, G.N.L., *Purification and properties of hydrogenase, an iron sulfur protein, from Clostridium pasteurianum W5*. Biochimica et Biophysica Acta, 1971. **227**: p. 576-583.
94. Akhmanova, A., et al., *A hydrogenosome with a genome*. Nature, 1998. **396**(6711): p. 527-528.
95. Yvain Nicolet, C.P., Pierre Legrand, Claude E Hatchikian and Juan C Fontecilla-Camps, *Desulfovibrio desulfuricans iron hydrogenase: the structure shows unusual coordination to an active site Fe binuclear center*. Structure, 1999. **7**: p. 13-23.
96. Zambrano, I.C., et al., *Magnetic Circular Dichroism and Electron Paramagnetic Resonance Studies of Hydrogenases I and II from Clostridium pasteurianum*. Journal of Biological Chemistry, 1989. **264**(35): p. 20974-20983.
97. Peters, J.W., W.N. Lanzilotta, B.J. Lemon, and L.C. Seefeldt, *X-ray Crystal Structure of the Fe-Only Hydrogenase (Cpl) from Clostridium pasteurianum to 1.8 Angstrom Resolution*. Science, 1998. **282**(5395): p. 1853-1858.

98. Pierik, A.J., M. Hulstein, W.R. Hagen, and S.P. Albracht, *A low-spin iron with CN and CO as intrinsic ligands forms the core of the active site in [Fe]-hydrogenases*. Eur J Biochem, 1998. **258**(2): p. 572-8.
99. Seefeldt, J.W.P.W.N.L.B.J.L.L.C., *X-ray Crystal Structure of the Fe-Only Hydrogenase (Cpl) from Clostridium pasteurianum to 1.8 Angstrom Resolution*. Science, 1998. **282**: p. 1853-1858.
100. Silakov, A., B. Wenk, E. Reijerse, and W. Lubitz, *14N HYSCORE investigation of the H-cluster of [FeFe] hydrogenase: evidence for a nitrogen in the dithiol bridge*. Physical Chemistry Chemical Physics, 2009. **11**(31): p. 6592-6599.
101. Lampret, O., et al., *Interplay between CN(-) Ligands and the Secondary Coordination Sphere of the H-Cluster in [FeFe]-Hydrogenases*. J Am Chem Soc, 2017. **139**(50): p. 18222-18230.
102. Adam J. Cornish, B.G., Adam Thelen, Julio C. S. da Silva, Thereza A. Soares, Simone Raugei, Michel Dupuis, Wendy J. Shaw*, and Eric L. Hegg, *Single-Amino Acid Modifications Reveal Additional Controls on the Proton Pathway of [FeFe]-Hydrogenase.pdf*. Biochemistry, 2016. **55**(22): p. 3165-3173.
103. Sanchez, M.L.K., et al., *Investigating the Kinetic Competency of CrHydA1 [FeFe] Hydrogenase Intermediate States via Time-Resolved Infrared Spectroscopy*. J Am Chem Soc, 2019. **141**(40): p. 16064-16070.
104. Morra, S., et al., *Electrochemical control of [FeFe]-hydrogenase single crystals reveals complex redox populations at the catalytic site*. Dalton Trans, 2021. **50**(36): p. 12655-12663.
105. Armstrong, J.P.M.F.A., *Protein film cryovoltammetry: demonstrations with a 7Fe ([3Fe-4S] + [4Fe-4S]) ferredoxin*. Chemical Communications, 1999(17): p. 1635-1636.
106. Vincent Fourmond, M.S., Pascal Arnoux, Patrick Bertrand, David Pignol, and Christophe Léger, *Reassessing the Strategies for Trapping Catalytic Intermediates during Nitrate Reductase Turnover*. J. Phys. Chem. B, 2010. **114**(9): p. 3341-3347.
107. DeBeer, S., *Advanced X-ray Spectroscopic Methods for Studying Iron-Sulfur-Containing Proteins and Model Complexes*. Methods Enzymol, 2018. **599**: p. 427-450.
108. Beinert, H., R.H. Holm, and E. Münck, *Iron-sulfur clusters: nature's modular, multipurpose structures*. Science, 1997. **277**(5326): p. 653-9.
109. Cammack, R., *Iron-sulfur clusters in enzymes: Themes and variations*, in *Advances in inorganic chemistry*. 1992, Elsevier. p. 281-322.
110. Meyer, J., *Iron-sulfur protein folds, iron-sulfur chemistry, and evolution*. JBIC Journal of Biological Inorganic Chemistry, 2008. **13**(2): p. 157-170.
111. Lindahl, P.A., et al., *Mössbauer, EPR, and magnetization studies of the Azotobacter vinelandii Fe protein. Evidence for a [4Fe-4S]¹⁺ cluster with spin S = 3/2*. Journal of Biological Chemistry, 1985. **260**(20): p. 11160-11173.
112. Hans, M., W. Buckel, and E. Bill, *Spectroscopic evidence for an all-ferrous [4Fe-4S]0 cluster in the superreduced activator of 2-hydroxyglutaryl-CoA dehydratase from Acidaminococcus fermentans*. Journal of Biological Inorganic Chemistry, 2008. **13**(4): p. 563-574.
113. Mössbauer, R.L., *Kernresonanzfluoreszenz von Gammastrahlung in Ir¹⁹¹*. Zeitschrift für Physik, 1958. **151**(2): p. 124-143.
114. Gütlich, P., E. Bill, and A.X. Trautwein, *Mössbauer spectroscopy and transition metal chemistry: fundamentals and applications*. 2010: Springer Science & Business Media.
115. Münck, E., *[20] Mössbauer spectroscopy of proteins: Electron carriers*, in *Methods in Enzymology*. 1978, Academic Press. p. 346-379.
116. Münck, E., *Physical Methods in Bioinorganic Chemistry*. University Science Books, Sausalito, California, 2000: p. 287-320.

117. J. C. Kendrew, G.B., H. M. Dintzis, R. G. Parrish, H. Wyckoff, D. C. Phillips *A three-dimensional model of the myoglobin molecule obtained by X-ray analysis*. *Nature*, 1958. **181**: p. 662-666.
118. Sarma, R., et al., *Insights into substrate binding at FeMo-cofactor in nitrogenase from the structure of an alpha-70(Ile) MoFe protein variant*. *J Inorg Biochem*, 2010. **104**(4): p. 385-9.
119. Einsle, O., et al., *Nitrogenase MoFe-protein at 1.16 Å resolution: a central ligand in the FeMo-cofactor*. *Science*, 2002. **297**(5587): p. 1696-1700.
120. Spatzal, T., et al., *Evidence for interstitial carbon in nitrogenase FeMo cofactor*. *Science*, 2011. **334**(6058): p. 940-940.
121. George, S.J., et al., *Extended X-ray Absorption Fine Structure and Nuclear Resonance Vibrational Spectroscopy Reveal that NifB-co, a FeMo-co Precursor, Comprises a 6Fe Core with an Interstitial Light Atom*. *Journal of the American Chemical Society*, 2008. **130**(17): p. 5673-5680.
122. Birrell, J.A., P. Rodríguez-Maciá, and A. Hery-Barranco, *A Beginner's Guide to Thermodynamic Modelling of [FeFe] Hydrogenase*. *Catalysts*, 2021. **11**(2).
123. Kaim, W. and J. Fiedler, *Spectroelectrochemistry: the best of two worlds*. *Chemical Society Reviews*, 2009. **38**(12): p. 3373-3382.
124. Lozeman, J.J.A., P. Führer, W. Olthuis, and M. Odijk, *Spectroelectrochemistry, the future of visualizing electrode processes by hyphenating electrochemistry with spectroscopic techniques*. *Analyst*, 2020. **145**(7): p. 2482-2509.
125. Holze, R., *Fundamentals and applications of near infrared spectroscopy in spectroelectrochemistry*. *Journal of Solid State Electrochemistry*, 2004. **8**(12): p. 982-997.
126. Ashley, K. and S. Pons, *Infrared spectroelectrochemistry*. *Chemical Reviews*, 1988. **88**(4): p. 673-695.
127. Dias, M., et al., *Electrochemistry coupled to fluorescence spectroscopy: a new versatile approach*. *Electrochemistry Communications*, 2004. **6**(3): p. 325-330.
128. Prenzler, P.D., R. Bramley, S.R. Downing, and G.A. Heath, *High-field NMR spectroelectrochemistry of spinning solutions: simultaneous in situ detection of electrogenerated species in a standard probe under potentiostatic control* *1A preliminary account of this work was presented at AISAS 99, Melbourne, Australia, July 1999 [1].1*. *Electrochemistry Communications*, 2000. **2**(7): p. 516-521.
129. Nakamoto, K., *Applications in Inorganic Chemistry*, in *Infrared and Raman Spectra of Inorganic and Coordination Compounds*. 2008. p. 149-354.
130. Jones, L.H., *Nature of Bonding in Metal Cyanide Complexes as Related to Intensity and Frequency of Infrared Absorption Spectra*. *Inorganic Chemistry*, 1963. **2**(4): p. 777-780.
131. Drew, D.M., *Simultaneous Determination of Ferrocyanide and Ferricyanide in Aqueous Solutions Using Infrared Spectrometry*. *Analytical Chemistry*, 1973. **45**(14): p. 2423-2424.
132. Cai, R., et al., *Electroenzymatic C-C bond formation from CO₂*. *Journal of the American Chemical Society*, 2018. **140**(15): p. 5041-5044.
133. Cameron, L.M. and B.J. Hales, *Investigation of CO binding and release from Mo-nitrogenase during catalytic turnover*. *Biochemistry*, 1998. **37**(26): p. 9449-9456.
134. Chen, T., *Understanding substrate and inhibitor interactions with Mo-nitrogenase*, in *Department of Chemistry*. 2019, University of Oxford.
135. Chen, T., P.A. Ash, L.C. Seefeldt, and K.A. Vincent, *Electrochemical experiments define potentials associated with binding of substrates and inhibitors to nitrogenase MoFe protein*. *Faraday Discuss*, 2023. **243**(0): p. 270-286.
136. Dance, I., *How does vanadium nitrogenase reduce CO to hydrocarbons?* *Dalton Transactions*, 2011. **40**(20): p. 5516-5527.

137. Lee, C.C., et al., *Uncoupling binding of substrate CO from turnover by vanadium nitrogenase*. Proceedings of the National Academy of Sciences of the United States of America, 2015. **112**(45): p. 13845-13849.
138. Healy, A.J., H.A. Reeve, and K.A. Vincent, *Development of an infrared spectroscopic approach for studying metalloenzyme active site chemistry under direct electrochemical control*. Faraday Discussions, 2011. **148**: p. 345-357.
139. Adamska-Venkatesh, A., et al., *New Redox States Observed in [FeFe] Hydrogenases Reveal Redox Coupling Within the H-Cluster*. Journal of the American Chemical Society, 2014. **136**(32): p. 11339-11346.
140. Maciá, P.R., *From Hydrogenases to Molecular Catalysts: Electrochemical and Spectroscopic Investigations*. 2017.
141. Winkler, M., J. Esselborn, and T. Happe, *Molecular basis of [FeFe]-hydrogenase function An insight into the complex interplay between protein and catalytic cofactor*. 2013, Elsevier B.V. p. 974-985.
142. Yu, L., et al., *Targeting Intermediates of [FeFe]-Hydrogenase by CO and CN Vibrational Signatures*. Inorganic Chemistry, 2011. **50**(9): p. 3888-3900.
143. Stuart, B., *Infrared spectroscopy : fundamentals and applications*. 2004: Chichester, West Sussex, England ; Hoboken, NJ : J. Wiley, [2004] ©2004.
144. Schmid, F.-X., *Biological Macromolecules: UV-visible Spectrophotometry*, in *Encyclopedia of Life Sciences*. 2001.
145. Hopp, M.-T., et al., *Heme Determination and Quantification Methods and Their Suitability for Practical Applications and Everyday Use*. Analytical Chemistry, 2020. **92**(14): p. 9429-9440.
146. Rodger, A., *UV Absorbance Spectroscopy of Biological Macromolecules*, in *Encyclopedia of Biophysics*, G.C.K. Roberts, Editor. 2013, Springer Berlin Heidelberg: Berlin, Heidelberg. p. 2714-2718.
147. Kelly, S.M., T.J. Jess, and N.C. Price, *How to study proteins by circular dichroism*. Biochimica et Biophysica Acta (BBA) - Proteins and Proteomics, 2005. **1751**(2): p. 119-139.
148. Jarrett, J.T., *Iron–Sulfur Clusters*, in *Encyclopedia of Biophysics*, G.C.K. Roberts, Editor. 2013, Springer Berlin Heidelberg: Berlin, Heidelberg. p. 1153-1156.
149. Sims, L.P., et al., *Purification and Characterization of the Isoprene Monooxygenase from Rhodococcus sp. Strain AD45*. Appl Environ Microbiol, 2022. **88**(7): p. e0002922.
150. Cammack, R., *EPR Spectroscopy: General Principles*, in *Encyclopedia of Biophysics*, G.C.K. Roberts, Editor. 2013, Springer Berlin Heidelberg: Berlin, Heidelberg. p. 695-706.
151. Kroneck, P.M.H., et al., *Multifrequency EPR evidence for a bimetallic center at the CuA site in cytochrome c oxidase*. FEBS Letters, 1990. **268**(1): p. 274-276.
152. Harrington, P.C., R.G. Wilkins, B.B. Muhoberac, and D.C. Wharton. *Substitution and Electron Transfer Processes in Hemerythrin*. in *The Biological Chemistry of Iron*. 1982. Dordrecht: Springer Netherlands.
153. Więckowski, A.B., et al., *EPR study and structural aspects of ferredoxins obtained from Thiobacillus ferrooxidans*. Applied Microbiology and Biotechnology, 1999. **52**(1): p. 96-98.
154. Cammack, R., *EPR and ENDOR of Radicals and Metalloproteins in Biological Systems*, in *Encyclopedia of Biophysics*, G.C.K. Roberts, Editor. 2013, Springer Berlin Heidelberg: Berlin, Heidelberg. p. 685-695.
155. Beinert, H., R.H. Holm, and E. Münck, *Iron-Sulfur Clusters: Nature's Modular, Multipurpose Structures*. Science, 1997. **277**(5326): p. 653-659.

156. DerVartanian, D.V., et al., *Identification of sulfur as component of the EPR signal at $g = 1.94$ by isotopic substitution*. Biochemical and Biophysical Research Communications, 1967. **26**(5): p. 569-576.
157. BEINERT, H. and M.C. KENNEDY, *Engineering of protein bound iron-sulfur clusters*. European Journal of Biochemistry, 1989. **186**(1-2): p. 5-15.
158. Brown, N.M., et al., *Detection of a [3Fe-4S] Cluster Intermediate of Cytosolic Aconitase in Yeast Expressing Iron Regulatory Protein 1: Insights into the mechanism of Fe-S cluster cycling*. Journal of Biological Chemistry, 2002. **277**(9): p. 7246-7254.
159. Priem, A.H., et al., *EPR analysis of multiple forms of [4Fe-4S]₃₊ clusters in HiPIPs*. JBIC Journal of Biological Inorganic Chemistry, 2005. **10**(4): p. 417-424.
160. Fourmond, V. and C. Léger, *An introduction to electrochemical methods for the functional analysis of metalloproteins*, in *Practical Approaches to Biological Inorganic Chemistry*. 2020. p. 325-373.
161. Badalyan, A., Z.Y. Yang, and L.C. Seefeldt, *A Voltammetric Study of Nitrogenase Catalysis Using Electron Transfer Mediators*. ACS Catalysis, 2019. **9**(2): p. 1366-1372.
162. Verhagen, M.F.J.M., T.A. Link, and W.R. Hagen, *Electrochemical study of the redox properties of [2Fe-2S] ferredoxins Evidence for superreduction of the Rieske [2Fe-2S] cluster*. FEBS Letters, 1995. **361**(1): p. 75-78.
163. Armstrong, F.A., *Voltammetry of Proteins*, in *Encyclopedia of Electrochemistry*.
164. Léger, C. and P. Bertrand, *Direct Electrochemistry of Redox Enzymes as a Tool for Mechanistic Studies*. Chemical Reviews, 2008. **108**(7): p. 2379-2438.
165. Chen, K., et al., *Atomically defined mechanism for proton transfer to a buried redox centre in a protein*. Nature, 2000. **405**(6788): p. 814-817.
166. Léger, C., F. Lederer, B. Guigliarelli, and P. Bertrand, *Electron flow in multicenter enzymes: theory, applications, and consequences on the natural design of redox chains*. J Am Chem Soc, 2006. **128**(1): p. 180-7.
167. Fourmond, V., et al., *Steady-State Catalytic Wave-Shapes for 2-Electron Reversible Electrocatalysts and Enzymes*. Journal of the American Chemical Society, 2013. **135**(10): p. 3926-3938.
168. Leroux, F., et al., *Experimental approaches to kinetics of gas diffusion in hydrogenase*. Proceedings of the National Academy of Sciences, 2008. **105**(32): p. 11188-11193.
169. Liebgott, P.P., et al., *Relating diffusion along the substrate tunnel and oxygen sensitivity in hydrogenase*. Nature Chemical Biology, 2010. **6**(1): p. 63-70.
170. Brown, J.H., *Development and Use of a Cyclic Voltammetry Simulator To Introduce Undergraduate Students to Electrochemical Simulations*. Journal of Chemical Education, 2015. **92**(9): p. 1490-1496.
171. Léger, C., et al., *Inhibition and Aerobic Inactivation Kinetics of Desulfovibrio fructosovorans NiFe Hydrogenase Studied by Protein Film Voltammetry*. Journal of the American Chemical Society, 2004. **126**(38): p. 12162-12172.
172. Heineman, W.R., B.J. Norris, and J.F. Goelz, *Measurement of enzyme $E_{deg.}$ values by optically transparent thin layer electrochemical cells*. Analytical Chemistry, 1975. **47**(1): p. 79-84.
173. Zhou, Z.Y., S.C. Lin, S.P. Chen, and S.G. Sun, *In situ step-scan time-resolved microscope FTIR spectroscopy working with a thin-layer cell*. Electrochemistry Communications, 2005. **7**(5): p. 490-495.
174. Zhou, Z.Y. and S.G. Sun, *In situ step-scan time-resolved microscope FTIR spectroscopy applied in irreversible electrochemical reactions*. Electrochimica Acta, 2005. **50**(25): p. 5163-5171.
175. Rosendahl, S.M., F. Borondics, T.E. May, and I.J. Burgess, *Step-Scan IR Spectroelectrochemistry with Ultramicroelectrodes: Nonsurface Enhanced Detection*

- of Near Femtomole Quantities Using Synchrotron Radiation*. Analytical Chemistry, 2013. **85**(18): p. 8722-8727.
176. Ash, P.A., et al., *Synchrotron-Based Infrared Microanalysis of Biological Redox Processes under Electrochemical Control*. Analytical Chemistry, 2016. **88**(13): p. 6666-6671.
 177. Ash, P.A., et al., *Generating single metalloprotein crystals in well-defined redox states: electrochemical control combined with infrared imaging of a NiFe hydrogenase crystal*. Chemical Communications, 2017. **53**(43): p. 5858-5861.
 178. Ash, P.A., et al., *The crystalline state as a dynamic system: IR microspectroscopy under electrochemical control for a [NiFe] hydrogenase*. Chemical Science, 2021. **12**(39): p. 12959-12970.
 179. Morra, S., et al., *Electrochemical control of [FeFe]-hydrogenase single crystals reveals complex redox populations at the catalytic site*. Dalton Transactions, 2021. **50**(36): p. 12655-12663.
 180. Dinis, P., et al., *X-ray crystallographic and EPR spectroscopic analysis of HydG, a maturase in [FeFe]-hydrogenase H-cluster assembly*. Proceedings of the National Academy of Sciences, 2015. **112**(5): p. 1362-1367.
 181. Suess, D.L.M., et al., *The Radical SAM Enzyme HydG Requires Cysteine and a Dangler Iron for Generating an Organometallic Precursor to the [FeFe]-Hydrogenase H-Cluster*. Journal of the American Chemical Society, 2016. **138**(4): p. 1146-1149.
 182. Suess, D.L.M., et al., *Biosynthesis of the [FeFe] Hydrogenase H Cluster: A Central Role for the Radical SAM Enzyme HydG*. Inorganic Chemistry, 2016. **55**(2): p. 478-487.
 183. Betz, J.N., et al., *[FeFe]-Hydrogenase Maturation: Insights into the Role HydE Plays in Dithiomethylamine Biosynthesis*. Biochemistry, 2015. **54**(9): p. 1807-1818.
 184. Glick, B.R., W.G. Martin, and S.M. Martin, *Purification and properties of the periplasmic hydrogenase from Desulfovibrio desulfuricans*. Canadian Journal of Microbiology, 1980. **26**(10): p. 1214-1223.
 185. Posewitz, M.C., et al., *Identification of genes required for hydrogenase activity in Chlamydomonas reinhardtii*. Biochemical Society Transactions, 2005. **33**(1): p. 102-104.
 186. Esselborn, J., et al., *Spontaneous activation of [FeFe]-hydrogenases by an inorganic [2Fe] active site mimic*. Nature Chemical Biology, 2013. **9**(10): p. 607-609.
 187. Birrell, J.A., O. Rüdiger, E.J. Reijerse, and W. Lubitz, *Semisynthetic Hydrogenases Propel Biological Energy Research into a New Era*. Joule, 2017. **1**(1): p. 61-76.
 188. Birrell, J.A., et al., *Artificial Maturation of the Highly Active Heterodimeric [FeFe] Hydrogenase from Desulfovibrio desulfuricans ATCC 7757*. Israel Journal of Chemistry, 2016. **56**(9-10): p. 852-863.
 189. Kuchenreuther, J.M., et al., *High-Yield Expression of Heterologous [FeFe] Hydrogenases in Escherichia coli*. PLOS ONE, 2010. **5**(11): p. e15491.
 190. De Lacey, A.L., et al., *FTIR Characterization of the Active Site of the Fe-hydrogenase from Desulfovibrio desulfuricans*. Journal of the American Chemical Society, 2000. **122**(45): p. 11232-11233.
 191. PIERIK, A.J. and M.H.W.R.H.S.P.J. ALBRACHT, *A low-spin iron with CN and CO as intrinsic ligands forms the core of the active site in [Fe]-hydrogenases*. European Journal of Biochemistry, 1998. **258**: p. 572-578.
 192. Roseboom, W., et al., *The active site of the [FeFe]-hydrogenase from Desulfovibrio desulfuricans. II. Redox properties, light sensitivity and CO-ligand exchange as observed by infrared spectroscopy*. Journal of Biological Inorganic Chemistry, 2006. **11**(1): p. 102-118.

193. Martin, A.E., et al., *Construction and characterization of an Azotobacter vinelandii strain with mutations in the genes encoding flavodoxin and ferredoxin I*. Journal of Bacteriology, 1989. **171**(6): p. 3162-3167.
194. Thorneley, R.N. and J. Deistung, *Electron-transfer studies involving flavodoxin and a natural redox partner, the iron protein of nitrogenase. Conformational constraints on protein-protein interactions and the kinetics of electron transfer within the protein complex*. Biochemical Journal, 1988. **253**(2): p. 587-595.
195. Duyvis, M.G., H. Wassink, and H. Haaker, *Nitrogenase of Azotobacter vinelandii: Kinetic Analysis of the Fe Protein Redox Cycle*. Biochemistry, 1998. **37**(50): p. 17345-17354.
196. Angove, H.C., S.J. Yoo, E. Münck, and B.K. Burgess, *An all-ferrous state of the Fe protein of nitrogenase. Interaction with nucleotides and electron transfer to the MoFe protein*. Journal of Biological Chemistry, 1998. **273**(41): p. 26330-26337.
197. Parkin, A., et al., *Rapid and Efficient Electrocatalytic CO₂/CO Interconversions by Carboxydotherrmus hydrogenoformans CO Dehydrogenase I on an Electrode*. Journal of the American Chemical Society, 2007. **129**(34): p. 10328-10329.
198. Wittenborn, E.C., et al., *Redox-dependent rearrangements of the NiFeS cluster of carbon monoxide dehydrogenase*. eLife, 2018. **7**: p. e39451.
199. Watt, G.D., Z.C. Wang, R.R. Knotts, and G.D.W.F. Battelle-C, *Redox Reactions of and Nucleotide Binding to the Iron Protein of Azotobacter vinelandii*. 1986. p. 8156-8162.
200. Trncik, C., T. Muller, P. Franke, and O. Einsle, *Structural analysis of the reductase component AnfH of iron-only nitrogenase from Azotobacter vinelandii*. J Inorg Biochem, 2022. **227**: p. 111690.
201. Jenner, L.P. and J.N. Butt, *Electrochemistry of surface-confined enzymes: Inspiration, insight and opportunity for sustainable biotechnology*. Current Opinion in Electrochemistry, 2018. **8**: p. 81-88.
202. Siritanaratkul, B., et al., *Transfer of photosynthetic NADP⁺/NADPH recycling activity to a porous metal oxide for highly specific, electrochemically-driven organic synthesis*. Chemical Science, 2017. **8**(6): p. 4579-4586.
203. Reuillard, B., et al., *High Performance Reduction of H₂O₂ with an Electron Transport Decaheme Cytochrome on a Porous ITO Electrode*. Journal of the American Chemical Society, 2017. **139**(9): p. 3324-3327.
204. O'Reilly, J.E., *Oxidation-reduction potential of the ferro-ferricyanide system in buffer solutions*. Biochimica et Biophysica Acta, 1973. **292**(3): p. 509-515.
205. Van der Zee, F.P. and F.J. Cervantes, *Impact and application of electron shuttles on the redox (bio)transformation of contaminants: A review*. Biotechnology Advances, 2009. **27**(3): p. 256-277.
206. van den Bosch, M., et al., *Calculation of the redox potential of the protein azurin and some mutants*. ChemBioChem, 2005. **6**(4): p. 738-746.
207. Teufel, R., V. Agarwal, and B.S. Moore, *Unusual flavoenzyme catalysis in marine bacteria*. 2016. p. 31-39.
208. Walsh, C.T. and T.A. Wenczewicz, *Flavoenzymes: Versatile catalysts in biosynthetic pathways*. Natural Product Reports, 2013. **30**(1): p. 175-200.
209. Battistuzzi, G., et al., *Redox Thermodynamics of Blue Copper Proteins*. Journal of the American Chemical Society, 1999. **121**(3): p. 501-506.
210. Milton, R.D. and S.D. Minteer, *Nitrogenase Bioelectrochemistry for Synthesis Applications*. Accounts of Chemical Research, 2019. **52**(12): p. 3351-3360.
211. Silveira, C.M., et al., *SERR spectroelectrochemical study of cytochrome cd₁ nitrite reductase coimmobilized with physiological redox partner Cytochrome C₅₅₂ on biocompatible metal electrodes*. PLoS ONE, 2015. **10**(6): p. 1-18.

212. Hagedoorn, P.L., et al., *Purification and characterization of the tungsten enzyme aldehyde:ferredoxin oxidoreductase from the hyperthermophilic denitrifier Pyrobaculum aerophilum*. J Biol Inorg Chem, 2005. **10**(3): p. 259-69.
213. Lindahl, P.A., E.P. Day, and T.A. Kent, *Mossbauer, EPR, and magnetization studies of the Azotobacter vinelandii Fe protein*. Journal of Biological Chemistry, 1985. **260**(20): p. 11160-11173.
214. Yoo, S.J., et al., *Mossbauer and integer-spin EPR studies and spin-coupling analysis of the [4Fe-4S]O cluster of the Fe protein from Azotobacter vinelandii nitrogenase*. Journal of the American Chemical Society, 1999. **121**(11): p. 2534-2545.
215. Blank, M.A., et al., *Structural Models of the [Fe4S4] Clusters of Homologous Nitrogenase Fe Proteins*. Inorganic Chemistry, 2011. **50**(15): p. 7123-7128.
216. Hiller, C.J., et al., *Tuning Electron Flux through Nitrogenase with Methanogen Iron Protein Homologues*. Chemistry – A European Journal, 2017. **23**(64): p. 16152-16156.
217. Vedalankar, P. and B.C. Tripathy, *Evolution of light-independent protochlorophyllide oxidoreductase*. Protoplasma, 2019. **256**(2): p. 293-312.
218. Milton, R.D., et al., *Nitrogenase bioelectrocatalysis: Heterogeneous ammonia and hydrogen production by MoFe protein*. Energy and Environmental Science, 2016. **9**(8): p. 2550-2554.
219. Danyal, K., et al., *Uncoupling nitrogenase: Catalytic reduction of hydrazine to ammonia by a MoFe protein in the absence of Fe protein-ATP*. Journal of the American Chemical Society, 2010. **132**(38): p. 13197-13199.
220. Brown, K.A., et al., *Light-driven dinitrogen reduction catalyzed by a CdS:nitrogenase MoFe protein biohybrid*. Science, 2016. **352**(6284): p. 448-450.
221. Moser, J., et al., *Structure of ADP-aluminium fluoride-stabilized protochlorophyllide oxidoreductase complex*. Proceedings of the National Academy of Sciences, 2013. **110**(6): p. 2094-2098.
222. Haladjian, J., et al., *Direct electrochemical reduction of spinach and desulfovibrio desulfuricans Norway ferredoxins*. Electrochimica Acta, 1986. **31**(12): p. 1513-1517.
223. Claudia Binda, A.C., Alessandro Aliverti, Giuliana Zanetti and Andrea Mattevi, *Structure of the Mutant E92K of 2Fe 2S Ferredoxin I from Spinacia at 1.7 Å Resolution*. Acta Crystallographica, 1998(D54): p. 1353-1358.
224. Rutledge, H.L. and F.A. Tezcan, *Electron Transfer in Nitrogenase*. Chemical Reviews, 2020.
225. Watzlich, D., et al., *Chimeric nitrogenase-like enzymes of (bacterio)chlorophyll biosynthesis*. J Biol Chem, 2009. **284**(23): p. 15530-40.
226. Nomata, J., et al., *Dark-operative protochlorophyllide oxidoreductase generates substrate radicals by an iron-sulphur cluster in bacteriochlorophyll biosynthesis*. Scientific Reports, 2014. **4**(1): p. 5455.
227. Chen, L., et al., *MgATP-induced conformational changes in the iron protein from Azotobacter vinelandii, as studied by small-angle x-ray scattering*. J Biol Chem, 1994. **269**(5): p. 3290-4.
228. Lanzilotta, W.N., M.J. Ryle, and L.C. Seefeldt, *Nucleotide Hydrolysis and Protein Conformational Changes in Azotobacter vinelandii Nitrogenase Iron Protein: Defining the Function of Aspartate 1291*. Biochemistry, 1995. **34**(34): p. 10713-10723.
229. Ryle, M.J. and L.C. Seefeldt, *Elucidation of a MgATP signal transduction pathway in the nitrogenase iron protein: formation of a conformation resembling the MgATP-bound state by protein engineering*. Biochemistry, 1996. **35**(15): p. 4766-75.
230. Tezcan, F.A., et al., *Nitrogenase complexes: multiple docking sites for a nucleotide switch protein*. Science, 2005. **309**(5739): p. 1377-80.
231. Jasper, J., et al., *Chimeric Interaction of Nitrogenase-Like Reductases with the MoFe Protein of Nitrogenase*. Chembiochem, 2020. **21**(12): p. 1733-1741.

232. Bröcker, M.J., et al., *Biosynthesis of (bacterio)chlorophylls: ATP-dependent transient subunit interaction and electron transfer of dark operative protochlorophyllide oxidoreductase*. *Journal of Biological Chemistry*, 2010. **285**(11): p. 8268-8277.
233. Bröcker, M.J., et al., *Substrate recognition of nitrogenase-like dark operative protochlorophyllide oxidoreductase from Prochlorococcus marinus*. *Journal of Biological Chemistry*, 2008. **283**(44): p. 29873-29881.
234. Jackson, P.J., et al., *Absolute quantification of cellular levels of photosynthesis-related proteins in Synechocystis sp. PCC 6803*. *Photosynth Res*, 2023. **155**(3): p. 219-245.
235. Hirai, M., et al., *Direct Evidence for the Effect of Glycerol on Protein Hydration and Thermal Structural Transition*. *Biophysical Journal*, 2018. **115**(2): p. 313-327.
236. Vagenende, V., M.G.S. Yap, and B.L. Trout, *Mechanisms of Protein Stabilization and Prevention of Protein Aggregation by Glycerol*. *Biochemistry*, 2009. **48**(46): p. 11084-11096.
237. Ding, J., et al., *Viologen-inspired functional materials: synthetic strategies and applications*. *Journal of Materials Chemistry A*, 2019. **7**(41): p. 23337-23360.
238. Khoshtariya, D.E., et al., *Fundamental signatures of short- and long-range electron transfer for the blue copper protein azurin at Au/SAM junctions*. *Proceedings of the National Academy of Sciences*, 2010. **107**(7): p. 2757-2762.
239. Li, Y., *Mechanical denaturation : forced unfolding of proteins*. 2013.
240. Au - Hagedoorn, P.-L., L. Au - van der Weel, and W.R. Au - Hagen, *EPR Monitored Redox Titration of the Cofactors of Saccharomyces cerevisiae Nar1*. *JoVE*, 2014(93): p. e51611.
241. Bedendi, G., A. Kulkarni, P. Maroni, and R.D. Milton, *Alternative Electron Donors for the Nitrogenase-like Dark-Operative Protochlorophyllide Oxidoreductase (DPOR)*. *ChemElectroChem*, 2022. **9**(21): p. e202200774.
242. Armstrong, F.A., et al., *From Protein Film Electrochemistry to Nanoconfined Enzyme Cascades and the Electrochemical Leaf*. *Chemical Reviews*, 2023. **123**(9): p. 5421-5458.
243. Rodrigues, R.C., et al., *Stabilization of enzymes via immobilization: Multipoint covalent attachment and other stabilization strategies*. *Biotechnology Advances*, 2021. **52**: p. 107821.
244. Chen, T., *Understanding substrate and inhibitor interactions with Mo-nitrogenase*. 2019, University of Oxford.
245. Vincent, K.A., A. Parkin, and F.A. Armstrong, *Investigating and Exploiting the Electrocatalytic Properties of Hydrogenases*. *Chemical Reviews*, 2007. **107**(10): p. 4366-4413.
246. Sensi, M., et al., *New perspectives in hydrogenase direct electrochemistry*. *Current Opinion in Electrochemistry*, 2017. **5**(1): p. 135-145.
247. Kurth, J.M., C. Dahl, and J.N. Butt, *Catalytic Protein Film Electrochemistry Provides a Direct Measure of the Tetrathionate/Thiosulfate Reduction Potential*. *Journal of the American Chemical Society*, 2015. **137**(41): p. 13232-13235.
248. Gulaboski, R., V. Mirčeski, I. Bogeski, and M. Hoth, *Protein film voltammetry: electrochemical enzymatic spectroscopy. A review on recent progress*. *Journal of Solid State Electrochemistry*, 2012. **16**(7): p. 2315-2328.
249. Armstrong, F.A., et al., *Guiding Principles of Hydrogenase Catalysis Instigated and Clarified by Protein Film Electrochemistry*. *Accounts of Chemical Research*, 2016. **49**(5): p. 884-892.
250. Stripp, S.T. and T. Happe, *How algae produce hydrogen—news from the photosynthetic hydrogenase*. *Dalton Transactions*, 2009(45): p. 9960-9969.
251. Vignais, P.M. and B. Billoud, *Occurrence, Classification, and Biological Function of Hydrogenases: An Overview*. *Chemical Reviews*, 2007. **107**(10): p. 4206-4272.

252. Birrell, J.A., et al., *The catalytic cycle of [FeFe] hydrogenase: A tale of two sites*. 2021, Elsevier B.V.
253. Stripp, S.T., S. Mebs, and M. Haumann, *Temperature Dependence of Structural Dynamics at the Catalytic Cofactor of [FeFe]-hydrogenase*. *Inorganic Chemistry*, 2020. **59**(22): p. 16474-16488.
254. Hatchikian, E.C., et al., *Further characterization of the [Fe]-hydrogenase from *Desulfovibrio desulfuricans* ATCC 7757*. *Eur J Biochem*, 1992. **209**(1): p. 357-65.
255. Pierik, A.J., M. Hulstein, W.R. Hagen, and S.P.J. Albracht, *A low-spin iron with CN and CO as intrinsic ligands forms the core of the active site in [Fe]-hydrogenases*. *European Journal of Biochemistry*, 1998. **258**(2): p. 572-578.
256. Rodríguez-Maciá, P., et al., *Sulfide Protects [FeFe] Hydrogenases from O₂*. *Journal of the American Chemical Society*, 2018. **140**(30): p. 9346-9350.
257. Rodríguez-Maciá, P., et al., *Caught in the Hinact: Crystal Structure and Spectroscopy Reveal a Sulfur Bound to the Active Site of an O₂-stable State of [FeFe] Hydrogenase*. *Angewandte Chemie - International Edition*, 2020. **59**(38): p. 16786-16794.
258. Rodríguez-Maciá, P., et al., *Intercluster Redox Coupling Influences Protonation at the H-cluster in [FeFe] Hydrogenases*. *Journal of the American Chemical Society*, 2017. **139**(42): p. 15122-15134.
259. Lorent, C., et al., *Shedding Light on Proton and Electron Dynamics in [FeFe] Hydrogenases*. *Journal of the American Chemical Society*, 2020. **142**(12): p. 5493-5497.
260. Mebs, S., et al., *Bridging Hydride at Reduced H-Cluster Species in [FeFe]-Hydrogenases Revealed by Infrared Spectroscopy, Isotope Editing, and Quantum Chemistry*. *Journal of the American Chemical Society*, 2017. **139**(35): p. 12157-12160.
261. Sommer, C., et al., *Proton Coupled Electronic Rearrangement within the H-Cluster as an Essential Step in the Catalytic Cycle of [FeFe] Hydrogenases*. *Journal of the American Chemical Society*, 2017. **139**(4): p. 1440-1443.
262. Ratzloff, M.W., et al., *CO-Bridged H-Cluster Intermediates in the Catalytic Mechanism of [FeFe]-Hydrogenase Cal*. *Journal of the American Chemical Society*, 2018. **140**(24): p. 7623-7628.
263. Martini, M.A., et al., *Binding of exogenous cyanide reveals new active-site states in [FeFe] hydrogenases*. *Chemical Science*, 2023. **14**(11): p. 2826-2838.
264. Silakov, A., et al., *Spectroelectrochemical characterization of the active site of the [FeFe] hydrogenase HydA1 from *Chlamydomonas reinhardtii**. *Biochemistry*, 2009. **48**(33): p. 7780-6.
265. Lemon, B.J. and J.W. Peters, *Binding of exogenously added carbon monoxide at the active site of the iron-only hydrogenase (Cpl) from *Clostridium pasteurianum**. *Biochemistry*, 1999. **38**(40): p. 12969-73.
266. Parkin, A., C. Cavazza, J.C. Fontecilla-Camps, and F.A. Armstrong, *Electrochemical Investigations of the Interconversions between Catalytic and Inhibited States of the [FeFe]-Hydrogenase from *Desulfovibrio desulfuricans**. *Journal of the American Chemical Society*, 2006. **128**(51): p. 16808-16815.
267. Albracht, S.P., W. Roseboom, and E.C. Hatchikian, *The active site of the [FeFe]-hydrogenase from *Desulfovibrio desulfuricans*. I. Light sensitivity and magnetic hyperfine interactions as observed by electron paramagnetic resonance*. *JBIC Journal of Biological Inorganic Chemistry*, 2006. **11**(1): p. 88-101.
268. McKinnie, R.E. and J.S. Olson, *Effects of solvent composition and viscosity on the rates of CO binding to heme proteins*. *Journal of Biological Chemistry*, 1981. **256**(17): p. 8928-8932.

269. Thauer, R.K., B. Käfer, K. Jungermann, and M. Zähringer, *The Reaction of the Iron-Sulfur Protein Hydrogenase with Carbon Monoxide*. European Journal of Biochemistry, 1974. **42**(2): p. 447-452.
270. Lampret, O., et al., *The roles of long-range proton-coupled electron transfer in the directionality and efficiency of [FeFe]-hydrogenases*. Proceedings of the National Academy of Sciences, 2020. **117**(34): p. 20520-20529.
271. Roseboom, W., et al., *The active site of the [FeFe]-hydrogenase from Desulfovibrio desulfuricans. II. Redox properties, light sensitivity and CO-ligand exchange as observed by infrared spectroscopy*. JBIC Journal of Biological Inorganic Chemistry, 2006. **11**(1): p. 102-118.
272. Senger, M., et al., *Protonation/reduction dynamics at the [4Fe-4S] cluster of the hydrogen-forming cofactor in [FeFe]-hydrogenases*. Phys Chem Chem Phys, 2018. **20**(5): p. 3128-3140.
273. Rodríguez-Maciá, P., et al., *Spectroscopic Evidence of Reversible Disassembly of the [FeFe] Hydrogenase Active Site*. The Journal of Physical Chemistry Letters, 2017. **8**(16): p. 3834-3839.